Design of a Microwave Tomography System for Medical Imaging Applications

Ahsan, Syed Naveed

Awarding institution:
King's College London

Design of a Microwave Tomography System for Medical Imaging Applications

Syed N. Ahsan

Department of Informatics

King's College London

This dissertation is submitted for the degree of

Doctor of Philosophy

Centre for Telecommunications
Research (CTR)

June 2018

To my parents and Panos

Declaration

I hereby declare that except where specific reference is made to the work of others, the contents of this dissertation are original and have not been submitted in whole or in part for consideration for any other degree or qualification in this, or any other University. This dissertation is the result of my own work and includes nothing which is the outcome of work done in collaboration, except where specifically indicated in the text. This dissertation contains less than 65,000 words including appendices, bibliography, footnotes, tables and equations and has less than 150 figures.

Syed N. Ahsan
June 2018

Acknowledgements

This work is multidisciplinary in its nature and therefore I believe that it would not have been possible to complete it without the help of some individuals.

First of all I would like to thank my supervisors, Dr. Panos Kosmas and Dr. Efthymios Kallos for their great support. Their insightful thoughts, suggestions and guidance have materialized this study. Without the invaluable contributions, patience and assistance from them I would not have been able to complete this study. I really thank them not only for sharing their expertise, inspiring ideas and feedbacks but also for directing and facilitating me throughout the course of my PhD.

I want to express my deepest gratitude to School of Natural and Mathematical Sciences who have funded me for my PhD.

I would like to thank COST Action for funding me and Prof. Francesca Vipiana and her group (Jorge, Marco and Mario) at Ploitecnico di Torino, Italy for giving me the opportunity to work with them. I really gained valuable experience working at Polito and learnt a great deal about physical system for microwave imaging.

I owe a big thanks to all my colleagues at MediWise Ltd., Institute of Pharmaceutical Sciences and Centre for Telecommunications Research. My special thanks to Zhenzhuang Miao for all his contributions to this study as an algorithm expert. I thank John Sotiriou for his valuable support in building the prototype. I appreciate the contributions from Rachita and Mohammed for their help in creating phantoms for this study.

I have learnt a great deal from Ioannis, Maria and Helena Cano Garcia, many thanks for being there and helping me. I also owe a big thanks to Bright who got me started on CST and Ziwen for all his support with creating reconstructed images. I am grateful to Dr. Ehsan Ghoreishi and Aravindh for their great support with my thesis editing and formatting.

Lastly, I would like to express my deepest gratitude to my parents, wife and family for having belief in me and continuously and unconditionally supporting me along every step of the way.

Abstract

Microwave tomography (MT) is an emerging imaging modality which aims to recover the dielectric profile of a domain by solving an inverse problem. This is a challenging problem that requires sophisticated algorithms as well as hardware design. This thesis presents a simple and low cost design of a MT system that can operate in the 1-3 GHz frequency range. The hardware prototype of the system is developed from concept to physical realization and is validated against numerical and experimental studies using an in-house inversion algorithm. As with most experimental MT systems presented in the literature, this thesis focuses on cylindrical setups that can be imaged efficiently with a two-dimensional (2-D) inversion algorithm.

Using an antenna that can operate efficiently in the desired MT frequency spectrum is essential for any MT system. To this end, the thesis studies several antenna designs and evaluates their performance by calculating return loss and transmission levels in the desired frequency range. Based on this analysis, we select a custom-made printed monopole antenna with very small size which can operate efficiently across the selected frequency range when immersed in various materials that are used as coupling liquids in microwave tomographic systems.

The selection of coupling medium is quite vital in the design of a microwave imaging system, which is subject to various signals that obscure the response from the object to be imaged. In particular, multipath signal propagation and surface waves along with other degrading factors such as noise, coupling etc., pose significant challenges to data integrity. We address this issue by studying the performance of the selected antenna (stand-alone and as an array) in various coupling liquids, such as water mixed with glycerine or corn syrup. The aim of this study is to ensure that the sensitivity of our MT system is sufficient to detect weak target responses in a practical measurement with a standard vector network analyzer (VNA), while at the same time effects such as antenna coupling and multi-path propagation are minimised.

The thesis also presents a comparison of two possible MT setups: non-immersed configuration, where the array of antennas operates in free space but very close to the imaging

chamber, and an eight-element antenna array immersed inside different coupling liquids. The array performance in the aforementioned configurations is also experimentally assessed, by acquiring data with a two-port vector network analyser (VNA). In terms of the reconstruction scenarios, we focus on two cases that are studied numerically and experimentally: a target inside a cylinder filled with coupling medium, and the target inside a cylinder filled with a low-loss liquid, surrounded by the coupling liquid where the antennas are immersed.

Comparison of our experiments to numerical data suggests that measurements are very sensitive to errors such as cable movements or imprecise spatial positioning of antennas relative to the imaging chamber. To circumvent these issues, we synthesise the array by acquiring data in a bi-static configuration using a robust, mechanically calibrated system which can guarantee accurate antenna positioning. Comparing the measurement data from the bi-static configuration with CST simulation results lead to a much better agreement. This suggests that a significant source of measurement error can be introduced if the multi-static system is not designed with a lot of care on cables positioning.

An in-house inversion algorithm is applied to the acquired data to validate our system's ability to reconstruct cylindrical targets. The cylindrical target is reconstructed successfully using the inversion algorithm with both experimental and simulation data for both imaging scenarios of one and two-layer phantoms. The system is among world's first experimental imaging systems that can reconstruct targets successfully in the wide frequency range of 1-3 GHz.

Table of contents

List of figures

List of tables

Chapter 1

Introduction

1.1 Overview and Motivation for Microwave Imaging

Microwaves range from 300 MHz to 300 GHz range in the electromagnetic spectrum and their wavelengths in free space range from 1 m at 300 MHz to 1 mm at 300 GHz. The interaction of electromagnetic waves with human body has been a topic of interest and has been well studied in [1–3].

Microwaves have been used in therapeutic medicine successfully. Microwave radiometry and hyperthermia have been actively researched for investigating the biological effects and applications of microwaves for several decades [4, 5]. It has been established that hyperthermia assisted cancer therapy renders better survival chances than any of the other forms of cancer treatment acting alone [4, 6]. Therapeutic applications of microwaves also include; RF/Microwave Ablation for the Treatment of Cardiac Arrhythmias, Treatment of Benign Prostatic Hypertrophy (BPH), Microwave Balloon Angioplasty (HMBA), RF in the Treatment of Obstructive Sleep Apnea (OSA), Microwave Assisted Lipoplasty (MAL), Nerve Ablation for the Treatment of Gastro-Esophageal Reflux Disease (GERD), RF Ablation of the Liver (Hepatic RF Ablation), Electrothermal Arthroscopic Surgery [7]. Moreover, microwave enhanced liposuction, RF/ microwaves for enhanced drug delivery, RF/microwaves in treatment of bladder cancer are the newer modalities being researched actively [7]. Above mentioned technologies are some of the therapeutic applications where microwaves have played a vital role in the betterment of human lives.

Microwaves and millimetre waves possess inherent attributes that can be exploited for imaging applications. Long wavelengths of microwaves can penetrate optically opaque objects such as plastics, concrete, soil, etc. As the operating wavelength at microwave frequencies is in the order of few centimetres, the wave can penetrate deep into the object

being imaged. Resolution of an imaging system is greatly affected by the diffraction phenomenon at microwave frequencies but it could be mitigated and optimized by operating in the near field and by using large apertures. Near field microwave imaging applications are generally divided into two categories. In the first category of these applications microwaves or millimetre waves are used to penetrate inside the optical obscurants, for example inner wall and through wall imaging, concealed weapon detection and Ground Penetrating Radar (GPR). The second category of these microwave imaging applications measures properties of the target under study directly for example Radar Cross Section (RCS) and non-destructive evaluation of materials.

Cancer is a generic term for a large group of diseases which involve abnormal growth of cells, with the potential to invade or spread into other parts of the body. According to World Health Organization World Health Organization (WHO) statistics, cancer accounted for more than 8.2 million deaths worldwide in 2012, which is projected to be 22 million within two decades. The breast cancer accounted for 521,000 deaths worldwide, according to 2012 statistics by WHO [8]. It is the second most common cause of the cancer death among women in the UK. However the survival rate of cancer patients is increasing due to the intensive research being carried out to combat cancer. The survival chances of a cancer patient can be increased and mortality rate due to cancer related diseases can be reduced if cancer is detected at an early stage. Therefore, there is a huge demand of cancer diagnostic systems which are precise, reliable and cost effective to use with no or minimal risks to the health of a patient. System designers for cancer diagnostics should also put examinee's safety and comfort at the forefront of their designs.

Cancer detection is one of the emerging application of microwaves where a lot of research and focus has been paid. Breast cancer detection and brain imaging are two examples of microwave diagnostic applications. Microwave medical imaging exploits differences in dielectric properties of tissues that are related to physiological factors such as water content and temperature [9]. Electrical properties of tissues at microwave frequencies have been studied vastly and results from these numerous studies have been published in the literature. Dielectric contrast between healthy and malignant tissues at microwave frequencies forms the basis of microwave medical imaging.

In microwave imaging the potentially infected region of a body is illuminated with electromagnetic pulses at microwave frequencies. The transmitted signals are recorded by an array of sensors (antennas) circumferentially situated around the body of a patient. One antenna transmits while others receive. Electromagnetic pulses coupled into the human body undergo scattering due to non-homogeneity of biological domain comprised of different

tissues. Transmitted pulses inside the body of an examinee, upon interaction with the target, tumour in this case, change direction. Due to this change, circumferentially placed receivers around the body of a patient receive different signals in terms of magnitudes and phases as compared to the case when there is no contrasting object present in the path of propagation. The variation in received signal magnitude and phase is processed through the imaging algorithm and the data is thus translated into useful and informative medical images.

There are two categories of microwave imaging; Radar Based Imaging and Microwave Tomography. In radar-based algorithms, an imaging problem is treated as a linear inverse problem and the resulting images indicate the points of origin of reflected signals of the incident ultra-wideband pulse that was used to illuminate the object being imaged. The frequency of interest ranges from 3-10 GHz in radar based approach. Tomography-based approaches differ from the radar-based category in that they seek to reconstruct the distribution of constitutive parameters of the object. This is usually done iteratively and thus requires significantly more computational power than the radar-based approaches. However, these methods also seem to be better at handling large contrasts between the parameters in the breast, thus leading to algorithms which can be used for a wider range of breast types. The optimum frequencies of operation in microwave tomography are low, in the region of 1-3 GHz.

At present breast cancer detection is mainly carried out with X-ray mammography which is considered as a golden standard for breast cancer detection. Magnetic Resonance Imaging (MRI) is another established method of breast screening. There is a constant ongoing research in quest of finding the best imaging method in terms of quality and cost. X-ray mammography and MRI, despite being established for a long period of time as well as being the most commonly used methods for breast screening, both have their pros and cons. X-ray mammography suffers from high false positive rate and its radiation is ionizing. During the X-ray scan there is a need of breast compression so that the best possible image may be realised. Compression of breast is not a comfortable procedure for a vast majority of patients. MRI is not cost effective and is not suitable for claustrophobic patients as the MRI scanning procedure requires eaximinees to lay inside system's tunnel for the scan. Microwave imaging can potentially address these issues, as microwave radiation is a non-ionizing radiation and the screening procedure does not require breast compression. Due to the non-ionizing nature of the microwave radiation frequent examinations can be carried out in order to diagnose or monitor malignancies. Screening process using microwave imaging modalities only requires the examinee to lay on a bench in prone position for the length of scanning procedure.

Moreover, microwave imaging systems can potentially be very cost effective due to the availability of off-the-shelf RF circuits required to realise the hardware systems.

Microwave technology is also being used in sensing devices which monitor health parameters. Active research has been ongoing on the concept of realization of unobtrusive and wearable sensing devices that can be embedded or worn on-body [10]. Moreover, use of microwaves has also been reported in the intracellular analysis based on microwave dielectric spectroscopy [10].

1.2 Review of State of the Art Microwave Medical Imaging

The first experiments with regards to microwaves as medical imaging modality took place in 1970s when Larsen and Jacobi performed a detailed study on imaging a canine kidney using microwave radiation [11–13]. They successfully imaged the kidney of a canine in 2–D in both frequency and time domain. The variation in the data collected over different tissues was clearly seen in both cases. As a result of Larsen and Jacobi's studies, microwaves rapidly started to become the focus of imaging applications. Early research in the field of microwave imaging identified majority of the challenges involved in near-field imaging of biological tissues. These challenges emerge from the very nature of the microwaves and how they interact with living tissues. Microwaves as imaging application attracted a lot of focus in 1970s and 1980s with radiometry, microwave acoustic systems and microwave imaging.

Dielectric properties of biological tissues form the basis of microwave imaging. Therefore, tissue properties have been studied extensively to enhance the understanding of interaction between tissues and electromagnetic waves at microwave frequencies. Factors such as breakdown of cell membrane due to necrosis and inflammation, charging of the cell membrane, change in the relaxation time of the dielectric and difference in sodium content in the cells affect the contrast between healthy and malignant tissues as described in [14–16]. Foster and Schwan [17] give a comprehensive review on the existing work in the field of dielectric properties of biological tissues and their interaction with microwaves.

Gabriel and Gabriel [18] provide summary of the measurements of different tissues and also report the data obtained from their extensive measurements on healthy cells in [19]. Differences between dielectric properties of healthy cells and malignancies have been specifically studied in the context of breast cancer by various different groups and substantial contrast has been found between the healthy and malignant tissues for e.g. Chaudhary *et al* [20], Suroweic *et al* [21], Campbell and Land [22], Joines *et al* [23], Lazebnik *et al* [24] and many others. Fatty tissues exhibit a large difference in the dielectric values as compared with

malignant tissues, but studies such as in [25] and [26] show that the composition of breast is complex and fibroglandular tissues do not exhibit the same level of dielectric contrast as fatty tissues when compared with malignancies. The fact that fibroglandular tissues demonstrate low contrast ratio with malignancies is very critical. Radiographically denser breasts (rich in fibroglandular content) are common among young women. Therefore, the probability of false positive rate could be higher when screening younger women. Relatively recent work such as presented in [27], [28] and [29] involves use of contrast agents to overcome the challenge posed by low contrast between malignancies and fibroglandular tissues.

An efficient and robust antenna operating at microwave frequency range is a fundamental element of any microwave imaging system, whether tomography or radar based. There are different requirements of antenna characteristics depending on which category of imaging it will be used for. Microwave tomography requires an antenna to operate within 0.5 to 3 GHz as suggested in [30, 31]. Inverse imaging algorithm for microwave tomography requires low frequency operation of antenna used in the system for algorithm stability and higher frequencies are used for resolution enhancement. Radar based microwave imaging methods require the antenna to operate in a wideband range typically between 3-10 GHz. Several antenna designs have been proposed in the context of microwave imaging in literature. Conventional and resistively loaded dipoles and monopoles, double ridged horns, TEM horns, Vivaldi, antipodal slots, bow tie antennas, cavity backed slots, corrugated Vivaldi antenna and printed patch antennas are a few examples of the antenna elements used in microwave imaging systems [32–48]. Most widely used antennas in microwave tomography systems are monopoles [49], double layered Vivaldis [50], waveguides [51] and triangular patches [52]. Radar based microwave imaging category requires transmission and reception of ultra-wideband (UWB) signals, therefore the design of UWB antennas and arrays such as [53], [39], [40] have attracted a lot of attention in the recent past.

Impedance matching with skin layer and crosscoupling between the antenna elements of the array used for data acquisition necessitate the use of an appropriate coupling medium, firstly to couple the energy into the imaging domain and secondly to reduce crosscoupling between the array elements. There is a trade off between signal transmission level and minimization of crosscoupling between antennas, multipath signals, interference and surface wave propagation. Different background dielectric media have been used in the systems realized so far. Water, glycerine-water mixtures with varying degrees of water concentrations and low loss media such as safflower or canola oil are reported in the literature for example [39, 47, 49, 54]. Bindu *et al.* propose different concentrations of water in corn syrup [55] for application in microwave breast imaging. Use of saline and salt water has also been

reported in the literature, for example [56]. A detailed study on the wave propagation through inhomogeneous tissues is reported in [57] where the choice of immersion liquid has been reported from wave propagation point of view. Another comprehensive study on the use of background media is reported in [58, 59].

Microwave tomography is used to reconstruct the dielectric profile of the biological tissue of interior of the imaging domain by solving an inverse problem. The inverse problem is computationally expensive, however, computing power continued to develop and advancement in processing power enabled researchers to exploit non-linear optimization techniques which led to the emergence of iterative methods such as Born Iterative Method and Distorted Born Iterative Method (DBIM) for quantitative imaging [60]. In DBIM algorithms the first task is to linearise the problem by using approximation techniques such as the Born approximation, that gives rise to an ill-posed problem. The linear ill-posed problem can be solved using linear iterative methods such as TwIST or CGLS which are most widely used. A plethora of tomography methods for medical imaging has been reported in literature, for example [61–80].

In radar based imaging methods such as [81] [82], received scattered signal is spatially focused to locate strong scatterers. Confocal microwave imaging [33], beamforming [83] and tissue sensing adaptive radar [84] are some of the examples of qualitative imaging algorithms. The time-reversal technique such as [85] has also been reported in the context of radar based imaging methods. Some preliminary clinical data [86], [87] has also been collected using radar based imaging systems for breast cancer detection. Several alternative approaches to active microwave imaging have also been reported in the literature such as microwave-induced thermos-acoustic tomography (MI-TAT) [88], [89], [90].

Both, microwave tomography and radar based imaging systems have been studied and developed in parallel. As a result of extensive research on dielectric properties of tissues at microwave frequencies to explore contrast ratio between healthy and malignant tissues, antenna designs capable of operating in microwave frequency range and advances in imaging algorithm development, a variety of laboratory microwave imaging prototypes have been developed. Reconstructed images using these prototypes have been reported using the mimicked tissue samples as well as the actual tissues e.g. [51]. Meaney *et al.* developed a tomographic imaging system in Dartmouth College (USA) which was initially designed for non-invasive thermometry but then progressively upgraded into the first laboratory microwave imaging system available for clinical use for breast cancer detection [49]. This system uses 16 monopole antennas in a water coupled environment. Liu *et al.* at Duke University (USA) have been working actively on a tomographic system [91]. Parallel efforts in microwave

tomography from Semenov *et al.* have also been reported [51, 92] where they were able to reconstruct 2-D and 3-D images of heart as well as of the whole body. A wideband microwave system for head imaging has been reported in [93] that employs 16 corrugated tapered slot antennas operating in 1-4 GHz frequency range capable of capturing the backscattered signals to detect stroke or haemorrhage. Reference [94] presents a proof-of-concept microwave bone imaging system using Vivaldi antennas with multilayer phantom. Vipiana *et al.* propose a low cost hardware comprised of in-house off the shelf microwave circuitry and antennas that can compete with the performance of VNA [52]. A planar microwave camera for breast imaging, comprised of 30*30 cm aperture horn antennas is proposed in [95] that operates at 2.45 GHz. Another hardware design for 3D microwave imaging for breast cancer detection has been proposed in [96], where 32 monopole antennas operate between 0.3-3 GHz. A theoretical presentation of a multi-view experimental system for microwave imaging was presented by [97] in early 90s. LoVetri *et al.* present a 2D wideband microwave imaging system that has 24 co resident vivaldi antennas connected to VNA via multi-port switch matrix [50].

Ultra WideBand microwave radar system presented in [98] has shown comparable results with X-Ray mammography. A confocal microwave imaging system is presented in [99]. Parallel efforts on radar based microwave imaging systems and methods have also been reported in [100–102].

The performance of microwave imaging systems has to be assessed ex-vivo before the clinical applications. Therefore, there is a need of developing anatomically detailed anthropomorphic phantoms. Referennce [103] Presents 3D printed head and breast phantoms filled with liquid solutions mimicking biological tissues. A detailed study on fabrication and validation of breast tissue phantoms is presented in [104] where fat, skin, gland and tumour phantoms are made from a combination of chemicals. Fibroglandular content in the breast composition brings complexity in the breast tissue from imaging point of view, as contrast between malignant tissues and fibroglandular content is quite low as compared with the contrast between fatty and malignant tissues. Thus there is a strong urge to study effect of introducing fibroglandular content in the breast phantom. Reference [105] Presents the time domain study of this effect.

In the previous section, importance and significance of microwave imaging has been discussed. This emerging modality is still in its early days and a lot of research needs to be carried out before clinical systems become widespread. There are a few critical challenges being faced in the development of microwave imaging systems. Some of the key challenges are: 1) Low contrast between fibroglandular tissues and malignancies, 2) Requirement of

matching medium, 3) Emergence of surface waves and multipath signals, 4) Need of compact, robust and efficient antenna and 5) Image resolution issue. We have made an attempt to design a microwave tomography system. Our prototype is comprised of a compact printed monopole that exhibits a wideband response when immersed in an appropriate medium, hence allowing us to work with multiple frequencies which is particularly useful in image reconstruction to address ill-posedness of the inverse problem. Our antenna operates between 1-3 GHz frequency range, therefore we can also address the image resolution (high frequency) and penetration depth (low frequency) issues. We have also studied performance of our antenna in an array form with various coupling media to address the key challenges posed by excitation of surface waves and multipath signal propagation.

1.3 Contributions and Relevant Publications

This thesis focuses on the design of a new microwave tomography system that can operate efficiently in the 1-3 GHz frequency range. The thesis' key contributions are listed below:

- Antennas for microwave tomography in the operating frequency range of 1-3 GHz have been designed for microwave imaging application (Chapter 2).
- Non immersed or dielectric loaded antenna array configuration, where the antenna array operates in a very close proximity of dielectric filled imaging chamber is studied numerically and experimentally (Chapter 3).
- Simulation and results of the 16 element antenna array in immersed configuration have been presented where the effect of system geometry and spatial distribution of antenna array is studied (Chapter 4).
- Study on the selection and optimization of coupling medium to assess the system sensitivity is carried out for immersed antenna array (Chapter 5).
- Two data acquisition systems are studied in Chapter 6. A system prototype is proposed with robust mechanical features to minimize the experimental errors. Different coupling media have been used to experimentally study the impact of dielectric media on the array performance in the physical environment. Two layer phantom for enhanced transmission is experimentally studied and validated. The reconstruction algorithm has been applied to experimental and 3D CST simulation data for image reconstruction (Chapter 6).

The publications related to the key contributions of this work are stated below:

1. S. Ahsan, B. Yeboah-Akowuah, P. Kosmas *et al.*, "Balanced antipodal vivaldi antenna for microwave tomography" 20 Jan 2015 Proceedings of the 2014 4th International Conference on Wireless Mobile Communication and Healthcare, MOBIHEALTH 2014. Athens : Institute of Electrical and Electronics Engineers Inc., p. 316-319 7015974

2. S. Ahsan, P. Kosmas *et al.*, "Balanced antipodal antenna array for microwave tomography", 6 Jan 2015 2014 IEEE Conference on Antenna Measurements and Applications, CAMA 2014. Institute of Electrical and Electronics Engineers Inc., p. 1-3 7003359

3. S. Ahsan, Z. Guo, I. Gouzouasis, E. Kallos, P. Kosmas, "Development of a slotted triangular patch antenna for microwave tomography", 31 May 2016 2016 10th European Conference on Antennas and Propagation, EuCAP 2016. Institute of Electrical and Electronics Engineers Inc., 7481670

4. Z. Miao, S. Ahsan, P. Kosmas *et al.*, "Application of the DBIM-TwIST algorithm to experimental microwave imaging data", 5 May 2017 2017 11th European Conference on Antennas and Propagation, EUCAP 2017. Institute of Electrical and Electronics Engineers Inc., p. 1611-1614 7928605

5. M. Koutsoupidou, P. Kosmas, S. Ahsan *et al.* "Towards a microwave imaging prototype based on the DBIMTwIST algorithm and a custom-made transceiver system", 2017 International Conference on Electromagnetics in Advanced Applications (ICEAA), Verona, 2017, pp. 1004-1007.

Submitting Papers

1. S. Ahsan, Z. Miao, P. Kosmas, “Design and Experimental validation of a wideband microwave tomography system”. (Ch.6)

2. Z. Miao, S. Ahsan, et al., “A frequency selection method to reduce errors in microwave tomography”. (Ch.6)

1.3.1 Thesis Structure

The remainder of this thesis is structured as follows. Antenna designs for microwave tomography system are presented in Chapter 2, where we propose various antenna designs suitable for

microwave tomography frequency range operating inside and outside of dielectric medium. The study of four element antenna array operating outside of a dielectric filled cuboid has been discussed in Chapter 3, where the results of simulations as well as experiments are presented. Chapter 4 presents the performance of an antenna array immersed in coupling medium, where the focus is to study the effects of array location within the imaging chamber on signal propagation and how to mitigate the different signal degrading factors. Chapter 5 presents study of a variety of coupling media to be used in our imaging system for the performance evaluation of an immersed array from signal propagation point of view. The purpose is to choose the best matching liquid for our future experiments. The hardware development and experimental results using two different prototypes constituting of 16 and 8 antenna locations are presented in Chapter 6. At first, experimental results with a rotary data acquisition system representing 16 antenna locations in different target and without target scenarios are presented. Subsequently results from our in-house prototype capable of recording 8 antenna locations are presented in Chapter 6. Experimental analysis of the impact of different dielectric media in single and two layer phantom formation on signal propagation is also presented in Chapter 6. Finally, our in-house reconstruction algorithm (developed by our colleague Zhenzhuang Miao) based on DBIM TwIST has been tested with our experimental data and the resulting images are presented in Chapter 6. Conclusion of the thesis and future work is provided in Chapter 7.

Chapter 2

Background and Antenna Design

2.1 Overview and Motivation

Antenna design is one the most important and foremost aspect of a microwave imaging system. There are several constraints which make antenna design for such systems more challenging. Study presented in [106] shows that the degree of ill-posedness of the inverse algorithm varies with the number and location of observations, hence prompting for the need of compact antennas. The number of frequencies used also effect ill-posedness of the inverse algorithm which leads to the requirement of a wideband antenna for the tomographic system [30, 31]. Each antenna element should occupy a very small footprint relative to the total surface area of breast that necessitates the need of as much directional antennas as possible. Higher gain at the designed frequencies is very crucial as it provides a higher signal to noise ratio and imaging sensitivity, in particular when the high loss coupling medium is applied for impedance matching.

Tomographic systems, hence, require antenna elements that operate in the frequency range of 1–3 GHz. Frequencies below and above this range are non-optimal for the spatial resolution and penetration depth respectively. Double layered Vivaldi [50], waveguide antennas [51] and simple monopoles [107] have been reported in the literature for microwave tomography applications. Aforementioned antennas operate in high loss dielectric media to obtain wideband response and low frequency operation.

Antenna performance also depends on the type of immersion being used for matching. Antenna distance from the examinee's tissue is also critical as the tissue imposes a bulk load of high permittivity on antenna's radiating near-field. Therefore, an antenna design is required whose performance doesn't significantly change under the above mentioned factors. For radar based imaging systems an Ultra Wideband (UWB) antenna is the fundamental

requirement for sending and receiving electromagnetic pulses. Different antenna designs have been reported in the literature such as resistively loaded dipole [84], planar tapered slot antenna [43], ridged pyramidal horn antenna [37] and stacked patch antenna [108], balanced antipodal Vivaldi antenna (BAVA) with director [39] among many others.

Based upon the needs of a microwave imaging system and the challenges being faced in achieving the goals to successfully implement a microwave imaging prototype, we are making an effort to design the antennas that can combat with these challenges. Our rationale for antenna design is to make them as compact as possible and to achieve an efficient operation between 1-3 GHz frequency range. This frequency band of antenna operation is very critical in microwave tomography due to the above mentioned challenges. Our proposed designs will also focus on optimizing dimensions of the antenna structures. Performance of the imaging algorithm greatly depends on the number of antenna elements in an array form to send and receive pulses through the imaging domain, hence compact antennas are required to capture multiple views of imaging domain by installing multiple compact antennas inside the imaging chamber to deal with ill-posed inverse problem and consequently obtain better quality images. Efficiency of an antenna is also very important as there are existing antennas that can perform the imaging tasks but they suffer from efficiency issues, such as monopole antennas. These antennas have omnidirectional radiation pattern, this results in mutual coupling between antenna elements of the array and propagation of energy in the undesired direction.

2.2 Background Theory

We start with presenting the preliminary information from the basic text of fields and waves, antenna theory and microwaves in communication electronics. Our overall study entails design of antenna and performance of the array of antenna elements in dielectric media which requires basic understanding of the wave propagation in media as well as antenna design and its key parameters such as gain, impedance, directivity, polarization and radiation pattern etc. As our antennas will be operating either outside of a dielectric filled imaging chamber or immersed inside the cavity filled with coupling liquid, therefore we will also present the dispersive characterization of dielectric media.

2.2.1 Maxwell's Equations

James Clerk Maxwell described the electric and magnetic phenomenon at macroscopic scale which comes from the fundamental postulate for electromagnetic induction in the case where

time varying magnetic field gives rise to electric field [109]. Maxwell's equations formulate relationship between the varying electric and magnetic fields, hence they play a vital role in the study of electromagnetism where we deal with time varying electromagnetic fields. Maxwell's equations can be represented in point or differential form, integral form or phasor form depending on the requirement of the analyses. We mention only the differential form here for brevity.

Gauss's law:

$$\overrightarrow{\nabla} \cdot \overrightarrow{E} = \rho \tag{2.1}$$

No isolated magnetic charge:

$$\overrightarrow{\nabla} \cdot \overrightarrow{B} = 0 \tag{2.2}$$

Faraday's Law:

$$\overrightarrow{\nabla} \times \overrightarrow{E} = -\frac{\partial \overrightarrow{B}}{\partial t} \tag{2.3}$$

Ampere's Law:

$$\overrightarrow{\nabla} \times \overrightarrow{H} = \frac{\partial \overrightarrow{D}}{\partial t} + \overrightarrow{J} \tag{2.4}$$

In the above equations $\overrightarrow{E}$ is electric field with MKS units $\frac{V}{m}$, $\overrightarrow{H}$ is magnetic field with the units $\frac{A}{m}$, $\overrightarrow{D}$ is the flux density with the units of $\frac{Coul}{m^2}$, $\overrightarrow{B}$ is the magnetic flux density with units $\frac{Wb}{m^2}$, M is the fictitious magnetic charge, $\overrightarrow{J}$ is the electric current density in $\frac{A}{m^2}$ and ρ is the electric charge density with the units of $\frac{Coul}{m^3}$.

Following constitutive relations hold between electric and magnetic field intensities and flux densities:

$$\overrightarrow{B} = \mu_0 \overrightarrow{H} \tag{2.5}$$

$$\overrightarrow{D} = \varepsilon_0 \overrightarrow{E} \tag{2.6}$$

$$\overrightarrow{J} = \sigma \overrightarrow{E} \tag{2.7}$$

Where μ_0 is $4\pi \times 10^{-7}$ $\frac{Henry}{m}$ is permeability of the free space and ε_0 8.854×10^{-12} $\frac{Farad}{m}$ is permittivity of the free space and σ is the material conductivity in $\frac{S}{m}$.

Field vectors in media are related to each other by the constitutive relations. An applied field $\overrightarrow{E}$ causes the polarization of the molecules or atoms of the material which gives rise to

the dipole moment that augments the displacement flux, $\overrightarrow{D}$.

$$\overrightarrow{D} = \varepsilon_0 \overrightarrow{E} + \overrightarrow{P_e} \tag{2.8}$$

This additional vector is called electric polarization $\overrightarrow{P_e}$ where,

$$\overrightarrow{P_e} = \varepsilon_0 \chi \overrightarrow{E} \tag{2.9}$$

Where χ_e is the electric susceptibility and may be a complex value. Hence,

$$\varepsilon = \varepsilon' - j\varepsilon'' = \varepsilon_0(1 + \chi_e) \tag{2.10}$$

Where, ε is the complex permittivity, the imaginary part of ε accounts for the losses in the medium due to damping of the vibrating dipole moments. Microwave materials are usually characterized by their real permittivity ε' and the loss tangent (defined below) at a specific frequency.

$$\tan\delta = \frac{(\omega\varepsilon'' + \sigma)}{\omega\varepsilon'} \tag{2.11}$$

Equation 2.11 represents the loss tangent of a material.

Electromagnetic field properties can be formulated using Maxwell's equations in a 3D space. 3D representation results in a computationally heavy 3D vectorial problem. *A priori* information about the system under consideration can lead to simplify the 3D problem by making some logical assumptions and converting the problem into 2D. Therefore, if the object of interest is considered to be non-magnetic and is assumed to be infinite and its dielectric properties remain unchanged along vertical axis then the problem can be reduced to a 2D scalar version (TM polarization) and a scalar wave equation can be used when the field is along vertical axis, whereby implicit time dependence can be chosen as $e^{-j\omega t}$ and ω being the angular frequency.

Electric field in homogeneous media can be represented in the wave form described by Helmholtz equation as below:

$$\nabla^2 \overrightarrow{E} + \omega^2 \mu\varepsilon \overrightarrow{E} = 0 \tag{2.12}$$

Where $\omega\sqrt{\mu\varepsilon}$ can be replaced with a constant 'k' known as propagation constant or wave number.

Total electric field is the field propagating through the inhomogeneous medium. Helmholtz equation for inhomogeneous medium can be written as:

$$(\nabla^2 + k^2(\overrightarrow{r}))E(\overrightarrow{r}) = 0 \tag{2.13}$$

The term 'k' in equation 2.13 depends on the dielectric properties of the medium in which the wave propagates.

2.2.2 Antenna Parameters

An antenna is a component that converts a wave propagating on a transmission line to a wave propagating in a medium or free space. Antennas are capable of transmitting and receiving the electromagnetic waves.There are different types of antennas such as dipole, monopole, loop, horn, helical, patch, Yagi-Uda, parabolic antennas etc. The choice of antenna is quite application specific, however there are some antenna parameters that can describe any antenna. A brief introduction to the antenna parameters is given below.

Radiation Pattern: Power received at an antenna is a function of angular position and radial distance from the transmitting antenna that radiates power. At electrically larger distances (multiple wavelengths λ away from the source) the power density drops off as $\frac{1}{R^2}$ in any given direction. The variation of power density with angular position is determined by the type of antenna. The graphical representation of the power with the radial and angular distance is called the 'Radiation Pattern' of an antenna. The radiation plots can be either three dimensional graphs of power versus the elevation and azimuth angles, however in general the radiation patterns are represented by principal plane pattern plots such as the E-plane or H-plane where one angle is held fixed and the other varied.

Far Field: Region away from antenna where the radiated energy from the antenna element takes the shape of a plane wave is called the far field region. A typical criteria for identifying far field region is $\frac{2D^2}{\lambda}$ where 'D' is the largest dimension of the antenna and λ is the operating wavelength in the medium. It is also worthwhile noting that the radiation patterns are valid in far field regions.

Directivity: Directivity is a parameter that depends on the radiation pattern of the antenna. A quantitative measure of the radiation pattern in a fixed direction is called the directive gain of the antenna. Maximum value of the directive gain is 'Directivity' of the antenna. In the 1983 version of *IEEE* Standard Definitions of Terms of Antennas, directivity is defined as the ratio of the radiation intensity in a given direction from the antenna to the radiation intensity averaged over all directions. The directive gain of an antenna is represented as $D(\theta, \phi)$. The

directive gain compares the radiant intensity (power per unit solid angle) that an antenna creates in a particular direction against the average overall value over all directions. If $U(\theta,\phi)$ represents the radiant intensity of the antenna then the directivity can be formulated as follows:

$$D(\theta,\phi) = \frac{U(\theta,\phi)}{P_{total}/(4\pi)} \tag{2.14}$$

The denominator of equation 2.14 is the averaged power, that is obtained by dividing the total power by 4π; solid angle.

$$P_{total} = \int_{\phi=0}^{\phi=2\pi} \int_{\theta=0}^{\theta=\pi} U sin\theta d\theta d\phi \tag{2.15}$$

As per definition, directivity is the maximum radiation intensity in a given direction, therefore equation 2.16 represents the directivity of the antenna mathematically.

$$D = max\left(\frac{U(\theta,\phi)}{P_{total}/(4\pi)}\right) = \frac{U(\theta,\phi)_{max}}{\frac{1}{4\pi}\int_0^{2\pi}\int_0^{\pi} U(\theta,\phi) sin\theta d\theta d\phi} \tag{2.16}$$

Efficiency: Ratio of total radiated power by the antenna to the input power is known as the efficiency of the antenna. There are different factors such as ohmic or dielectric losses which may account to the power not being radiated thus efficiency is an important parameter of the antenna that quantitatively describes how efficient is an antenna.

Gain: Product of directive gain and efficiency of the antenna is called 'Gain'. The impact of losses on radiation power density in a given direction is accounted for with the gain parameter.

Impedance: An antenna presents a driving point impedance to the source or load connected with it, impedance matching is of fundamental significance in order for the antenna to absorb power, thus input impedance of an antenna should be matched with feed line. The impedance mismatch degrades performance of the antenna significantly.

Bandwidth: Bandwidth of an antenna is defined as the range of frequencies over which antenna is able to operate correctly. Bandwidth is typically represented by voltage standing wave ratio (VSWR). The acceptable value of reflection coefficient that indicates a good matching is application specific, however, an S_{11} of -10 dB is typically considered as a good reflection parameter of an antenna, indicative of a good impedance match. The range of frequencies for which $VSWR < 2$ (equivalent of -10 dB reflection parameter) is called bandwidth of an antenna. Usable bandwidth of an antenna is limited by the impedance

mismatch and pattern deterioration. Matching circuits are used to increase impedance bandwidth of the antenna.

Polarisation: The orientation of electric field vector is called polarization of the radiated wave. There are different types of polarizations such as vertical, horizontal, circular or elliptical. Circular polarization is further divided into two: Right Hand Circular Polarization (RHCP) and Left Hand Circular Polarization (LHCP).

2.2.3 Dispersive Characterization of Dielectric Media

Our inversion algorithm is based upon Finite Difference Time Domain (FDTD) method. In computational electrodynamics modelling interaction of electromagnetic wave with materials having frequency dispersive characteristics at the wavelength or sub-wavelength scale requires electromagnetic characterisation of these materials. The frequency dependence of materials can lead to non-linearity and/or gain. The key electromagnetic characteristics of a material are 1) Linear dispersion 2) Nonlinearity 3) Nonlinear dispersion and 4) Gain.

There are three general classes of linear, isotropic material dispersions amenable to FDTD modelling 1) the Debye relaxation, 2) the Lorentzian resonance and 3) the Drude model of metals.

Debye Model for Materials: A complex valued susceptibility function $\chi(\omega)$, characterizes Debye media in frequency domain. $\chi(\omega)$ has one or more real poles at different frequencies. A single pole Debye medium can be described as:

$$\chi_p(\omega) = \frac{\varepsilon_{s,p} - \varepsilon_{\infty,p}}{1 + j\omega\tau_p} \tag{2.17}$$

where $\varepsilon_{s,p}$ is the static (non zero) relative permittivity, $\varepsilon_{\infty,p}$ is the relative permittivity at infinite frequency and $\Delta\varepsilon_p = \varepsilon_{s,p} - \varepsilon_{\infty,p}$ is the change in relative permittivity due to Debye pole and τ_p is the pole relaxation time. Equation 2.14 can be extended to 'p' pole Debye medium:

$$\varepsilon(\omega) = \varepsilon_\infty + \sum_{p=1}^{p} \frac{\Delta\varepsilon_p}{1 + j\omega\tau_p} \tag{2.18}$$

The Cole-Cole model of materials is defined as:

$$\varepsilon_r(\omega) = \varepsilon_r'(\omega) - \varepsilon_r''(\omega) = \varepsilon_\infty + \frac{\varepsilon_s - \varepsilon_\infty}{1 + (j\omega\tau)^{1-\alpha}} + \frac{\sigma_s}{j\omega\varepsilon_0} \tag{2.19}$$

where ω is the angular frequency, $\varepsilon_r'(\omega)$ is the frequency dependent term of permittivity and $\varepsilon_r''(\omega)$ is the frequency dependant dielectric loss that can be converted into effective

conductivity $\sigma(\omega) = \omega\varepsilon_0\varepsilon''(\omega)$. α is a fitting parameter. A single pole Cole-Cole model is given below:

$$\frac{\varepsilon(\omega)}{\varepsilon_0} = \varepsilon_\infty + \frac{\varepsilon_s - \varepsilon_\infty}{1 + (j\omega\tau)} + \frac{\sigma_s}{j\omega\varepsilon_0} \tag{2.20}$$

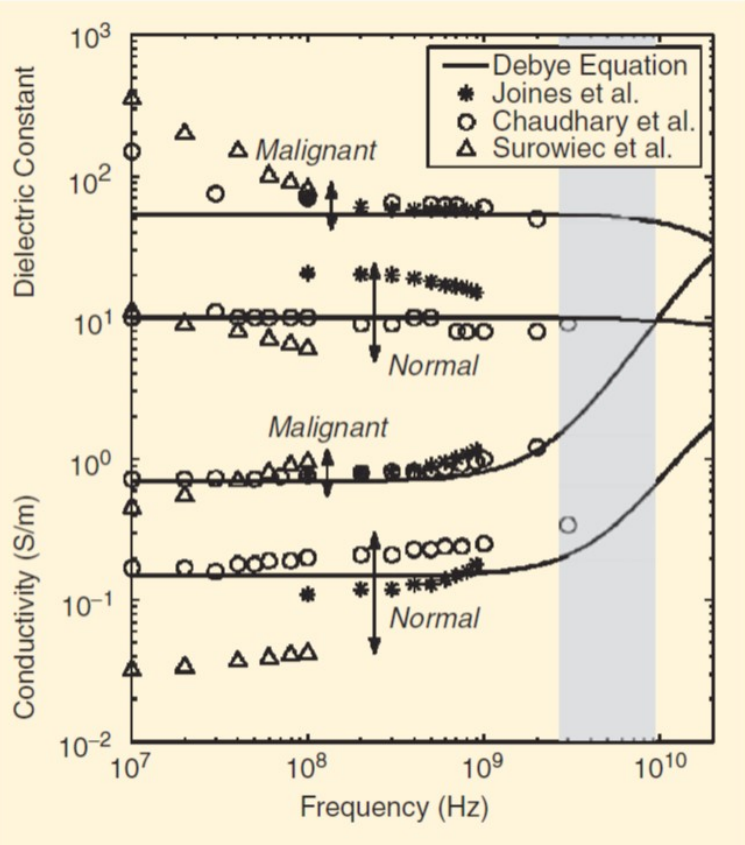

Fig. 2.1 Measured dielectric-properties data for normal and malignant breast tissue at radio and microwave frequencies [99].

Measured dielectric properties of healthy and malignant breast tissues by different research groups are summarized in Fig. 2.1. Dielectric contrast between malignant and healthy tissues is observed to be 10:1. However this contrast ratio between the high fibroglandular content and malignancies drops down to 10% which is a big challenge in MT to deal with.

2.2.4 Introduction to Patch Antennas

Our objective is to design a compact and wideband antenna for the microwave tomography system being sought. Patch antennas are planar, compact and can be made wideband using

different techniques proposed in the literature. Therefore, a patch antenna can potentially be a good candidate for our imaging system requirements.

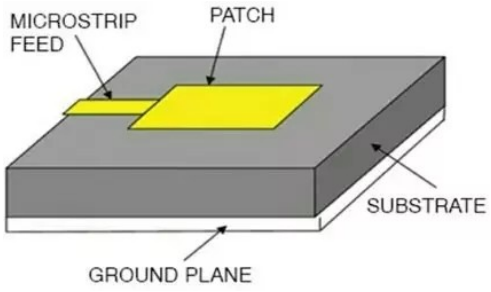

(a)

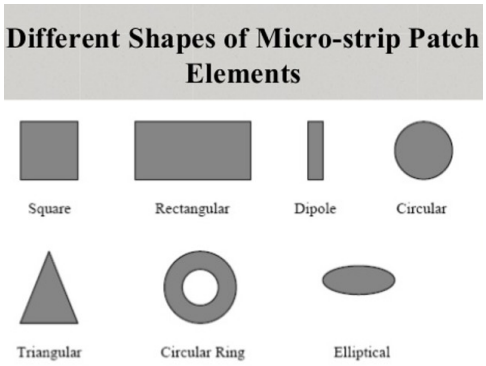

(b)

Fig. 2.2 (a) Simple rectangular patch antenna, (b) different shapes of patch elements.

Patch antenna concept was first proposed by Deschamps in 1953, however micro-strip/ patch antennas gained popularity in 1970s when Munson and Howell made further developments of the concept. There are many advantages of patch antennas such as low cost of fabrication, conformal structure, easy to form arrays, light weight etc. Patch antenna has a few disadvantages such as limited bandwidth and low power handling. Bandwidth can be enhanced by using different techniques and adding complexity in the antenna design. The increasing demand of personal and mobile communication that requires conformal, compact and low profile antennas has become reason for the popularity of patch antennas over the recent years.

A radiating element known as patch, a ground plane and a dielectric substrate are constituting elements of a patch antenna. Radiating patch of the antenna is on one side of a dielectric substrate and a ground plane on the other side. Fig. 2.2 (a) shows a simple rectangular patch antenna with substrate, ground plane and microstrip feed line. There are different shapes of the radiating elements of a patch antenna such as square, circular, triangular, semicircular, sectoral, and annular ring as shown in Fig. 2.2 (b). Most commonly used feeding techniques of a microstip patch antenna are 1) probe feed, 2) microstrip transmission line, 3) proximity coupling, 4) aperture coupling and 5) coplanar waveguide feed. Principle of radiation of the patch antenna emerges from fringing fields between the periphery of patch and ground plane.

Patch antenna analysis methods are divided into two groups. Analytical methods of the first group are based on magnetic current distribution around the patch edges. Three popular techniques based on magnetic current distributions are 1) Transmission line model, 2) Cavity

model and 3) Multiport Network Model (MNM). The second group of analytical methods are based on distribution of electric current on the patch conductor and on ground plane. There are various numerical techniques for this group of analyses such as 1) method of moments (MOM), 2) finite element method (FEM) 3) finite difference time domain method (FDTD).

Rectangular patch antenna is the most widely used microstrip antenna. A rectangular patch is defined by its length and width. Typically, the length and width of a patch antenna are comparable in size as opposed to microstrip lines where width is much smaller than the length. For the fundamental mode TM_{10}, the length of patch antenna is slightly less than half the wavelength $\frac{\lambda}{2}$ inside a dielectric medium. λ is the wavelength in dielectric medium of ε_r ($\frac{\lambda_0}{\sqrt{\varepsilon_e}}$). ε_e is the effective permittivity and is slightly lower than ε_r and is computed as below:

$$\varepsilon_e = \frac{(\varepsilon_r + 1)}{2} + (\frac{\varepsilon_r - 1}{2})[1 + \frac{10h}{W}]^{-\frac{1}{2}} \tag{2.21}$$

where h is the height of substrate and W is the width of patch. The resonant frequency of rectangular patch is [110]:

$$f_0 = \frac{c}{2\sqrt{\varepsilon_e}}[(\frac{m}{L})^2 + (\frac{n}{W})^2]^{-\frac{1}{2}} \tag{2.22}$$

The terms 'm' and 'n' represent the number of half cycle field variations along the length and width of the antenna respectively. The modes of propagation of the antenna are represented by the terms 'm' and 'n' where the dominant mode of propagation is determined by the combination of these terms that yield the lowest resonant frequency. TM_{10} is the dominant mode of operation for rectangular patch antennas where L $>$ W.

Rectangular patch antennas yield linear polarization, circular polarization can be achieved by dual feeding the antenna with 180° phase difference between the feeds.

Resonant frequency of a circular patch is [110]:

$$f_0 = \frac{K_{mn}c}{2\pi a_e\sqrt{\varepsilon_e}} \tag{2.23}$$

where K_{mn} is the mth root of the derivative of Bessel function of order n. The value of Kmn is 1.84118 for fundamental mode TM_{11}. a_e and ε_e are the effective area and permittivity respectively.

Resonant frequency of an equilateral triangular patch is [110]:

$$f_{mn} = \frac{2c(m^2 + mn + n^2)^{-\frac{1}{2}}}{3S_e\sqrt{\varepsilon_e}} \tag{2.24}$$

where S_e is the effective side length and has a simplified formula:

$$S_e = S + \frac{4h}{\sqrt{\varepsilon_e}} \tag{2.25}$$

S is the length of a side of the triangular patch of the antenna. TM_{10} is the fundamental mode of triangular patch antennas.

The performance of regular shaped patch antennas is generally almost very similar to each other, however rectangular and circular patches yield slightly higher gain and bandwidth as compared to other standard shape patches whereas triangular patch can be used where compact design of the antenna is required.

To design a compact patch antenna in UHF frequency range and also to achieve a broadband operation the regular rectangular or circular patch configuration has to be modified. Compact microstrip antenna can be designed using a high dielectric substrate, however the bandwidth in this case is narrow. In order to achieve a compact antenna design, use of shorting posts and cutting slots in the patch has been reported in literature. Shorting the zero potential surface of the patch results in halving the patch dimensions, however the resulting antenna suffers from poor gain and degradation of radiation pattern. Cutting slots on the patch also results in dropping the operational frequency of the antenna by making surface currents travel longer paths on patch surface and keeping the antenna compact. A hybrid of using shorting pin and etching slots can result in achiving a compact patch antenna. Bandwidth of these planar compact patch antennas can be increased by using a thick layer of substrate or by using multiresonator technique. planar monopole antennas with wide impedance bandwidth are also reported in literature for wideband operation.

2.2.5 Existing Microwave imaging System Prototypes

We present three state of the art microwave imaging systems in this section. Two of the systems presented here are designed for microwave tomography and the third system is based on radar based reconstruction method.

The clinical prototype of a microwave imaging system shown in Fig. 2.3 proposed by researchers at Dartmouth College in the US is one of the first microwave tomography

Fig. 2.3 Existing microwave tomography system at Dartmouth College USA [49].

systems. The breast is actively illuminated with a 16-element transceiving monopole antenna array in the 300–1000 MHz range. In-vivo studies have been carried out on five women subjects. Water-coupled interface is used as a matching medium to couple the microwave energy into the pendant breast with the subject positioned prone on an examination table. The examination sessions last 10–15 minutes per breast and includes full tomographic data acquisition at seven different array heights beginning at the chest wall and moving anteriorly toward the nipple for seven different frequencies at each array position. The system has a dynamic range of 130 dB and channel to channel isolation of 120 dB.

The microwave tomography system shown in Fig. 2.4 (left) is developed at University of Manitoba Canada. This system employs 24 co-resident double layer Vivaldi antennas inside a dielectric filled chamber. The double layered Vivaldi antennas used in this system operate from 3 to 10 GHz frequency range. Double layer construction of these antennas results in reducing the cross polar levels. This system is capable of collecting data in 3 to 6 GHz frequency range. The antenna elements of this setup are connected to a vector network analyzer via a 2×24 port cross bar switch. Crosscoupling between the antenna elements of this system has been reported to be one of the major sources of error which is attempted to be minimized by the use of special frequency selection method [50]. The dynamic range of this system is 122 dB which can be extended by 15 dB by using configurable test set. The channel isolation of this system is reported to be greater than 95 dB. The imaging chamber is of 22 cm diameter and 50.8 cm tall.

The system shown in Fig. 2.4 (right) is the UWB microwave radar. Cavity backed aperture stacked-patch antennas operating in 4.5 to 10 GHz frequency range are used in

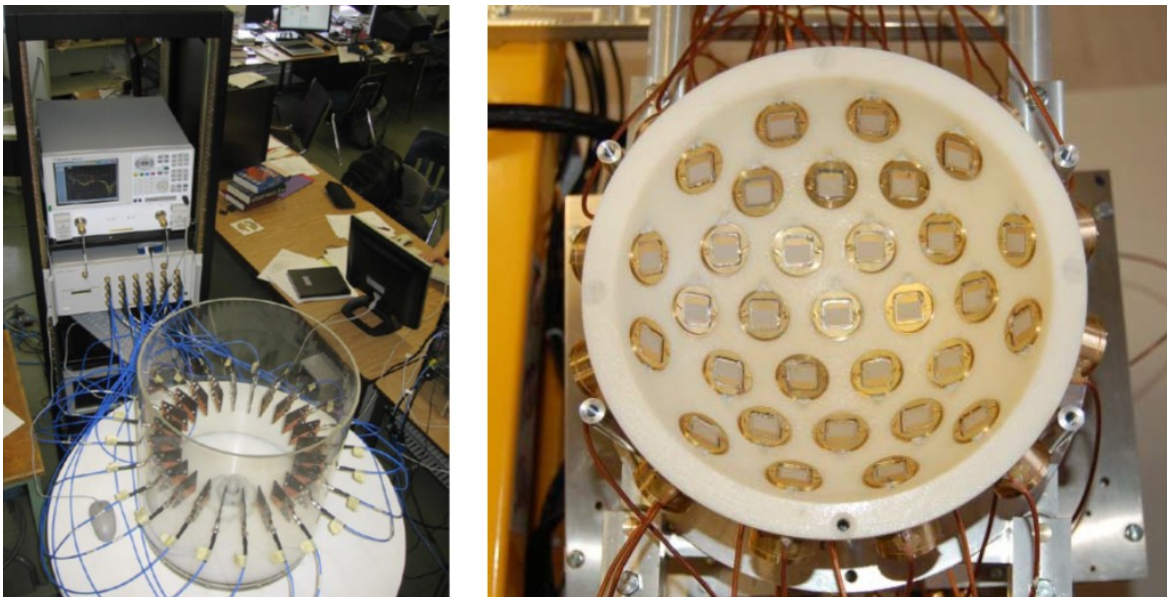

Fig. 2.4 Existing microwave tomography system prototype (left) at the University of Manitoba Canada [50] and radar based imaging system prototype (right) at Bristol University [98].

the form of a hemispherical conformal array in this setup. The conformal array is formed around lower section of a 78 mm hemisphere. The matching liquid used in this setup has a relative dielectric constant of approximately 9.5 and attenuation of 1.2 dB/cm at 6 GHz. The measurements are taken with the custom built electromechanical switches which select all the possible pairs of antennas within the array. 3D breast phantoms are also created where a 2mm thick skin layer of 58 mm radius hemisphere lies 20 mm above the antennas. The materials used to mimic skin, fat and tumour are dispersive. The relative permittivity of skin at 6 GHz is 30 and attenuation constant is 16 dB/cm, for tumour the permittivity is 50 and conductivity is 7 S/m at the same frequency. To obtain the 3D images post-reception synthetic focusing is employed where Delay and Sum (DAS) beam-forming and data-adaptive focusing algorithm based on robust Capon beamforming (RCB)are applied.

2.3 Antennas for Microwave Imaging

Microwave imaging system requires efficient, reliable, compact and robust antenna element for the optimum performance therefore the first step towards designing such systems is the selection of appropriate antenna. Six different types of antennas have been considered in this study, which include:

- Multi Band Patch Antenna

- Balanced Antipodal Vivaldi Antenna (BAVA)
- Triangular Patch V Slot Antenna
- Monopole Antenna
- Circular Patch Antenna
- Printed Monopole Antenna

We considered multiband patch antenna due to its compact size and dual band operation which is suitable for our tomography system. We study the mutliband antenna for low frequency operation for the dominant mode as close as possible to 1 GHz. BAVA is an ultra wideband antenna that operates in 3-10 GHz frequency range, we make an attempt to lower the operational frequency range of BAVA to our required tomography frequency of interest.

Triangular patch V slot antenna has been designed for hyperthermia application, we optimize this antenna operating in front of a dielectric filled chamber for our microwave tomography system, we also present a smaller more compact version of V slot antenna. We propose a very simple and compact resonant circular patch antenna with full ground plane, operating in front of a dielectric filled tank.

Monopole antennas have been widely studied in the context of microwave tomography, we use this wire antenna to study the pros and cons of using long wire antennas in imaging system design.

Our final design is a planar compact printed monopole antenna. Our printed monopole exhibits wideband response in the desired frequency range of a microwave tomography system. We designed this antenna after carefully considering all the challenges we encountered with various different designs we proposed previously. For example, the compact size of this antenna is particularly advantageous when incorporating multiple antennas in the array form. Our Vivaldi design was 100*70 mm as opposed to 12*15 mm printed monopole.

Our triangular patch V slot antenna despite showing multiple resonances at low (1.5 GHz) and high (3 GHz) frequencies did not offer a wide range of frequencies in 1-3 GHz band, whereas this printed monopole shows a complete wideband response in 1-3 GHz range. Large thickness (14.4 mm) of V slot antenna resulted in a heavy structure which was an undesired feature for the implementation of the hardware prototype in sight, on contrary the planar printed monopole has a substrate thickness of 1mm.

The monopole antenna is 154 mm long, therefore we require a very large imaging chamber to be able to work with it, on the other hand our printed monopole is on 15 mm long a tenth of wire monopole, that allows us to build a simple and low cost prototype. In

summary the compact size and wideband operation of printed monopole antenna makes it the most suitable candidate for our MT system prototype.

The details of each type of antenna considered for this research are given in the subsequent sections.

2.3.1 Multiband Patch Antenna

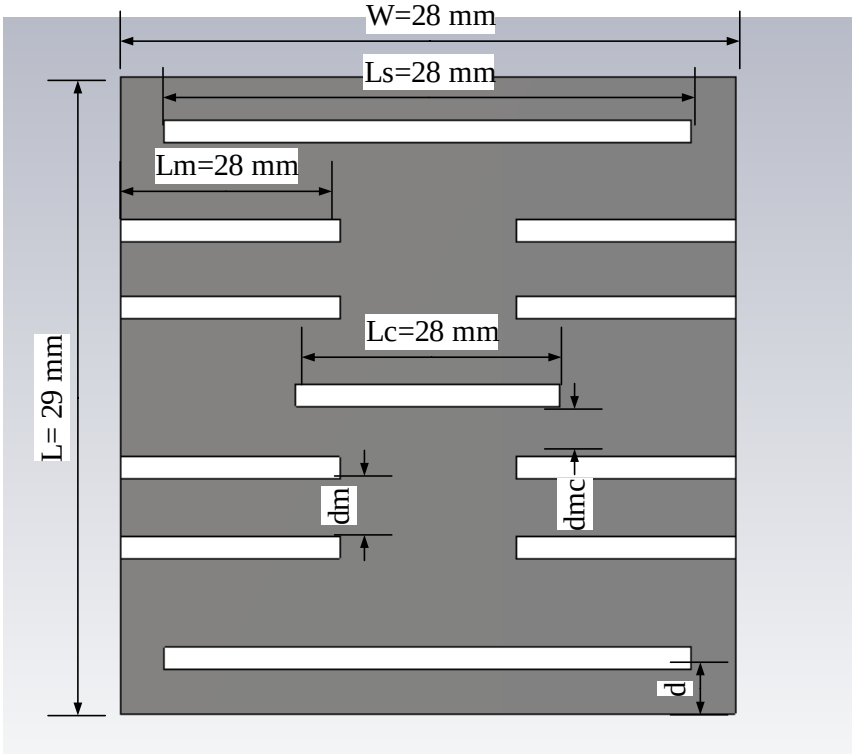

Fig. 2.5 Slot loaded multi-band antenna modelled in CST MWS with dimensions in mm [47].

Multiband approach in microwave imaging algorithms is becoming popular as it offers ways to combat and mitigate the ill-posed problem by offering more frequency samples, therefore researchers have been trying to design antennas that can operate at multiple frequencies. Dual band antenna with meandering slots has been proposed in [47]. The antenna with radiating edge slot (Ls) has been optimized for slot lengths and is reported in [111].

The structure of multiband antenna modelled in Computer Simulation Technology (CST) Microwave Studio (MWS) and its respective design parameters are shown in Fig. 2.5. Multiband rectangular patch antenna has been immersed in low loss Safflower oil. First order Debye properties of the immersion have been considered for this study. The first order Debye parameters of the liquid immersion are $\varepsilon_\infty = 2.24$, $\varepsilon_s = 2.97$, $\sigma_s = 0$ and $\tau = 5$ ps.

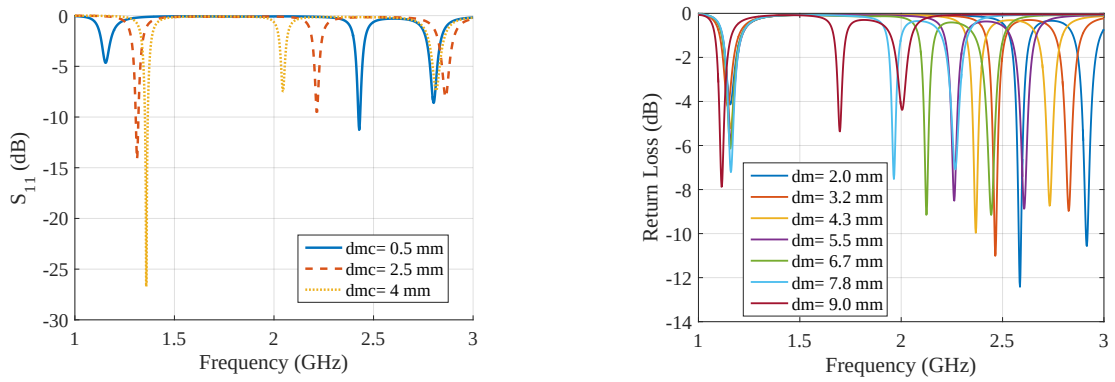

(a) (b)

Fig. 2.6 Optimization of multi-band antenna. (a) parametric sweep on centre slot to meandering slot distance 'dmc' at constant meandering slot distance 'dm' 3.5 mm, (b) variation in meandering slot distance 'dm' while 'dmc' is constant at 0.5 mm.

Top view of the antenna modelled in CST MWS is shown in Fig. 2.5 where the dimensions shown are in 'mm'. Parameters dm (distance between meandering slots) and ds (distance of the nearer meandering slot from the centre slot (Lc) are varied to optimize the antenna in this study.

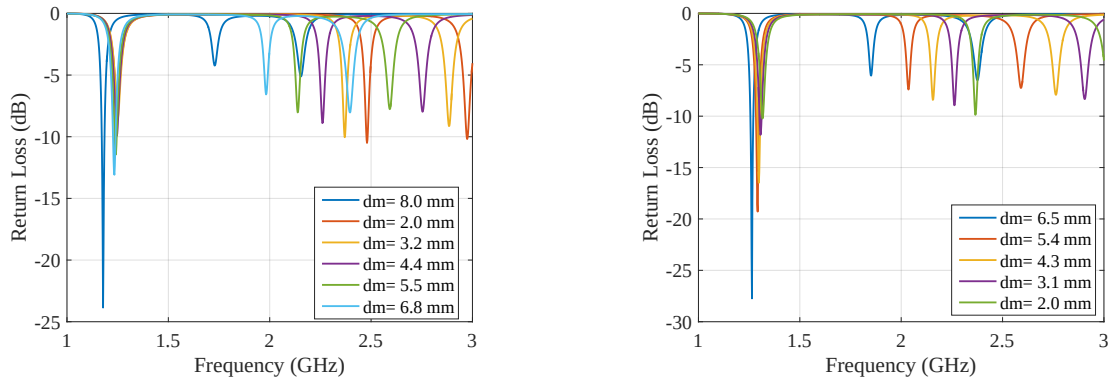

(a) (b)

Fig. 2.7 Effect of varying meandering slot distance (dm) for constant centre slot to closer meandering slot distance (dmc) (a) 1.5 mm (b) 2.5mm

To optimize this antenna we vary meandering slot distance, dm and the distance between the centre slot to the nearer end of the meandering slot 'dmc'. First we keep 'dm' (meandering slots distance) constant at 3.5 mm and vary the distance of meandering slots from the centre slot 'dmc'. Fig. 2.6 shows the resulting plots for 'dmc' 0.5, 2.5 and 4 mm. The antennas

shows triple resonances in all of the cases, however the best matching is achieved at around 1.4 GHz when the distance from meandering slot to the centre slot is 4 mm.

We continue our efforts to optimize the multi-band antenna, this time by varying the distance between meandering slots 'dm' for a set of constant centre slot to meandering slot distances i.e 0.5, 1.5, 2.5, 3.5 and 4.5 mm to observe the impact of this variation on the dominant resonant mode and subsequent higher modes.

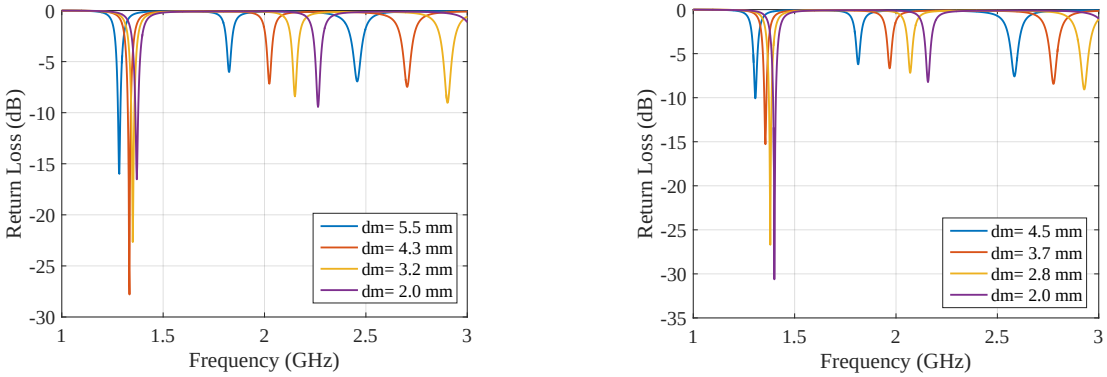

(a) (b)

Fig. 2.8 Effect of varying meandering slot distance (dm) for constant centre slot to closer meandering slot distances (dmc) (a) 3.5 mm (b) 4.5mm

We observe that for the constant distance between the meandering slots, as the distance between centre slot and meandering slot increases it results in better antenna matching for the dominant mode. Figures 2.7 and 2.8 depict this variation. We also observe that as the distance between lower end of the meandering slot and centre slot is increased the dominant mode drifts further away from the lowest frequency of operation, 1 GHz, however the antenna matches very well at distance 'dmc' 1.5 mm and above. Furthermore, it has also been observed that the higher order modes ar affected by the increasing distance between the centre slot and the nearer end of the meandering slot, the best matching for the second dominant mode has been observed at dmc 1.5 mm and 3.5 mm where the second dominant mode approaches the -10 dB mark on return loss plot, the lower frequency of operation is also required, therefore the modes of operation which show good matching and low frequency of operation are considered to finalise the design.

The optimum design, considering all the requirement constraints, has been achieved at meandering slot distance (dm) 3.5 mm and centre slot to nearer meandering slot distance (dmc) 3.5 mm. The respective resonant frequencies for the modes are 1.31, 2.2 and 2.84 GHz for first second and third modes of operation respectively. The return loss for the second

mode is just below -7 dB, whereas for third mode of operation it reaches below -8 dB. The return loss of final design is shown in Fig. 2.9. We optimized the multiband antenna for

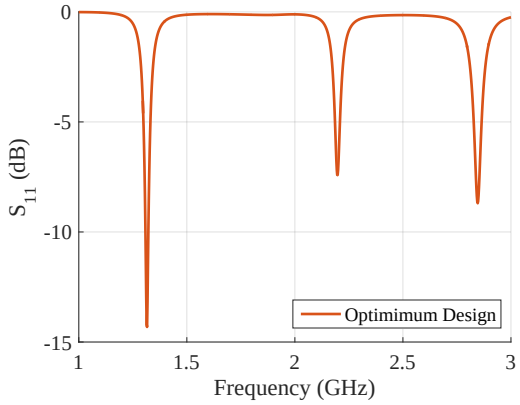

Fig. 2.9 Return loss of optimized multi band antenna immersed in safflower oil.

our imaging system. We achieve three narrowband frequencies of operation which allow us choice of three different frequency samples to perform the reconstruction and deal with the ill-posed problem. However the antenna operates in low loss medium that will not be sufficient to curb the degrading undesired phenomena of surface wave propagation and multipath signals etc as reported in [56, 107]. Moreover, the second resonant mode exhibits broadside nulls, thus we continue our efforts to find a broadband antenna so that we have sufficient choice of frequencies to work with for our reconstruction process.

2.3.2 Antipodal Vivaldi Antenna

Ultra-wideband antennas are required in microwave imaging for the optimal implementation of the inverse scattering algorithm and to deal with the ill-posed problems by having a possibility to work with multiple frequencies of operation. Balanced Antipodal Vivaldi Antenna (BAVA) is an ultra-wideband antenna with a lot of attractive features such as end-fire radiation pattern, compact design and low cross polarization to name a few. BAVA has been reported in [39] in the context of radar based imaging where a wideband directive antenna is required. The antenna operates in a low loss immersion medium of canola oil for impedance matching. The debye parameters of matching medium are $\varepsilon_\infty = 2.28$, $\varepsilon_s = 2.514$ and $\tau = 27.84$ ps. We examine this antenna for microwave tomography application by reducing its operational bandwidth from 3 to 10 GHz down to 1 to 3 GHz.

We optimize the BAVA antenna using CST microwave studio simulations, where we first use two techniques to excite the antenna under study i.e. with discrete port and with

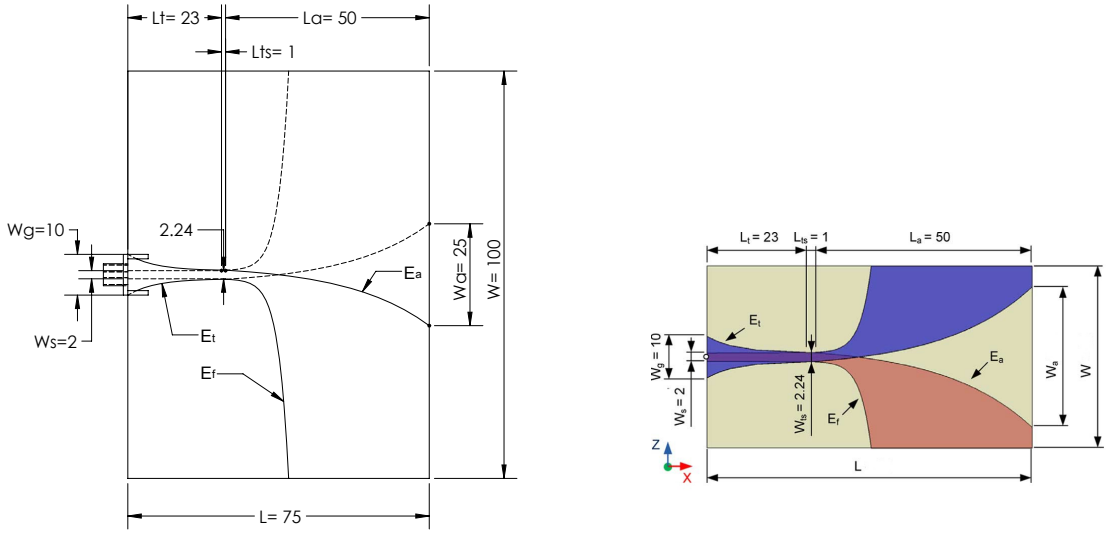

Fig. 2.10 The dimensions of antipodal Vivaldi antenna (a) large Vivaldi antenna operational from 1GHz (b) Vivaldi antenna with lumped elements operational from 1 GHz

waveguide port with SMA connector. We observe significant difference between the two feeding methods and due to the ease of implementation using the SMA connector we finalise SMA connector to feed the antenna for our further study. Reference [39] argues the stacking layers of substrate material used as superstrates help reduce the cross polar level. Reference [39] also argues about introducing a high dielectric diamond shape structure 'director' at the radiating edge of the antenna to obtain more directional radiation. However, in our study we first optimize the antenna in free space to operate at lower frequency range; 1 to 3 GHz by eliminating the suprstrate layers. The main objective of optimizing antenna in free space is to be able to miniaturize an ergonomic system in sight as shown in Fig. 2.11 (a). The initial plan is to introduce a meta-material matching layer and make an attempt to avoid using the immersion liquid layer from the system altogether.

Large Vivaldi: We present our modified version of antipodal Vivaldi antenna capable of operating at lower frequencies in free space [112]. We propose a larger version of the Vivaldi antenna with and without director that operates in free space and shows first resonance at 1 GHz. We also immerse our antenna in water and produce the return loss plot of the antenna immersed in water. Structure of the optimized Vivaldi antenna for low frequency operation in free space is shown in Fig. 2.10 (a). The return loss of the large Vivaldi in free space with and without director and immersed in water is shown in Fig. 2.11 (b).

Vivaldi with lumped elements: The study presented in [112] shows a good low frequency operation of the Vivaldi antenna, however this operation has been achieved at the cost of

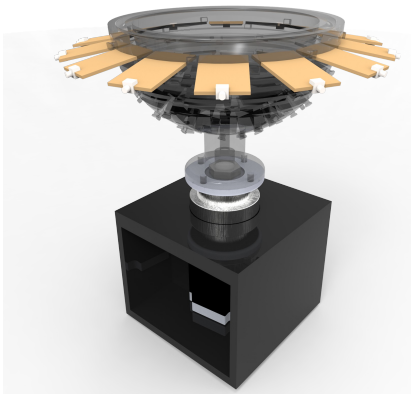

(a)

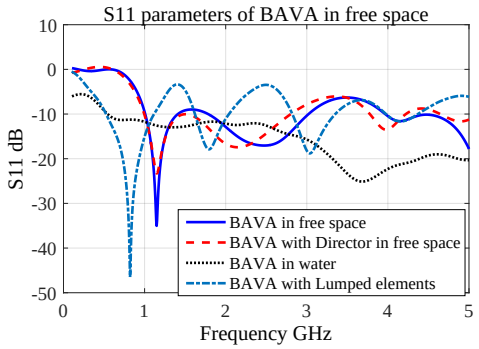

(b)

Fig. 2.11 (a) Vivaldi antenna with a rotational cup of the initial envisioned imaging system (b) return loss of large and lumped element Vivaldi antenna

large dimensions. The microwave tomography system in sight requires antenna elements to be compact and wideband, therefore we proceed with alternative method to achieve low frequency operation. We introduce lumped elements between the transmission line and the feed point of the antenna to lower the operational frequency from 3 GHz down to 1 GHz. Our matching circuit is comprised of three passive elements; resistor, inductor and capacitor connected in parallel. Dimensions of the Vivaldi antenna with lumped elements are shown in Fig. 2.10 (b) and the resulting return loss in free space is shown in Fig. 2.11 (b). Inclusion of parallel RLC circuit drops the -10 dB return loss point at 1 GHz. We present our results of the antenna array comprised of 12 Vivaldi elements with lumped circuit in [113]. We observe that despite showing resonances at low frequencies we don't achieve desired radiation characteristics from our designed antenna. The lack of efficient operation of the designed antenna is attributed to the use of resistive element in the tuning circuit which results in the heating of resistor and consuming significant energy supplied to it. However, other feeding techniques for the optimization of Vivaldi antenna also exist for example use of LC tuning circuits or modifying the feed location for lower frequency operation. Considering the fact that the Vivaldi antenna is structurally more complex than the wire or printed monopoles (which offer ease of incorporation in the imaging algorithms) and its relatively larger physical size to monopoles we do not proceed with any further optimization of this antenna.

We studied Vivaldi antenna in great depth. Our study of the Vivaldi was motivated by achieving low frequency operation in free space. We accomplished the task with optimizing the antenna dimensions, however resulting dimensions for our desired frequency of operation are found to be too large to miniaturize a mechanical setup. We optimize the Vivaldi antenna

for lower frequency operation in free space by introducing lumped element tuning circuit, however introducing lumped passive elements results in the lower efficiency of the antenna. Moreover, we realise that the surface waves degrade microwave tomography system and in order to combat with this phenomenon we need to use an appropriate coupling medium to immerse the antennas for better matching and curbing the multipath and surface wave propagation.

2.3.3 Triangular Patch V Slot Antenna

Triangular patch V slot antenna has been proposed in [114] in the context of head and neck hyperthermia treatment as shown in Fig. 2.12, here, in this study we re-examine this applicator in the context of imaging applications.

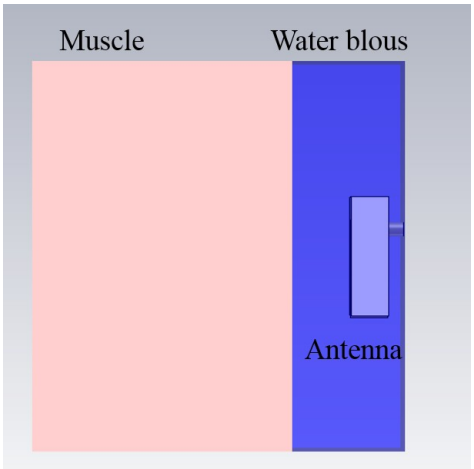

Fig. 2.12 Structure of V slot triangular patch antenna loaded with muscle phantom modelled in CST microwave studio [114].

The antenna proposed in [114] has a 14.4 mm thick layer of a hypothetical substrate of permittivity 2.3, the patch layer is a triangle with the base length 25 mm and altitude of 37 mm. A V shaped slot is cut out from the triangular patch. The base of triangular patch is shorted with the ground plane using a rectangular shorting pin of width 12 mm. The resulting structure from the above mentioned geometry is shown in Fig. 2.13.

We model the antenna in CST microwave studio and study the effects of different feeds i.e. coaxial feed with SMA connector and discrete port on the reflection parameters of the V slot triangular patch antenna. The proposed antenna design in [114] is performed with the phantom loading and different waterboli materials where the antennas is immersed in water bolus and the muscle phantom is loaded infront of the waterbolus containing the antenna.

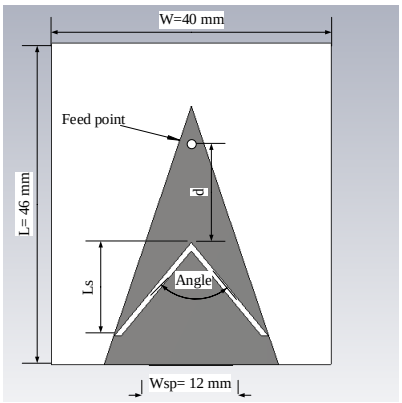

Fig. 2.13 Structure of V slot triangular patch antenna with dimensions in mm modelled in CST microwave studio.

We choose the same hypothetical values of the materials to immerse our antenna in, at first instance as proposed in [114] and examine the feed impact on return loss of the antenna. Relative permittivity values for the hypothetical materials are 20, 40, and 78. We also examine the antenna performance in free space. We select the biological muscle phantom properties for loading from the CST Microwave Studio's material library.

Return loss of the triangular patch antenna with waveguide and discrete ports immersed in different materials are shown in Fig. 2.14. Return loss obtained by using different feeds agree with each other, thus there is not much impact of feeding method in the mentioned configuration. The agreement between waveguide and discrete port results particularly enhances when antennas are immersed. However, significant variation in the return loss of the antenna operating in free space have been observed when feeding methods is altered. Dotted lines shown in Fig. 2.14 represent the return loss obtained by feeding the antenna with discrete port whereas the solid lines denote reflections obtained when the antenna is fed with the coaxial waveguide port.

We consider fabrication of the antenna in the future, therefore we extend our simulation study from hypothetical substrate materials to the realizable materials, i.e. FR-4 and Rogers RT 6002. We compare our antenna performance in 3D simulations for different substrate materials. We alter the geometry for this study and considering our vision for realizing a conformal prototype of the imaging hardware we place the antenna in front of a plexiglas tank filled with 90% glycerine-water mixture. Note that antenna operates in free space while there is a dielectric filled tank in front of it. Use of 90% glycerol is proposed in [49], therefore we also model the same coupling liquid in our study. Fig. 2.14 (b) depicts return loss of the V slot triangular patch antenna with different substrates and excitations.

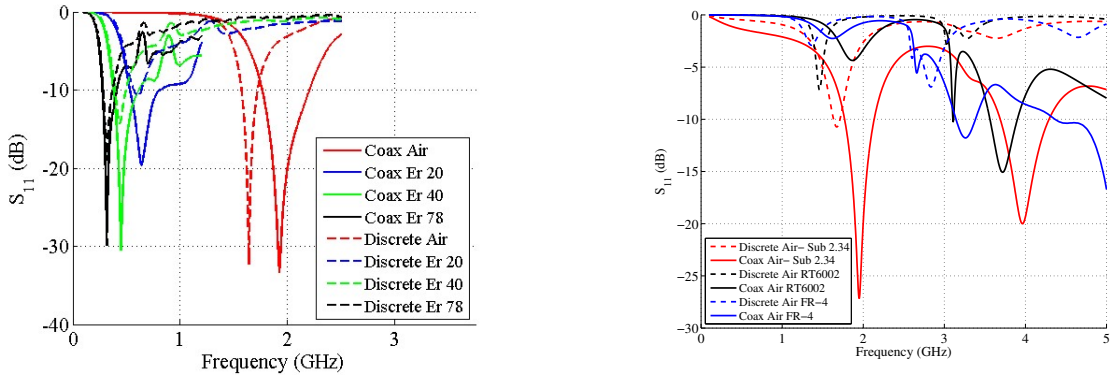

Fig. 2.14 Return loss of V slot antenna (a) immersed in different water-boli with different feeds (b) with different feeds and substrate materials.

Feeding the antenna with coaxial feed is more realistic and is potentially closer to the realized antenna's performance therefore, we use SMA connector model to feed the antenna in our simulation study. The effect of different substrates on antenna performance is also of significance, as big deviations in respective return losses is observed for different substrate materials when excited in front of 90% glycerol loading. Change in electrical properties of the substrate material results in changes of antenna radiation characteristics due to the mismatch with dielectric loading and substrate layer. We study large V slot antenna in greater

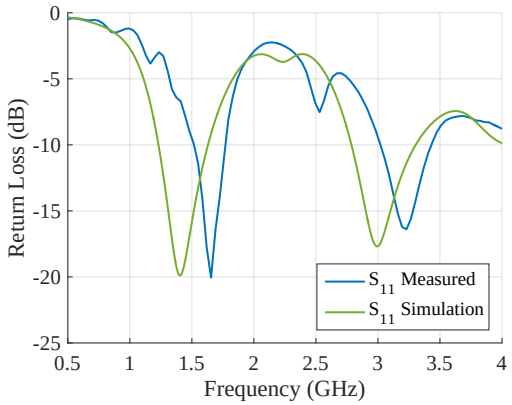

Fig. 2.15 The optimized V slot antenna simulation and measured return loss. Distance from the feed point is 16 mm, vertical length of slot is 13.89 mm and slot angle is 69.21°.

depth and make an effort to optimize it in front of the plexiglas tank containing 90% glycerol. Process of optimization of the antenna entails investigation of return loss when we vary the slot distance with reference to inner conductor of the SMA connector. We also vary length and angle of the slot to optimize the antenna.

We rigorously perform our parametric study on the parameters ‘d’, ‘Ls’ and ‘Angle’ as shown in Fig. 2.13 to achieve multi resonance operation at low and high frequencies. Our choice of frequency is focused on 1 and 3 GHz for this design. References [30, 31] demonstrate that low frequency such as 1 GHz and availability of multiple high frequencies can lead to better inversion results. We optimize our design by fine tuning the parameters and find that the best and most efficient design to meet our needs of microwave tomography where our focus is to design an antenna that can operate at 1 and 3 GHz is achieved for d= 13 mm, Ls= 13 mm and slot angle 69 degree. We also realized our proposed simulation design on FR-4 substrate. Return loss of the optimum antenna design from measured as well as simulated data is shown in Fig. 2.15. Simulation and experimental results are in good agreement.

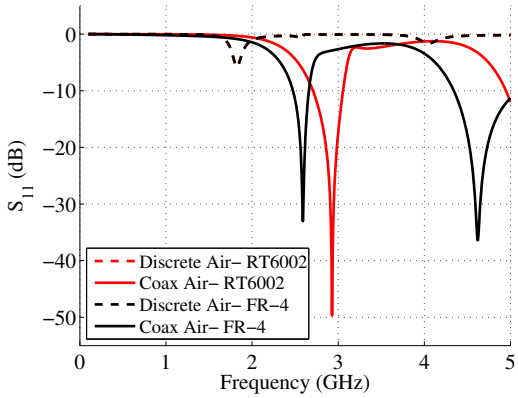

Fig. 2.16 Return loss of the compact triangular patch V slot antenna modelled in CST on FR-4 and RT 6002 substrate layers with coaxial feed (solid lines) and discrete port (dotted lines)

We continue our study to make this antenna compact. We design small V slot antenna with the conformal imaging system design in mind. Therefore, the optimum dimensions for the antenna with reference to the conformal design compatible with our initial vision of the system prototype has the design parameters: width 28 mm, Length 29 mm, height of substrate 12 mm. We model The compact V slot antenna in CST with the above mentioned parameters. Return loss of the compact V slot antenna design is shown in Fig. 2.16. Shorting pin and triangular patch width are same as the larger V slot antenna, however the length (altitude of the triangle) of the patch has been reduced. The new optimum feed position has also been changed to the best matching location. Fig. 2.16 shows the behaviour of antenna with different substrates and feeding methods. Antennas with discrete ports show very similar response, in fact the curves are overlapping each other, however better matching has been

achieved using the coaxial feeds with SMA connectors where deep resonances have been observed for both substrate materials. The antenna modelled on FR-4 substrate layer shows first resonance at a lower frequency than the one with RT 6002. We present the dimensions of both of our designs in Table 2.1.

Table 2.1 Design parameters of V slot triangular patch antenna

Antenna Parameters	Large (mm)	Small (mm)
Length	46	29
Width	40	28
Height	14.4	12
Thickness	0.1	0.1
Patch Length	37	-
Patch Width	25	25
Shorting Pin Width	12	12

2.3.4 Monopole Antenna

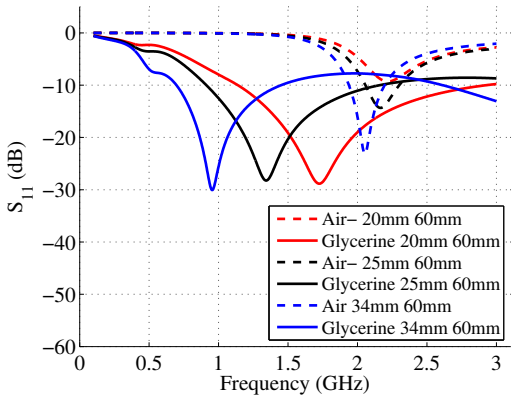

Fig. 2.17 Return loss of 60 mm long (coaxial line) monopole antenna with 20, 25 and 34 mm radiating tip lengths in free space and in 90% glycerine water mixture.

Monopole antenna has been extensively studied by Meaney *et al.* at Dartmouth College USA in their microwave tomography system, [49] and [107] have reported monopole antennas in the context of microwave imaging and the issues/ challenges attributed to them. It is worthwhile investigating monopole antennas in the context of microwave tomography as they have been used in the lab prototypes and some clinical trials at Dartmouth College have also been conducted using the systems with monopole antennas.

Structure of the monopole antenna is very simple. In current study we use a coaxial cable of length 60 and 100 mm and strip the outer conductor by 20, 25 and 34 mm to create a simple monopole antenna. We analyse the performance of monopoles in free space as well as inside 90% glycerine mixed with water. Return loss from CST simulations of each of the aforementioned cases are shown in Figures 2.18 and 2.17.

Return loss of monopole antenna with coaxial feed length 60 mm and the radiating tip (stripped outer conductor) lengths of 20, 25 and 34 mm is shown in Fig. 2.17. We observe that resonant frequencies depend on antenna length and the immersion medium, for example, antenna with longest length (34 mm) immersed in the matching liquid (90% glycerol in this case) resonates at the lowest frequency. However, it is also evident from Fig. 2.17 that antenna with 34 mm length in free space resonates at around 2 GHz as opposed to 0.9 GHz when immersed in 90% glycerol. This prompts to the need of immersion medium for better matching and also to achieve the wideband response from antennas. Wideband behaviour of an antenna makes multiple frequencies available for imaging algorithm that can help in mitigating the ill-posedness of the inversion problem, by sampling more frequencies.

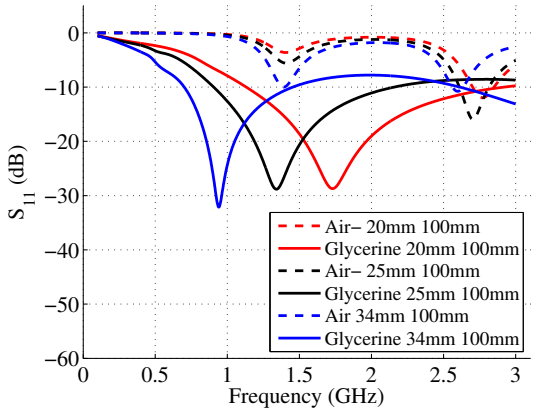

Fig. 2.18 Return loss of 100 mm long (coaxial line) monopole antenna with 20, 25 and 34 mm radiating tip lengths in free space and in 90% glycerine water mixture.

We make similar comparisons as above with longer coaxial line antennas (100 mm). We plot the results of 20, 25 and 34 mm radiating tips of 100 mm coaxial line antenna in Fig. 2.18. We observe that the monopoles with 100 mm length line show dual band response in the desired frequency band of microwave tomography when operating in free space. We immerse 100 mm coaxial line antenna in 90% glycerol and consequently they start to exhibit a wideband response at lower frequencies as expected from our earlier observation. -10 dB return loss mark is achieved at approximately 0.7 GHz. [107] argues that the use of lossy liquid and longer feed line mitigate the degrading phenomenon known as surface wave

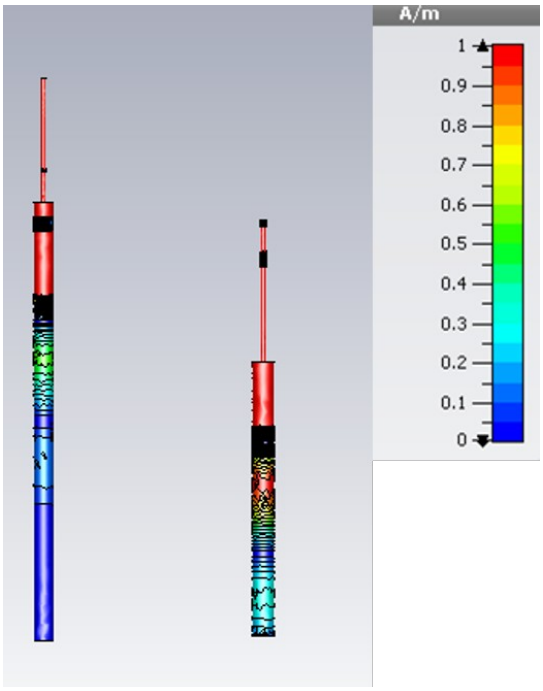

Fig. 2.19 Surface current distribution on the monopole antenna for two lengths of the outer conductors 120 mm (left) and 66 mm (right). The radiating tip in both cases is 34 mm.

propagation and multipath signal that result in unrealistic signal reception of the imaging domain.

Longer coaxial cable of 150 mm is also proposed to curb surface currents travelling on the coaxial line itself. The longer length of the line makes signal travel longer distance on the line and as a result surface currents get attenuated due to extra bit of distance it has to travel in a lossy medium, as proposed in [107]. Fig. 2.19 depicts the surface current distribution on two different length monopole antenna elements. The surface current distribution on the shorter antenna is seen to be much higher than the longer antenna thus justifying the need of longer antenna element to suppress surface current and hence any undesired surface waves propagation along the antenna element.

2.3.5 Circular Patch Antenna

We study a very simple circular patch antenna operating in front of a dielectric filled imaging chamber. Purpose here is to optimize the circular patch antenna in the loaded configuration to be able to operate in MT desirable frequency band. Circular patch antenna exhibits lower side lobe in ‘X’ band as compared with rectangular patch.

We model our compact circular patch antenna in Computer Simulation Technology microwave studio on two different substrates, FR-4 and RT 6002. We compare the performance of the antenna with the materials used. Our circular patch antenna has a full ground plane covering the entire surface area of the substrate (28*29 mm). Circular patch of the antenna has same diameter as width of the antenna substrate layer. Height of this antenna substrate is 2.5 mm, width is 28 mm and length of the antenna is 29 mm. We study performance of

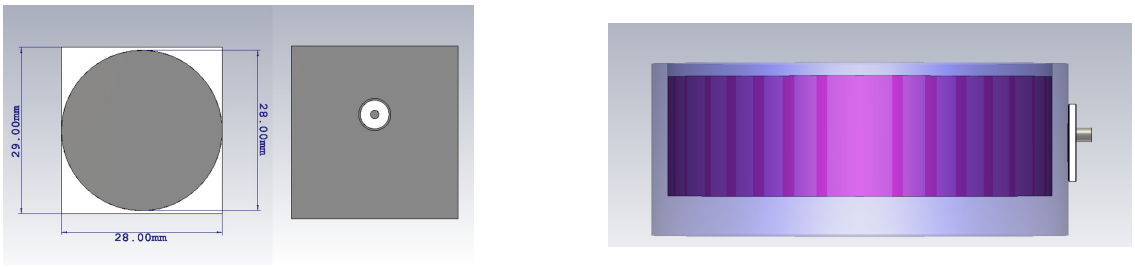

(a) (b)

Fig. 2.20 Circular patch antenna (a) CST schematic (b) in front of the dielectric filled imaging chamber.

our compact circular patch antenna in front of the dielectric filled chamber. Schematic of standalone antenna and antenna in front of a dielectric chamber modelled in CST microwave studio is shown Fig. 2.20. Fig. 2.21 shows the reflection parameters of the circular patch antenna in the free space and in the presence of loading.

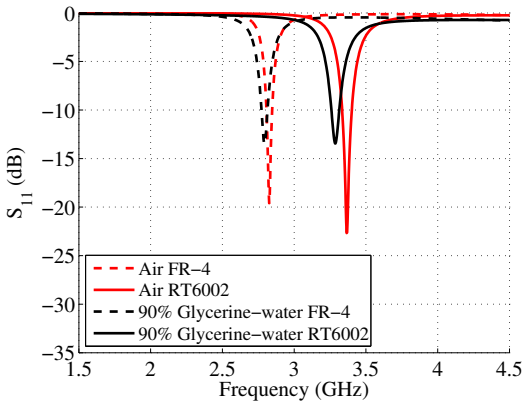

Fig. 2.21 Return loss of circular patch antenna in free space and in front of 90% glycerine water mixture for both substrates FR-4 and RT 6002.

Performance of circular patch in free space and in front of the dielectric filled chamber is shown in Fig. 2.21. We observe that antenna operating in front of a tank filled with dielectric immersion medium results in lowering the resonant frequency of the antenna as shown in

Fig. 2.21. The observed resonant frequency of circular patch in free space is approximately 3.25 GHz whereas when loaded with dielectric filled immersion tank the resonant frequency drops to approximately 2.5 GHz.

No significant difference, however, has been observed between the two compared substrate materials, although RT 6002 does show -10 dB reflection at a slightly higher frequency than the circular patch antenna on FR-4 substrate. We also observe that increasing the thickness of substrate helps lowering the resonant frequency.

We observe that the circular patch antenna is resonant and has a very narrow band. Moreover it operates at higher frequency (2.5 GHz) in loaded configuration. For our algorithm stability a lower frequency around 1 GHz is also important. Increasing thickness of the substrate results in having a bulky and heavy antenna which isn't quite suitable for our intended design of tomography system.

2.3.6 Triangular Patch Printed Monopole Antenna

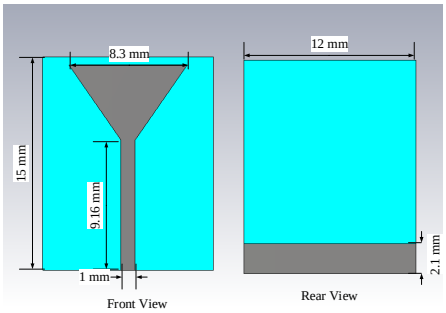

Fig. 2.22 The schematic of triangular patch printed monopole antenna. Front and rear view with the geometry and dimensions of the proposed triangular patch printed monopole for imaging.

Microwave imaging requires antennas to be immersed in a lossy immersion so that cross coupling between antenna elements and all other undesired signal transmissions can be prevented in order to acquire clean data from the imaging domain. Wideband operation of the antennas constituting an array for data acquisition is another important requirement that may be achieved by immersing the antenna array in a lossy liquid. We propose a compact, robust and simple printed monopole antenna design that operates in wideband when immersed in a lossy liquid.

So far, we have proposed antennas which are either optimized in free space or in front of a dielectric filled chamber but operating in free space. We design our printed monopole antenna inside a lossy immersion liquid, as we will eventually immerse it in coupling liquid when we

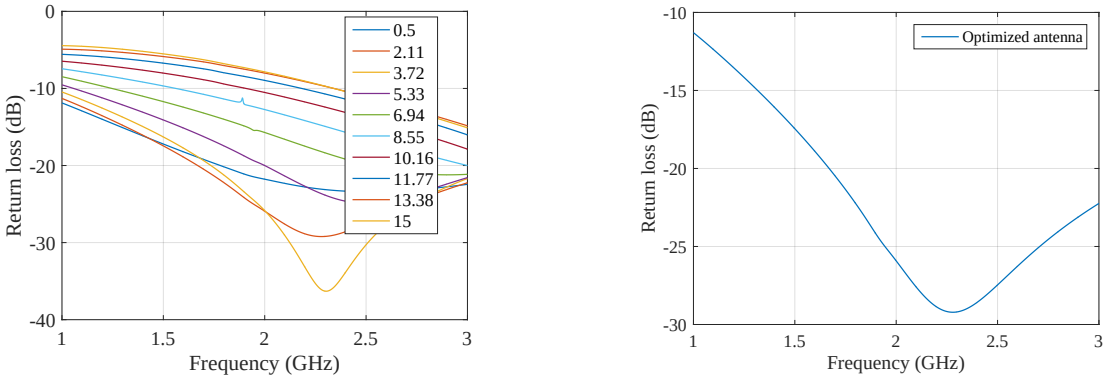

(a) (b)

Fig. 2.23 Optimization of triangular patch printed monopole and return loss of optimized design. (a) parametric sweep on ground length for impedance matching, (b) optimized design at ground length 2.1 mm.

create an array for our microwave imaging prototype. We optimize our printed monopole in 80% glycerine-water solution which has been widely reported in the literature for imaging applications [107]. We design and fabricate our triangular patch printed monopole antenna on FR-4 substrate. Being a robust and extensively used material in antenna fabrication, FR-4 allows us the ease of realization and ability to submerge the array of antennas fabricated on FR-4 in a coupling medium.

Front and rear views of our proposed printed monopole antenna modelled in CST microwave studio are shown in Fig. 2.22. Complete dimensions of the proposed antenna are given in Table 2.2. Printed monopole under study is constructed of a triangular active patch, a transmission line of length 9.16 mm and width 1 mm is used to match the antenna impedance with the 50 ohm coaxial feed. We immerse the antenna in 80% glycerol and carry out a parametric sweep on the ground plane length of the antenna to achieve a wideband response in the frequency range 1-3 GHz.

Table 2.2 Printed monopole antenna dimensions

Substrate length 15mm	Substrate width 12mm	Substrate thickness 1mm
Patch length 5.2mm	Patch width 8.3mm	Side angle 55.3°
Ground length 2.1mm	Ground width 12mm	
Transmission line length 9.2mm	Transmission line width 1mm	Metallization thickness 0.035mm

Return loss of the printed monopole immersed inside 80% glycerol is shown in Fig. 2.23. Return loss falls below -10 dB for the ground length of 5.33 mm and below at 1 GHz which is the cut off frequency for our desired operational range for microwave tomography, moreover it has been observed that the antenna return loss stays well below -10dB for the entire frequency range of interest for the ground length of 5.33 mm and below. We choose 2.1 mm ground length for our final design as it renders best matching for full operational range of frequency of interest.

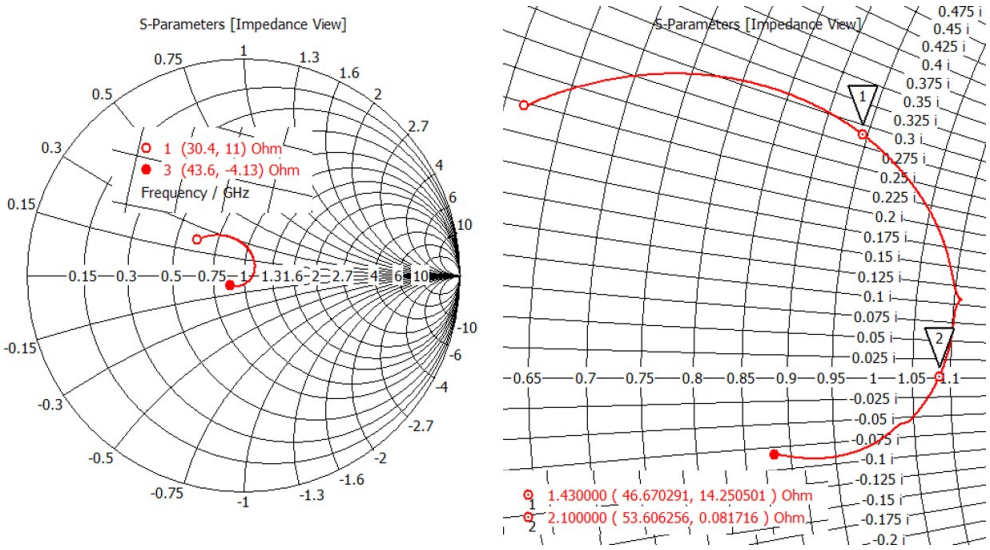

Fig. 2.24 Smith chart analysis for impedance matching.

The Smith chart for antenna impedance 'Z' is shown in Fig 2.24, we have specified the critical points on the smith chart for example at 1 GHz where return loss falls below -10 dB has a real resistance of 30.4 ohms and an inductive reactance of 11 ohms, whereas at the other extreme of frequency band under consideration i.e. at 3 GHz we observe the capacitive susceptance of 4.13 ohms and the real resistance is 43.6 relatively closer to the characteristic impedance of the 50 ohms feed source. We note that at 2.1 GHz the input impedance of the antenna becomes almost completely resistive however the input resistance of 54 ohms is not fully matched with the characteristic impedance of the source. Voltage Standing Wave Ratio (VSWR) plot is shown in Fig. 2.25 (a). VSWR of the antenna stays below 2 over the entire frequency range of interest indicating the good match has been achieved.

We also look at the surface current distribution on the patch of optimized printed monopole antenna design. Current distribution at five frequency samples between 1 and 3 GHz at a step of 0.5 GHz is shown in Fig. 2.26. Strong surface currents on the patch have

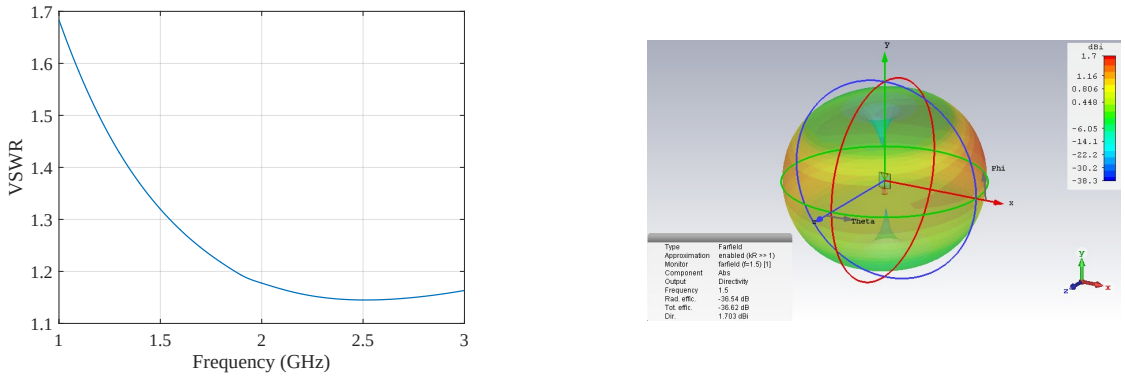

Fig. 2.25 (a) VSWR of the antenna and (b) far-field directivity at 1.5 GHz.

been observed at 1 and 3 GHz, however the distribution of these high magnitude currents isn't uniform and the anti-phase currents give rise to non-omnidirectional radiation patterns. From the Smith chart of the impedance characteristics we observe that the parasitic inductive and capacitive elements are pronounced at the given frequencies and are responsible of the anti-phase orientation of the surface currents.

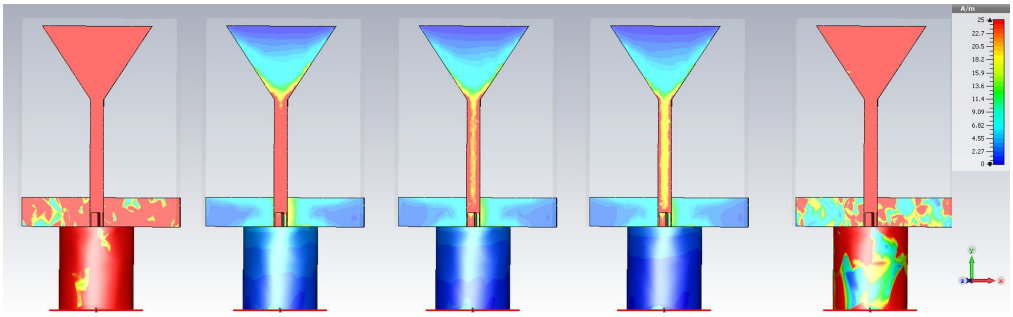

Fig. 2.26 Surface current distribution on triangular patch printed monopole at 1, 1.5, 2, 2.5 and 3 GHz from left to right.

2.4 Conclusion

This chapter presents background theory of antennas and wave propagation. We present our antenna designs for microwave tomography. Multiband antenna with three resonant frequencies operating in low loss safflower oil is optimized for low frequency operation (1-3 GHz). Ultra wideband antipodal Vivaldi antenna has been optimized for 1-3 GHz operation in free space by optimizing its dimensions as well as by introducing lumped elements. A triangular patch V slot antenna and its compact version operating in front of a dielectric filled

imaging chamber has been optimized to operate within the desired frequency range of 1-3 GHz. A compact and simple resonant circular patch antenna also operating in front of an imaging chamber is proposed. Monopole wire antenna from the literature has been studied for various lengths of the cable and radiating tips. Finally, a compact, robust and simple printed monopole antenna is proposed that operates in wideband and has small dimensions.

Chapter 3

Analysis of Non Immersed Antenna Arrays

3.1 Introduction

MT methods reconstruct inner profile of the imaging domain by solving an inverse ill-posed problem that requires multiple sources of information to reconstruct the dielectric profile. Therefore, multiple antennas have to be installed around an imaging domain in the form of an array. Doing so allows us to capture information from different angles of the interior of the domain. Thus, enabling us to acquire different views of the imaging domain.

The main purpose of matching medium is to couple energy within the imaging domain. While choosing an immersion medium bio-compatibility of the medium is of importance, as the used medium will be in direct contact with biological tissue. In the case of breast imaging, breast will be submerged in the matching medium. Thus, the focus here will be to optimize the antenna array performance with various dielectric background media. We start our study with non immersed configuration of antennas. In the non immersed configuration, antennas are placed tangent at the outer periphery of imaging chamber. First, we analyse signal propagation without any inhomogeneity in the imaging domain and subsequently we introduce a metallic scatterer and study the impact of introduced discontinuity on the signals received at different locations.

Electromagnetic wave incident on a discontinuity inside homogeneous medium undergoes scattering. Scattered signals are received by the array of receivers placed around the imaging domain. Each receiver receives the scattered signal in a particular fashion depending on its relative location with respect to the discontinuity present in the domain and the transmitter

that transmits the incident signal. We refer to this discontinuity in our discussions as 'Target'. We use various matching media with different dielectric properties in this study.

The purpose of this study is to gain an understanding of various different requirement parameters of the MT system. As stated above, the number of antennas in an array, coupling medium and target location and its material are all vital in data acquisition process for MT. The main motivation of this study comes from studying the basic properties of the MT systems. We present simulation and experimental study of a preliminary imaging system to test the performance of the system for microwave tomography.

3.2 Non Immersed Array Setup

Our non immersed arrays setup is comprised of four antenna elements surrounding a cube of acrylic tank containing dielectric medium. We install all four antennas at the external surface of the tank. We call this array setup a 'non immersed array configuration'. Schematic of four antenna setup modelled in the Computer Simulation Technology (CST)® Three Dimensional (3D) Electromagnetic (EM)solver is shown in Fig. 3.1.

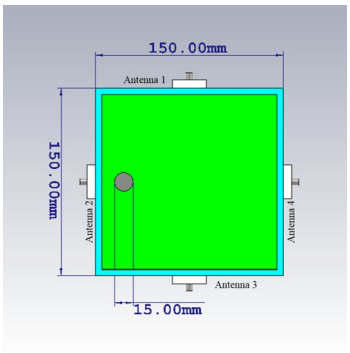

Fig. 3.1 Four element antenna array with acrylic tank, antennas and target in non immersed array configuration modelled in CST® MWS.

In the setup shown in Fig. 3.1 antennas are placed at centre of each of the four walls of the container at 90 degree angle with respect to the adjacent antenna element measured from centre of the imaging domain (acrylic tank). The tank wall thickness is considered to be 5mm and dielectric medium is inserted inside the simulation model. A target of 15 mm diameter made of PEC is then inserted inside the matching medium. Target material has been chosen to impart the characteristics of a strong scatterer to observe the impact of target on transmitted signals at the receivers and on the wave propagation through the coupling medium.

Dielectric materials used in this study are made up of 40%, 80% and 90% Glycerine-water mixtures. We measure the dielectric media properties using a probe kit and Agilent PNA

Fig. 3.2 Dielectric material measurement setup using probe kit and VNA.

series VNA. Fig. 3.2 shows a typical setup for the measurement of materials to be used in this study. Dielectric material measurements yield real and imaginary value of the permittivity of materials being studied at distinct frequency points (as defined in the settings of VNA), typically 100 points in the frequency range of 1 to 4 GHz. We use imaginary values of the material permittivity to extract conductivity as a function of frequency.

Real part of permittivity of the materials being used in this study is shown in Fig. 3.3 (a) and Fig. 3.3 (b) shows conductivity of these mixtures. It is quite clear from Fig. 3.3 (b) that higher percentage of water leads to increase in the conductivity of the liquid which accounts for the dielectric loss of the medium. For example, 40% glycerine-water at 3 GHz exhibits a conductivity value in excess of 4 S/m! Measured values of real and imaginary permittivity of the solutions are supplied to CST® software where user defined dispersion characteristic has been applied to the data. 2nd order fit has been considered for the curve fitting using CST® software for simulations.

3.3 Analysis of Non immersed Four Antenna Array of V Slot Triangular Patch Antennas

We study V slot triangular patch antenna presented in chapter 2 in four element non immersed antenna array configuration with different dielectric materials. Performance of the V slot antenna has been studied using different substrate materials and the optimized design is

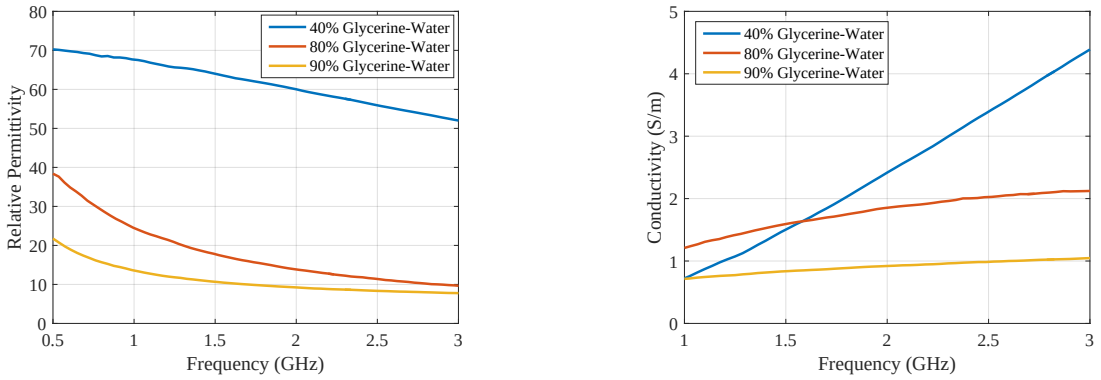

(a) (b)

Fig. 3.3 (a) Relative permittivity and (b) conductivity of different concentrations of glycerine-water mixtures used in this study.

presented in [115]. We use the optimized design presented in [115] to evaluate our imaging system performance of 4 antennas loaded with varying concentrations of glycerol. The purpose of this study is to evaluate the effect of scattering due to the presence of strong scatterer in the given geometry with an ultimate objective of being able to reconstruct the scattered signals and image the object.

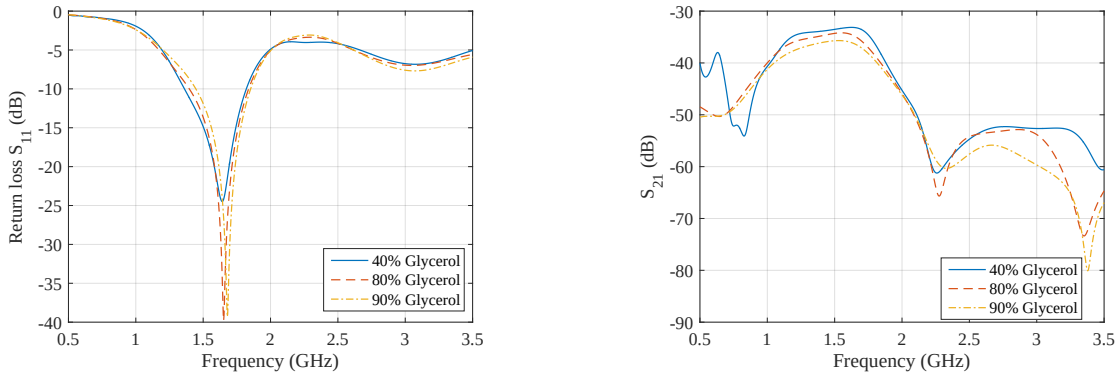

(a) (b)

Fig. 3.4 (a) Return loss of V slot antenna in non immersed antenna array configuration (b) transmission coefficient S21 when V slot antenna array operates in front of 40%, 80% and 90% glycerol solution.

We install four V slot antennas around an acrylic tank containing dielectric matching medium at 90° with respect to the adjacent antenna element placed at centre of the tank wall as shown in Fig. 3.1. We place a Perfect Electric Conductor (PEC) cylinder of 15 mm diameter 1 cm away from the inner wall of the tank where antenna 2 is installed. First, we

proceed with performing computer simulation of the said geometry modelled in CST MWS. We plot S parameters (S_{m1}) of the system when antenna 1 is excited. The term 'm' in the following plots (S_{m1}) represents the receiving element and '1' is the transmitting antenna located at position 1. Each 'mth' receiving antenna is placed at 90° with respect to the adjacent element. Thus, m=2 is the antenna at 90° with respect to transmitter 1 and m=3 represents the 3rd antenna of the array placed at 180° with respect to transmitting antenna 1. Simulation results of the four element non immersed antenna array imaging system are shown in Fig. 3.4 and Fig. 3.5.

Return loss (converted in dB) of antenna number 1 of four element array loaded with three different dielectric materials is shown in Fig. 3.4 (a). Transmitted signals at receiver number 2 due to antenna 1 (S21) are shown in Fig. 3.4 (b) in a homogeneous (without any discontinuity/ inhomogeneity) set-up.

Forward transmitted gain plots over the entire frequency range of interest; 1-3 GHz for receivers 3 and 4 in homogeneous background media comprised of 40, 80 and 90% glycerol samples are shown in Fig. 3.5 (a) and (b). From Figures 3.4 and 3.5 few interesting conclusions can be drawn. Reflection coefficient of the antenna does not vary significantly for dielectric media under study, although a deeper resonance at 1.6 GHz has been observed for 80 and 90% media as compared to 40% glycerol loading, indicating that the antenna matches better when loaded with 80% and 90% glycerol at 1.6 GHz. However, in all three cases the best match and hence the deepest resonance has been observed at almost the same frequency.

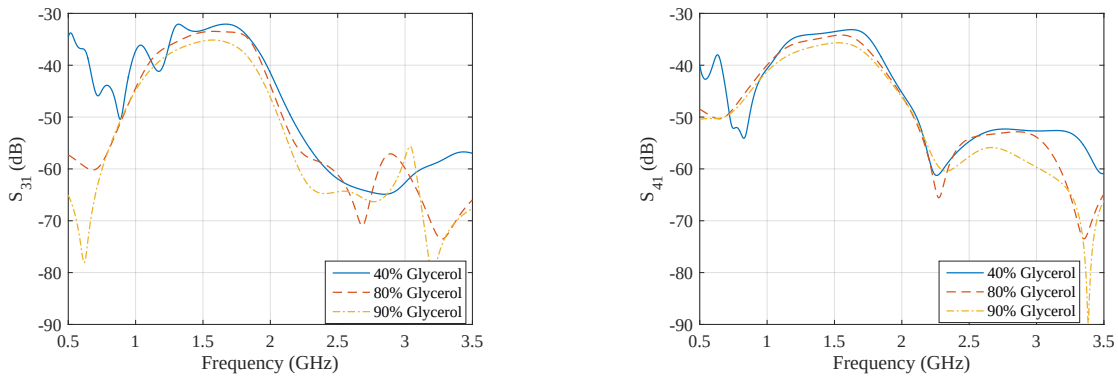

(a) (b)

Fig. 3.5 Transmission coefficients (a) S31 and (b) S41 when V slot antenna array operates in front of 40%, 80% and 90% glycerol solution.

Peak transmission has been observed at the resonant frequency for all three media under study which confirms that better transmission levels are achieved when the antenna is matched well with the background media. We compare transmitted gain at antenna 2 and 4 which are placed symmetrically with respect to transmitter (antenna 1 in this example) in the array. When studied for homogeneous media case, the comparison reveals that transmission levels and trends of transmitted gain at these two receivers are quite identical as seen in Fig. 3.4 (b) and Fig.3.5 (b). Similarity of transmission levels observed at antenna 2 and 4 indicate the fact that signal propagates uniformly in all directions when the array of antennas is loaded with homogeneous background. The transmitted gain has been observed to be above -40 dB at resonant frequency od the antenna for all three dielectric background media. Transmitted gain at antenna 3 (situated at 180° with respect to transmitter) is slightly above -70 dB between 2.5 and 3 GHz where the antenna is not fully matched but shows -5 dB bandwidth.

Glycerol sample with 40% glycerine concentration is the most lossy of the three media being studied, however transmission levels when 40% glycerol is used as dielectric for loading is slightly higher as compared to 80 and 90% matching liquids. This is an unexpected finding as we predict weaker transmitted gain for high loss material.

We introduce a metallic scatterer in the imaging domain and study impact of this introduced inhomogeneity on signal propagation. Introduction of a metallic scatterer should, in theory, result in causing scattering of the electromagnetic wave which in turn is expected to be reflected on the transmitted gain depending on the relative position of the receiver with respect to target and transmitter.

We analyse differences in dB values of the signals received before and after including the target in our imaging domain. Figures 3.6 and 3.7 depict differences in transmitted gain due to the inclusion of strong scatterer. Fig 3.6 (a), (b) and Fig 3.7 (a) show differences in transmitted gain as a function of receiver for five discrete frequency samples from 1 to 3 GHz at a step of 0.5 GHz. Fig. 3.7 (b) depicts 80% glycerol loading case only over the complete range of frequency of interest.

The plots in Fig. 3.6 (a) show that the impact of scatterer is quite varied at 1, 2.5 and 3 GHz when the array operates in front of 40% glycerol solution loading. At 1, 2.5 and 3 GHz we observe 'some' difference (maximum of 1.5 dB) in the transmitted gain at all three receivers. However, at 1.5 and 2 GHz the difference in transmitted gainstrength for with and without scatter cases is only seen at antenna receiver 2. The differences in transmitted gain observed at receivers 3 and 4, which are least expected to be affected by the presence of scatterer, is almost zero at 1.5 and 2 GHz. Nevertheless the impact of scatterer at 1.5 and 2 GHz is also very minimal even for antenna receiver 2; less than 0.5 dB.

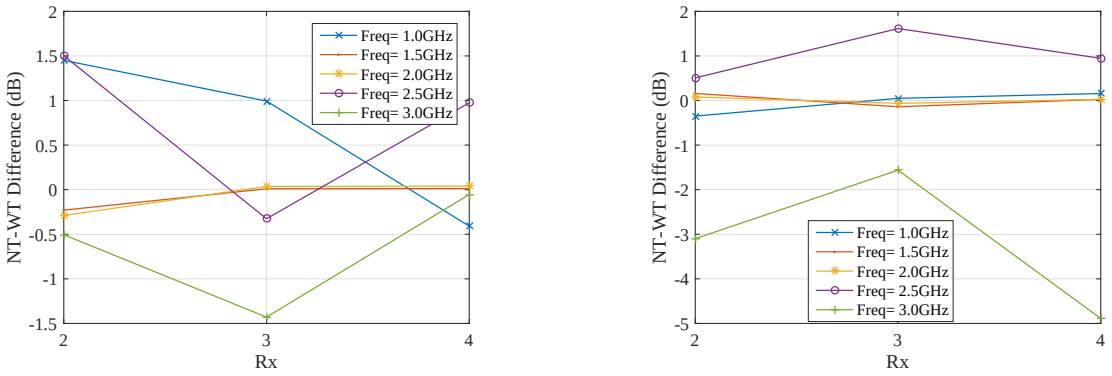

Fig. 3.6 Differences of transmitted gain plotted as a function of receivers for receivers 2, 3 and 4 (a) 40% glycerol (b) 80% glycerol loading. Five frequency samples have been taken into considerations from 1 to 3 GHz at a step of 0.5 GHz. The difference has been calculated by subtracting signal strength in the presence of target (dB) from homogeneous background transmitted gain (dB) for the particular receiver and frequency.

Transmitted gain differences observed for the array operating in front of the chamber filled with 80% glycerol as matching medium are shown in Fig. 3.6 (b). Differences observed at 1, 1.5 and 2 GHz are almost negligible. At 2.5 GHz maximum difference of 1.7 dB is observed at receiver 3, whereas the differences recorded at receivers 2 and 4 are 0.5 and 1 dB respectively. Again we observe that antenna 2 shows very little difference in transmitted gain while it is expected to be most affected receiver after the inclusion of a strong scatterer. The unexpected results, such as, low differences observed at receiver 2 and high deviation in difference of transmitted gain at receiver 3 are indicative of the fact that signals are not propagating through the imaging domain. In general the impact of scatterer and hence the difference at higher frequencies such as 2 and 2.5 for the 40% glycerol loading is not in line with the theoretical understanding of the wave propagation phenomenon through the dielectric, however for 90% glycerol case we observe a little bit more consistent perturbance at all the frequencies except at 3 GHz. Unexpected behaviour of the transmitted gain patterns is attributed to the surface wave propagation and multipath signals. Fig. 3.7 (b) is a representative example of differences of signal strength over the entire frequency range for 80% glycerol loading case. We also observe that the two symmetric receivers i.e receiver 2 and 4 have a very similar response over the desired frequency range, from that we conclude that the significant contribution of the transmitted gain does not come through the imaging domain.

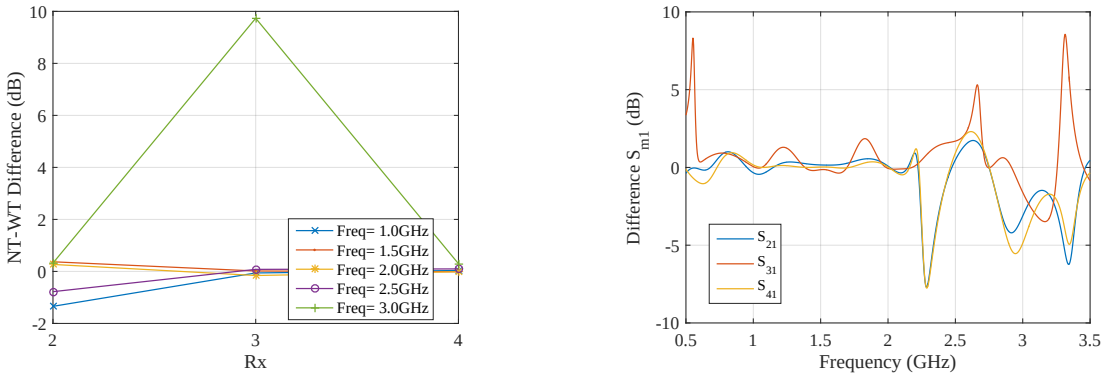

(a) (b)

Fig. 3.7 Differences of transmitted gain: (a) plotted as a function of receivers for receivers 2, 3 and 4. Five frequency samples have been taken into considerations from 1 to 3 GHz at a step of 0.5 GHz. The difference has been calculated by subtracting the signal strength in the presence of the target from homogeneous background signal strength for the particular receiver and frequency, the difference in transmitted gain magnitude stays below 2 dB except for 3 GHz where it shoots to 10 dB unexpectedly (b) differences in transmitted gain over the entire frequency range for 80% glycerol.

To gain a quantitative insight into the phenomenon of surface wave propagation we show electric field distribution plots for two planes of the array geometry. We show the field distribution at the first resonant frequency of the antenna when loaded in front of the dielectric as shown in Fig.3.1. Fig. 3.8 shows the field distribution when port 1 is excited and the 2D reference plane is placed at the outer boundary of the tank (left) and then at the inner boundary of the tank (right). The face chosen for this comparison is the one situated opposite to the antenna 1. From Fig. 3.8 we can clearly see that the fields at the outer boundary of the face are significantly higher than that of inner section which is even 2.5 mm closer to the excited antenna. Therefore, we conclude that the transmission occurs along th exterior boundary of the chamber and no significant amount of energy is transferred from inside the imaging domain.

We investigate this claim further by looking at the xz plane for three different heights. First, we consider the top surface (immersion) and plot the electric field propagating along this plane at y=70 mm of the setup. Subsequently we plot the field at the bottom exterior surface of the tank located at -75 mm of th setup. Lastly, the fields are plotted along y=0 plane. Comparing the three field distributions we can clearly see that the field strengths at the surfaces (top and bottom) are much higher than the fields propagating along the plane in the middle of the structure (y=0). Therefore, we conclude that significant amount of energy

is transmitted to the surrounding receivers after traversing along the surfaces of the chamber rather than from inside the chamber.

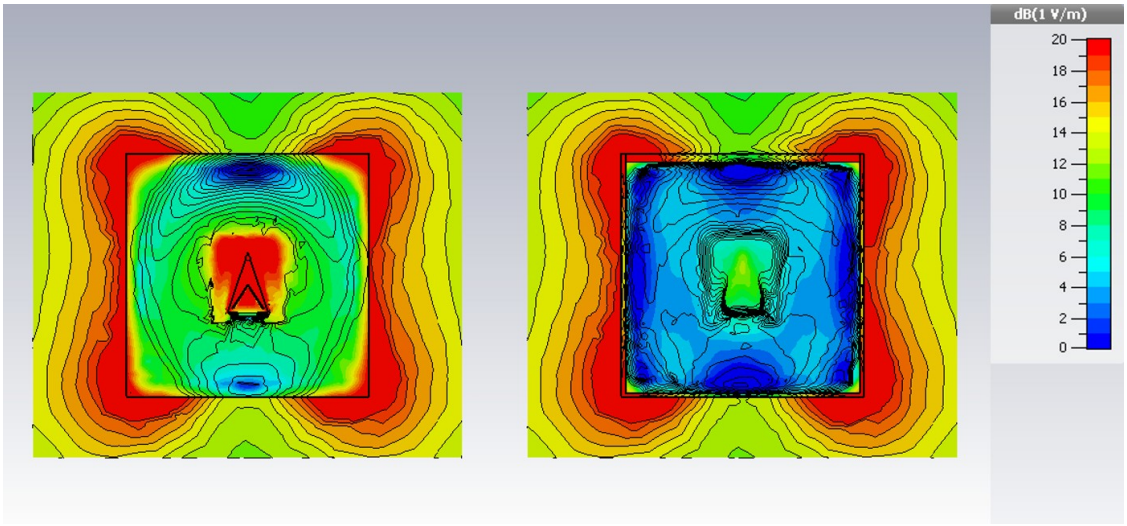

Fig. 3.8 Electric field distribution on xy plane for z= 74.9 mm, outer boundary of the tank (left) and at z=72.4 mm, inner boundary of the tank (right).

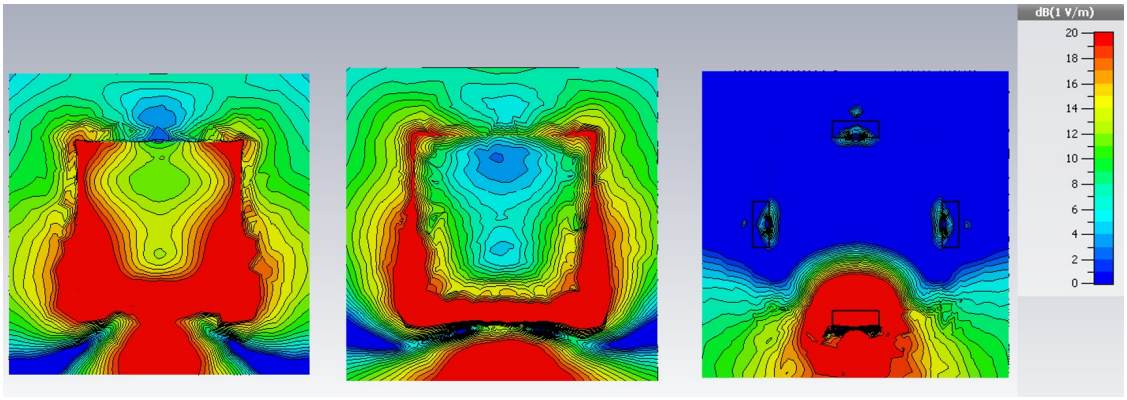

Fig. 3.9 Electric field distribution on xz plane for y= -75 mm, bottom surface of the tank (left), at 70 mm top surface of the immersion (middle) and at y=0, through the centre of the chamber (right).

3.3.1 Experimental Results of Non Immersed V Slot Antenna Array

We create a mechanical structure and print the V slot antennas to realize our system modelled in the software. Fig. 3.10 shows the complete physical system with mechanical structure, acrylic tank, antennas and multi-channel Vector Network Analyzer (VNA).

Mechanical structure holding the antennas is comprised of four vertical columns fixed on a horizontal base. The immersion tank is situated in between the four columns. Each column has two positions to install the antennas, a high and a low position. The antennas when placed at low position are situated at the base of the immersion tank which is quite vital in our study of signal propagation. We use 90% glycerol for this study. We assemble the setup

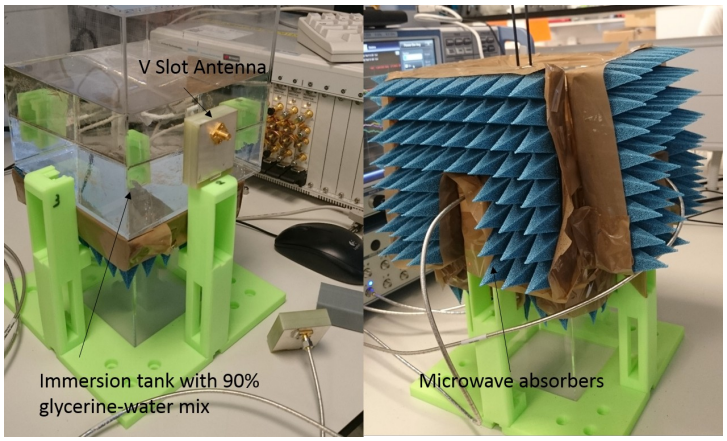

Fig. 3.10 Full experimental setup of the antenna array with V slot antenna, mechanical structure, acrylic tank and absorbers.

and fill up 90% glycerol in the tank. Subsequently we excite the antennas and introduce a scatterer inside the imaging domain. Resulting transmission parameters are shown in Figures 3.11 and 3.12 for 'with and without target' cases.

Fig. 3.11 (a) shows transmitted gain at receiver 2 for 'with target' and 'without target' cases from our experimental measurements. Similar plots for antenna receivers 3 and 4 are also shown in Figures 3.11 (b) and 3.12.

Introducing a target in the loaded configuration in our experimental measurements has not shown significant differences in forward transmitted gain from the homogeneous background case. However, we observe some spikes and ripples in the S_{m1} curves of the experimental setup, which suggest that the signals received at the receivers are deteriorated by interference, surface wave propagation and multipath signals. We observe slight changes in transmitted gain at higher frequencies predominantly imminent at 2nd and 4th receivers at 3 GHz and above, that suggests the impact of undesired signal propagation to be more profound at the given frequencies.

We expect similar levels of transmission and trends over the spectrum under study for antenna element 2 and 4 in homogeneous background setup as these two receivers are symmetric when antenna 1 transmits. Therefore we plot S21 and S41 to check symmetry of

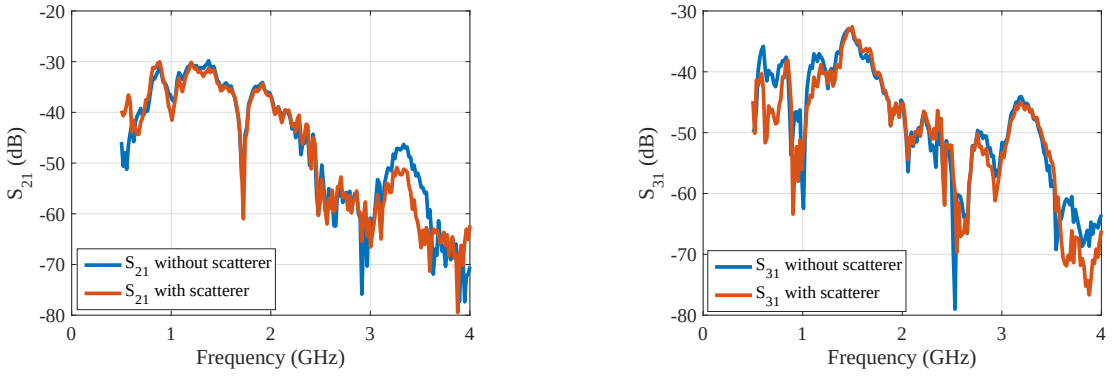

(a) (b)

Fig. 3.11 Forward transmitted gain of triangular patch V slot antenna array at receivers: (a) Rx= 2 and (b) Rx= 3 with and without scatterer from experimental data.

the signals shown in Fig. 3.12 (b). We observe significant difference between the signals received at antenna 2 and 4 between 1.2 to 1.8 GHz where our V slot triangular patch antenna operates well. Therefore, we conclude that symmetry does not hold for the acquired data. Thus the antenna array exposed in the free space to operate in front of a dielectric suffers from lack of data symmetry and is prone to degrading factors such as interference, surface waves and multi path signal propagation. These are very challenging phenomena to combat with and without mitigating the degrading effects clean data can not be acquired for good reconstruction of images.

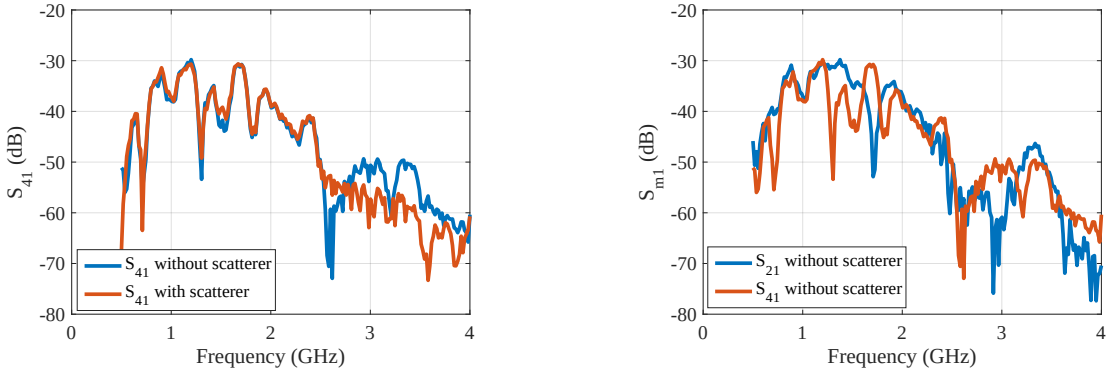

(a) (b)

Fig. 3.12 (a) Forward transmitted gain of triangular patch V slot antenna array at receiver 4, (b) signal symmetry check using experimental data.

3.4 Anaysis of Non Immersed Four Element Planar Wearable ISM Band Antenna Array

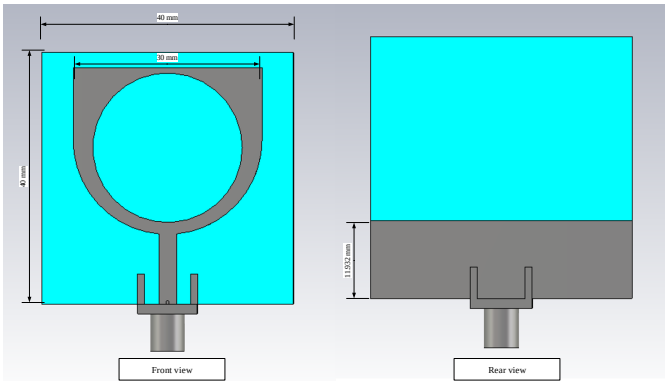

Fig. 3.13 ISM band antenna modelled in CST MWS [116].

ISM band antenna is a planar wearable antenna [116]. This radiator has been proposed in the context of on-body applications, designed at King's College London. The ISM band antenna resonates at 2.5 GHz in free space. Return loss of this antenna stays below -10 dB between 2.3 to 2.8 GHz in free space. At the time of experiments we had the fabricated ISM band antenna available, therefore we utilised it for our non-immersed imaging array performance evaluation. We examine performance of this antenna in the same scenarios as mentioned for our study of V slot antenna above. Results of the study and comments on our findings are given below.

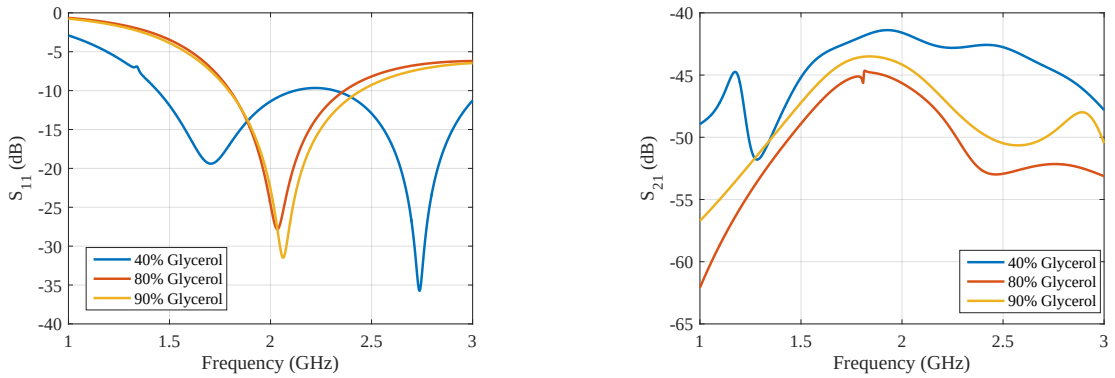

(a) (b)

Fig. 3.14 (a) ISM band antenna reflection parameter in front of different media (b) transmitted signal at receiver 2 when antenna 1 transmits, when the array operates in front of homogeneous 40%, 80% and 90% glycerine-water as coupling media.

Fig. 3.13 shows the CST schematic of the ISM band antenna. The antenna operates well infront of the dielectrics being used as can be seen from Fig. 3.14 (a). Full wideband behaviour has been observed from 1.4 GHz and above when the antenna is loaded with 40% glycerol. A wideband trend around centre frequency of 2 GHz has been observed when it operates in front of acrylic tank filled with 80 and 90% glycerol. ISM band antenna shows maximum level of signal transmission for 40% glycerol, while the transmitted signals for the case of 80% and 90% glycerol solutions show similar behaviour to each other. 90% immersion results in slightly higher transmitted signal.

Figures 3.14 (b), 3.15 (a) and (b) show the transmission levels when antenna 1 radiates and the remaining three antennas of the array receive. Transmitted signal levels stay above -55 dB level for 1.5 to 3 GHz range for all three media at receivers 2 and 4, however transmitted gain at antenna 3 are about 10 dB weaker as compared to the signals received at antennas 2 and 4.

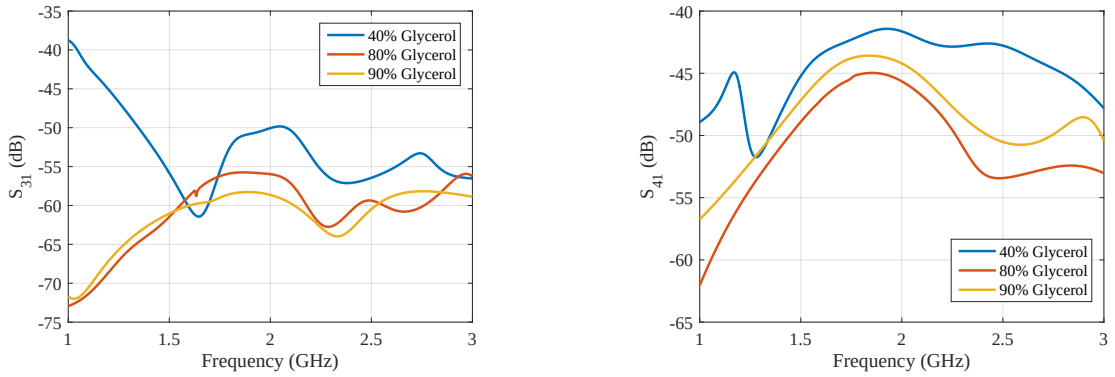

(a) (b)

Fig. 3.15 Received signals at ISM band antenna receivers (a) S31 (b) S41. Non immersed antenna array configuration for homogeneous 40%, 80% and 90% glycerine-water background media for the full range of frequencies (1-3 GHz).

Forward transmitted gain plots as function of receivers at discrete frequency samples for 40%, 90% and 80% glycerol are shown in Figures 3.16 and 3.17. Plots shown in Fig. 3.16 (a) depict transmitted gain when the ISM antenna array is loaded with 40% glycerol sample. Comparing the transmitted gain plots for all three coupling media we observe that maximum transmission occurs for 40% glycerol where the minima at 3 GHz for receiver number 3 is almost -55 dB while for 80% and 90% glycerol cases the value of minima is around -70 dB at 1 GHz.

ISM antenna when operating in front of tank filled with 80% and 90% glycerol immersion shows the best matching at 2 GHz. Therefore, transmitted gain at this frequency is relatively

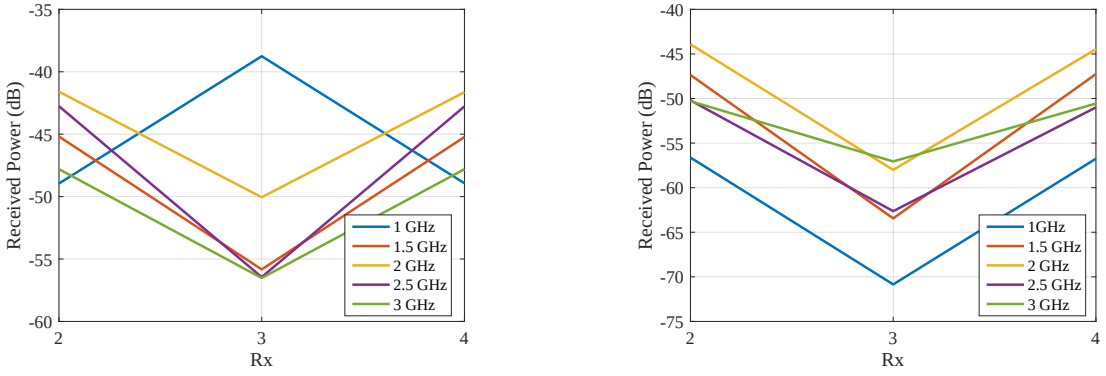

(a) (b)

Fig. 3.16 Transmitted gain at antennas 2, 3 and 4 in a non immersed array configuration for homogeneous (a) 40% and (b) 90% glycerine-water background media at 1, 1.5, 2, 2.5 and 3 GHz of four element ISM band antenna array.

better (higher than minima at 1 GHz of -70 dB) but still about 5 dB below corresponding signal strength of array operating in front of 40% glycerol immersion.

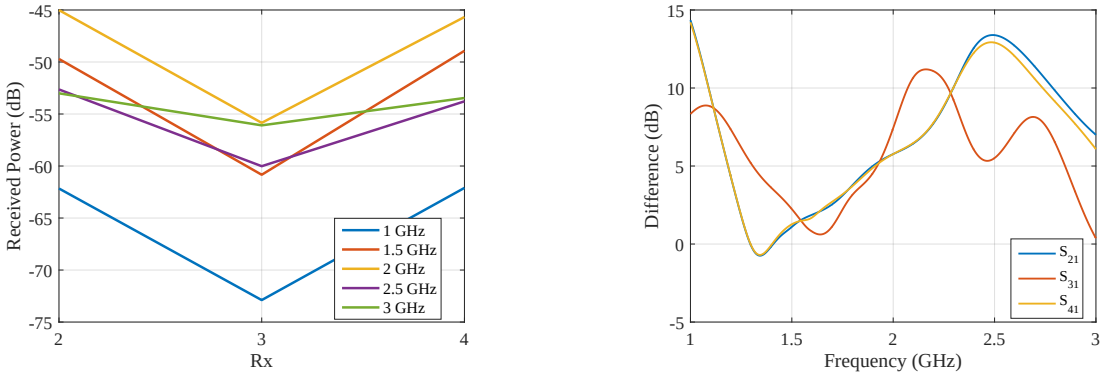

(a) (b)

Fig. 3.17 (a) Transmitted gain at ISM band antennas 2, 3 and 4 in non immersed configuration for homogeneous 80% glycerine-water coupling media at 1, 1.5, 2, 2.5 and 3 GHz. (b) differences (in dB) in signal strength when a scatterer is introduced inside 80% glycerol and antenna 1 transmits.

Differences of forward transmitted gain with and without scatterer of an array of ISM antennas operating in front of 80% glycerol over the entire frequency of interest (1-3 GHz) are shown in Fig. 3.17 (b). Unlike V slot antenna we observe very high level of variation when scatterer has been introduced. We observe difference level of approximately 5 dB at 1.9 GHz for all the receivers when antenna 1 transmits. If the signal is to propagate through

the imaging chamber and reach receivers of the array after travelling inside the domain then maximum differences (of transmitted gain in the presence and absence of a target) must be observed at the receiver located at position 2, however from the simulation results depicted in Fig. 3.17 (b) we observe that this behaviour has not been exhibited. This discrepancy leads us to conclude that the signals do not propagate inside the chamber and instead reach the receivers from outside the domain. The simulated results however show equal level of difference for all the receivers.

3.4.1 Experimental Results of Non Immersed Planar ISM Band Antenna Array

Subsequently we proceed with experimental verification of the results observed in simulation studies of our ISM band antenna arrays operating in non immersed configuration. Using the same mechanical set-up as we used for our study of V slot triangular patch antenna array we install four ISM band antennas and observe transmitted signals at the receivers when antenna 1 is excited.

We observe significant discrepancy between simulated and experimental results. Transmitted gain plots for with and without target scenarios of an ISM band antenna array operating in front of 90% glycerol filled acrylic tank are shown in Fig.3.18 (a). Experimental transmitted gain observed at 2 GHz frequency sample, where antenna is well matched in the given configuration, for receiver 2, 3 and 4 are around approximately -30 dB mark for without target case. Corresponding values from simulation results are approximately -55 dB as shown in Fig. 3.16. Experimental and simulation data exhibit significant level of discrepancy and therefore it leads us to conclude that antenna arrays operating in non immersed configurations are prone to signal degradation due to unwanted signal propagations such as surface waves, multipath signals and interference etc.

In simulation scenario we have perfect absorbing conditions at the boundary of simulation domain (bounding box). The signals reflected from the dielectric interface are absorbed at the boundary of simulation domain and hence we observe relatively better trends of the transmitted gain characteristic curves in our simulation results. However, in the actual experiment effect of interference is prevalent and as a result we observe vastly different readings as compared to the simulation data, such as signals as strong as -20 dB at receiver 2 and 4 at 1 GHz as opposed to -55 dB mark in simulation for the same frequency with 90% glycerol as a dielectric medium. At 2 GHz where the antenna is fully matched in front of

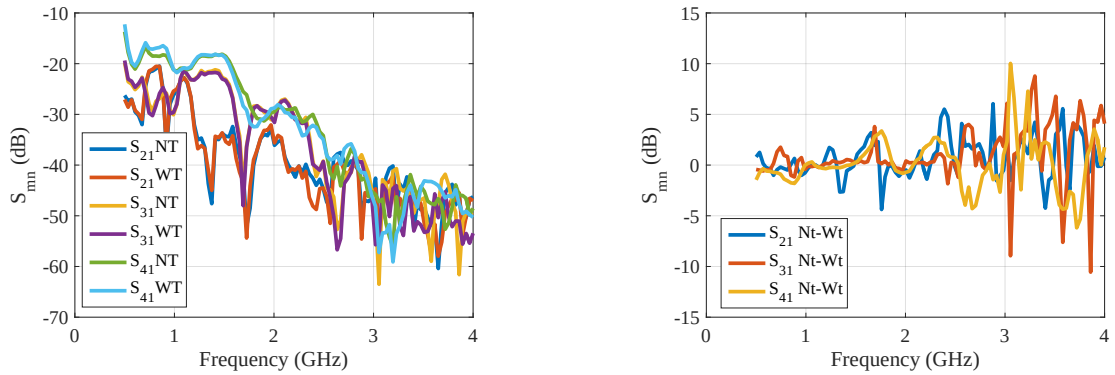

Fig. 3.18 (a) Experimental results of forward transmitted gain of ISM band antenna array operating in front of 90% glycerol filled tank (b) plots of differences in the transmitted gain for with and without target cases (in dB) acquired from experimental data obtained when array operates in front of 90% glycerol.

90% glycerol we observe approximately -30 dB transmission in measurements while for the same scenario in simulations we achieve below -55 dB transmission.

3.5 Conclusion

We present arrays constructed of four antenna elements in loaded configuration both numerically and experimentally. We use V slot patch antenna and ISM band band antenna to construct the two arrays. Experimental results obtained do not show agreement with corresponding simulation data due to several factors involved such as interference, surface wave propagation, multipath signals and mutual coupling between the array elements. Non immersed configuration of arrays poses many challenges in terms of acquiring clean useful data for imaging. To mitigate interference and surface waves we have introduce a layer of microwave absorbers around the periphery of the imaging chamber which shows slightly improved response of the transmitted gain trends, however not completely in line with theoretical understanding and simulation results. The impact of absorbing layer on the signal propagation motivates us to believe that there is an indication of acquiring better results if we control signal degrading phenomena such as coupling, surface waves and multipath signal propagation etc. Therefore, we decide to close our further study of arrays in non immersed configuration and pursue an alternative mean to mitigate the aforementioned unwanted phenomena and acquire more reliable results for our imaging application.

Chapter 4

Analysis of Immersed Antenna Arrays

4.1 Introduction

Information from multiple antennas in the form of an array is required for MT so that different views of the imaging domain can be captured and then supplied to the inverse imaging algorithm. Installing multiple antennas in close proximity (within a suitable diameter for breast imaging) with each other naturally requires the same number of cables to feed the antennas, hence there is a challenge to deal with crosscoupling between the array elements and the cables. Electromagnetic wave propagation in the imaging chamber suffers from various challenges such as interference, cross coupling between the antenna elements, multi-path signal and surface wave propagation.

Imaging algorithm solves an inverse problem using the information collected from the data acquisition system, therefore it requires the collected data to be the true representation of the interaction of EM wave with the interior dielectric properties of the imaging domain. To mitigate or minimize the aforementioned unwanted characteristics there is a need to comprehensively study these phenomena and propose potential solutions. System dimensions and choice of background medium are the two potential solutions to address these issues.

Lossy liquids used as background matching media inside the imagining chamber introduce attenuation in the system which in turn helps mitigate cross coupling between the antenna elements, suppression of surface waves and multi-path signal propagation. There is a disadvantage attributed to the use of high loss liquid as a background as it not only helps suppress the unwanted signals but also reduces the useful signal strength significantly which in turn leads to a need of costly high sensitivity transceivers that has a strong bearing on overall system cost.

Imaging chamber dimensions also contribute significantly in mitigating the unwanted signals. Geometry and dimensions of the imaging tank and lossy liquid material level above and below the antenna has to be optimized in order to acquire useful data and suppress unwanted signals. In this chapter we present a detailed study on optimizing the dimension of imaging chamber comprised of monopole antennas submerged in 80% glycerol. Software system calibration methods such as [117] have also been reported in the literature to address the non-idealities involved in data acquisition and experimental errors.

4.2 Impact of Antenna Array Positioning

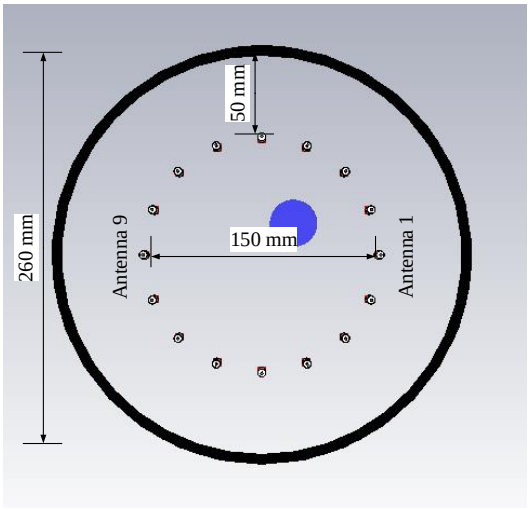

(a)

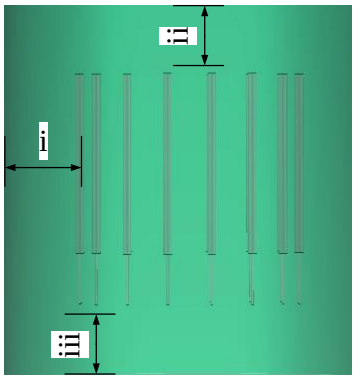

i: Array to inner wall
ii:Array ports to immersion surface distance
iii: Radiating tips to tank floor distance

(b)

Fig. 4.1 (a) Array of 16 monopole antennas modelled in CST MWS., (b) Different locations of array inside the chamber to be studied for signal propagation analysis.

Reflection and refraction of electromagnetic wave incident on top, bottom and peripheral interfaces of the imaging chamber affect transmitted gain at the receivers significantly. Waves propagating on surface of the liquid and along the walls of containers are not affected by the scatterer situated inside of the imaging domain and can potentially interfere with the waves which propagate through the imaging domain before they reach receivers. To analyse the impact of dimensions of imaging chamber on transmitted gain characteristics, we perform a detailed study on sixteen monopole antenna array installed in our imaging chamber.

Monopole antennas used in this study are 154 mm long (34 mm radiating tip) and hence the effect of surface waves can be analysed in a better fashion within the proposed geometry

of our setup. Due to the length of antenna, radiating tip could potentially be quite close to surface of immersion or to the floor of imaging tank, depending on the orientation of antennas. We have presented optimization of radiating tip of a monopole antenna in chapter 2 for our required frequency of operation. In this study we choose a simple design where total length of the antenna is comprised of 34mm radiating tip and 120 mm outer conductor length making it a total of 154 mm. We carry out our study of the 16 element monopole antenna array immersed in 80% glycerol. Dielectric properties of the used immersion medium are shown in Fig. 3.3.

Schematic of the array model of 16 monopoles is shown in Fig. 4.1 (a). We consider a cylindrical geometry to carry out this analysis as cylindrical geometry of imaging setups has several advantages and is widely reported in literature. Antennas are placed at an angle of 22.5° with respect to each other. Diameter of a circular ring of antennas forming the array is 150 mm. Diameter of the container is 260 mm that allows 5 cm gap between the antennas and inner wall of the container for a 150 mm array diameter. We keep length of the imaging tank flexible in our CST model to ensure that it allows the variability of immersion height with respect to the antenna. This allows us to study the impact of height of lossy immersion with respect to antenna tip on signal propagation. We place a 30 mm target at (20, 20) on the xy plane where 'origin' (0,0) is considered at centre of the tank as shown in Fig. 4.1 (a).

Return loss of the monopole antenna immersed in 80% glycerol is shown in Fig. 4.2 (a), where we can see that the monopole antenna under study is well matched in 80% glycerol and return loss stays below -10 dB throughout 1-3 GHz frequency band under consideration. Moreover, S_{ii} (return loss) response for each of the antennas in our array is very similar in each individual transmitter case and hence there is a negligible effect of antenna loading in the array.

We perform our study of monopole antenna arrays by considering a homogeneous background case of 80% glycerol. We consider several cases as depicted in Fig. 4.1 (b) to gain deeper understanding of the wave propagation through lossy homogeneous medium using CST simulation results:

- Immersion level 5 cm above and below antennas and 6 mm to the tank wall (array close to the peripheral boundary of the chamber).
- Ports at the top surface of immersion.
- Tip of the antenna at the floor level of the chamber.
- Immersion level 5 cm in all directions of the imaging chamber.

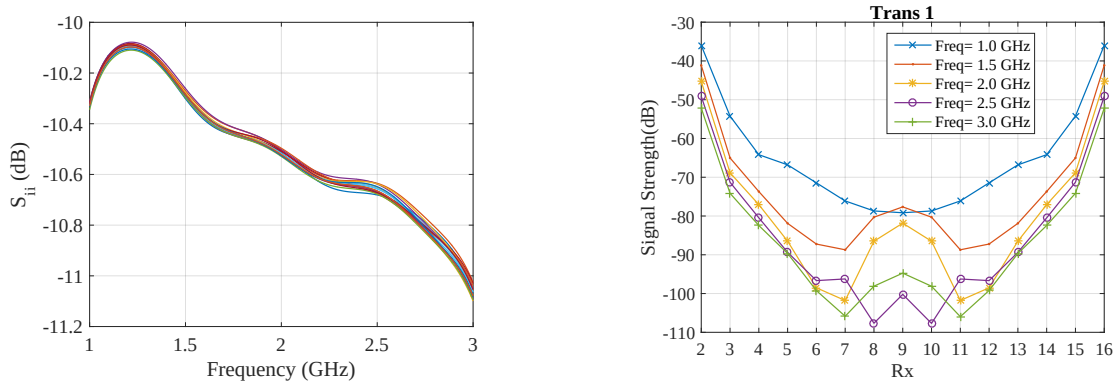

(a) (b)

Fig. 4.2 Simulation results of 16 element monopole antenna array (a) S_{11} of each element of the 16 antenna array immersed in 80% glycerol. (b) Forward transmitted gain at each receiver when the antenna array to tank wall distance is 6 mm and the immersion level above and below the antennas is 5 cm. Transmitted gain is plotted as a function of receivers for receivers 2 to 16 in homogeneous background where antenna 1 transmits.

- Immersion level 5 cm in all directions and inclusion of absorbers at the outer periphery of chamber.

- Immersion level 5 cm in all directions with a metallic shield covering absorbers.

Array located near the inner walls of imaging chamber: In the first case, antennas are near border walls of the tank and there is no absorber enclosing the tank. We expect a parabolic response of transmitted gain when plotted as function of receiver number for discrete frequency samples as the signal strength drops proportionally with increasing distance between transmitter and the receivers. Transmitted gain response is also expected to be symmetric because the signal propagates through a homogeneous medium and geometry of the setup is cylindrical.

Transmitted gain plots in this test case do not exhibit the expected parabolic characteristics. Receivers most affected (deviating from the expected trends) in this configuration are # 7, 8, 9 and 10 as shown in Fig. 4.2 (b). Aforementioned receivers receive unexpectedly higher power despite being geometrically further away from the transmitting antenna (antenna 1 in this case) with respect to relatively closer neighbouring receivers. Signal level received in the worst case scenario is -110 dB. The unexpected response of transmitted gain is caused due to the waves escaping inner domain of the tank where there is lossy liquid and start propagating along periphery of the tank. Waves propagating along the external walls of the imaging chamber undergo lesser attenuation in surrounding vacuum as compared to the

signals propagating inside the liquid and therefore receivers receive higher signal strength. From our observations we conclude that antennas must not be situated very close to border walls of the immersion tank.

Array ports located at the top surface of coupling medium: We now investigate the impact of bringing ports to upper level of the immersion medium and keeping side walls to antenna centres and antenna tips to tank floor distance 5 cm. As can be seen in Fig. 4.3 (a) the respective transmitted gain plots show better parabolic characteristic. Only receiver 9 at 3 GHz shows a very minimal exception to this parabolic trend. The trends observed in this case manifest the fact that radiating element of the antennas is well below the immersion surface and also considerably above the floor level, where potential surface waves are likely to propagate. As the tank floor is 5 cm below the radiating tip therefore significant suppression of the waves due to lossy nature of the background material takes place. By the time these surface waves reach floor of the tank they become significantly attenuated that is why there is no compelling contribution to the signals being received at the receivers from surface waves propagating on antenna outer conductor and floor tank. It is also quite obvious from the comparison of Figures 4.2 (b) and 4.3 (a) that the transmitted gain in latter case are much weaker than the former; minima -180 dB for latter as opposed to -110 dB for the former. Significant differences in transmitted gain levels verify our previous assumption that signals received at antennas 2 to 16 when they are placed closer to border of the tank do not propagate inside the chamber and reach receivers from outside of the tank and hence undergo lesser attenuation.

Array radiating tips located at the floor of the imaging chamber: Transmitted gain plots for the case when antenna tips have been placed at the floor of immersion tank and the immersion level above the ports (feeding point) of the antennas as well as to the side walls of the tank is 5 cm are shown in Fig. 4.3 (b). We keep 5 cm distance between the inner walls to antenna array and between immersion surface to antenna ports to suppress any surface waves on immersion surface and around periphery of the tank. As can be seen from Fig. 4.3 (b) transmitted gain exhibit 'near' parabolic response for all frequencies being investigated except for 1.5 GHz. Transmitted gain level has also risen by 40 dB approximately as compared to the previous case shown in Fig. 4.3 (a), this proves that the surface waves have been excited and propagate along floor of the tank and hence undergo lesser attenuation and consequently we receive higher signal levels across the array.

Array located at 5 cm inside the imaging chamber in all directions: We continue our study by raising antennas 5 cm above the tank floor and hence keeping 5 cm immersion level all around the antenna array. Note that we only change the immersion level and the vertical

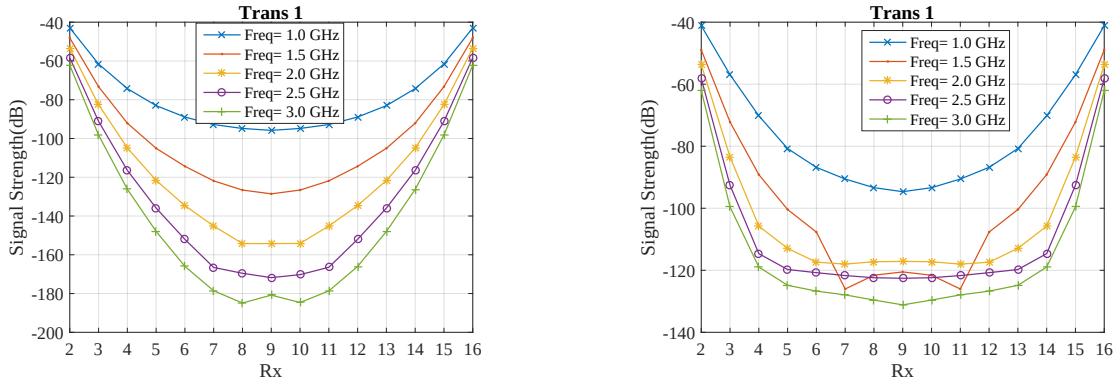

(a) (b)

Fig. 4.3 Simulated forward transmitted gain at each receiver when (a) feed points situated at the top surface of immersion (b) radiating tips touching floor of the tank. Transmitted gain is plotted as a function of receiver # for receivers 2 to 16 in homogeneous background where antenna 1 transmits. Five frequency samples have been chosen at a step of 0.5 GHz between 1 to 3 GHz

position of the antennas while diameter of the array ring remains constant in all the cases studied. Plots of transmitted gain as function of receivers in homogeneous background of 80% glycerol when immersion medium covers the antenna array by 5 cm in all directions are shown Fig. 4.4 (a). Transmitted gain show a good parabolic response except at 2.5 GHz for receiver 9 which suddenly dips below sharply. Potential cause for this dip is interfering signals and also multi-path signals. However, overall response is symmetric as expected. It is also evident from Fig. 4.4 (a) that transmitted gain levels have dropped significantly again (-180 dB approx.), thus revealing that signals received at the receivers propagate through the imaging domain and therefore undergo higher attenuation.

4.3 Impact of Enclosing the Tank with an Absorber

We keep the same geometry as described in previous case and introduce an absorber, EC-COSORB MCS around the tank periphery to suppress any surface waves propagating along boundary of the tank. Resulting transmitted gain response, upon introduction of an absorber layer around the chamber is depicted in Fig. 4.4 (b). We observe that the previously seen sudden dip at 2.5 GHz has been flattened out after introducing the absorber around imaging chamber. Removal of the dip at 2.5 GHz is due to impact of the absorber which suppresses multipath signals and hence reduces interference from those stray signals. We also observe that signal levels at 2.5 and 3 GHz have been slightly dropped, which also points to the fact

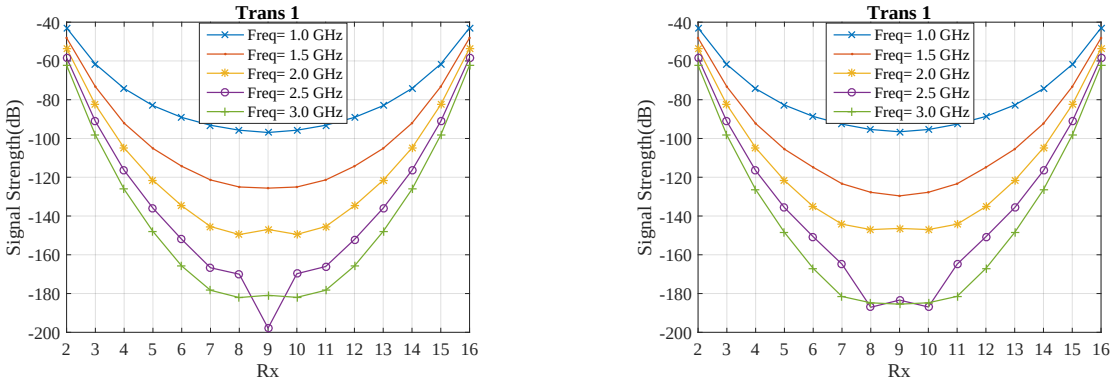

(a) (b)

Fig. 4.4 Simulated forward transmitted gain at each receiver when (a) distance from the top, bottom of immersion and tank walls is 5 cm (b) the distance from top, bottom of immersion and side walls of the tank is 5 cm and a layer of microwave absorbers is added on the outer periphery of the tank. Transmitted gain is plotted as a function of receiver # for receivers 2 to 16 in homogeneous background where antenna 1 transmits. Five frequency samples have been chosen at a step of 0.5 GHz between 1 to 3 GHz

that multipath signals may have been causing constructive interference too that might have resulted in higher transmitted gain previously in the absence of absorbers.

We introduce a thin PEC metallic sheet layer on the exterior surface of the absorber to ensure that the imaging domain become as much isolated from the outside signals as possible. Resulting transmitted gain after including the metallic shield are plotted in Fig. 4.5 (a). It is evident from Fig. 4.5 (a) that the best parabolic response as compared with all previous cases studied so far has been achieved in this configuration. Transmitted gain levels are considerably low, however signal trends are in line with the theoretical understanding of wave propagation phenomenon in homogeneous dielectric medium. The lowest signal has been received at 3 GHz at receiver 9; the most distant receiver when antenna 1 transmits.

To gain a quantitative insight into the effect of introducing absorber and shield in the simulations, we subtract the signal strength response (in dB values) with the absorber and shield from the case without it while keeping immersion levels at 5 cm in all directions i.e. above below and on the sides of antenna array. Resulting plots are depicted in Fig. 4.5 (b). We observe that at lower frequencies - less than 2 GHz and at closer receivers- # 2 to 6, the transmitted gain response does not vary significantly in both cases, hence the difference is very close to zero. However, at higher frequencies such as at 2, 2.5 and 3 GHz, difference between transmitted gain of the mentioned cases starts to become large for receivers 7, 8, 9, 10 and 11. We also observe that at higher frequencies, closer receivers with respect to

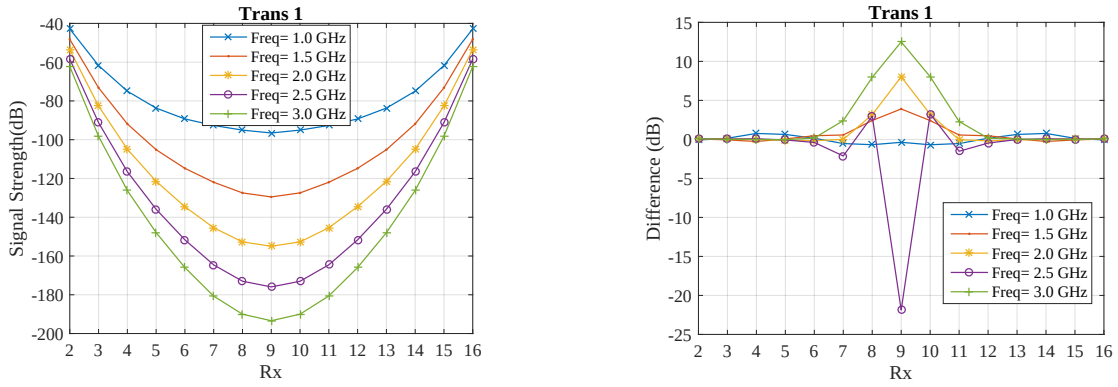

(a) (b)

Fig. 4.5 Simulated forward transmitted gain at each receiver when (a) the distance from top, bottom of immersion and side walls of the tank is 5 cm and a layer of microwave absorbers with metallic sheet is added on the outer periphery of the tank, (b) differences of transmitted gain (in dB) with absorber and metallic sheet covering Fig. 4.5 (a) case subtracted from without absorbers and shielding case Fig. 4.4(a). Transmitted gain is plotted as a function of receiver # for receivers 2 to 16 in homogeneous background where antenna 1 transmits. Five frequency samples have been chosen at a step of 0.5 GHz between 1 to 3 GHz

transmitter (antenna 1 here) i.e. receivers 2 to 6 and 12 to 16 do not get affected significantly. The phenomenon of variation of signal strength at higher frequencies can be attributed to the radiation characteristics of the antenna at these frequencies and also to the weaker signal (surface waves and multipath) contributions.

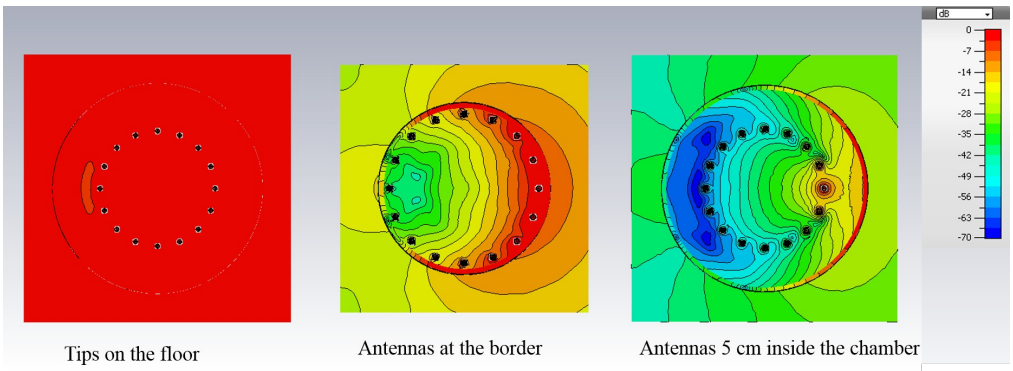

Fig. 4.6 Simulated electric field distribution on the XY plane at Y=0 for three different cases (left to right) antenna tips on the floor of the tank, antenna array touching the tank border and antenna array immersed 5 cm inside the matching liquid in all directions.

Fig. 4.6 shows the electric field distribution inside the chamber at 1 GHz when an array of 16 monopole antennas is excited. The field distribution is shown for three different cases

to quatitaviley evaluate the effect of surface waves on the transmitted gain at the receivers. We observe that when antenna tips are touching the floor there is very high field intensity on the Y=0 plane in all directions. When the array has been raised by 5 cm and the distance between the tank periphery to antenna is minimized (6mm) we observe very high fields around the periphery of the chamber hence verifying the qualitative assumption that the fields tend to propagate along the surface of the container. Finally we present the field distribution when the antenna array is fully submerged 5 cm inside of the lossy dielectric medium. We observe that the impact of surface waves propagating along the periphery of the domain has been significantly reduced and the transmitted gain is indicative of the signals that propagate inside the imaging chamber. This proves that in order to acquire good quality data there is a need of lossy liquid to suppress signal degrading phenomena.

4.4 Analysis of Immersed Monopole Antenna Array with Target Using Simulation Results

We introduce a target made of 30 mm cylindrical water object inserted inside 80% glycerol filled imaging chamber centred at (20, 20) on XY plane concentric with centre of the tank. Length of the target is kept same as monopole antenna length in 'Z' direction. Purpose of this study is to evaluate impact of a high dielectric target on transmitted gain and wave propagation through the domain in general.

Geometry of target and antenna array with the tank is shown in Fig. 4.1, note that the antennas are placed in anticlockwise direction. Figures 4.7 and 4.8 show the transmitted gain at each receiver in the array when antenna Txi transmits after the inclusion of aforementioned target object inside the domain. Note that receiver 2 corresponds to the adjacent antenna with respect to the transmitter 'i' in the counter clockwise sense. The depictions in Figures 4.7 and 4.8 clearly show that trend of the curves for each of the frequency sample under consideration does not have a complete parabolic trend and exhibit some level of skewness corresponding to the receiver positions with respect to the transmitter and target. The trends observed in Figures 4.7 and 4.8 are the indicators of occurrence of scattering phenomenon due to the inclusion of high dielectric target.

To have a clearer look at this phenomenon of scattering, we present the magnified version of the Fig. 4.7 for only one transmitter (antenna 1) for both 'no target' and 'with target' cases in subsequent figures.

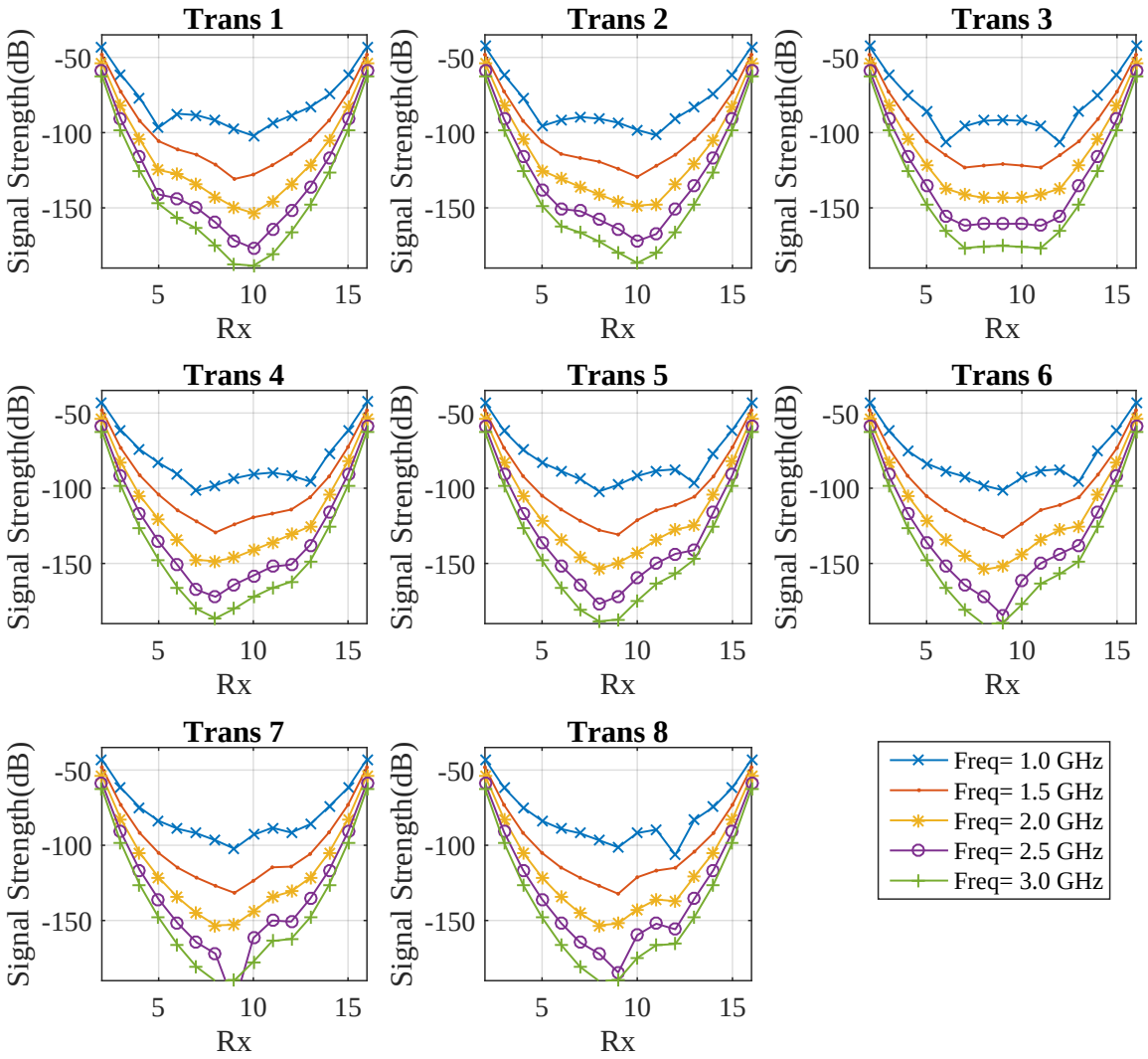

Fig. 4.7 Simulated transmitted gain of the monopole antenna array immersed in 80% glycerol for receivers 2 to 16. Each sub plot depicts the individual transmitter from 1 to 8.

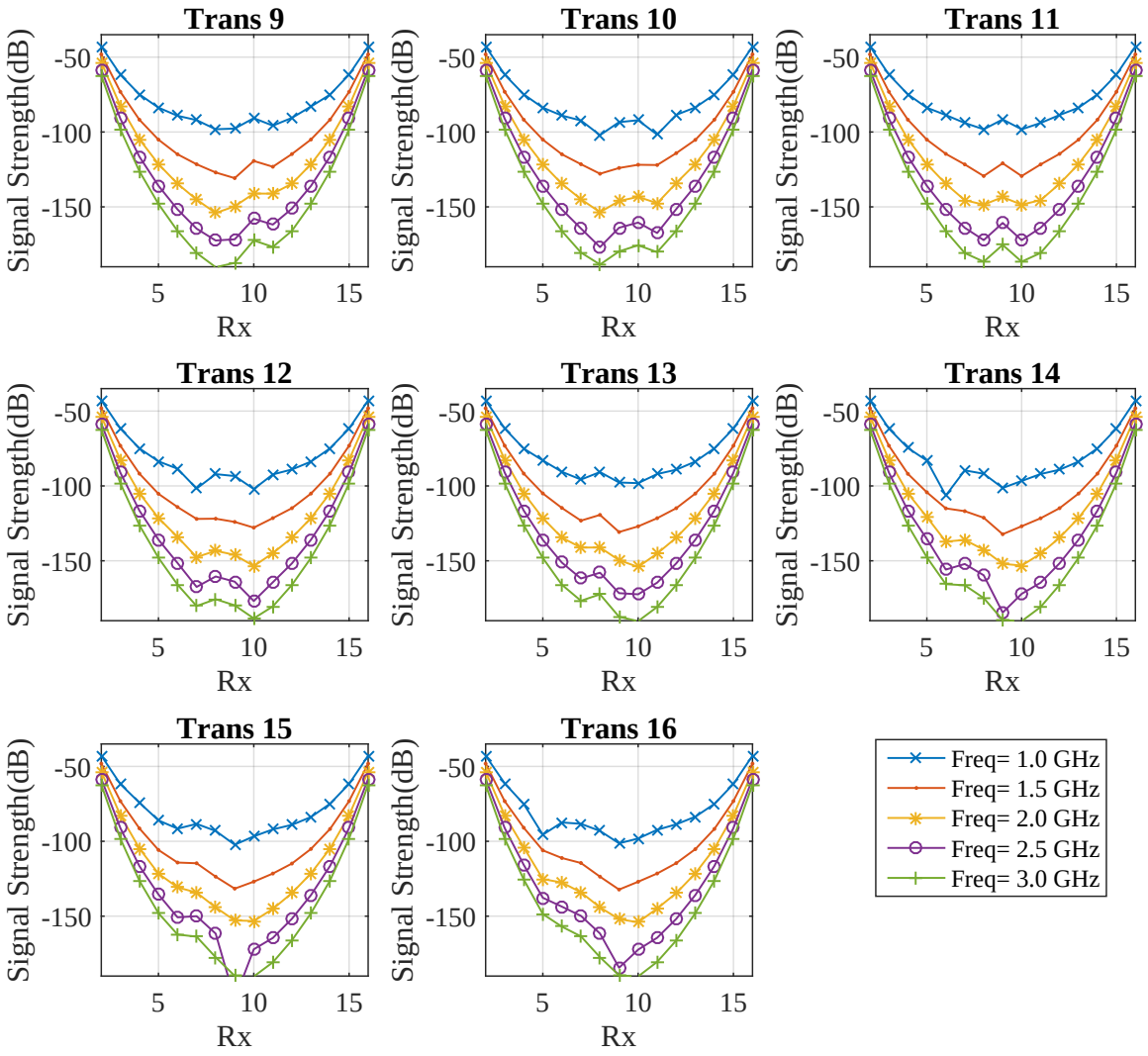

Fig. 4.8 Simulated forward transmitted gain of the monopole antenna array immersed in 80% glycerol for receivers 2 to 16. Each sub plot depicts the individual transmitter from 9 to 16.

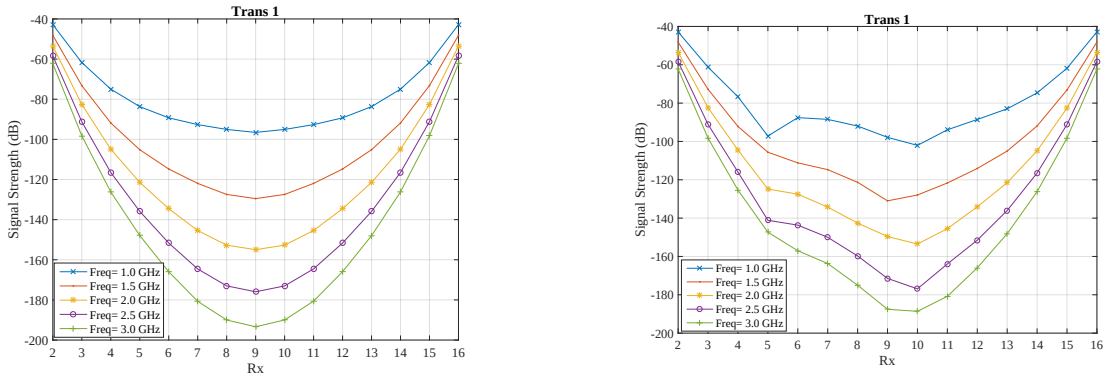

(a) (b)

Fig. 4.9 Simulated forward transmitted gain at each receiver when (a) the distance from top, bottom of immersion and side walls of the tank is 5 cm and a layer of microwave absorbers with metallic sheet is added on the outer periphery of the tank, (b) received strength at each receiver when a water target object is introduced in the configuration of 4.9(a). Transmitted gain is plotted as a function of receiver # for receivers 2 to 16 of the monopole antenna array immersed in 80% glycerol homogeneous background where antenna 1 transmits. Five frequency samples have been chosen at a step of 0.5 GHz between 1 to 3 GHz

Transmitted gain as a function of receiver # for the frequency range 1-3 GHz at a step of 0.5 GHz for homogeneous background case is presented in Fig. 4.9 (a). Parabolic trend of the curves for considered frequency samples is a representation of attenuation of signals as a function of receiver # with respect to relative position of the transmitter. Signals received at the receivers become weaker when distance between the transmitter and receiver increases. We observe fully symmetric trends in Fig. 4.9 (a) indicating that in homogeneous background transmitted gain is symmetric for symmetrically placed receivers.

Transmitted gain plots of the monopole antenna array immersed in 80% glycerol with water target included inside the imaging domain are given in Fig. 4.9 (b). Trends observed in Fig. 4.9 (b) represent the corresponding plots of transmitted gain for the case when a high dielectric target (water) is introduced. As a result of inclusion of high contrast discontinuity, we observe skewed response of the transmitted gain trends.

To quantitatively study this effect we plot graphs that show the difference in dB values of the transmitted gain when signals with inclusion of target (in dB) is subtracted from the corresponding signals (in dB) from homogeneous domain. Differences in magnitudes of the transmitted gain in dB values are calculated for two cases ‘with target’ and ‘without target’ by subtracting with target signals from corresponding without target signals, both in dB values. Differences reach upto 20 dB, indicating the effect of scattering from high

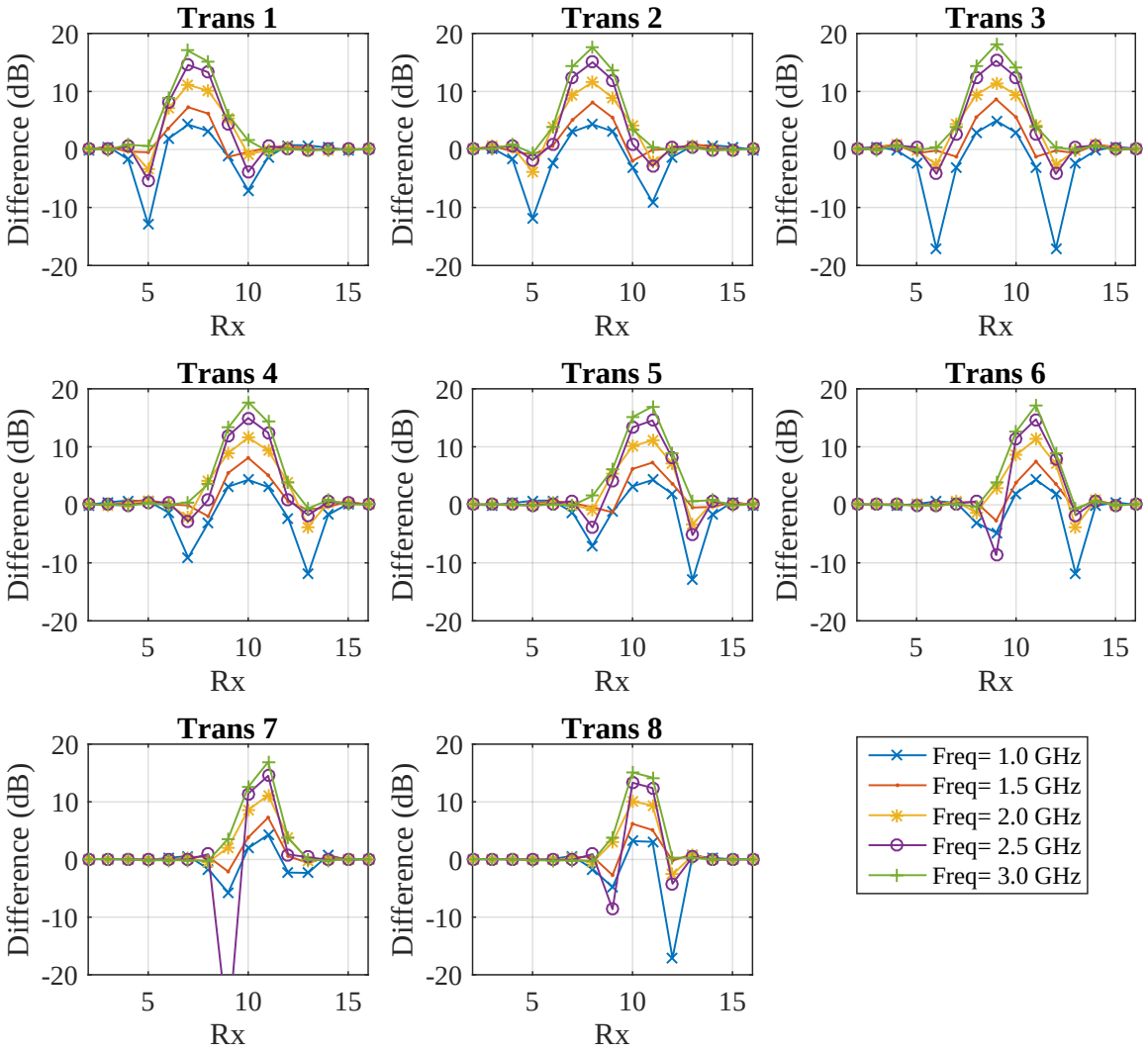

Fig. 4.10 Differences (in dB) in simulated forward transmitted gain of the monopole antenna array immersed in 80% glycerol for receivers 2 to 16. Each sub plot depicts the individual differences of no target case subtracted from with target case, for each of the transmitters 1 to 8 in dB values.

dielectric discontinuity as shown in Figures 4.10 and 4.11. It is evident from differences plots that the most affected receivers are the ones which lie in close proximity to the target, for example when antenna 1 transmits, receivers 5 to 10 are the most affected, which in the light of Fig. 4.1 are the antennas situated in the top half of the circular geometry of the setup, where the target also resides. Antennas 10 to 16, on the other hand, are located in the bottom half, which is situated further away from the target and hence the impact of scattering due to target is not expected to be as high as the top half, therefore from the differences plot in Fig. 4.10 for transmitter 1 we see that difference in transmitted gain for receivers 2 to 4 and 10 to 16 is very minimal and in most cases very close to 0 dB.

Thus, from the above mentioned analyses of the setup geometry, inclusion of absorbing surface and metallic shield we understand that impact of various unwanted phenomena such as surface wave propagation and multipath signals interference can be minimized. Inclusion of high dielectric discontinuity significantly alters course of propagation and the information collected at the receivers can be used for reconstruction of dielectric profile of the imaging domain using an inverse problem solving algorithm.

4.5 Analysis of Immersed Printed Monopole Antenna Array Using Simulation Results

We analysed various factors affecting wave propagation inside the imaging chamber and ways to combat with unwanted phenomena using system geometry in the previous section. Now, we will use the above findings to analyse performance of our printed monopole antenna presented in Chapter 2. Our printed monopole is a compact antenna with very small dimensions (12*15 mm^2), therefore depending on the performance of this compact planar antenna in an array it can be a good candidate for the potential microwave tomography system in sight. Smaller dimensions of our compact printed monopole can potentially allow us to realize the more practical and ergonomic microwave tomography system as compared to the long (154 mm) monopole antennas studied in previous section.

We study an array formed of 16 triangular patch printed monopole antennas, immersed in 80% Glycerol and 90% corn syrup mixed with 10% water. We consider the aforementioned media to have an insight into how the signal propagation is affected for the same geometry when the antennas are immersed in different dielectric media, a complete study on the choice of background medium will be presented in the next chapter. We performed study on the impact of introducing an absorber and metallic sheet layer at the exterior of immersion tank

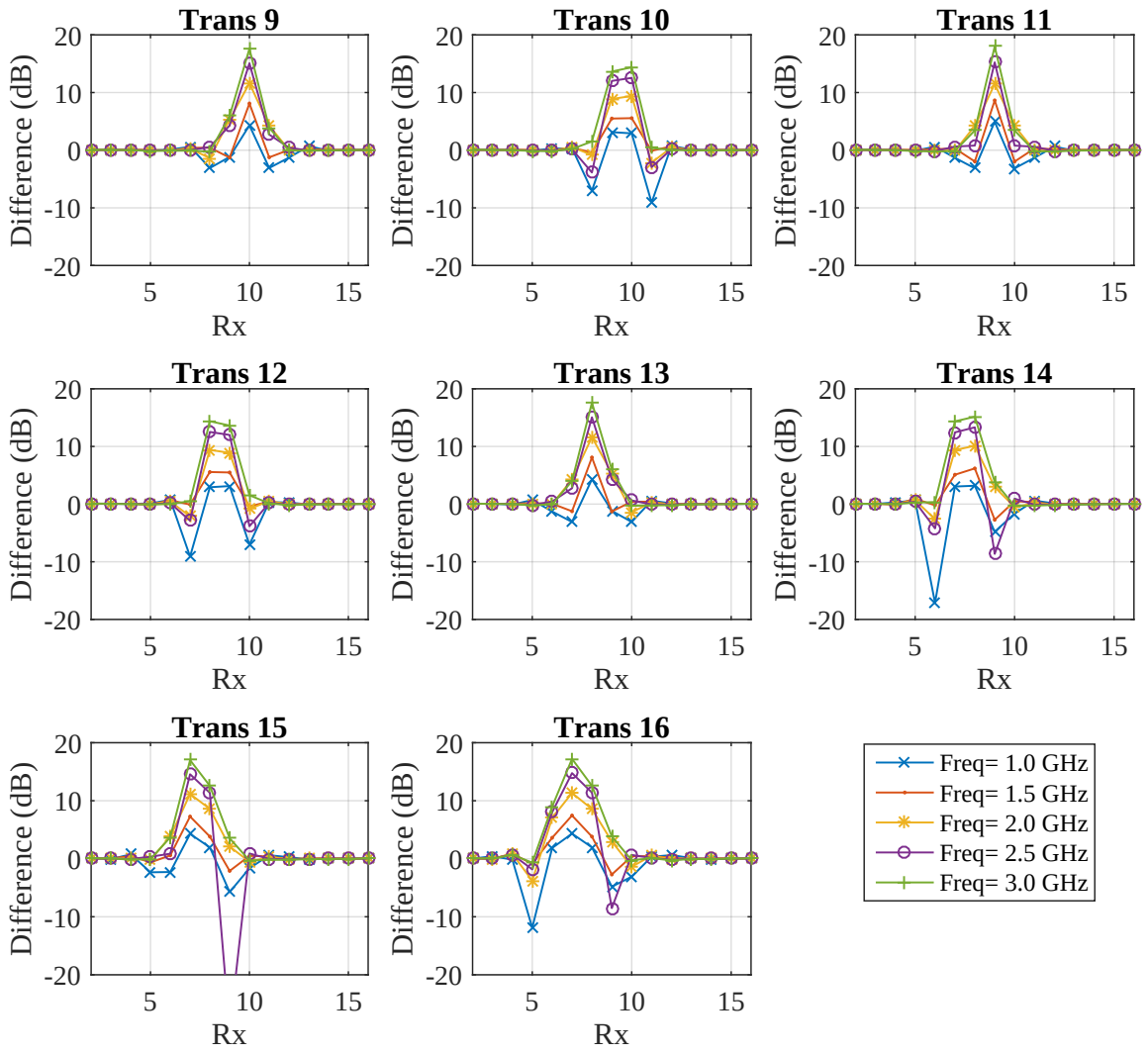

Fig. 4.11 Differences (in dB) in simulated forward transmitted gain of the monopole antenna array immersed in 80% glycerol for receivers 2 to 16. Each sub plot depicts the individual differences of no target case subtracted from with target case, for each of the transmitters 9 to 16 in dB values.

in the previous section, therefore we will not repeat the same analysis in this section and based upon our previous findings that the absorber and metallic sheet help reduce surface waves along the periphery of immersion tank, we will start our new analysis by incorporating this layer into our system model and subsequent simulations.

We begin our analysis by immersing the printed monopole antennas in 80% glycerol and studying the transmitted gain as a function of receiver for a given set of frequencies in a homogeneous background. As the antenna is matched well in glycerol for the entire range of frequencies of interest, therefore we will consider five frequency samples from 1 to 3 GHz at a step of 0.5 GHz to cover the whole range and study different behaviours of the antenna array in terms of signal propagation through the chamber at discrete frequencies.

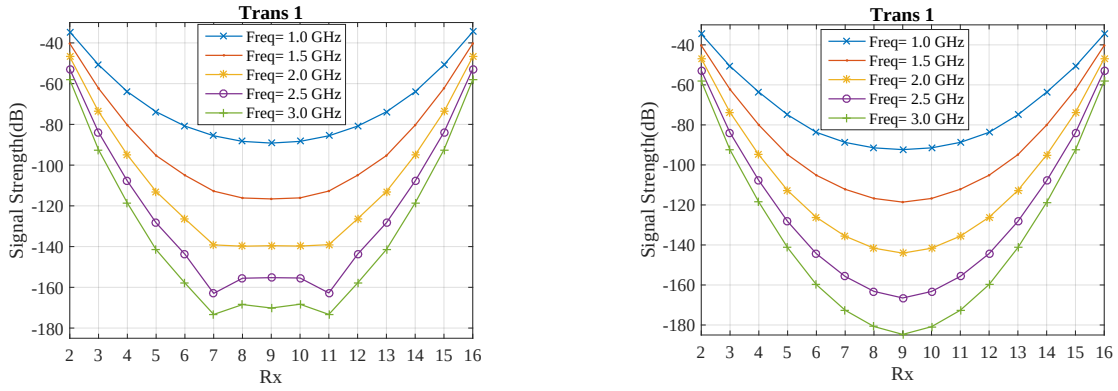

(a) (b)

Fig. 4.12 Simulated forward transmitted gain at each receiver when 16 printed monopole antenna array is immersed in (a) in 80% glycerol, 5 cm in all directions (b) 80% glycerol 6 cm above the floor. Transmitted gain is plotted as a function of receiver # for receivers 2 to 16 in homogeneous background where antenna 1 transmits. Five frequency samples have been chosen at a step of 0.5 GHz between 1 to 3 GHz

Transmitted gain of the triangular patch printed monopole array at each individual receiver (from 2 to 16) when immersed in 80% glycerol is shown in Fig. 4.12 (a) and Fig. 4.12 (b) shows same plots for the case when antenna array is raised 6 cm above floor of the tank as opposed to 5 cm as in previous case. We observe that trends of the curves shown in Fig. 4.12 (a) are not fully parabolic for the frequencies above 2 GHz, where antenna becomes more directive in end-fire direction, thus there is more reflection from the floor due to the antenna orientation. Consequently, we raise the antennas from floor level by 10 mm to observe the impact of increased distance from the floor in lossy immersion background on the transmitted gain trend.

The trends obtained after increasing the tank floor to antenna distance by 10 mm are shown in Fig. 4.12 (b). after making this height adjustment the trends become more parabolic for all of the frequencies under discussion, thus we deduce that the antenna radiation characteristic plays a vital role in transmitted gain. To minimize the unwanted phenomena such as surface wave propagation we can alter the geometry of system, for example increase the height of immersion. We note that in homogeneous background, the performance of array does not change significantly for different transmitters therefore we only show the transmitted gain plot for antenna receivers 2 to 16 when antenna 1 transmits in Fig. 4.12.

To study the effect of geometry and dimensions of the array setup on signal propagation further, we change the geometry of setup to smaller dimensions and also bring the antennas closer to each other. In this new setup we reduce the array diameter to 100 mm and tank diameter to 200 mm. We reduce height of the immersion medium to 100 mm also. Reduction of immersion height results in 42.5 mm distance from the antenna bottom to floor of the tank and antenna top to immersion liquid surface. Fig. 4.13 (a) shows transmitted gain as function of receivers in this new altered geometry. We note that the reduced array and tank diameters do not affect distance between the antennas and inner wall of the tank as it remains 5 cm in this new setup.

Parabolic trends for all the curves representing discrete frequencies from 1-3 GHz at a step of 0.5 GHz are observed as shown in Fig. 4.13 (a) . We observe that transmitted signal strength is also increased upto 40 dB due to shorter distance signals have to travel in lossy immersion background to reach the receiving ports (worst case scenario).

We introduce a background material made up of 90% corn syrup mixed with 10% water and consider the similar geometry as for Fig. 4.13 (a) and plot transmitted gain traces as function of receivers. Two cases i.e. Fig. 4.13 (a) and 4.13 (b) represent same geometrical scenarios of the setup however only difference between the two is different background dielectric materials.

Transmitted gain plots for 90% corn syrup show good parabolic trends, however, not perfect at all frequencies. Transmitted gain magnitude for 90% corn syrup is also higher by upto 60 dB approximately (for worst case corresponding scenarios) as compared with the same scenario signals for 80% glycerol background. Significant increase in transmitted gain is attributed to the differences of conductivity between the two media, which we will discuss in detail in next chapter. Purpose here for introducing a different background material is to compare the impact of same geometry on transmitted gain of two different media. Array immersed in 90% corn syrup shows very similar signal level for receivers 6 to 12 at 1 and 1.5 GHz, however true parabolic response of the transmitted gain for 90% corn syrup is observed

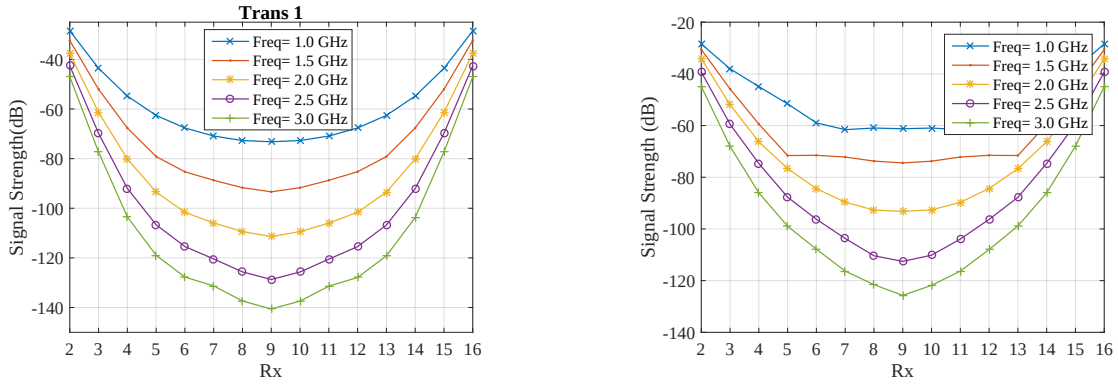

(a) (b)

Fig. 4.13 Simulated forward transmitted gain at each receiver when 16 printed monopole antenna array is immersed in (a) 80% glycerol 4.25 cm above the floor and 100 mm antenna array diameter (b) 90% corn syrup when distance between the array to tank walls is 5 cm and distance from antenna to immersion surface and tank floor is 4.25 cm. Transmitted gain is plotted as a function of receiver # for receivers 2 to 16 in homogeneous background where antenna 1 transmits. Five frequency samples have been chosen at a step of 0.5 GHz between 1 to 3 GHz.

from 2 GHz and above, this is due to radiation characteristics of the antenna when immersed in corn 90% background medium.

4.6 Conclusion

We presented effects of system geometry on propagation and scattering of electromagnetic waves in the imaging domain by arranging array of antennas in different locations inside the imaging chamber. We observed that if an antenna array operates near the tank floor or closer to the inner wall of the tank, surface waves are excited and have degrading effect on the transmitted gain at various receivers. We also studied the effect of introducing absorber and metallic shield on signal propagation where we concluded that microwave absorber helps minimize surface wave propagation and metallic shield isolates the system chamber from external interfering signals. Our printed monopole is a compact planar antenna which is a good candidate for our imaging system prototype as its small dimensions are advantageous to build a simple prototype that can cater for suppressing the degrading factors such as surface waves and multipath signals unlike long wire monopole antennas where large imaging chambers are required to achieve similar operation. We also studied the impact of reducing array diameter and using a different dielectric material (90% corn syrup) using our triangular

patch printed monopole antennas. We observed increased transmission levels in both cases due to closer distance for reduced diameter array and lower conductivity of 90% corn syrup as compared to 80% glycerol solution.

Chapter 5

Study of the Effect of Coupling Media on Microwave Imaging System

5.1 Introduction

We studied the operation of antenna arrays in front of different dielectric filled imaging chamber in Chapter 3 where we concluded that in order to obtain useful information representing inner dielectric profile of the imaging domain we must minimize multipath signals, surface waves and any other signal interferences or sources of errors. Thus, we concluded that the arrays will have to be immersed in an appropriate medium so that required objectives may be reached. In the previous chapter we analysed effects of location of an immersed array inside the imaging chamber on signal propagation. Based upon the information acquired in that study we optimized dimensions of the experimental setup for monopole antenna arrays (can be applied to omnidirectional antennas) immersed in 80% glycerol background. We only used 80% glycerol in our previous study for our analysis with both monopole and triangular patch printed monopole antenna arrays and briefly touched upon 90% corn syrup as background medium for the latter.

In this chapter we study different dielectric media to be used as coupling medium for microwave tomography system. We analyse the performance of our printed monopole antenna arrays immersed in each of these media and evaluate the different effects of matching liquids on signal transmission. Antenna characteristics are dependent on immersion material, for example, return loss of the same printed patch monopole antenna was seen to be different in 80% glycerol and Triton x-100 in last chapter. Different immersion media not only alter the antenna matching, but can also have a significant effect on the signal propagation through the medium, for example dielectric material with higher loss will attenuate the signal more

and weaker signals may not be detected by the typical vector network analysers or any other non specific high sensitivity RF transceiver. Therefore, there is a need to study impact of the dielectric background media used for energy coupling on signal propagation and select the best medium for our microwave tomography system in sight. The choice of background medium also has a great bearing on overall cost of the system, as high sensitivity transceiver systems incur additional cost.

5.2 Dielectric Properties of Coupling Media

We use a variety of coupling media with varying degree of relative permittivity and conductivity so that we can find the most suitable medium that can fulfil our requirements of the system design under study. Dielectric material used for microwave tomography system should be bio-compatible as breast (in breast tumour detection case) is required to be suspended inside the background medium and hence there is a direct contact between human tissue and the dielectric medium. We prepare coupling solutions by mixing varying concentrations of water in corn syrup and glycerine. Subsequently we measure the properties of thoroughly mixed solutions using probe kit with VNA. We use 85070 dielectric probekit by Agilent technologies with the PNA series E8362B VNA for these dielectric measurements. Typical accuracy of this probekit for real and imaginary dielectric constant and loss factor measurements is within $\pm 5\%$. Dielectric properties of the media considered in this study are shown in Fig. 5.1 where Fig. 5.1 (a) shows conductivity of the medium and Fig. 5.1 (b) depicts relative permittivity of the medium calculated from the measured imaginary component of permittivity.

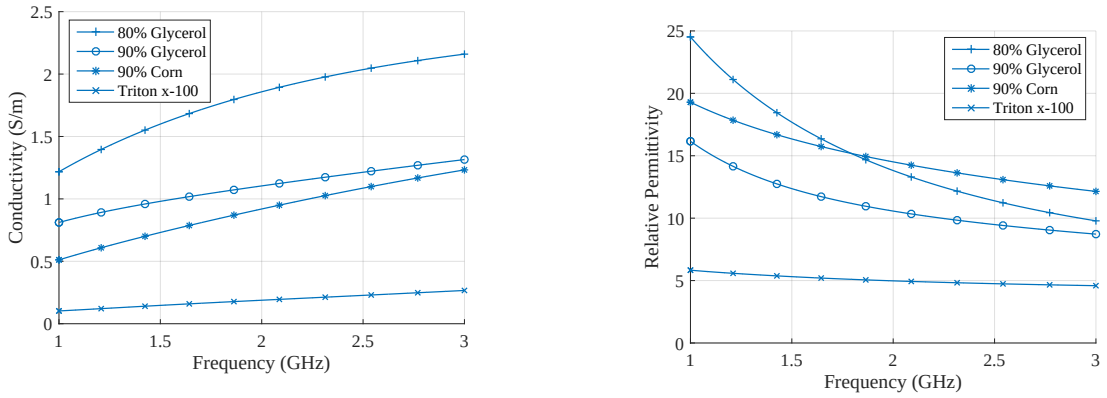

(a) (b)

Fig. 5.1 Dielectric properties of 80% glycerol, 90% glycerol, 90% corn syrup and Triton x-100. (a) Conductivity (b) Relative permittivity.

Dielectric properties shown in Fig. 5.1 reveal that higher water content increases conductivity of the material, for example 90% glycerol has a conductivity of less than 1 S/m at 1 GHz whereas 80% glycerol has a conductivity of 1.25 S/m at the same frequency. It is also evident from Fig. 5.1 (a) that the conductivity of a material depends on the frequency of operation and increases with the increase in frequency. Triton x-100 exhibits minimum conductivity among all the materials shown in Fig. 5.1. However, relative permittivity for 90% corn syrup is higher than 90% glycerol for the entire range of desired frequency (1 to 3 GHz) while exhibiting lower electric conductivity for the entire range. 90% corn syrup also shows higher permittivity than 80% glycerol from 1.7 GHz and above while maintaining low conductivity over the entire range against 80% glycerol. These are some interesting findings, we will elaborate the impact of these findings on signal transmission in the next section using 3D EM simulations of the system described in Chapter 4.

5.3 Effect of Different Coupling Media on Signal Transmission

We begin our analyses of effects of different dielectric media on the performance of an array comprised of 16 printed monopole antennas fully immersed in 80% glycerol, 90% glycerol, 90% corn syrup and Triton x-100. We, first study return loss of the antenna in each of the sought media. Fig.5.2 depicts return loss of our printed monopole antenna immersed in the aforementioned media. We observe that antenna return loss is below -10 dB for the entire frequency range (1-3 GHz) when immersed in 90% corn syrup and 80% glycerol, while for 90% glycerol -10 dB return loss point is achieved at approximately 1.2 GHz and then stays below -10 dB from thereon until 3 GHz. Triton x-100 however being the least lossy material with low relative permittivity when used as an immersion medium exhibits -10 dB return loss at 1.7 GHz and remains below this mark until 3 GHz in our simulation results. Thus, we conclude that our antenna is well matched in all four media in the desired range of frequency except for Triton x-100 where -10 dB return loss reaches at 1.7 GHz.

We turn our attention to the transmitted signal levels when an array of antennas is immersed in the aforementioned dielectric media. The geometry of our system modelled in CST MWS is shown in 4.1. Diameter of our antenna array is 150 mm, height of immersion medium is 100 mm and inner diameter of the tank is 250mm. We have used microwave absorber layer also to suppress the surface waves along periphery of the imaging chamber as explained in previous chapter.

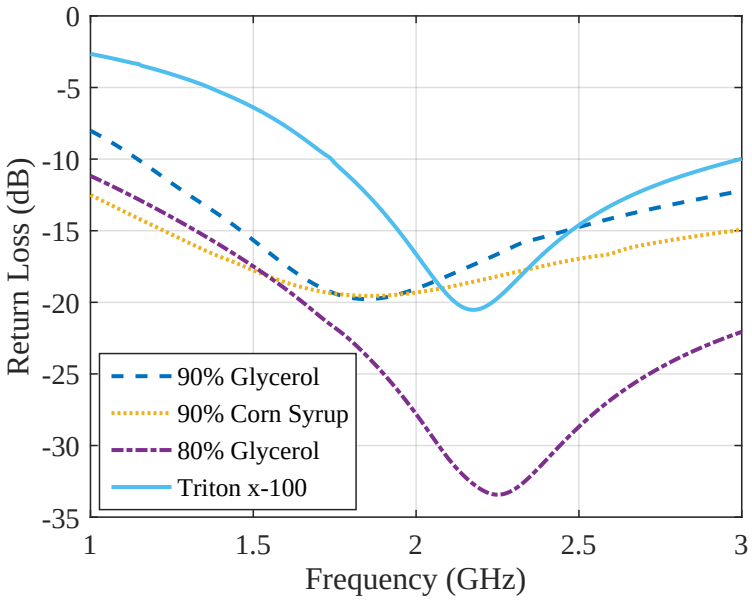

Fig. 5.2 Simulated return loss of printed monopole antenna immersed in 90% glycerol, 90% corn syrup, 80% glycerol and Triton x-100 using CST® MWS.

Transmitted gain plots as function of receivers in homogeneous 80% and 90% glycerol background media are shown in Fig. 5.3. Same model configuration for both cases i.e. 80% glycerol and 90% glycerol yields different results of the transmitted gain due to the differences in their respective dielectric material properties and hence different antenna characteristics. Form Fig. 5.1 we understand that 90% glycerol is less lossy as compared to 80% glycerol and therefore we observe higher transmitted signals in the case of former. We also observe better parabolic trends in the case of 90% glycerol for the same geometry confirming that the transmitted signals are stronger and are not affected by the deteriorating factors unlike 80% glycerol case where we observe some erratic signal behaviour at 2.5 and 3 GHz for receivers 7 to 11 as shown in 5.3 (a). We also observe an overall transmission increase in 90% glycerol case as compared to 80% glycerol background medium. We observe 40 dB increase in the transmitted gain when we compare the worst case scenario at 3 GHz at receiver 9 of 90% glycerol with that of 80% glycerol. Transmitted gain drops as the frequency goes higher confirming that the signal attenuates more at higher frequencies and the loss factor of the dielectric also increases at these frequencies, both of the aforementioned factors result in weaker transmitted gain in 2.5-3 GHz frequency range.

Transmitted gain plots when the printed monopole antenna array is immersed in 90% corn syrup and Triton x-100 are shown in Fig. 5.4 where Fig. 5.4 (a) represents the transmission

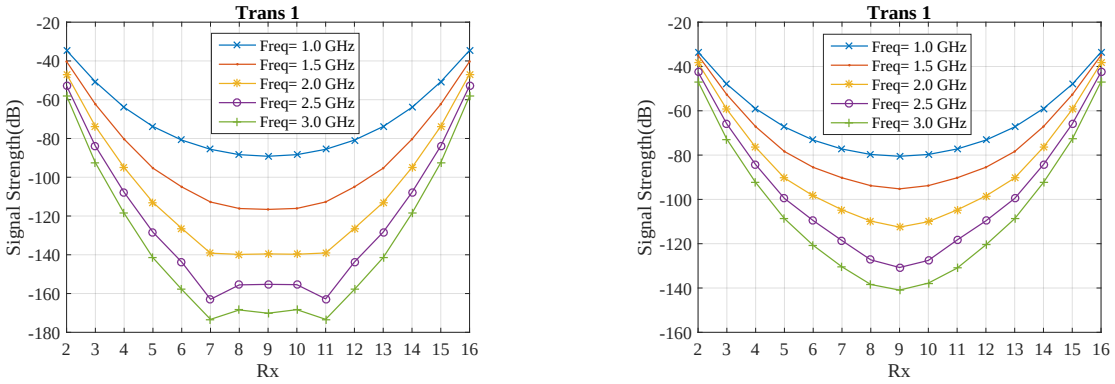

(a) (b)

Fig. 5.3 Forward transmitted gain at 1, 1.5, 2, 2.5 and 3 GHz as a function of receiver location in homogeneous background of (a) 80% glycerol (b) 90% glycerol.

levels from array immersed in 90% corn syrup and Fig. 5.4 (b) represents the corresponding case for the array immersed in Triton x-100. Transmission levels in both cases shown in Fig. 5.4 are higher than both glycerol cases shown in 5.3 due to lower conductivity of 90% corn syrup and Triton x-100 as compared to 90% and 80% glycerol solutions. Transmitted gain plots for 90% corn syrup as background medium show good parabolic trends for all frequency samples considered, however in case of Triton x-100 as background medium we observe some interesting phenomena. Plots of transmitted gain for the array immersed in Triton x-100 do not exhibit full parabolic trends, except for 2 and 2.5 GHz where the response is truly parabolic. We also observe that transmitted gain for 1 GHz frequency sample are weaker than the corresponding signals at 1.5, 2 and 2.5 GHz, this is due to the fact that antenna does not operate at lower frequencies and hence we receive weaker signals at 1 GHz unlike the other three cases (90% corn, 90% glycerol and 80% glycerol) where lowest frequency yields the highest transmitted gain for all receivers. We also observe that transmitted gain at 1.5 GHz for receivers 7 to 11 exhibits an increasing trend as we move towards the more distant receivers and reaches the highest value for antenna 9 when compared with receivers 5 to 13. The reason for this behaviour is the fact that there is a greater impact of interference and surface waves as well as the reflection from the tank floor and the radiation characteristics of the antenna. The minima of transmitted gain does not drop below -65 dB for Triton x-100 and -120 dB for 90% corn syrup, signifying the low conductivity of both the materials as compared to glycerol samples.

From Figures 5.3 and 5.4 we conclude that the highest transmission without too much effect of surface waves and other mitigating factors such as interference and reflections is

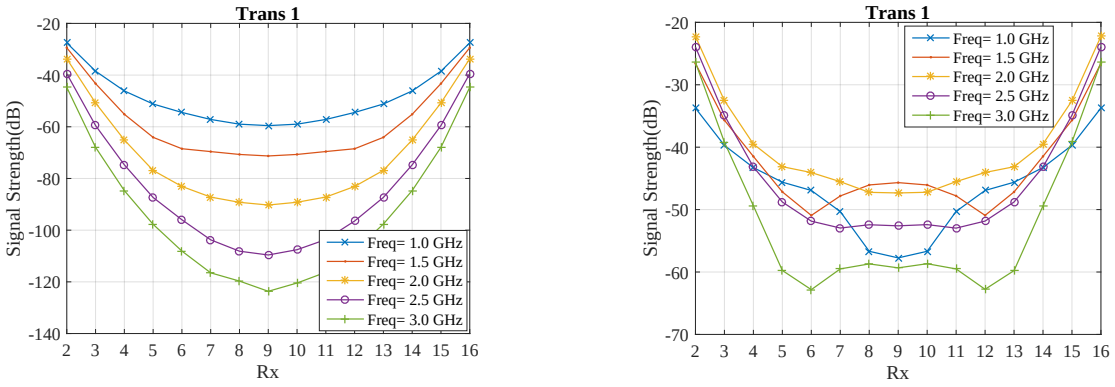

Fig. 5.4 Forward transmitted gain at 1, 1.5, 2, 2.5 and 3 GHz as a function of receiver # in homogeneous background medium comprised of (a) 90% corn syrup (b) Triton x-100.

achieved when array of printed monopole antennas is immersed in 90% corn syrup. 90% corn syrup has a higher dielectric permittivity as compared to 90% glycerol and Triton for the full range of 1-3 GHz and lower conductivity than 90% glycerol and 80% glycerol in the same range of frequency. We also observe that when transmitted gain is low, the impact of surface waves and multipath signal propagation becomes more profound as can be seen in 80% glycerol case where at high frequencies i.e. at 2.5 and 3 GHz we observe higher transmission at receivers 8 to 10 as compared to receiver 7 which lies in closer proximity with the transmitter as compared with receivers 8 to 10. To further investigate the relationship between signal strength and the impact of unwanted signal propagation phenomena we bring the antennas closer while keeping all the other geometry parameters of setup same as before.

We reduce diameter of array from 150 mm to 100 mm to investigate the impact of reduced distance on signal transmission. We consider two cases, 80% glycerol and Triton x-100 for this comparison. Transmitted gain as function of receiver # for 80% glycerol immersion case is shown in Fig. 5.5 (a) when the array diameter is reduced. Impact of the reduced array diameter is imminently seen on received strength levels of the signals at receivers. Minima of the transmitted gain in the larger array diameter (150 mm) case was seen to be approximately -180 dB, whereas after 50 mm reduction of the array diameter not only the transmitted gain is increased by 40 dB for the worst case scenario but also the erratic signal behaviour at 2.5 GHz and 3 GHz observed earlier in 150 mm diameter array case is also changed and more smooth parabolic curves are seen at the reduced diameter. Significant changes have also been observed in Triton x-100 case, however transmitted gain in Triton x-100 is only increased by approximately 5 dB while the parabolic trend of the plots have been preserved at 2 GHz

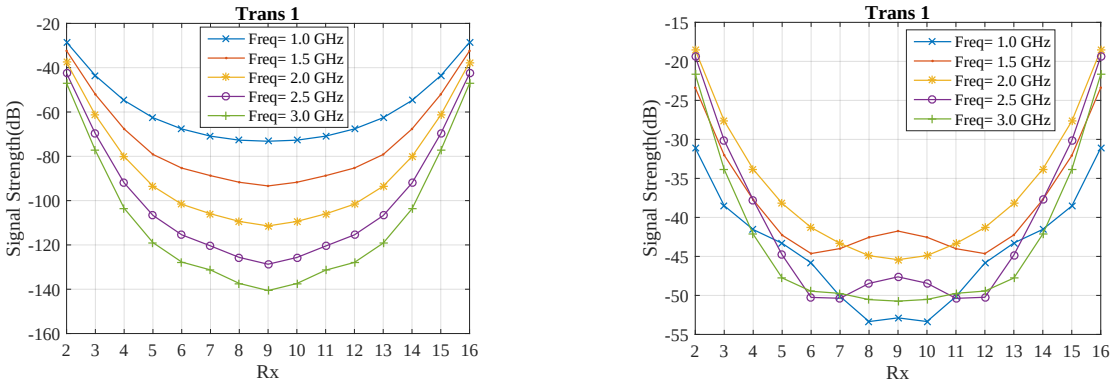

(a) (b)

Fig. 5.5 Forward transmitted gain at 1, 1.5, 2, 2.5 and 3 GHz as a function of receiver # in homogeneous background medium comprised of (a) 80% glycerol (b) Triton x-100 for an array diameter of 100 mm.

while the trend at 3 GHz is improved and has become more parabolic than in the previous case of larger array diameter. However the trend previously seen at 2.5 GHz has deteriorated after reducing the array diameter which is attributed to the reflections and interference effects being more pronounced at closer distance, prompting to the need of using lossy liquid as coupling medium to curb this phenomenon.

From our above mentioned study of the impact of different matching media on signal propagation we summarise the key point as below:

- Matching media is vital in coupling EM energy into the phantom by matching the impedance between phantom and the background
- Matching media helps in acquiring wideband operation of resonant antennas such as monopoles
- High loss matching media are required to curb the factors such as cross coupling, interference, multipath signal and surface wave propagation that degrade transmitted signals
- High loss media result in low transmitted gain levels that might not be detected by the receivers hence a trade off has to established between the transmitted forward gain and mitigation of undesired degarding factors

5.4 Effect of Low Loss Background Media on Signal Propagation

5.4.1 Analysis of Multiband Antenna Array

We analyse signal propagation in an array immersed in safflower oil constructed of multiband antenna proposed in chapter 2. The schematic of eight element multiband antenna array modelled in CST MWS is shown in Fig. 5.6 (a). The antenna was optimized in safflower oil, therefore to conduct the array study we've considered the same background medium. To model safflower oil, we have used the first order Debye model, the debye parameters are: ε_∞ = 2.24, ε_s = 2.97, σ_s= 0 and τ = 5 ps [47]. The material properties are then extracted from CST MWS for real and imaginary permittivity being used in the simulations and then plotted in terms of permittivity and conductivity in Fig. 5.7.

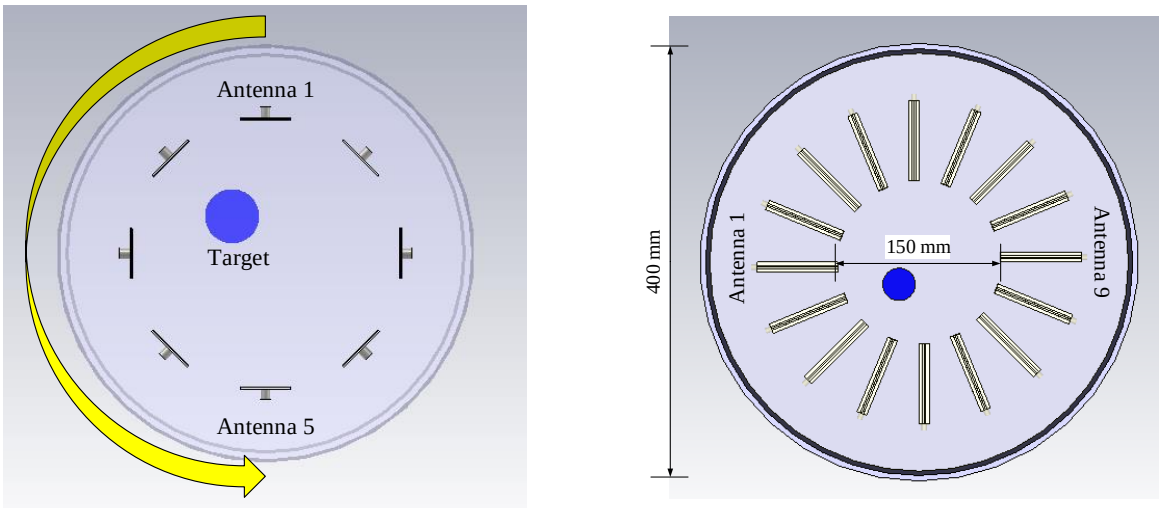

(a) (b)

Fig. 5.6 Arrays modelled in CST microwave studio (a) Eight element multiband antenna array immersed in low loss safflower oil, (b) Sixteen element BAVA array immersed in safflower oil.

Return loss of all antennas in the constructed array immersed in homogeneous safflower oil is plotted in Fig. 5.8 (a), where it can be seen that the return loss stays constant for each antenna element of the array, indicating that there is negligible dielectric loading effect due to the inclusion of other antenna elements in the domain. Multi-band antennas exhibit a tri-band response when immersed in the bio-compatible safflower oil. Resonant frequencies

of these antennas are 1.3, 2.2 and 2.8 GHz. Transmitted gain for each of the receivers at resonant frequencies is plotted in Fig. 5.8 (b).

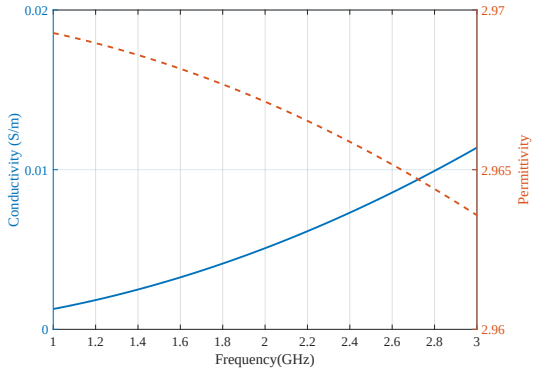

Fig. 5.7 Safflower oil material properties. Debye parameters are supplied to CST MWS material properties and the real and imaginary values have been extracted from CST material fit. Conductivity is calculated from the imaginary permittivity extracted from CST curve fit data.

Transmitted gain has significantly been improved as compared with the previous cases where we used high loss immersion media as background. For example, transmitted gain as high as -15 dB have been recorded at 1.3 GHz. As expected transmitted gain drops for higher frequencies such as at 2.8 GHz, where antenna elements adjacent to the transmitters receive -35 dB. Moreover, it has been noticed that transmitted gain plots do not exhibit the parabolic curves when plotted as function of receivers at specific frequencies. This is due to the radiation characteristics of the transmitters and crosscoupling between the elements. Multi-path signals and surface wave propagation also add to the non parabolic characteristic of the transmitted gain plots in Fig.5.8 (b).

We proceed with the further study of immersed multiband antenna array operating in safflower oil by introducing a high dielectric contrast target (water) inside the domain. As we expect different levels of transmission for varying transmitters, therefore the transmitted gain plots for each of the transmitting antenna case have been presented in Fig. 5.9. The resulting plots show no symmetry for different transmitters in terms of transmitted gain. To gain further insight into the effect of introducing the target we plot the difference in the transmitted gain by subtracting the signal value obtained after introducing the target from the signal strength obtained in the homogeneous background. We observe the variation of upto ± 10 dB in the magnitude differences plots shown in Fig. 5.9. However, the trends of differences plots for the resonant frequencies of operation show very little correlation. Antenna radiation behaviour at these frequencies is responsible for these varying trends in

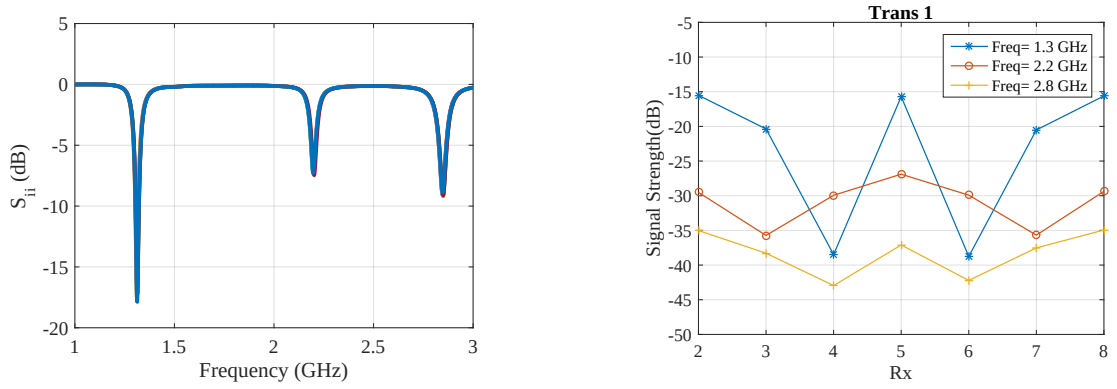

(a) (b)

Fig. 5.8 (a) Simulated reflection coefficient S_{11} of eight multiband antenna array immersed in safflower oil, (b) Forward transmitted gain as function of receiver # when antenna 1 transmits. Forward transmitted gain plots are only shown for the resonant frequencies of the antenna.

transmitted gain plots. Nevertheless, a significant change in the transmitted gain has been observed after instruction of the high dielectric target.

5.4.2 Analysis of Balanced Antipodal Vivaldi Antenna (BAVA) Array

Balanced antipodal vivaldi antenna (BAVA) has been presented in Chapter 2, where we have designed two derivatives of the BAVA proposed in [39]. However due to the larger dimensions of [112] and low efficiency of [113] due to the introduction of lumped elements, we will not proceed with the array study of those two designs due to the potential implementation constraints. We conduct our array study of BAVA with the design optimized in [39]. We construct and array of 16 BAVA elements in a cylindrical geometry as shown in Fig. 5.6 (b). The geometry of this setup is the same as before except for the size of tank holding the background material due to the dimensions of the antenna (70 mm length). The antennas are placed in a circular ring of 150 mm diameter, at 22.5 degree from the adjacent elements measured from the centre of the ring in anticlockwise direction. Safflower oil has been used as the background material in this study. Fig. 5.10 (a) and (b) depicts the reflection coefficient of all of the antenna elements immersed in safflower oil without and with target respectively. It has been observed that the return loss S_{ii} is not identical for both cases. This is due to the loading effect of the antennas as well as of the target. Forward transmitted gain has been plotted as function of receivers for discrete frequency samples as before, Fig. 5.11 shows forward transmitted gain at 1, 1.5, 2, 2.5 and 3 GHz for antennas 2 to 16 when antenna 1 transmits. Transmission gain as high as above -15 dB have been observed for the adjacent

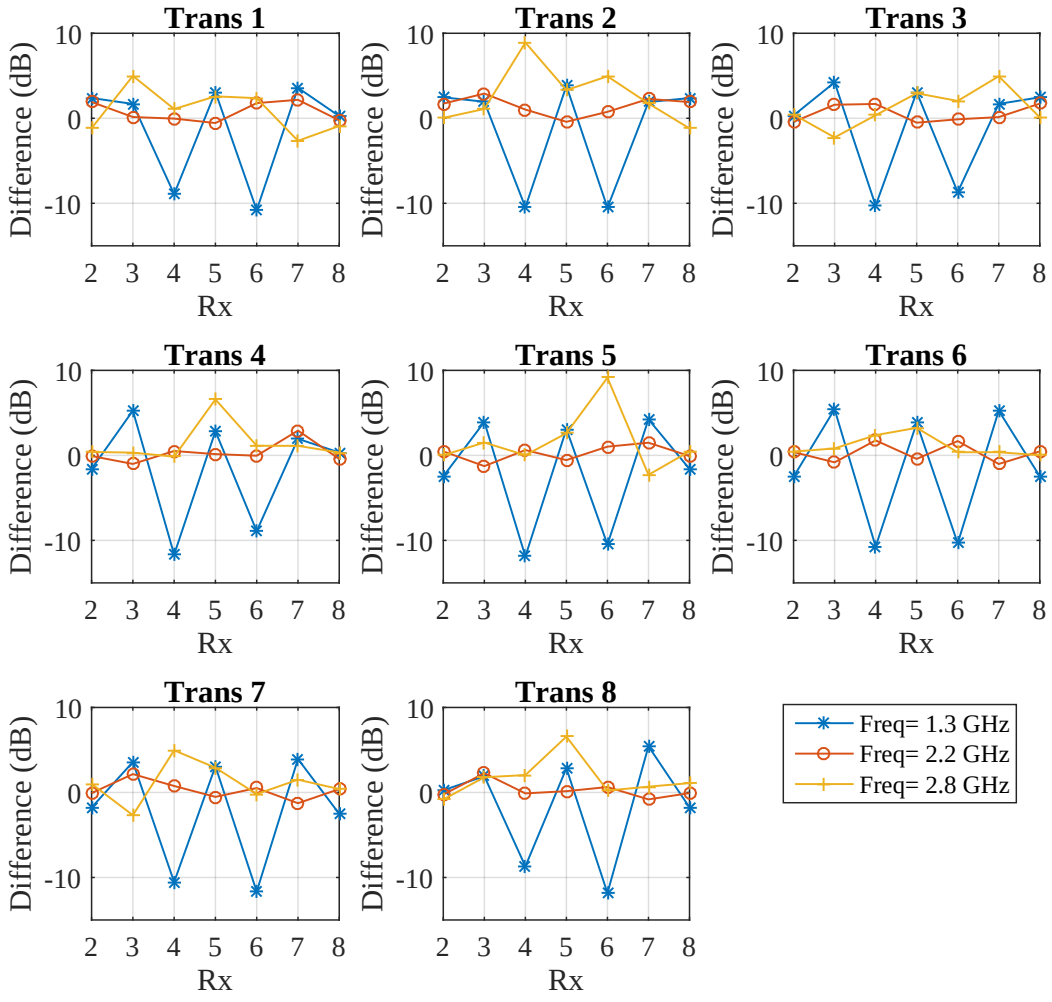

Fig. 5.9 Differences (No target (dB) minus with target (dB) in forward transmitted gain of eight element multiband antenna array immersed in safflower oil.

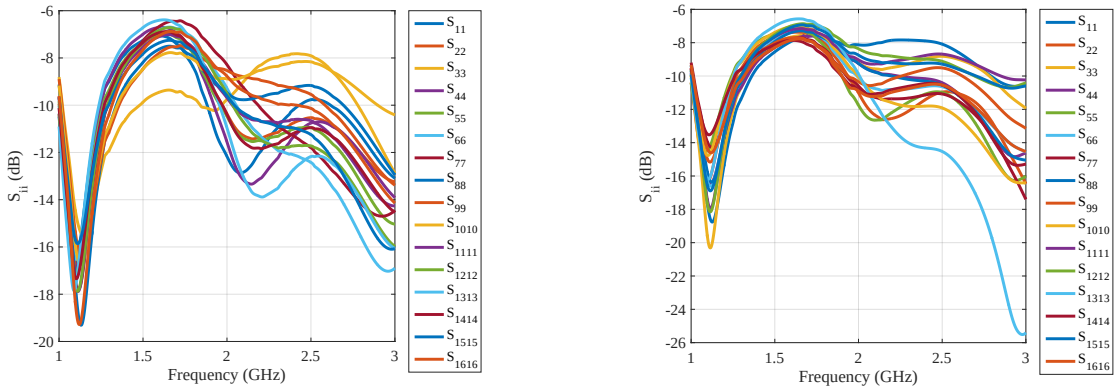

(a) (b)

Fig. 5.10 Reflection parameters of 16 element BAVA array immersed in safflower oil (a) without target (b) with target.

receivers and at worst above -45 dB for the most distant receiver at t1 GHz and 3 GHz, due to the array being immersed in low loss immersion medium. The transmitted gain is parabolic for all cases considered except at 1 GHz and 1.5 GHz. This is attributed to the radiation characteristics of the antenna at the mentioned frequencies.

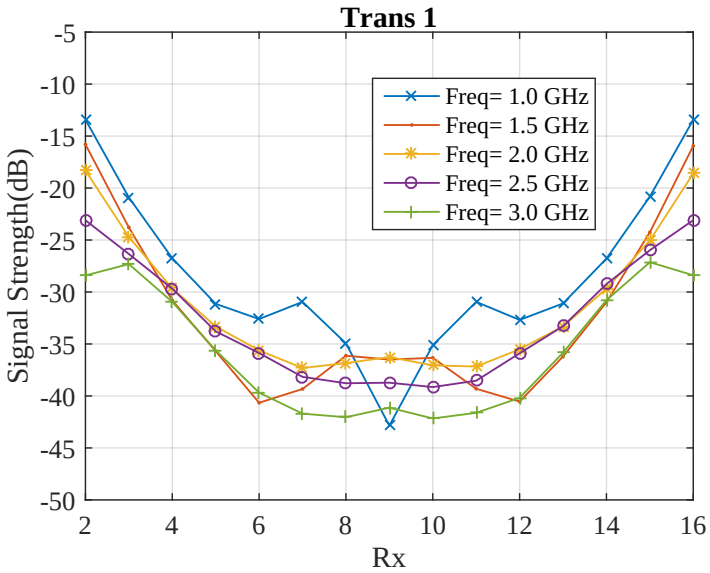

Fig. 5.11 Transmitted gain at BAVA array elements operating in homogeneous background (no target case) of safflower oil as function of receiver locations when antenna 1 is excited for full range of frequencies 1-3 GHz at a step of 0.5 GHz.

Transmitted gain trends alter due to the inclusion of target made of a different dielectric material. Differences of the signals without the target and with the inclusion of target are presented in Fig. 5.12 for receiver 1 to 8. The effect of high dielectric target has a significant impact on the transmitted gain where in some cases the difference between no target case and with target case reaches the order of 10 dB. The plots of differences at various frequencies do not exhibit good correlation. The return loss plots also differ within the no target and with target scenarios among different constituting transmitters, therefore we conclude that the low loss immersion medium is not suitable for imaging applications.

5.5 Effect of Different Target Media on Scattering

We have seen the impact of different homogeneous background media on signal propagation in previous section, where we concluded that high loss liquids as background media help suppress the unwanted propagation phenomena such as surface waves and multipath signals. Reduction of unwanted phenomena come at a price of low signal levels at the receivers, for example, when array is immersed in 80% glycerine our signal levels drop to -180 dB at 3 GHz for receiver situated at 180° with respect to the transmitter, however for the same receiver and geometry we observed -65 dB signal strength in Triton x-100 as a background medium case. In Triton x-100 case we also observed the erratic behaviours in transmitted gain plots which we relate to undesired interaction between signals inside the imaging domain. We reduced diameter of the antenna array and found out that reduction of array diameter resulted in higher signal transmission for high loss media whereas low loss immersion medium did not show significant change. Hence, we conclude that high loss immersion media can potentially give us better results in terms of useful information of the imaging domain as undesired surface waves and multipath signals are significantly suppressed due to the higher conductivity of the medium.

Thus far, in this chapter we have only seen impact of background matching media on signal propagation in the homogeneous imaging domain. Microwave Tomography method reconstructs the dielectric profile of interior of the imaging domain by running an inversion algorithm. Scattered fields change when there is a discontinuity in the path of electromagnetic signals propagating through the imaging domain. We have seen earlier in the homogeneous background case that transmitted gain at the receivers are unaltered in terms of signal strength and their trends regardless of which transmitter of the array sends in the pulses. We introduce a discontinuity in the imaging domain at a known location and refer to it as ‘target’ in our discussion. A Target is an object with different dielectric properties as

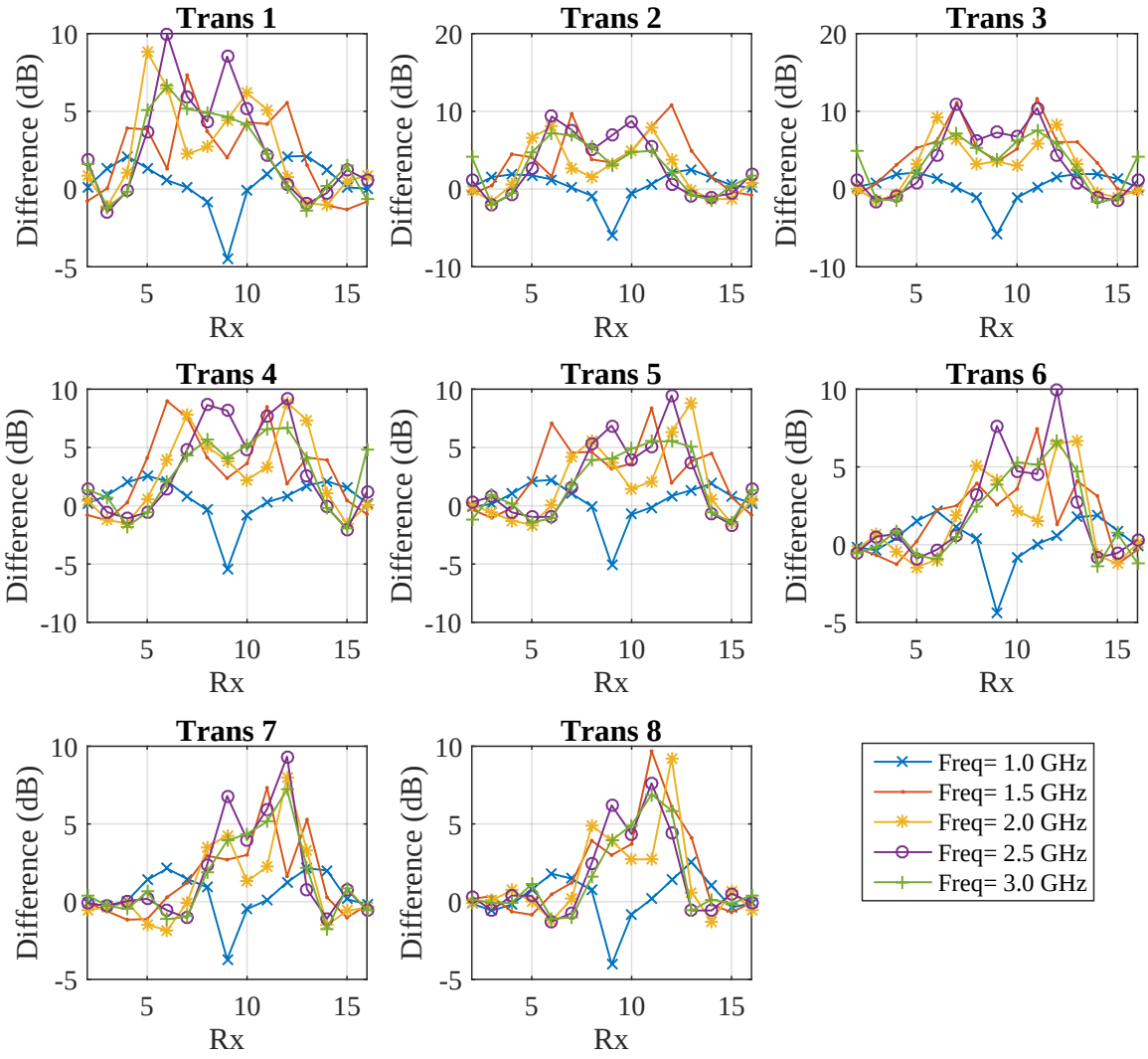

Fig. 5.12 Differences (in dB) in received strength as function of receiver # when an array of sixteen BAVA antennas is immersed in safflower oil and target is introduced. Figure shows differences plots for antenna transmitters 1 to 8 at 1, 1.5, 2, 2.5 and 3 GHz.

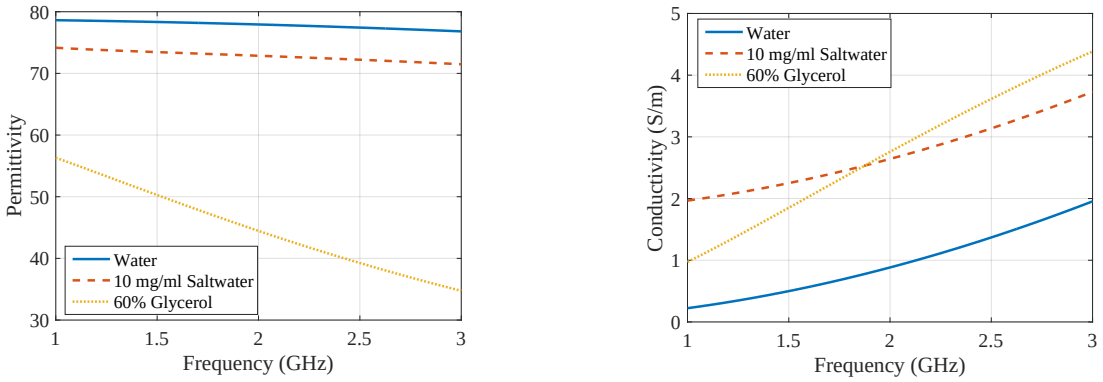

(a) (b)

Fig. 5.13 Dielectric properties of the 'Target' materials used in this study (a) Relative permittivity (b) Conductivity.

compared to the coupling liquid being used. Differences in electrical properties between target and background medium makes the EM wave propagating through imaging domain scatter upon interaction with the target object. Scattered signals are then received at receivers with different magnitudes and phases as compared to the homogeneous background case, which in turn is used to reconstruct the images. Dielectric properties of different target media we consider in our study are shown in Fig. 5.13.

We insert a metallic cylindrical object 'target' of 15 mm radius and same length as the background medium at (20, 20) on XY plane inside the coupling medium of 80% glycerol (Fig. 4.1). We perform similar analysis on all four materials discussed in previous section after including the high dielectric scatterer inside the imaging domain.

We plot differences in magnitudes of signals between the two cases (with and without target) by subtracting magnitudes (in dB) of the transmitted gain after including PEC target from magnitudes recorded earlier for the homogeneous background case to quantify our findings about the changing behaviour of transmitted gain due to inclusion of target inside the imaging domain. We observe a significant change in transmitted gain magnitudes over the entire range of frequencies. We show plots of difference in magnitudes (dB) as a function of receivers at 5 frequency samples in between 1 to 3 GHz range at a step of 0.5 GHz. Differences in transmitted gain are shown in Fig. 5.14 when we subtract the signal strength received at different receivers of the antenna array in the presence of metallic scatterer in dB from without scatterer case. We observe significant differences in the transmitted gain after including the metallic scatterer. Differences observed in 80% glycerol reach upto 20 dB while for 90% corn syrup and 90% glycerol solutions these differences values reach upto

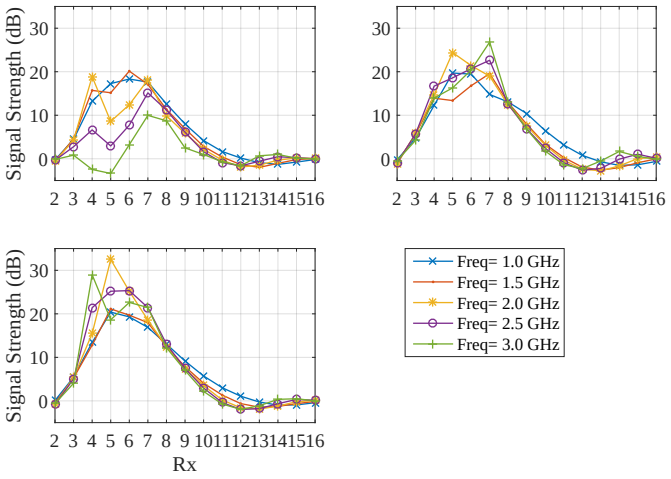

Fig. 5.14 Differences (in dB) in transmitted gain when a PEC scatterer is introduced inside an array immersed in 80% glycerol (top left), 90% corn syrup (top right) and 90% glycerol (bottom left) while antenna 1 transmits. The diameter of array is 100 mm. Differences are calculated by subtracting dB values of transmitted gain with target from homogeneous background case of the respective immersion material.

30 dB mark as shown in Fig. 5.14. We observe approximately upto 10 dB higher level of differences when antenna array operates in lower loss dielectric media such as 90% corn syrup and 90% glycerol as compared with 80% glycerol in this example.

We also observe that difference in magnitude for nearby antennas with respect to the transmitter is not too high, for example in case of transmitting element 1 of the array, differences of magnitudes recorded for the adjacent and close by elements in the clockwise direction where receiving antenna 11, 12, 13, 14, 15 and 16 reside, remain very close to zero. However, differences in magnitudes of transmitted gain starts to impact receivers as close as receiver 3 in the anticlockwise direction with respect to the transmitter (antenna 1). This is due to the relative position of the receivers with respect to transmitting antenna and the target.

We study the impact of different scattering material on transmitted gain at the receivers of arrays immersed in 80% glycerol and 90% corn syrup. Plots of transmitted gain as function of receiver locations for both media are shown in Figures 5.15 and 5.16. We observe that the transmitted gain plots for each of the target media for same configuration of array setup are different. We show the transmitted gain plots for antenna transmitter 1 only along with the no target case.

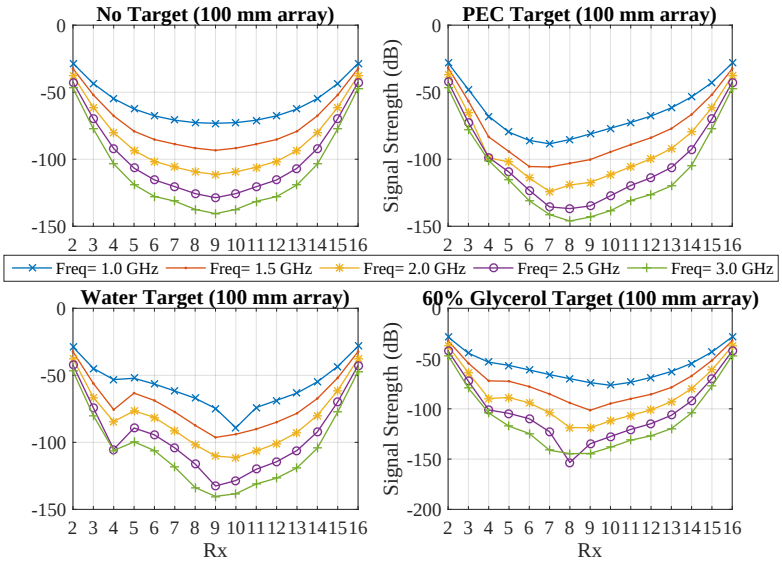

Fig. 5.15 Transmitted gain of the printed monopole antenna array immersed in 80% glycerol, no target (top left), PEC target (top right), water target (bottom left) and 60% glycerol (bottom right). The diameter of array is 100 mm.

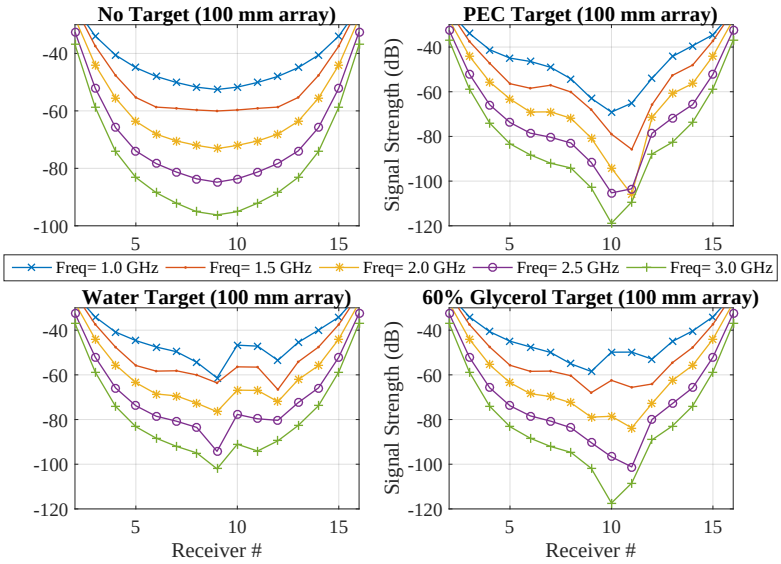

Fig. 5.16 Effect of different 'target' media on transmitted gain in 90% corn syrup background. Top left no target case, top right PEC target, bottom left water target and bottom right 60% glycerine water mixture targt. The diameter of array is 100 mm.

5.6 Two Layer Phantom Background Media

In the previous section we considered different dielectric background media and deduced that higher loss of immersion medium is vital to minimize the cross coupling between array elements, however the hardware requirement to collect these low signal levels is completely altered when we use high loss medium as background therefore there is a need of high sensitivity transceivers to collect the information which incurs higher cost to the system. Also, from practical point of view, considering the actual breast anatomy, we can confidently assume that the EM signal will not have to traverse in the lossy background medium across the entire array diameter, hence we introduce another layer in the imaging domain by inserting a small (100 mm) cylinder concentrically aligned inside the larger (200) cylinder filled with the background material used as immersion and then inserting low loss material inside the smaller cylinder that mimics low loss fatty tissues inside breast. Fig. 5.17 (a) depicts the schematic of this new double layer setup modelled in CST microwave studio. Transmitted

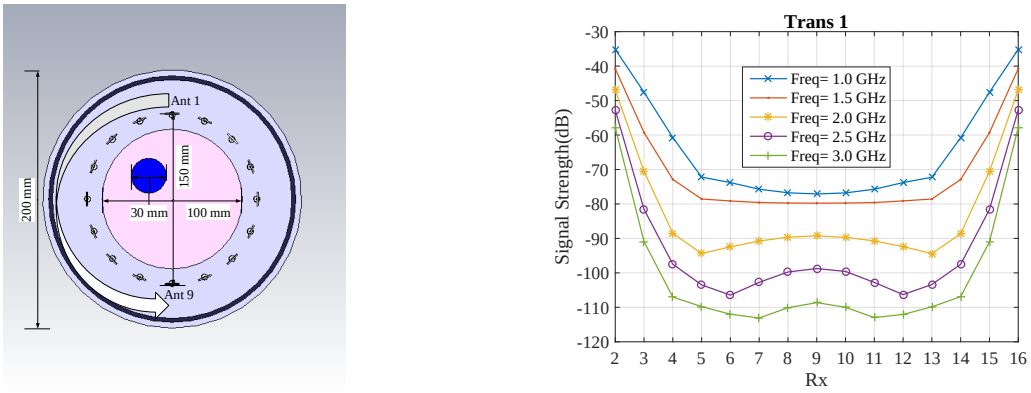

(a) (b)

Fig. 5.17 (a) Array of 16 triangular patch printed monopole antennas modelled in CST MWS with two dielectric media, (b) Transmitted gain as a function of receiver location in homogeneous background of double immersion setup of 80% glycerol and safflower oil.

gain plots for the double layer homogeneous background case are shown in Fig. 5.17 (b) for transmitter 1 only, the simulation data for all transmitters exhibit symmetry therefore we only show the plots for transmitting antenna 1 only. Second layer with low loss medium has a significant impact on transmitted gain for all transmitter receiver combinations at all frequencies. Transmitted gain minima for 150 mm diameter array immersed in 80% glycerol was previously seen at approximately -180 dB at the receiver situated at 180° with respect to transmitter, at 3 GHz, now with the introduction of low loss medium layer for the same geometry minima occurs at approximately -110 dB indicating a big increase (70 dB

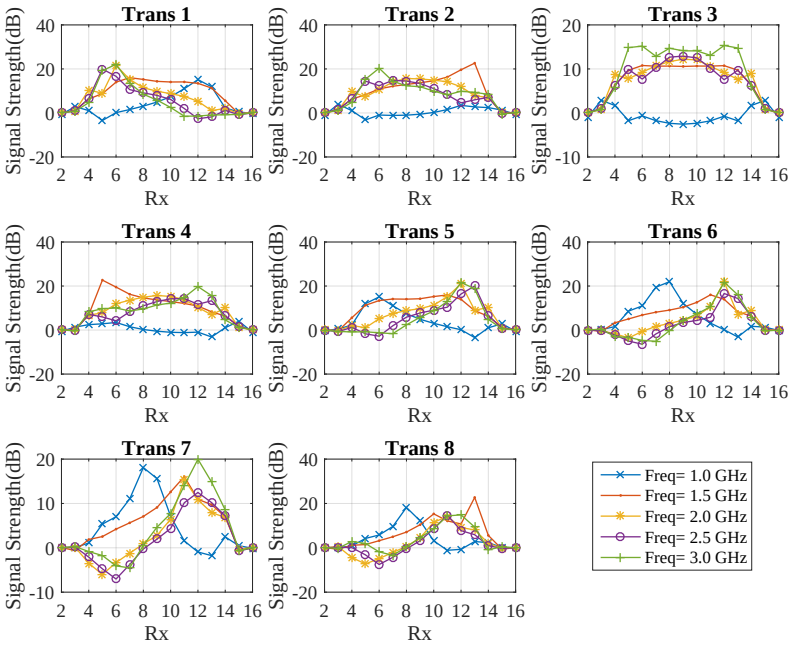

Fig. 5.18 Differences in dB of the transmitted gain for 150 mm antenna array immersed in 80% glycerol in two layer phantom configuration with and without target, safflower oil being the low loss layer of 100 mm diameter. Receivers 1 to 8.

approximately) in the transmitted signal level. Moreover, we have observed that the trend of the curves particularly at frequencies beyond 2 GHz are not truly parabolic as before, however there is a very little difference of signal levels (in the range of 5 dB) for antennas 7 to 11, this is due to the antenna radiation characteristic being altered due to the change in effective permittivity of the background medium as well as the impact of surface waves and multipath signal propagation being more pronounced in the presence of low loss immersion.

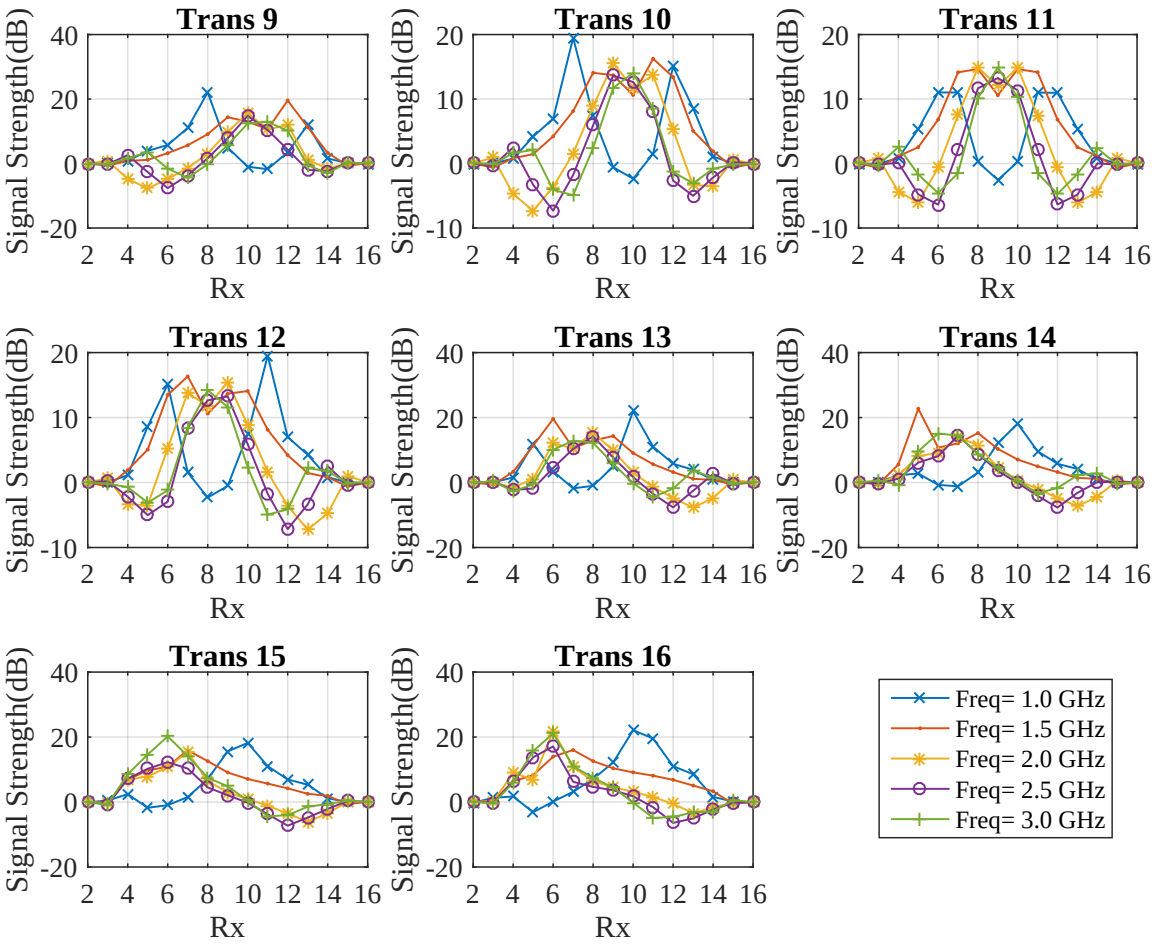

Fig. 5.19 Differences in dB of the transmitted gain for 150 mm antenna array immersed in 80% glycerol in two layer phantom configuration with and without target, safflower oil being the low loss layer of 100 mm diameter. Receivers 9 to 16.

Subsequently we introduce a cylindrical metallic (PEC) target inside safflower oil layer (inner tank of 100 mm). Furthermore to observe the differences in transmitted gain in the presence of a high dielectric scatterer and without it, we plot differences of the magnitudes

in dB units, by subtracting the data with target from without target for the corresponding transceivers at five discrete frequency. Difference values of upto 20 dB for the two cases, with and without target have been recorded. Variation in transmitted gain in the presence of high dielectric material as shown in Figures 5.18 and 5.19 is a clear indication of the impact of target dielectric properties on the electromagnetic wave propagation inside the domain.

5.7 Conclusion

We analyse performance of the array of 16 printed monopoles in different background media to optimise dielectric background medium for best transmission as well suppressing the unwanted signals for our microwave tomography system in sight. Dielectric media used in this study range from low loss (Triton x-100) to high loss (80% glycerol). We observe weak signals when 80% glycerol is used as background medium, however the behaviour of transmitted gain response when plotted as a function of receiver at discrete frequency samples is found to be symmetric and parabolic, thus indicating good propagation through the imaging domain largely unaffected by interference, noise, surface waves and multipath signals. However low loss background medium (Triton x-100) yields high transmission levels albeit with significant effect of undesired deteriorating phenomena such as multipath signals and surface waves. In order to mitigate effects of coupling and other undesired phenomena and to enhance transmission at the same time, we propose two layer phantom comprised of high and low loss media. We observe 79 dB increase in signal transmission for the same geometry when we use this new two layer phantom as compared to the case when 80% glycerol was used as single background in our 3D simulations. We also show the impact of different scattering materials on signal propagation and observe good level of relative signals for all background and target media.

Chapter 6

Results Using Two MT Experimental Prototypes

6.1 Introduction

MT system requires multiple antennas to be installed around the imaging domain for data acquisition from different angles within the chamber to capture a full 3D view of the domain. Such systems with the ability to incorporate multiple ports are commercially available multi-port multi-channel Vector Network Analysers (VNA). RF electronics manufacturers, however, have also developed their own in-house purpose built RF multi-port transceivers for various applications in 'K' band. One of the challenges being faced in system design of a microwave tomography system is to keep it as cost effective as possible without having to compromise on the quality of transmitted gain. We use a two port VNA for our study and improvise the multi/bi-static data acquisition procedure manually using our simple and low cost mechanical systems.

In this chapter we present our experimental results from the two data acquisition systems we used. First we present our collaborative work funded by COST action under the grant TD1301 Short Term Scientific Mission (STSM), as a joint effort in microwave imaging system development, between King's College London, UK and Politecnico di Torino, Italy. We use the mechanical set-up developed at Politecnico di Torino with our compact printed monopoles presented in Chapter 2 to collect our experimental data. We test MUSIC algorithm being employed at Politecnico di Torino [118] and DBIM TwIST algorithm [119] developed at King's College London for image reconstruction with our acquired simulation and experimental data to validate the system performance.

After examining results from our first experimental studies with the rotary system for data acquisition, we understand implications of the tiny errors on overall performance of the system particularly on inversion algorithm. Effect of inaccuracies incurred due to erroneous experimental data can lead the imaging algorithm to non-convergence. Precise and accurate setup can help achieve correct data with minimum errors from inside of the imaging domain that can then be used for image reconstruction. We modify our mechanical setup with respect to previously used setups; non immersed configuration and rotary mechanism for data acquisition. We attempt to make our system more robust to either mitigate or minimize the inaccuracies observed previously. From our experimental study of data acquisition using rotating chamber, we observe that positioning of antennas and the imaging chamber is of utmost importance. So we make an attempt to make the positioning more precise and robust by building a new low cost system that caters for the needs of precise positioning of constituting elements.

6.2 Experiments with a Bi-static Rotating System

The purpose of this STSM (collaborative work between King's College London and Politecnico di Torino) was to experimentally validate the compact antenna designed at King's College London for MT using the data acquisition system at Politecnico di Torino. The goal of this study was to test the MWI system with the Geps-L2S breast phantom available within the MiMed community, and to validate our antenna design and evaluate its performance experimentally using the experimental set-up. We also modelled the experimental system in commercially available 3D EM solver, CST® and simulated the similar scenarios as our experiments.

Our small printed monopole antenna operates from 1 GHz to beyond 3 GHz, when immersed in 80-20% glycerine-water mixture. We studied performance of this antenna experimentally in two dielectric media; low loss Triton x-100 and lossy 80% glycerine-water using the data acquisition setup at Politecnico di Torino. We inserted tumour target in different locations inside the phantom. Fibro-glandular mimicking material has also been introduced to study performance of system in the presence of a more complex phantom where there is lesser contrast between background material and the target. We inserted tumour mimic both, outside of fibro-glandular as well as inside it. We then processed the collected data with MUSIC algorithm for image reconstruction (as described in [118]). We also apply DBIM-TwIST algorithm to the measured data.

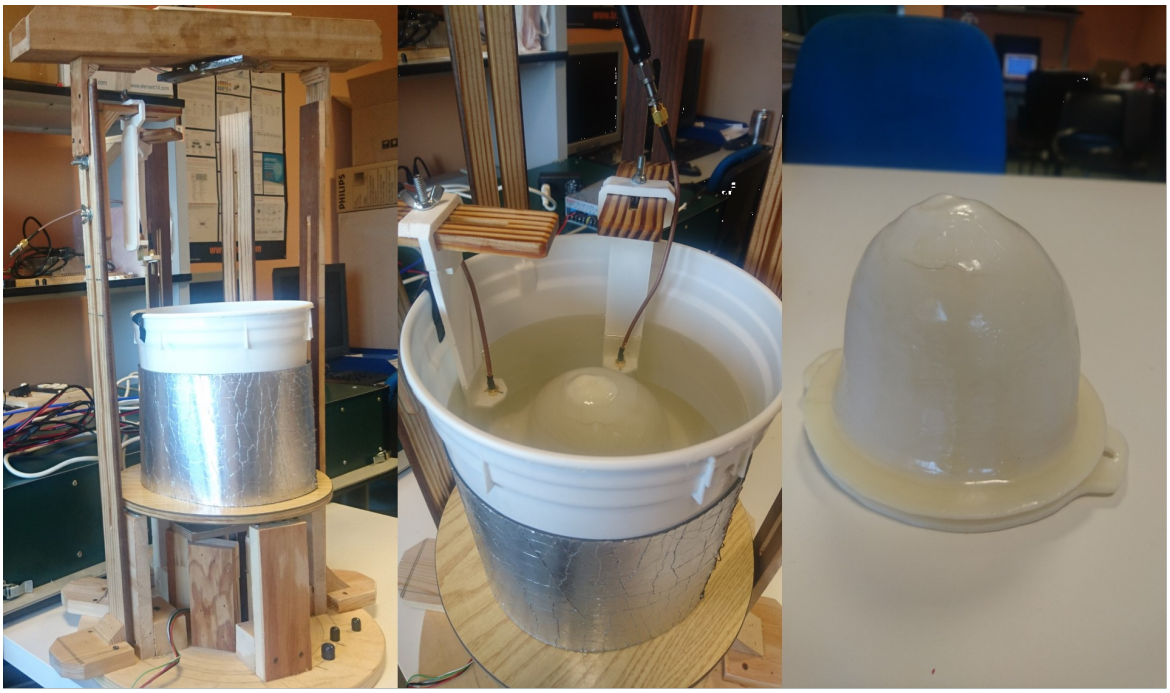

Fig. 6.1 The Microwave Imaging Setup at Politecnico di Torino with perspective view of the phantom being used

Fig. 6.1 shows the rotary microwave imaging set-up at Politecnico di Torino with the phantom being used in the experiments. Fig. 6.2 depicts bottom view of the phantom being used which indicates the tumour locations where a different dielectric medium may be inserted to mimic high dielectric target (tumour). Mechanical fixtures that hold the antenna at a steady position and 3D printed adaptive bracket that allows for the change of angle between the antennas are also shown in Fig. 6.2.

6.2.1 System Description and Data Acquisition Procedure

Fig. 6.1 shows mechanical structure of the rotary imaging setup used in this study. A static and robust circular base holds the entire structure. A programmable motor that creates desirable motion steps is placed above static base of the system. Another circular but movable wooden base is then placed above the motor to hold the cylinder containing immersion liquid to be used as background material. Four vertical wooden columns placed at 45° with respect to each other have been connected with the static base to form a support for antenna holding structures. 3D printed plastic supports that hold antennas are connected with horizontal wooden structures attached with vertical columns. A small 3D printed connecting bracket that attaches with a vertical plastic column is connected with the horizontal wooden slider,

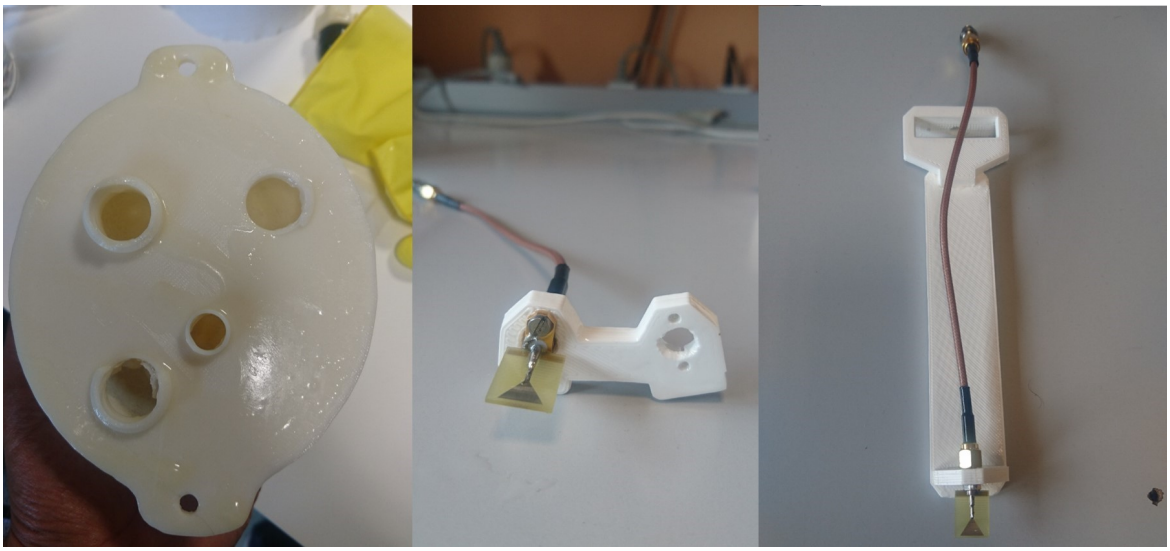

Fig. 6.2 From left to right: bottom view of Geps-L2S Phantom, the bracket to accommodate 22.5° angle between antennas and the vertical support of the antenna with our compact printed monopole mounted.

provides the ability to achieve adaptability of 22.5° or 45° angle between antennas of the bi-static array as shown in Fig. 6.1.

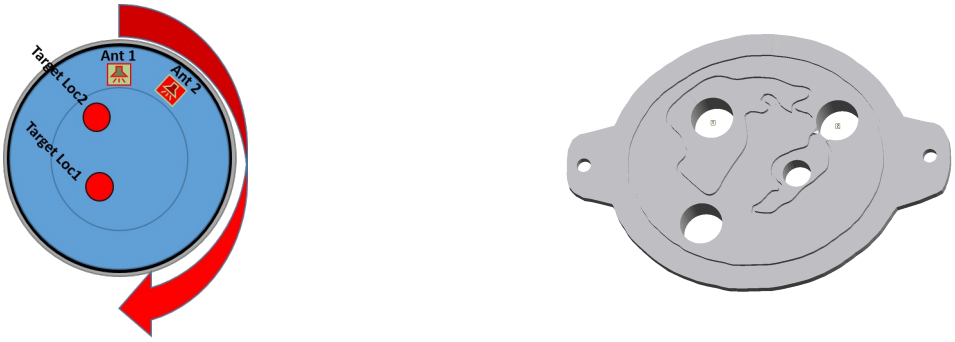

(a) (b)

Fig. 6.3 (a) The schematic of imaging setup with antenna and target locations. (b) base of the phantom showing target locations and fibroglandular position.

Our imaging domain for these experiments is comprised of a plastic cylindrical tank surrounded by an Eccosorb MCS absorber that is shielded with a metallic sheet. Purpose of incorporating an absorber is to minimize the effect of surface waves propagating along periphery of the container as described in our simulation study presented in Chapter 4.

Eccosorb MCS is a thin, flexible, magnetically loaded, silicone rubber material that is electrically non-conductive. This product is particularly suitable for cavity resonance reduction applications in the 800 MHZ to 6 GHz range. When placed within a cavity Eccosorb MCS is very effective at dampening resonances due to its high permittivity and permeability. Surface currents can also be suppressed with Eccosorb MCS. It is also useful in reducing RF coupling of antennas and microwave components. Eccosorb MCS is impervious to moisture which is another highly required attribute of the system.

There is a strong chance of occurrence of the aforementioned surface wave phenomenon due to the fact that distance between antenna and walls of the container is not large (approximately 25 mm). Our antenna has an omnidirectional radiation pattern, particularly upto 2 GHz (when immersed in 80% glycerol), therefore, there is significant radiation in the backward direction that results in electromagnetic energy to escape the imaging chamber and waves to propagate along periphery of the tank. As a result, transmitted gain can become distorted and hence would not manifest true "through" signal from the imaging domain.

We use two different materials to be used as background immersion media to test performance of the rotary experimental system at hand. Firstly, we consider low loss Triton x-100. Subsequently we study the performance of our system using 80% Glycerine-water mixture as a background material. 80% glycerol exhibits higher dielectric loss that has pros and cons attributed to it. The biggest benefit of using 80% glycerine-water mixture is the mitigation of crosscoupling between the antennas and surface wave propagation, however it comes at the cost of much attenuated transmitted gain. Sensitivity of the receivers has to be enhanced in order to detect weaker signals which in turn renders a higher cost to the over-all system.

In order to capture multiple views of the imaging domain with a two port network, we implement the idea of bi-static system. In this approach we install two antennas to create an array. We keep one antenna stationary and manually move location of the second antenna at a predefined step angle (45° in our setup). Once both the antennas have been placed in the desired locations then imaging domain i.e. cylinder with the immersion liquid and phantom is rotated through entire 360° on its axis. Complete rotation of the imaging chamber on it central axis enables us to capture multiple views of the imaging domain.

As the wooden columns, as stated in the mechanical set-up description are placed at 45° with respect to each other therefore we use an adaptive bracket to reduce the angle between adjacent antennas to 22.5°. Previously used 45° separation between antennas yields a sparse matrix which might not be desired for some imaging algorithms. Hence, we adapt the fixtures to use smaller angles and consequently increase motor step to the same angle as the antennas

i.e. 22.5°. The reduced angle between antennas and larger motor step yields the desired full S-Matrix.

Firstly, measurements are taken without phantom and then we introduce phantom in the domain. Subsequently we insert a target inside the phantom. We move antenna 2, as shown in the schematic of Fig. 6.3 (a), from its initial position i.e. 22.5° to subsequent positions at a step of 22.5°. For each subsequent location we take measurements without having to rotate the imaging domain, because it is not necessary to sweep through all angles when there is no discontinuity involved inside the imaging domain. On the other hand, however, when we introduce phantom and target a complete 360° sweep has to be carried out for each position of antenna# 2 (i.e. at 22.4, 45, 67.5, 90, 112.5, 135, 167.5 and 180°). As a whole, we carry out measurements for bi-static antenna system from 22.5° to 180° with a step of 22.5°, consequently we obtain 8 sets of 16 readings each to capture 16 different views for each pair of antennas. We perform all measurements using two port PNA series VNA.

6.2.2 Results and Discussion

We used two coupling media in this study, 80% glycerol and Triton x-100. We could not achieve detectable signals when we immerse antennas in 80% glycerol at 1.5 GHz and above for the locations far from transmitter such as location 7, 8, 9, 10, 11 and 12. Therefore we continue our study with Triton x-100 as our background medium. Results obtained from

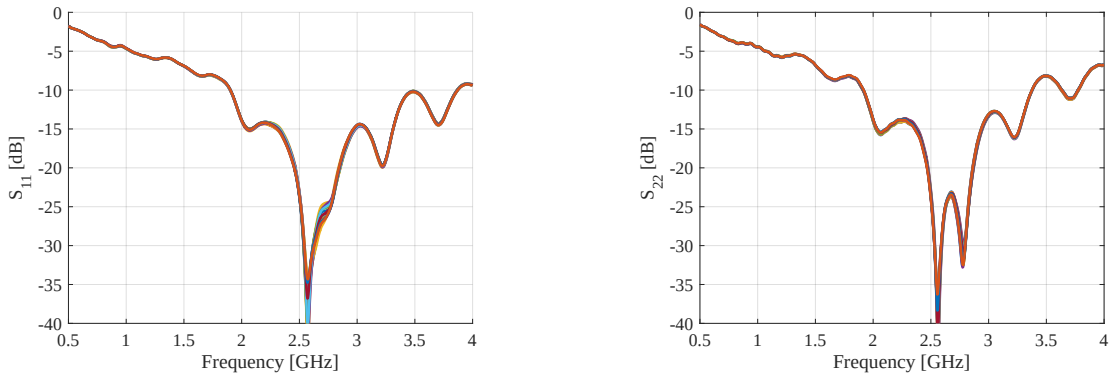

(a) (b)

Fig. 6.4 Return loss for the fabricated antenna prototypes connected to ports (a) 1, (S_{11}) and (b) 2, (S_{22}) of the VNA used for data acquisition. The antennas are immersed in Triton x-100.

rigorous experiments conducted as described in preceding sections are presented here. We begin with presenting the results obtained with four sets of data with a finer motor step of 15 degrees. We use Triton x-100 as background medium, as mentioned earlier, while antennas

are kept at 45°, 90°, 135° and 180° apart. Return loss of the antennas 1 and 2 for the complete sweep in the homogeneous background of Triton x-100 is shown in Fig. 6.4. This approach renders a sparse matrix, Fig. 6.5 (a), which we convert to full matrix, Fig. 6.5 (b) by adapting the hardware system with 22.5° bracket. Thus the new sets of data are acquired by placing antenna2 at steps of 22.5° until a 180° sweep is traversed from starting position of 22.5°.

Return loss of both antennas, when immersed in Triton x-100 shows a wide band characteristic from approximately 1.9 to 3 GHz, this behaviour has been observed consistently throughout the length of this joint study. The antenna behaviour suggests that these antennas are well suited for imaging application from 1.9 to 3 GHz when immersed in Triton x-100, where we expect good signal transmission. Note that Fig. 6.4 depicts return loss for all sixteen location.

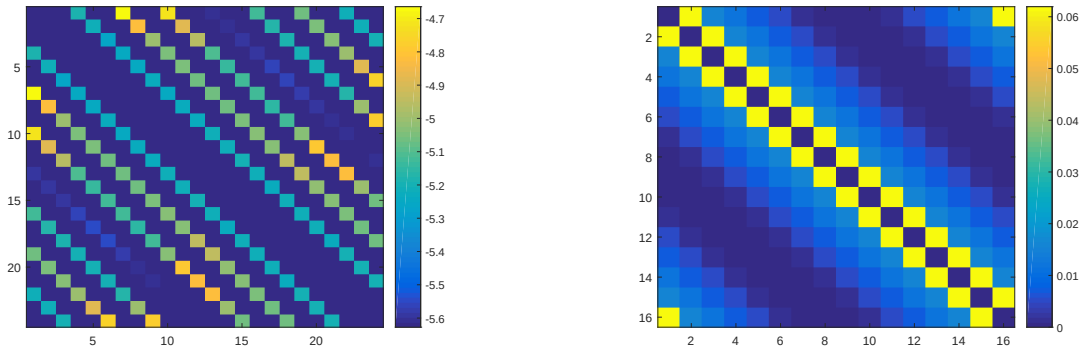

(a) (b)

Fig. 6.5 S-matrices obtained from two different antenna angle steps (a) 45° step yields sparse S-Matrix of 24*24 views (b) 22.5° step yields a full S-Matrix of 16*16 views.

After carefully examining position of antennas with respect to the target location and orientation, we conclude that there is a need of lowering the position of antennas to study the effect of scattering due to high dielectric contrast between the scatterer and matching medium. Fig 6.6 shows target position with respect to antennas on y-axis. Upon making these first adjustments of antenna and target relative positions we persist with this modified setup for our subsequent experiments, throughout the remainder of this study.

Once we finalize antenna positions with respect to target location, we proceed to the complete set of measurements where we implement the entire procedure as described above. We present results of the experiments in following figures. We use Triton x-100 as the background material and pure water as target. The location of water filled target conical tip cylindrical tube is at x=-0.02 cm and y=0.02 cm with respect to the origin, while both

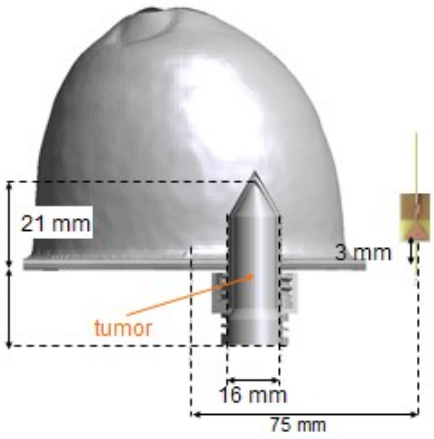

Fig. 6.6 Position of target with respect to the lower end of the antenna suspended inside the chamber.

antennas are placed 2.5 cm inside the dielectric filled plastic container's boundary on the positive x coordinate.

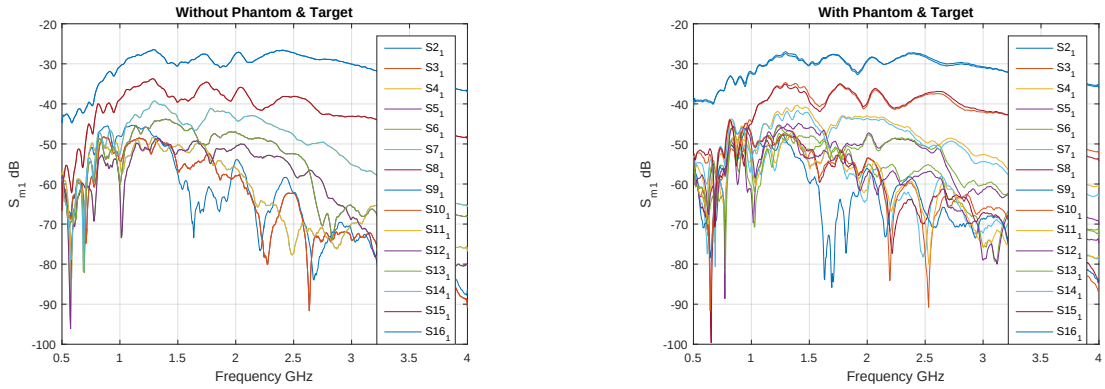

(a) (b)

Fig. 6.7 Transmitted gain at 16 locations inside the imaging domain over the full frequency spectrum under consideration when Antenna 1 transmits (a) in homogeneous background medium only, (b) with water target.

Fig. 6.7 (a) shows the transmitted signal for locations 2 to 16 when antennas are immersed in homogeneous background medium (i.e. no target or phantom). The phantom shell is made up of plastic, therefore inclusion of the phantom shell filled with the same material as the coupling liquid inside the imaging chamber does not alter transmitted gain trends and levels as compared with the homogeneous background only case. Fig. 6.7 (b) represents the transmitted signal over complete frequency band when water as a target has been introduced

in the imaging domain at location 2 highlighted in Fig. 6.3 (a). We observe good level of transmitted signal; above -80 dB over the entire frequency range, which is above the noise floor of the VNA.

We further simplify our findings of signal propagation in Triton x-100 background in the plots presented in Fig. 6.8 (a) and (b). We plot transmitted gain at specific frequency samples (1.5, 2, 2.5 and 3 GHz) as a function of locations, in homogeneous background medium Fig. 6.8 (a) and when water target is introduced, Fig. 6.8 (b). We observe variations in the transmitted gain after introducing a target as compared with the corresponding without target case. However, data received for without target case has not been symmetric and parabolic. We understand from the non-symmetry observed in our homogeneous background data that our experimental set of data suffers from errors, however the variations observed after introducing target point to the fact that there is an impact of high dielectric scatterer as well on signal propagation and as result transmitted gain varies at the receivers.

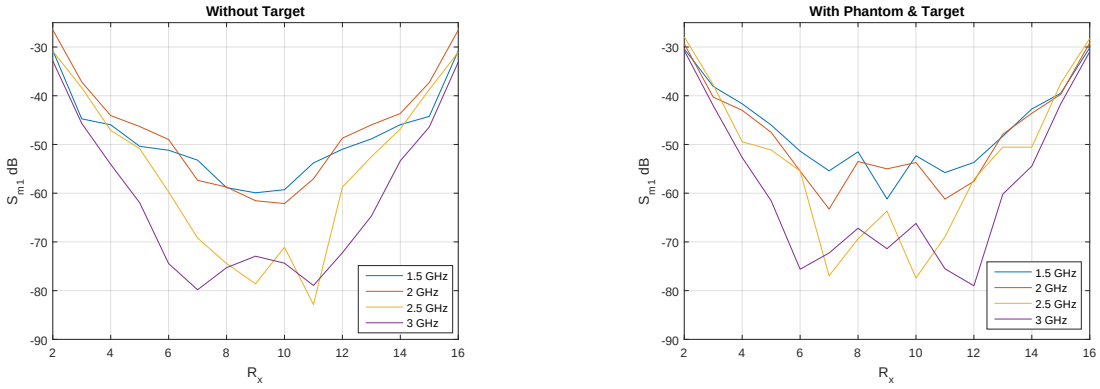

(a) (b)

Fig. 6.8 Transmitted gain as a function of position (a) in the presence of the phantom only, and (b) in the presence of phantom and target

Subsequently, we proceed with two different target materials to mimic tumour and study the impact of different dielectric property targets on signal scattering. Dielectric contrast between the constituting materials of an imaging domain is the key entity in microwave tomography. Rationale for using two different materials for targets stems from the fact that there will be different level of scattering from targets constructed of different materials. Dielectric contrast between tumour and the other inhomogeneities (fibroglandular content) present inside the mostly fatty breast tissue results in different level of scattering and this variability in scattering profile of materials has an important role to play in the imaging

process to distinguish between malignancies and low contrast (healthy) content. Thus, there is a need to fully understand the impact of different dielectric materials on scattering.

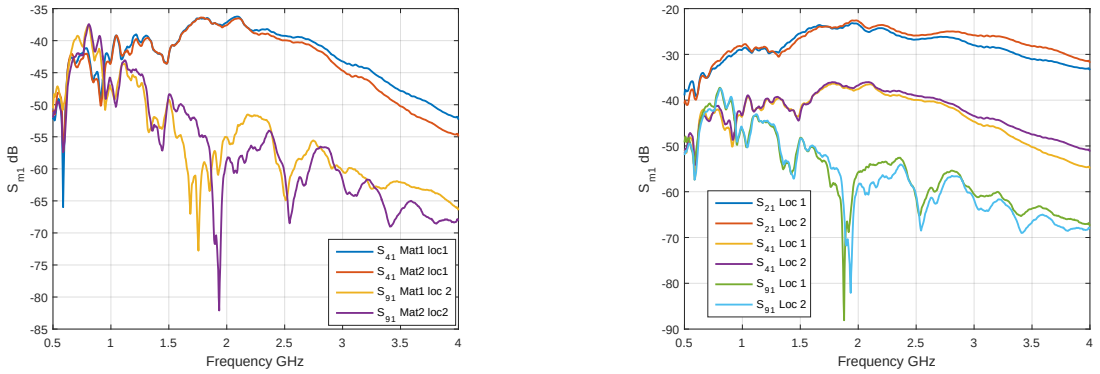

(a) (b)

Fig. 6.9 Transmitted signals for different target (a) materials and (b) locations

Target location also has a significant effect on the EM wave scattering. We study impact of target position on signal scattering by introducing targets at two different locations. We show target locations of our phantom in the schematic of Fig. 6.3. Location one as indicated by target Loc1 in Fig. 6.3 (a) is at x=-1.54 cm and y= -1.94 cm with respect to the origin, location 2 indicated by target Loc2 in the same figure is at x=-3.39 cm and y=-1.68 cm.

We first comment on observations for the case where same locations of target have been chosen for different materials of the same geometrical target. Here we discuss the impact seen on receivers 4 (at 90 °) and 9 (at 180°) for brevity. These receivers have been chosen due to their respective positions with respect to the target and distance from the transmitting antenna. Receiver 9 is geometrically the most distant element from transmitter 1, hence it allows us to understand how scattering phenomenon takes place when the signal is significantly attenuated. On the other hand, location 4 is situated at an angle from transmitter 1 such that the impact of target position will be more pronounced at that location as compared to the other locations which are adjacent to the transmitter (antenna 1).

Fig. 6.9 (a) shows the change in signal strength for receivers 4 and 9 when the system remains unchanged in its entire geometry but target material is changed indicated by Mat1 and Mat2 in Fig. 6.9 (a). We observe that transmitted gain changes for both receivers beyond 2 GHz which is also the operational frequency of our printed monopole antenna when immersed in Triton x-100. We conclude from this study that materials with different dielectric properties scatter the incident signals differently which in turn is reflected on the transmitted gain at the receivers. Transition of signal strength over the entire frequency

spectrum for antenna receiver 4 is more smooth than that of receiver 9, this is due to the fact that signal received at antenna 9 is weaker and is also affected by interference with the reflected waves inside the imaging domain. Transmitted gain level at 4 GHz for antenna 4 is -50 dB for material 1 and -55 dB for material 2. however these levels have seen to be dropped down to below -65 dB for antenna 9 respectively.

Fig. 6.9 (b) shows transmitted gain over the entire frequency spectrum under consideration for receivers 2 (22.5°), 4 (45°) and 9 (180°) while antenna 1 transmits and target is placed first at 'Loc1' and then at 'Loc2'. In this scenario the locations of targets have been altered for the same material so that we observe the impact of same target material placed at different locations on signal scattering. We observe change in transmitted gain at receivers 2, 4 and 9 from 2 to 3 GHz, Fig. 6.9 (b). The change in transmitted gain when the target positions have been altered points to the fact that location of target is also vital and has significant impact on the way signal scatters.

Breast tissue is heterogeneous in nature, meaning it contains fibroglandular tissues that have different dielectric properties to adipose content of the breast composition. Fibroglandular tissues exhibit lower contrast ratio with the malignancies and therefore we expect different level of scattering from the tumour mimic once fibroglandular content is also included inside the imaging domain. In order to design a system that is capable of extracting useful information from interior of the breast volume we should mimic our phantom in a more complex form such that it incorporates fibroglandular content inside the domain also. We try to explore this concept by introducing fibroglandular mimicking material inside the phantom and then studying two cases, 1) target inside the fibroglandular and 2) target outside of the fibroglandular.

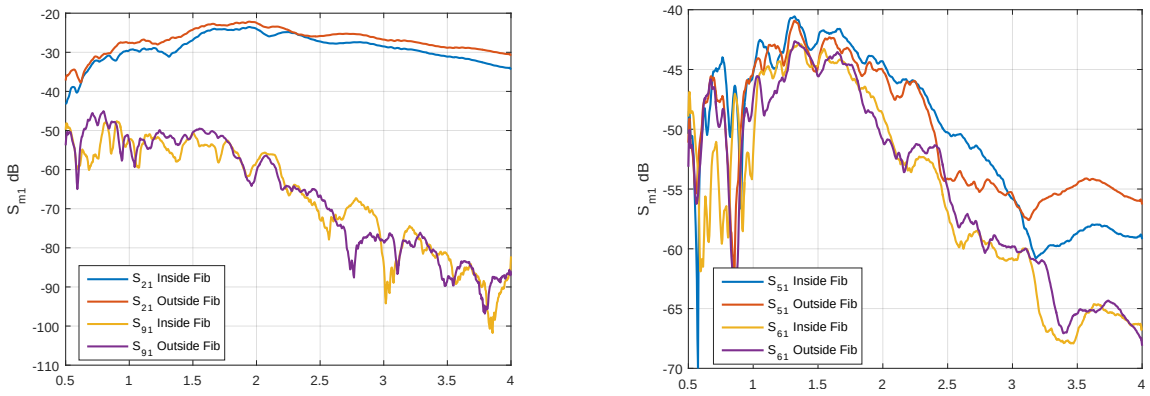

(a) (b)

Fig. 6.10 Transmitted gain (a) inside and (b) outside of Fibroglandular mimic

Fig. 6.10 shows the resulting transmitted gain in both configurations for locations at 22.5° and 180° (locations 2 and 9 respectively). We observe that addition of fibroglandular material results in increased attenuation of signals. Before introducing fibroglandular mimic we had observed signal level above -65 dB for the full range of frequencies, however after adding fibroglandular material the transmitted gain falls below -65 dB from 2 GHz upwards; region where antenna is operational. Difference in signal transmission shown in Fig. 6.10 indicates the impact of introduction of fibroglandular as the target material and location stay the same, hence any changes in transmission are attributed to the fibroglandular mimic.

6.2.3 CST® Simulation Results

We carry out simulations by recreating our experimental scenarios using CST® Microwave Studio. Results presented here are for two cases, with and without target for the antenna array immersed in Triton x-100 background. Fig. 6.11 shows the overall response of our system when antenna# 1 is excited for both with and without target cases.

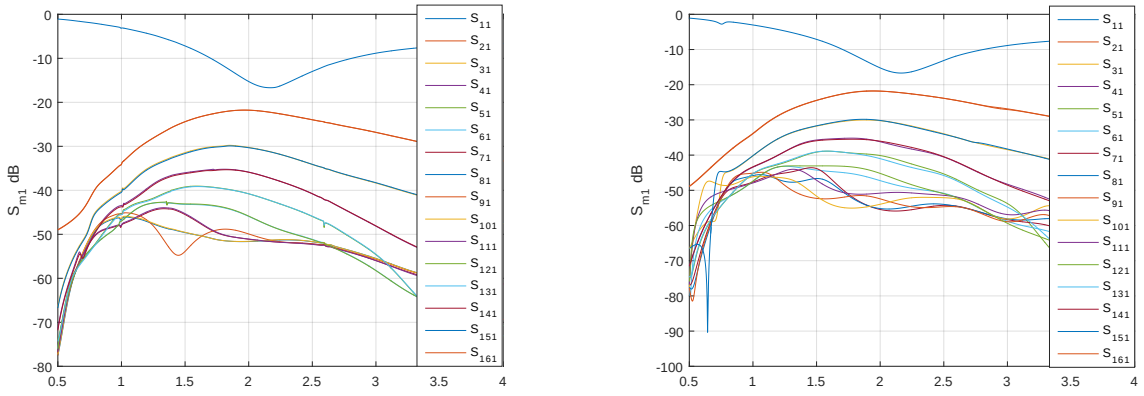

(a) (b)

Fig. 6.11 CST simulation results for (a) without target and (b) with target case.

We observe good transmission level of the signals when Triton x-100 is used as a background medium. Fig. 6.11 shows that location # 9 which lies opposite to the transmitter (Antenna 1) at 180°, receives above -60 dB signal upto 3 GHz. The transmitted gain between 1 to 3 GHz is not too different from our experimental transmission level (-70 dB). We also been observe that the antenna does not show below -10 dB return loss until 1.7 GHz and beyond 2.8 GHz, yet it is reasonably matched such that significant level of signal is being transmitted.

The difference of transmission as a result of inclusion of water target as a scatterer at the same location as our experimental setup is presented in Fig. 6.12 where we subtract the signal levels in dB values for with target case from without target. In order to make the plots more readable, the data from nearby receivers i.e receiver# 2 to 5 has been plotted in Fig. 6.12 (a) and for locations 6 to 9 the respective results are shown in Fig. 6.12 (b).

Transmitted gain does not vary significantly for receivers which lie in close proximity with the transmitter and are further away from target location. However, this variation in data is more pronounced in the cases where receiving locations are further away from transmitter and are in close proximity of target. Difference of transmitted gain in dB values for receivers 2 to 5 is within 0.5 range while for receiver 7 it reaches upto 4 at 2 GHz.

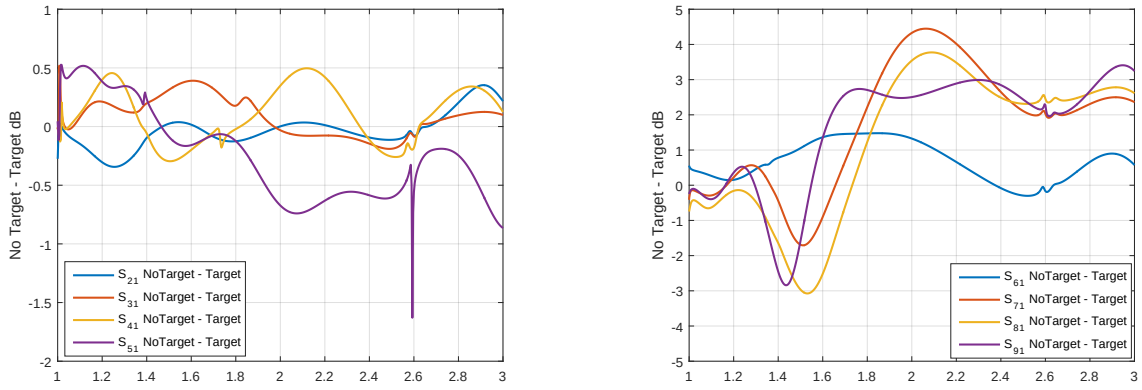

(a) (b)

Fig. 6.12 (a) Difference (in dB) of transmitted signal level in the case of without target and with target for location # 2 to 5 when antenna#1 transmits,(b) The difference of transmitted signal level (dB) in the case of without target and with target for location # 6 to 9 when antenna#1 transmits

Comparing simulation results with experimental data obtained from the rotating chamber data acquisition setup we observe that simulation data is smooth and exhibits good symmetry while experimental data due to the physical measurement errors does not hold symmetry and therefore experimental system needs to be improved.

6.2.4 Reconstruction Results

We use the data collected from our experiments for reconstruction. We apply inversion algorithm developed at KCL for imaging of the data [119, 120]. Our DBIM TwIST algorithm [120] is explained in the flow chart of Fig. 6.13. The differences between complex

permittivity of the object $\varepsilon(r)$ and background $\varepsilon_b(r)$ are defined as the contrast function $O(r)$, which is updated at each iteration. Under the Born approximation, the non-linear integral equation is linearised by replacing the unknown total electric field $E(r, r_m)$ with the known background field $E_b(r, r_m)$ which yields a linear equation $A(\omega)O = b(\omega)$ that can be discretized for all transmitter receiver pairs. The linear inverse problem is then solved using the iterative method such as TwIST [119] where a convex objective function is minimised. The matrix A_{m*n}, where $(m << n)$ 'm' is the number of measurements and 'n' is the number of unknown dielectric values is a severely ill-posed matrix. The matrix $A^{\mathrm{T}}A$ has some eigen values close to zero and others greater than 1 which lead to an unstable iterative process. Therefore, to apply TwIST the matrix is normalised by suitably choosing smallest eigen value. Another important aspect of the TwIST algorithm is the so-called tolerance that determines the number of the TwIST iterations at each DBIM iteration.

The DBIM-TwIST algorithm is further improved in terms of resolution and robustness, where a two-step reconstruction approach is implemented. In two-step approach at first the homogeneous breast interior is considered and DBIM is used to obtain an initial guess which corresponds to average properties of the true breast composition as very little *a priori* information is available. Our improved algorithm also introduces the novel method of regularization of uncontrained optimization problem based on L^1. Our algorithm also implements the Pareto curve for finding the L^1 norm regularization parameter of TwIST which defines the optimal trade-off between the L^2 norm of residual and the L^1 norm of the solution. Moreover, curve fitting method of cubic polynomials to smooth the Pareto curve are also applied to ensure differentiability and continuity of Pareto curve. The DBIM-TwIST algorithm is invoked both in the first step of finding the optimal initial guess and in the main reconstruction of the inhomogeneous breast structure. The Matlab code of the algorithm can be found in the PhD thesis of our colleague Zhenzhuang Miao [120].

We observe that experimental data lacks symmetry and hence reconstruction using DBIM-Twist algorithm will not converge. However, comparatively better results in terms of symmetry and transmission have been observed in the case of Triton x100 being used as background material as compared with 80% glycerol immersion. Lack of symmetry in experimentally acquired data is attributed to experimental errors which stem from positioning of antennas, position of tank, position of cables and environmental factors etc. Simulation results, however show better symmetry, but we observe transmitted gain of the order of -120 dB and below for the most distant receiver for 80% glycerol case. Thus, transmitted gain below the noise floor of the vector network analyser, -90 dB are not detectable. Hence, we have to use either a different background medium with lower losses or bring the antennas

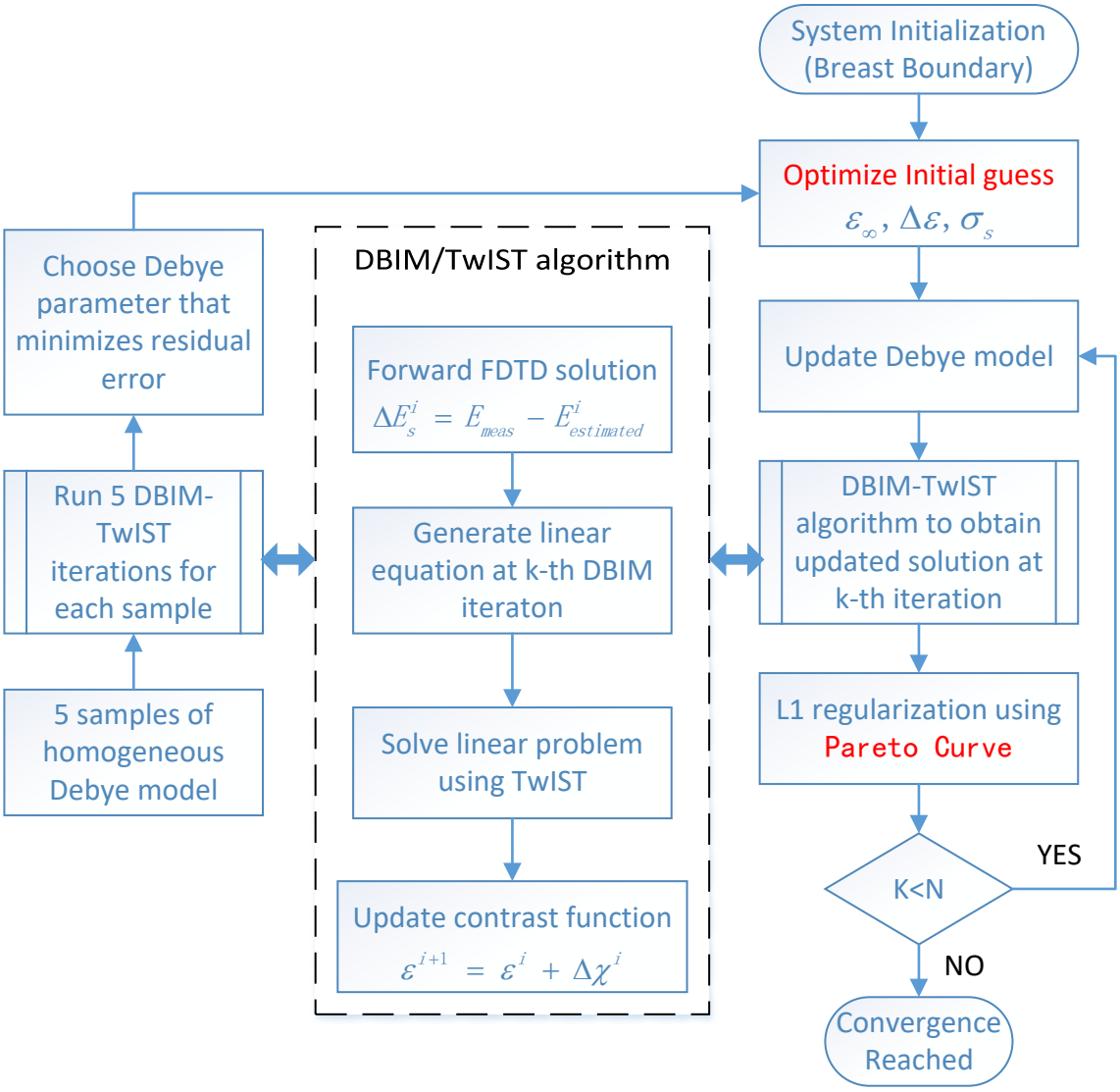

Fig. 6.13 Flow chart of the multiple-frequency DBIM–TwIST algorithm [120].

closer to each other. Triton having lower loss as compared to 80% Glycerine-water mixture renders better results from the transmission point of view.

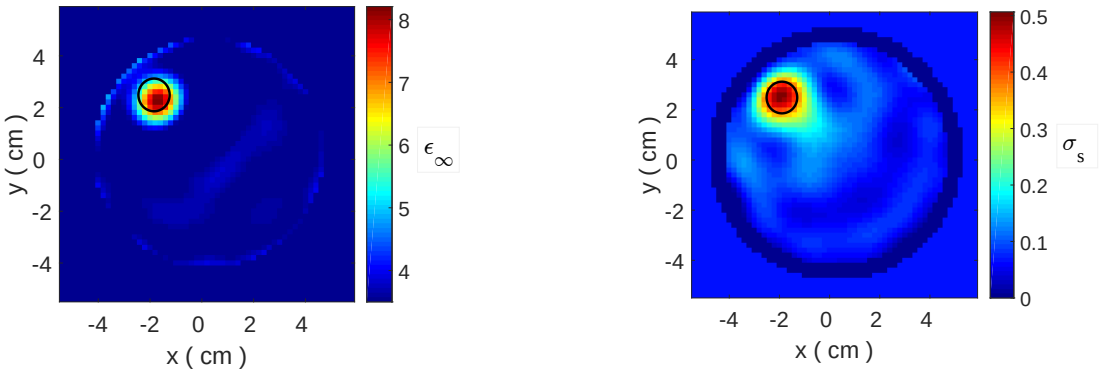

(a) (b)

Fig. 6.14 Reconstruction of the 3D CST frequency domain simulation data using DBIM TwIST algorithm, (a) ε_∞ (b) conductivity.

Fig. 6.14 depicts the images reconstructed from simulation data using DBIM TwIST. Images shown in Fig. 6.14 depict target location in Triton x-100 as background medium, position of the target detected by our algorithm is an accurate reconstruction of the water cylinder introduced in imaging domain to mimic the high contrast dielectric medium that acts as a strong scatterer. This simulation setup is a very close approximation of the actual experimental system at Politecnico di Torino. The results obtained from this study have been published in [121]. The reconstruction results using experimental data, however are not as accurate as the reconstruction results from simulations data. Target location has been captured by the algorithm however, some artefacts have also appeared in the reconstructed dielectric map of the imaging domain. Target location has not been reconstructed accurately as shown in Fig. 6.15. The experimental reconstruction is not as accurate as the inversion obtained from the simulation data due to experimental errors and dynamic range of the hardware.

6.3 Experiments with In-house Data Acquisition Prototype

We analysed results obtained from the rotating chamber data acquisition system in the last section. We observe that the data lacked symmetry due to inaccurate positioning of the antennas and imaging chamber along with other errors. We have gained significant insight into the development of a microwave tomography system by conducting experiments with

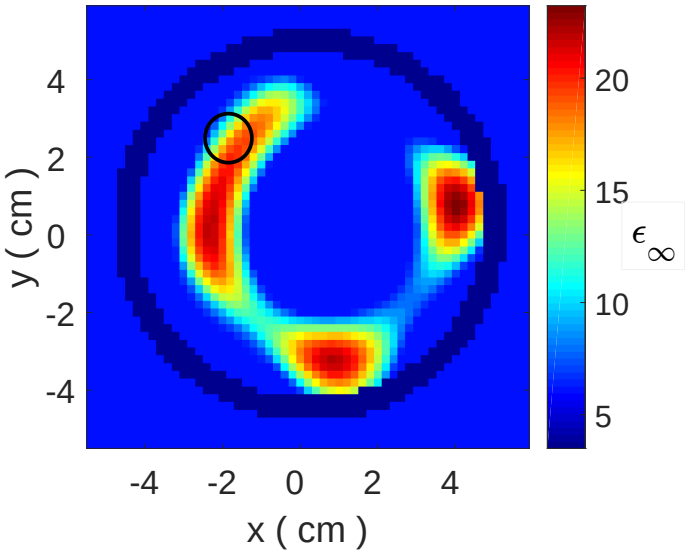

Fig. 6.15 Reconstruction of the experimental data using DBIM-Twist algorithm. ε_∞ is reconstructed in this case.

the rotary system and performing numerous numerical studies with CST. In this section we propose our in-house data acquisition prototype. The key purpose of this section is to introduce our system design with the rationale behind the construction of proposed prototype. The data acquisition procedure is also presented in this section, as, in the absence of a multi-port system we use bi-static configuration to collect data. This section also presents the mechanism of introducing the discontinuity in the imaging domain that will act as the target to be reconstructed.

6.3.1 The Hardware System Geometry

In this section we present our mechanical setup and the 'target' models that we will use in our subsequent studies. Fig. 6.16 depicts the schematic of mechanical structure of our proposed prototype developed for MT. The system is comprised of two large acrylic cylinders placed concentrically on a base calibrated for accurate repositioning of the inner cylinder. Precise positioning of the imaging chamber is very critical as we must keep spatial configuration of the hardware comprised of imaging chamber, target and antennas consistent throughout the study to observe impacts of scattering sources on signal propagation rather than change in signal responses due to inconsistent positioning of the system components. Moreover, it is also vital to remove the tank for washing and maintenance purposes, therefore in order to replace the tank back in the system we calibrate the tank holding base for correct and

consistent repositioning. The acrylic cylinders being used have a wall thickness of 5 mm. Diameter of the inner cylinder that also holds coupling liquids is 200 mm. Outermost cylinder (not shown in the schematic) is only used to provide support for mounting fixtures that hold antennas inside the medium.

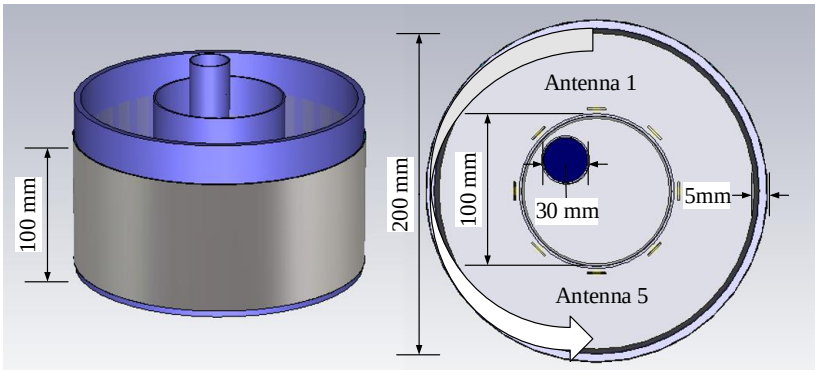

Fig. 6.16 Schematic of eight antenna system model.

We use two brackets to control vertical and horizontal positions of antennas inside the imaging chamber. Horizontal positioning of the antennas is achieved by inserting a calibrated scale through slot of the bracket being placed on the outer cylinder, hence allowing adjustment of the diameter of antenna array circle. Vertical positioning of antennas is acquired by placing slotted bracket at the edge of horizontal ruler and inserting another ruler through the slot that will have the ability to move up and down in vertical direction hence allowing full control of azimuthal position of the array. Flexibility and accuracy for positioning the antennas is of great importance because of the factors explained in preceding section.

We place a single 30 mm tube on a flat base screwed on the supports glued at the base of immersion holding tank. The purpose of this tube is to allow us to insert a different dielectric medium inside the domain that can mimic a high contrast target. The complete setup with single target tube is shown in Fig. 6.17.

We slightly modify this setup for incorporating the two layer phantom setup for our subsequent studies. We introduce a third cylinder of 100 mm diameter inside the 200 mm cylinder that holds background medium. Purpose of this 100 mm cylinder is to allow us to insert low loss material for enhancement of signal transmission. We can, however, use this same setup for our one layer immersion as well by filling up the same coupling medium in both cylinders (cylinder of 200 mm diameter as well as 100 mm diameter containing same liquid).

We also design a target holding mechanism that is slightly different as compared to previously used single tube screwed on a fixtures at the base of imaging tank. We design a

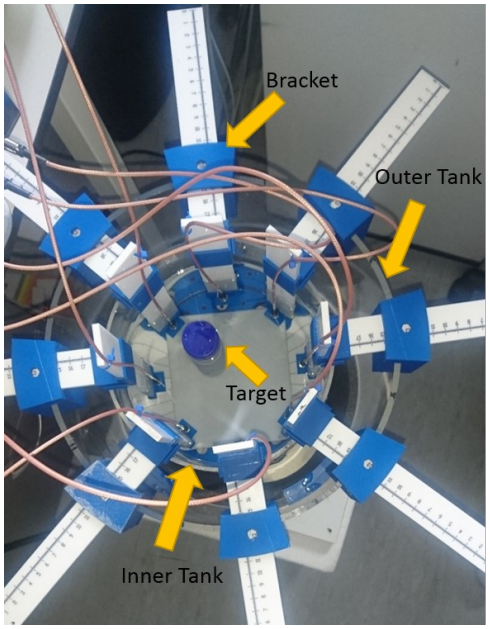

Fig. 6.17 Our proposed MT prototype depicting the calibrated attachments and a phantom mimicking 3D printed tubular structure.

new fixture capable of accommodating four target tubes inside the imaging domain. Our new target holder is a pair of 3D printed lids with 4 holes so that the target containing tubes can run through them. One lid resides inside the 100 mm cylinder base and the other one at the top of same cylinder. We can then run target containing tubes of the same length as the inner 100 mm cylinder or longer through holes provided in the disc. Tubes with high dielectric material stay firm when threaded through the two symmetric holes of lids in place. Diameters of holes on the lids are 31 and 21 mm. New target locations when the disc centre is concentrically aligned with the central axis of the whole system on the horizontal plane are – 1: (-20, 20), 2: (25, 30), 3: (25, -25) and 4: (-22.5, -25) as shown in Fig. 6.18[1].

6.3.2 Experimental Procedure

Our data acquisition system is shown in Fig. 6.17 (see also the schematics of Fig. 6.16). Setup consists of two concentric cylindrical tanks with 200 and 300 mm diameters as shown in Fig. 6.17. The outer tank shown in Fig. 6.17 is only used to support the antenna holders, where we place our printed monopole antennas. The modified system with an additional 100 mm cylinder is shown in Fig. 6.26. We can insert targets of different diameters inside the 100 mm inner tank using circular lids at the top and bottom of this cylinder, shown in Fig. 6.18.

[1] Picture courtesy MediWise Ltd.

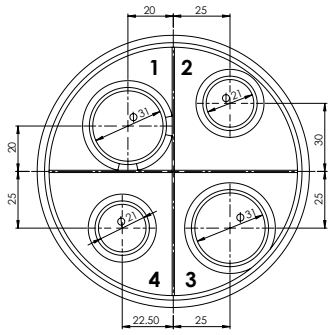

Fig. 6.18 Schematic of target holding disc.

We fill up the inner cylinder of 100 mm diameter with one of the coupling liquids studied in earlier chapters. Vertical and horizontal 3D printed holders allow us to control the antenna positions with good precision. We adjust the antennas to form an array of 130 mm and 150 mm diameter in our experiments. Outer periphery of the larger (200 mm) tank (containing immersion liquid) is surrounded with an absorber (ECCOSORB MCS) and is covered with a metallic (Styrofoam) shield to minimize surface waves and external interference.

In the absence of a switch matrix, we collect data in a bi-static configuration, using a two port vector network analyser. First we assemble the setup and calibrate our two port VNA, set to 201 data points with averaging factor of 5 and IF bandwidth of 200 Hz. We then collect 'empty tank' data from the tank filled with coupling liquid, by connecting the transmitting antenna to port 1 and recording sequentially the signal at each receiving antenna connected to port2. We then repeat the process for all the remaining seven antennas acting as transmitters. Subsequently we introduce a target inside the imaging domain and record the results for 'with target' case which yields the scattered signal information to be used by the algorithm for reconstruction.

6.4 Results without Target

In this section we present our experimental analysis of 8 element printed monopole antenna array operating in homogeneous background for three different coupling media: 1) 80% glycerol, 2) 90% corn syrup and 3) 90% glycerol.

We use 80% glycerol as background medium and install eight antennas in our imaging prototype. We keep the diameter of antenna array 150 mm in this experiment. 80% glycerol is a lossy medium and high level of attenuation is expected in this background, however there

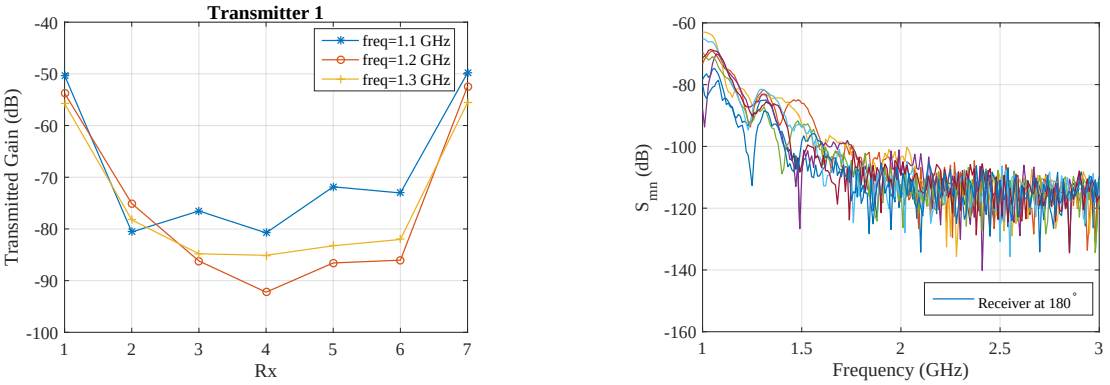

(a) (b)

Fig. 6.19 (a) Transmitted gain as a function of receiver locations at 1.1, 1.2 and 1.3 GHz in the absence of target. (b) Transmitted gain for the receiver placed at 180° for all the transmitters (1 to 8) of the array immersed in 80% glycerol.

are other benefits such as mitigation of cross coupling between the antenna elements and surface waves, therefore we study the signal propagation in this medium.

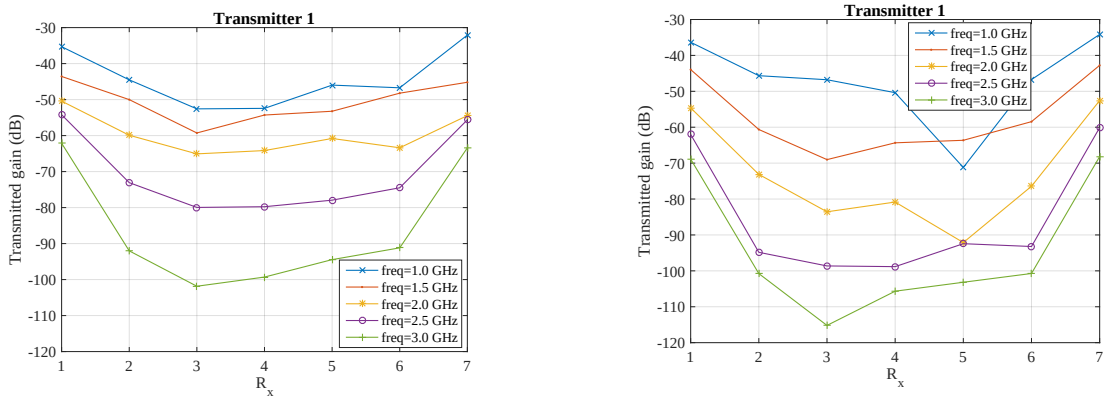

(a) (b)

Fig. 6.20 Transmitted gain as a function of receiver locations # (1 to 7) at 1, 1.5, 2, 2.5 & 3 GHz in homogeneous 90% corn syrup background (No target case) when the array diameter is (a) 130 mm (b) 150 mm.

From our experimental results we conclude that 80% glycerol is too lossy. Transmitted gain at frequencies as low as 1.3 GHz get seriously attenuated and fall below noise floor of the VNA being used. Fig. 6.19 elaborates this finding. Transmitted gain plots shown in Fig. 6.19 (a) show that signal strength falls below -90 dB at 1.3 GHz for receiver 4 situated at

180° with respect to the transmitter. Fig. 6.19 (b) shows signal strength for the same receiver over the entire frequency range (1 to 3 GHz) of interest for each of the transmitters. We observe significant amount of noise over majority of the spectrum of interest.

Our simulation study presented in Chapter 5 on the impact of different background media on signal propagation in the imaging domain highlights the fact that 90% corn syrup exhibits good dielectric properties for microwave imaging. Relative permittivity of 90% corn syrup mixture is close to 19 at 1 GHz and its conductivity stays below 0.5 S/m.

We perform our homogeneous background medium study using 90% corn syrup. We consider two different antenna array diameters; 130 mm and 150 mm in this experimental analysis. We implement the same experimental procedure as described before in the presence of 90% corn syrup as coupling medium and collect the data using our 2 port VNA.

We analyse the impact of array diameter on signal strength received at each receiver experimentally, for 150 mm and 130 mm array diameters. Increased diameter of the array is expected to result in more attenuated signals at receiving elements of the array. We quantitatively analyse this premise and present subsequent results in the following figures.

Transmitted gain plots for 130 mm and 150 mm diameter array cases immersed in homogeneous 90% corn syrup are shown in Fig. 6.20. Transmitted gain plots as function of location for each of the transmitters 1 to 8 of the antenna array of 130 mm diameter submerged in homogeneous background of 90% corn syrup are shown in Fig. 6.20 (a) and the same plots for 150 mm diameter array are shown in Fig. 6.20 (b). From the plots shown in Fig. 6.20 it is evident that transmitted gain response is not entirely symmetric and parabolic for both cases (large and small array). We also observe that transmitted gain at receivers for each of the transmitters have different trends, which in the homogeneous background should remain unchanged regardless of the position of transmitting element.

Comparison of Fig. 6.20 (a) (close) and Fig. 6.20 (b) (far) without target cases, with 2 cm difference in array diameters show that there is very slight change in transmitted gain after increasing the diameter of array ring. Transmitted gain levels for the smaller diameter array are slightly higher as expected. We observe almost 15 dB attenuated signals in the case of larger array as compared to 130 mm array. Signals at the frequencies beyond 2 GHz for 150 mm diameter array are attenuated significantly and are very close to the noise floor of the VNA, therefore, transmitted gain trends are not symmetric and parabolic. We observe that transmitted gain trends at 1 GHz frequency sample vary the most in all cases, this is due to higher coupling between the cables at this frequency as they also start to radiate at 1 GHz and the effect of this radiation is quite significant at close to 1 GHz.

Aforementioned discrepancies are derived from the inaccuracies attributed to the physical system. There are acrylic antenna holders, cables, environment factors, material properties and orientation of the cables which introduce nonidealities in the experimental data acquisition. Antenna radiation characteristics at different frequencies also change which impact signal propagation. Coupling between antenna elements and cables have significant effect on the transmitted gain characteristics also, as we use multi-static approach for data collection in these experiments.

We also investigate the impact of 90% glycerol background medium on signal propagation. We consider only 130 mm array diameter case. Fig. 6.21 shows transmitted gain plots for all combinations of transmitters and receiver locations in our prototype. Each subplot in Fig. 6.21 represents a transmitter, transmitted gain traces are shown as function of receiver locations. Transmitted gain traces as function of receiver locations show better symmetry as compared with previous cases studied so far, however not fully symmetric and parabolic.

Impact of coupling at lower frequencies is significant therefore we do not observe 100% symmetry at frequencies in the region of 1 to 1.4 GHz. At higher frequencies, however, impact of coupling between cables reduces but signal attenuation also increases. In our experiment this weakening of signals is not too pronounced that is why we observe good symmetry from 2 GHz and above. Transmitted gain levels for 2.5 GHz are at the border of noise floor of our VNA while at 3 GHz levels of signal strength fall below -90 dB. Thus we do not expect good reconstruction beyond 2.5 GHz as the data will not be sufficiently reliable for this frequency range due to hardware (VNA) sensitivity limitation.

6.5 Results with Target

In the last section we presented experimental results when the antenna array was immersed in three different homogeneous coupling media using our hardware prototype. We, now investigate the impact of introducing a discontinuity in the imaging domain of our proposed hardware prototype using 90% corn syrup and 90% glycerol as background media. Since, using 80% glycerol as a coupling medium resulted in high attenuation of the transmitted gain therefore, we will not consider it in this ‘with target’ study.

We insert a tube filled with water inside the imaging domain using the target holder disc shown in Fig. 6.18 at (-20, 20) to introduce a high dielectric medium accountable for signal scattering in 90% corn syrup background immersion.

We plot differences in transmitted gain (in dB) by subtracting transmitted gain obtained at each receiver after inserting a scatterer ‘with target’, from the corresponding signal strength

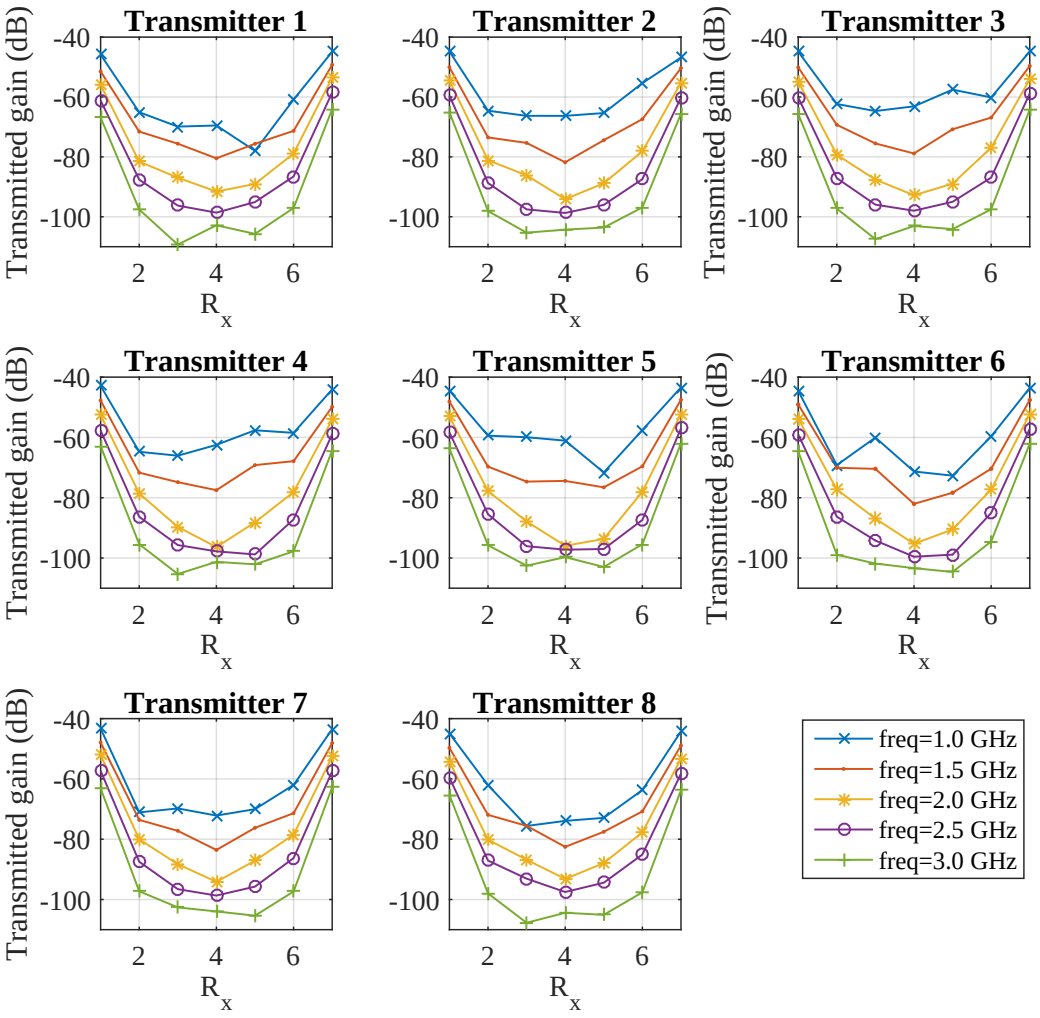

Fig. 6.21 Transmitted gain as a function of location when 130 mm diameter printed monopole antenna array is immersed in 90% glycerol homogeneous background.

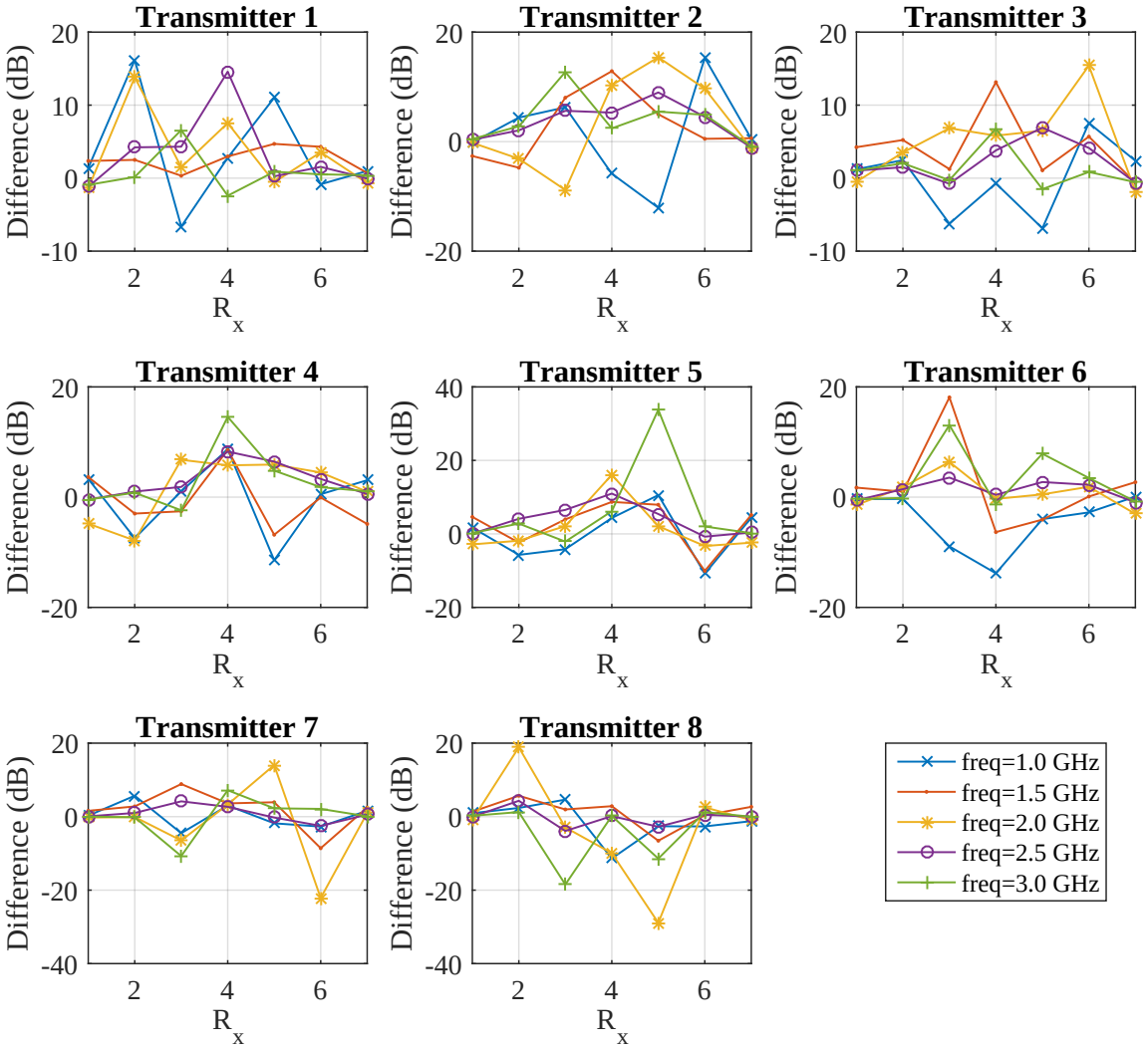

Fig. 6.22 Differences(in dB) between transmitted gain without target and with target when eight antenna array of 130 mm diameter is immersed in 90% corn syrup.

in homogeneous background case 'without target', to quantify the impact of scattering phenomenon on transmitted gain as a ratio of magnitudes. Fig. 6.22 shows differences in dB plots for 130 mm diameter array. It is clear from these plots that signal has undergone significant scattering as the changes of upto 20 dB in transmitted gain are observed.

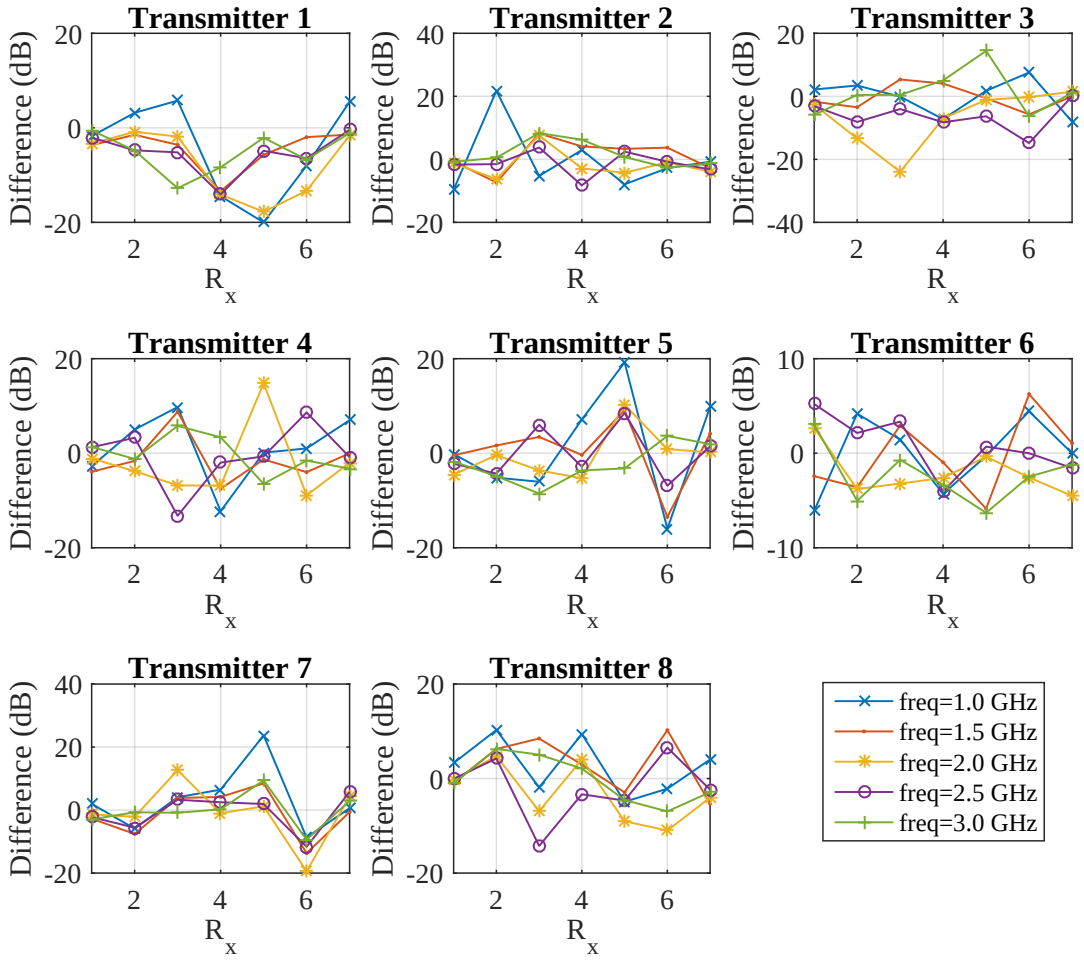

Fig. 6.23 Differences (in dB) between transmitted gain without target and with target when eight antenna array of 150 mm diameter is immersed in 90% corn syrup.

We perform the same analysis as before on 150 mm diameter antenna array immersed in 90% corn syrup. Resulting differences plots representing the magnitudes differences in dBs are shown in Fig. 6.23. Once again we observe significant perturbation in the transmitted gain after including an object with high dielectric characteristics as compared to the background medium. Difference in dB of upto 20 dB is observed in some cases.

We observe good correlation between the differences plots at some frequency samples. As an example for the smaller array diameter case (130 mm) for transmitter 5 the trend of differences for all frequency samples show very similar variation, however for transmitter 1 the trends are not as synchronized. The lack of similarity in trends of differences plots is due to the relative position of target with respect to the respective transmitting antenna, (antenna 1 in this case). The effect of reflection from the target is pronounced on the overall transmitted gain characteristics for antennas situated closer to target. Similarly, antenna 2 and 3 as transmitters which also reside in close proximity with the target suffer from high signal reflections from the target object. Transmitters 4 to 8 being away from target exhibit more correlated signal behaviour at almost all frequencies being considered.

For the larger, 150 mm array the effect of reflection is not so pronounced as it was seen in the 130 mm array case due to the additional distance a signal has to travel in order to reach the receivers, however overall response of transmitted gain plots for larger array is not quite correlated due to weak signals reaching the receivers.

We analyse the impact of introducing a discontinuity in 90% glycerol background imaging domain as well. We use two different target media for this study, pure water and salt water mixture (10 mg/mL). The dielectric properties of targets being considered are shown in Fig. 5.13. We introduce target medium inside a 1 mm thick acrylic tube of 8 mm radius centred at (-22.5, 25) on xy plane of the setup. We observe significant signal scattering due to the targets introduced. Fig. 6.24 shows the complete variation of differences in transmitted gain at the receiver locations when water target is inserted inside a coupling medium of 90% glycerol.

We observe differences of upto 10 dB in both target cases, this change in transmitted gain signifies that we have captured information about the imaging domain where the effect of scattering is pronounced. We will validate the obtained data using our imaging algorithm for reconstruction in subsequent section of this Chapter. We introduce two different target media to observe effect of target medium on the wave propagation and hence on scattering of the signal. Fig. 6.25 shows differences between simulation and experimental results for water and salt water targets. Simulation results are in good agreement with experimental findings, however the actual values of the transmitted gain are not exactly the same for measured data but the trends of plots are very similar.

6.5.1 Analysis of Two Layer Phantom Array Configuration

The use of lossy dielectric immersion medium as a matching liquid has its pros and cons. The biggest advantage of using high loss dielectric medium as a background is the minimization

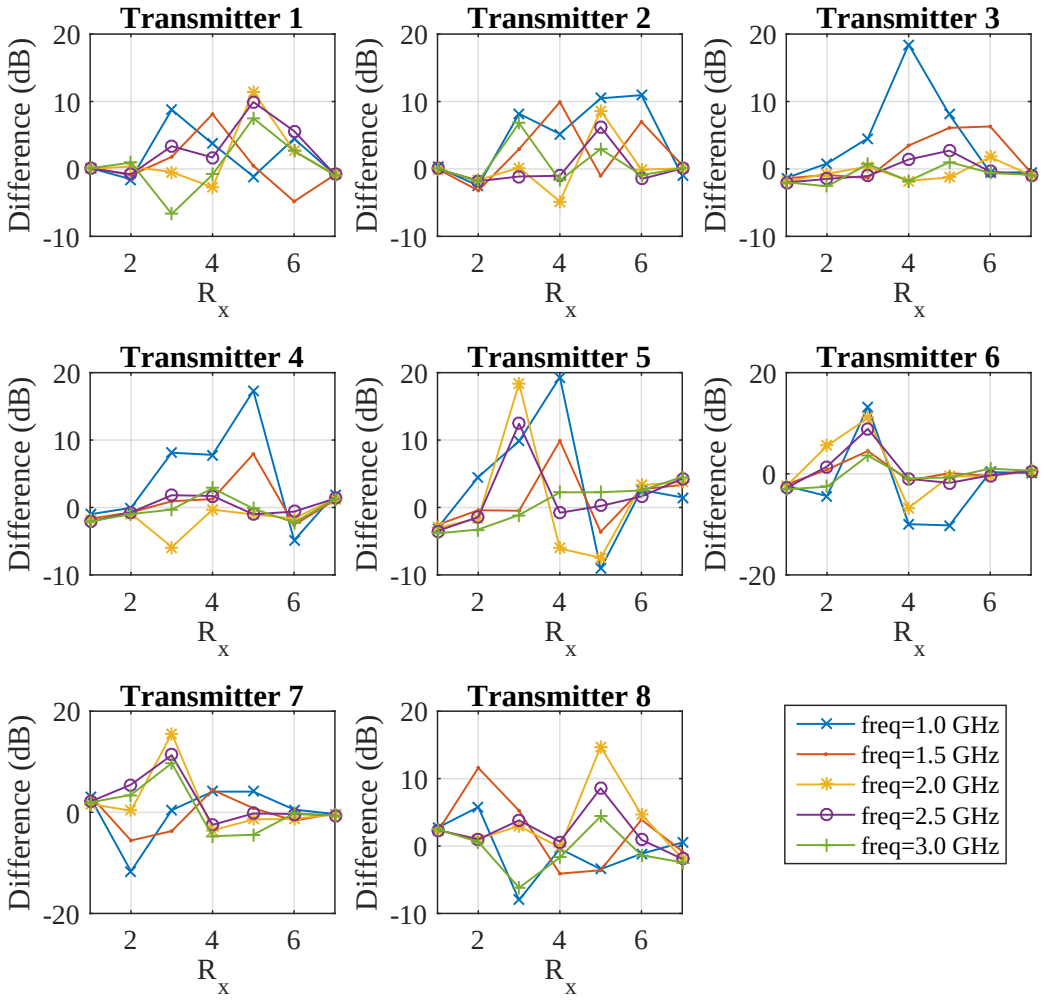

Fig. 6.24 Differences (in dB) in transmitted gain when water target is introduced in homogeneous background comprised of 90% glycerol. The array diameter is 130 mm.

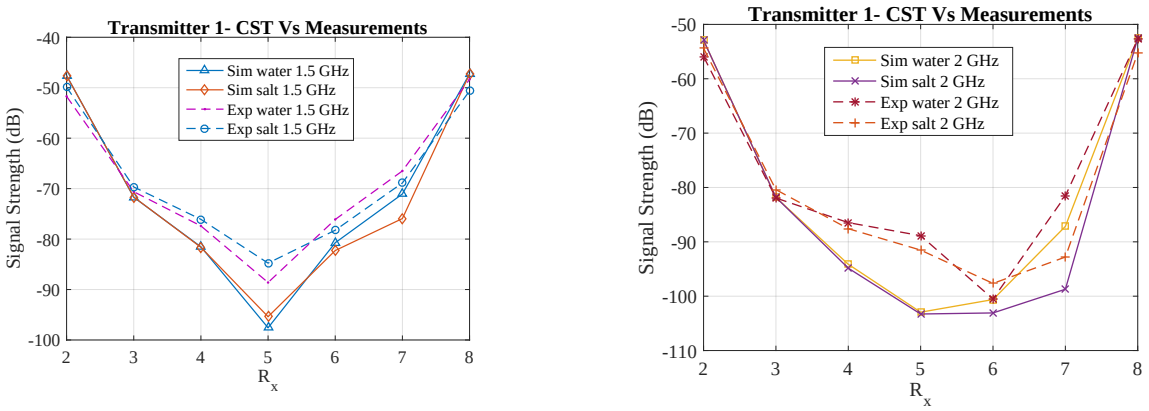

(a) (b)

Fig. 6.25 Comparison between simulations and experiments of two different target media in 90% glycerol background (a) at 1.5 GHz (b) at 2 GHz. The array diameter is 130 mm in both cases.

of crosscoupling between the array elements and suppression of surface waves and multipath signals. However that comes at a price; very low signal power at receiving antennas which requires high sensitivity receivers thus incurring high cost of the hardware.

Considering the anatomy of breast and appreciating the fact that signals propagating in the imaging domain will not have to traverse entire distance between antennas constituting the array in high loss immersion background, we propose a second layer in our imaging chamber, comprised of a low loss material. We perform our subsequent measurements in this newly proposed two layer phantom geometry where the inner tank diameter is 100 mm as shown in Fig. 6.26. Target coordinates have also been shown in Fig. 6.26, whereby diameter of the target container is 31 mm . Target material used is water which has a high dielectric contrast with that of background materials being used; 90% corn syrup and safflower oil. We study two diameters of the antenna array rings, 130 mm and 150 mm, geometrically similar to the prior cases of single layer 90% corn syrup.

Two Layer Phantom Comprised of 90% Corn Syrup and Safflower Oil

Transmitted gain plots of ‘close’ array (130 mm) in a two layer phantom geometry without target are shown in Fig. 6.27. From Fig. 6.27 it can be seen that the transmission has been enhanced by 20 dB generally for higher frequencies and distant receivers as compared to the case when 90% corn alone was used as background. Subplots in Fig. 6.27 i.e. ‘no target’ case

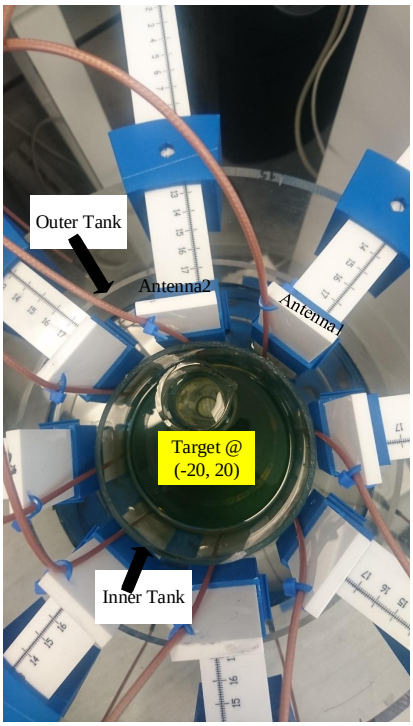

Fig. 6.26 Two layer phantom experimental setup with target.

show better symmetry as compared to the corn only case without target; albeit not perfect, for the similar reasons suggested earlier for single immersion 'no target' case.

Transmitted gain plots after inclusion of a target show significant change in the trend as compared to 'no target' case. We quantify the changes observed in transmitted gain magnitudes by taking difference between 'with' and 'with out' target cases. Resulting plots of differences in transmitted gain magnitudes in dB when signal strength data in dB with the inclusion of target is subtracted from 'no target' case for 130 mm in two layer phantom configuration.

The 'differences' plots shown in Fig. 6.28 suggest that significant scattering has taken place when a high dielectric target has been inserted in the domain. Difference upto 20 dB have been observed, an indication of scattering from the high dielectric medium. The trends of differences plots have also been quite similar for respective transmitters at most frequencies.

We continue our study of two layer phantom for larger array ring diameter. We proceed as before i.e. we start first present a 'no target' case to show the transmitted gain for the entire array. Subsequently we present differences of the 'with' and 'without' target cases in dB values.

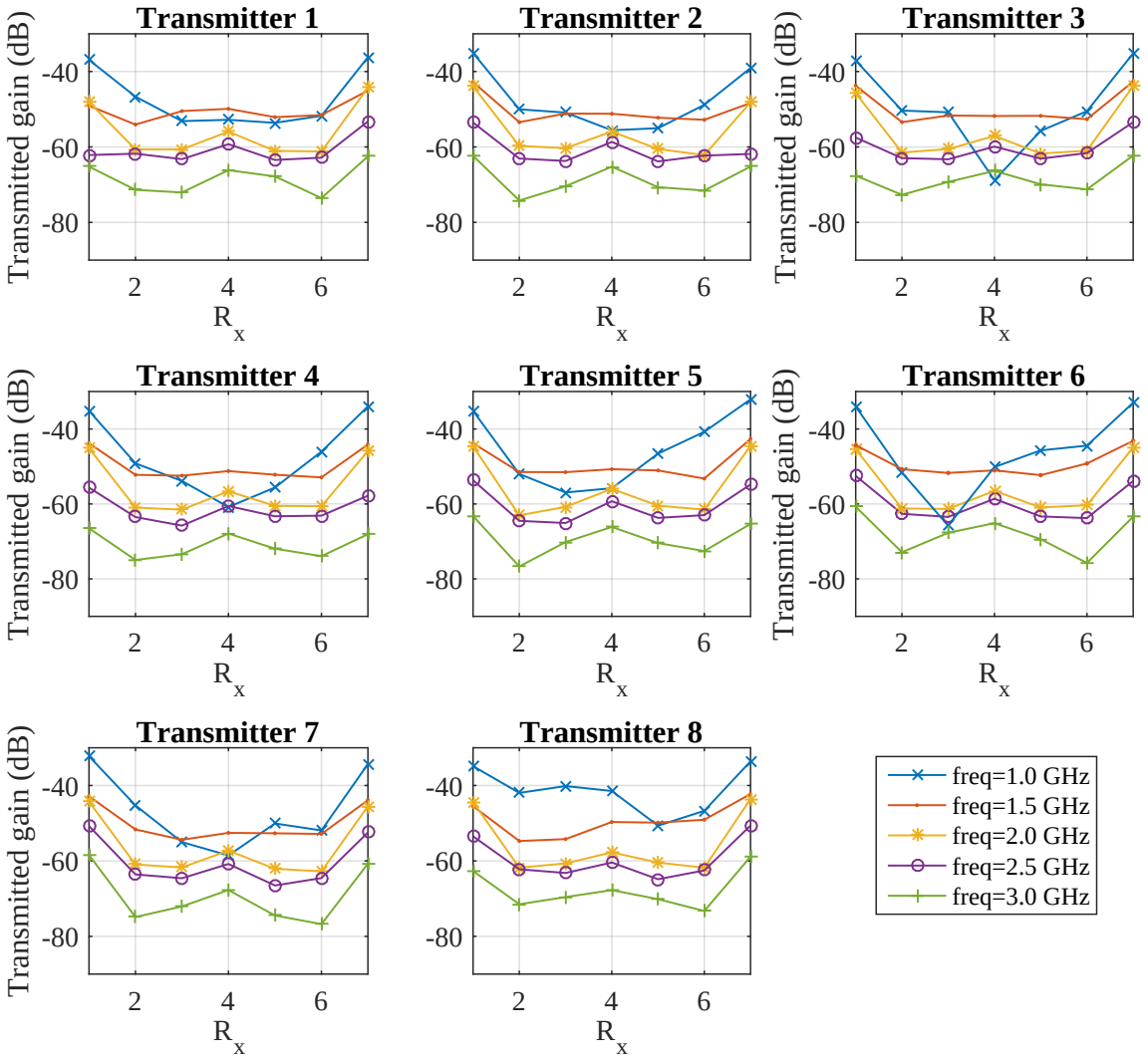

Fig. 6.27 Transmitted gain without target when an eight antenna array of 130 mm diameter is immersed in 90% corn syrup and a second layer of safflower oil is introduced.

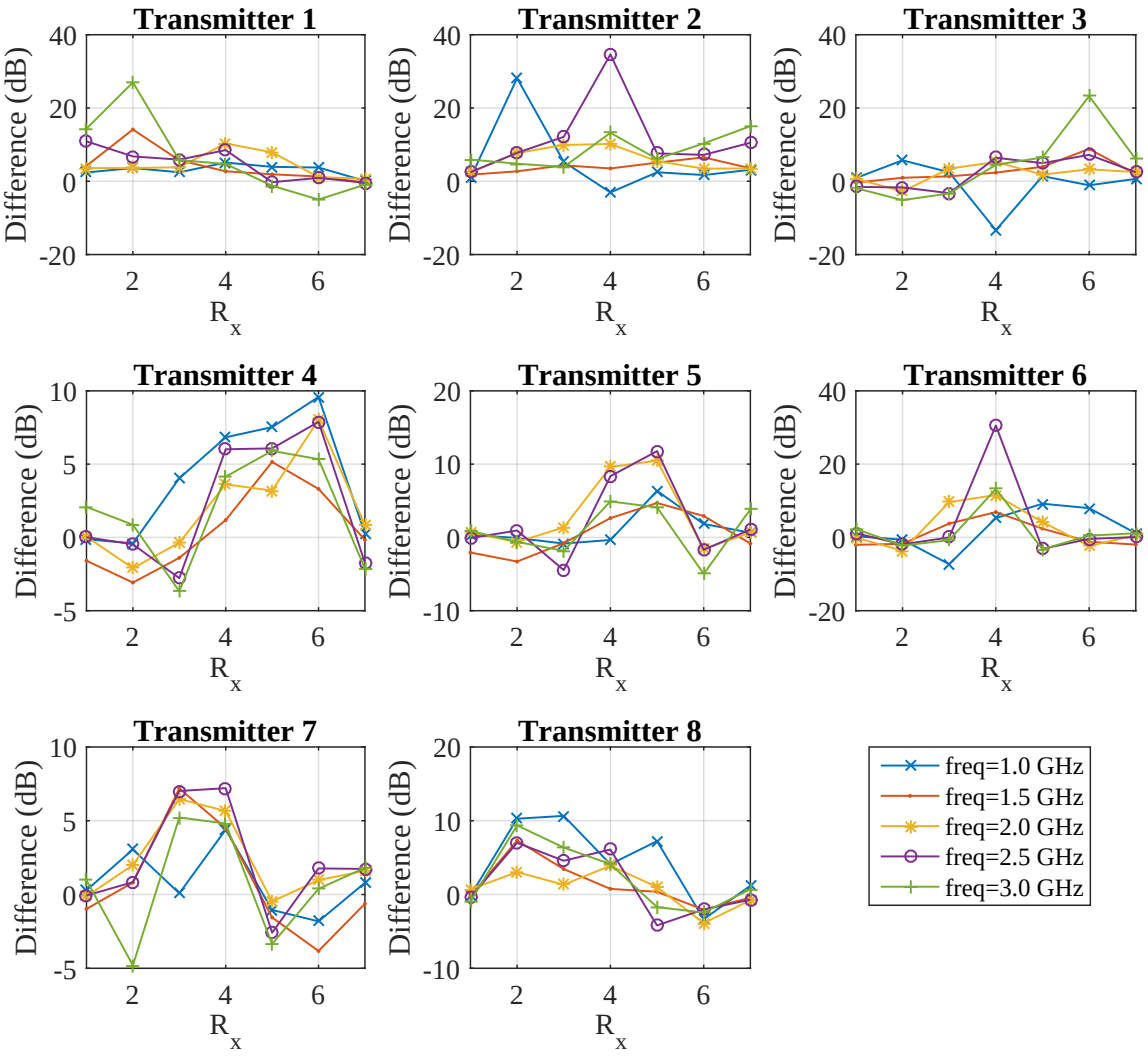

Fig. 6.28 Differences (in dB) between transmitted gain without target and with target when eight antenna array of 130 mm diameter is immersed in 90% corn syrup and a second layer of safflower oil is introduced.

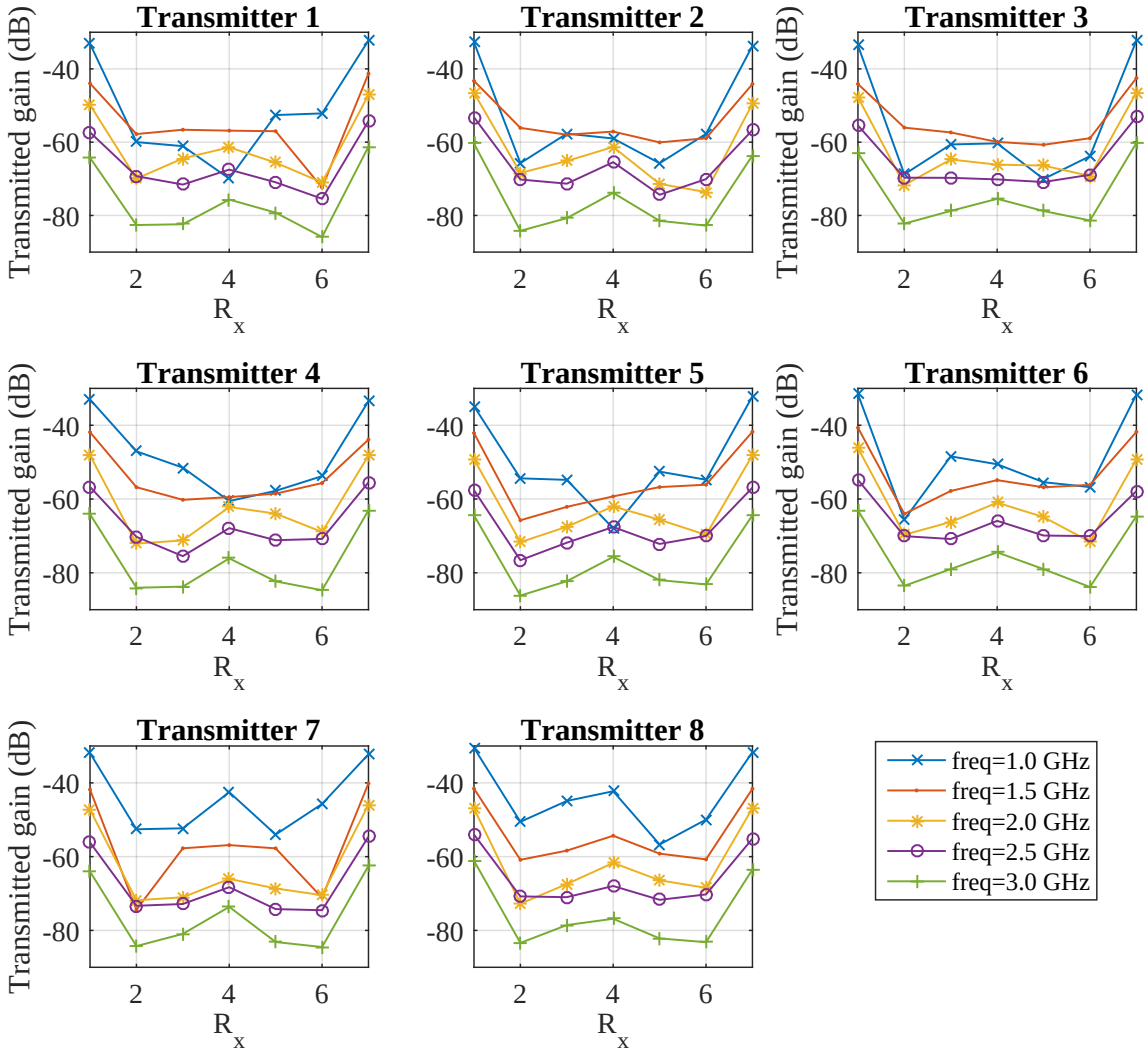

Fig. 6.29 Transmitted gain without target when the eight antenna array of 150 mm diameter is immersed in 90% corn syrup and a second layer of safflower oil is introduced.

Fig. 6.29 shows the no target case with larger array ring diameter where we can easily see that the transmitted gain minima has fallen below -80 dB at 3GHz frequency sample whereas for the smaller array (130 mm diameter) the minima has been well above -80 dB mark. The difference in minima for the corresponding array diameters is an indication of more attenuation of the signal when it has to travel through higher loss medium for longer distance. Trends of the received plots have not been ideally symmetric, however there is a close resemblance in the patterns for various transmitters and parabolic locus of the curves, albeit some erratic behaviour observed at 1 and 1.5 GHz.

Transmitted gain plots as function of receivers when the target has been introduced in the domain exhibit skewness in the previously seen trends of homogeneous two layer phantom configuration signals, therefore we deduce that scatterer has an impact on the transmitted gain response of the system. We plot differences (in dB) of the 'with target' case subtracted from the 'no target' case as depicted in Fig. 6.30. The differences curves at 1 GHz for all transmitters except for transmitter 6 show different trend as compared with the remainder of the frequency samples being plotted, other than that we see similar trends for all the transmitters involved in the system. Thus we can conclude that we have some good indicators in terms of dielectric contrast and this information can be passed on to the imaging algorithm for reconstruction of the dielectric profile of the domain.

As a general remark, we have observed some inconsistency in the data without target where symmetric parabolic response is expected. We attribute this discrepancy to the experimental errors and our premise is that, significant error contribution comes from the cross coupling between the cables particularly at low frequencies. Therefore, we chose different set of cables which are longer and as a result we can maneuver them more consistently and easily around our imaging setup. Consequently we expect that this will help in either minimizing the error or keeping it as static as possible. Minimizing the error or maintaining it in a more predictable fashion could be eliminated by software calibration in the forward solver of the algorithm code.

Two Layered Background Media 80% Glycerol and Safflower Oil

Earlier in the chapter we discussed experimental transmitted gain when our antenna array was immersed in 80% glycerol. Transmitted gain was found to be below noise floor of the VNA being used in this study for frequencies above 1.3 GHz. Therefore, we introduce a layer of low loss medium as we did in the case of 90% corn to enhance signal transmission. We perform same analyses as above for 80% glycerol background medium in a multilayer phantom. We observe significant increase in the transmission levels as compared to the single

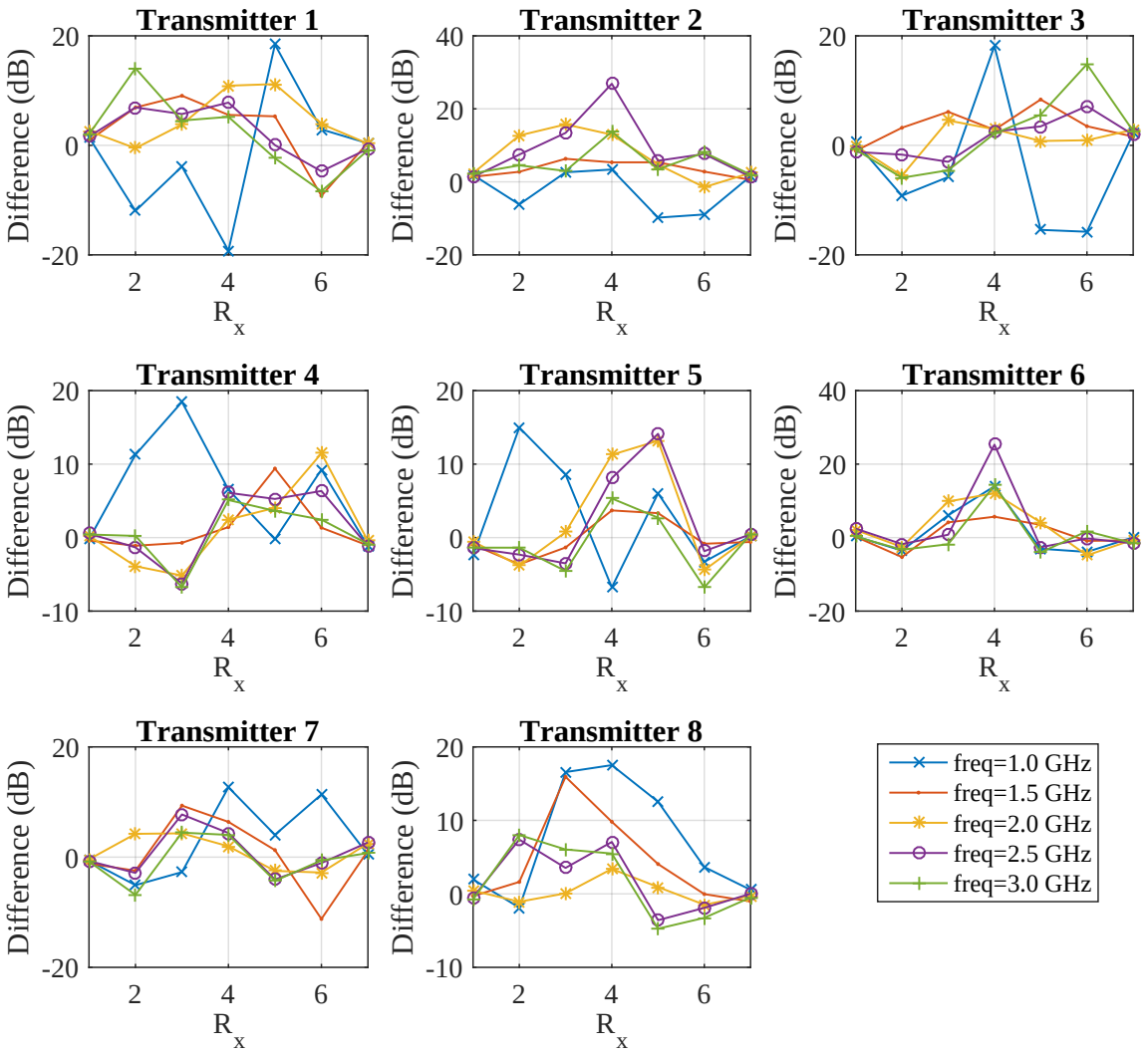

Fig. 6.30 Differences (in dB) between transmitted gain without target and with target when the eight antenna array of 150 mm diameter is immersed in 90% corn syrup and a second layer of safflower oil is introduced.

layer 80% glycerol case presented in section 6.6 where we could not retrieve any useful information beyond 1.3 GHz due to highly attenuated signals.

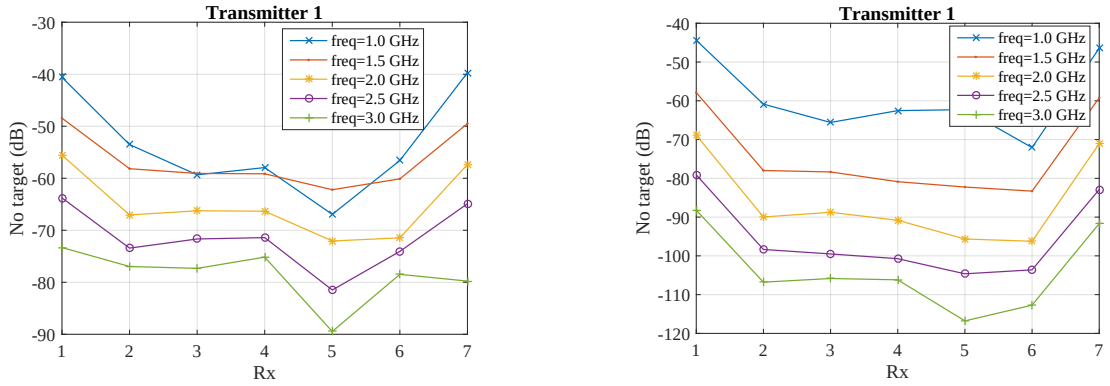

(a) (b)

Fig. 6.31 Signal strength as a function of locations at 1, 1.5, 2, 2.5 and 3 GHz of eight antenna array immersed in 80% glycerol with a second layer of safflower oil (a) 130 mm array diameter (b) 150 mm diameter.

Fig. 6.31 shows signal level for two layer imaging domain with 80% glycerol as immersion medium and a second layer of safflower oil. We measure transmitted gain in this two layer phantom configuration for two diameters of the array of antennas; 130 mm and 150 mm. Signal strength at receivers is improved due to newly added safflower oil layer that has lower loss than background immersion 80% glycerol layer. We also observe relatively good signal symmetry for both cases i.e 130 mm and 150 mm array sizes. Signal levels for the larger array are still either very close or below -90 dB therefore we continue with the analysis of effect of introducing a scatterer in the smaller (130 mm) array only.

Fig. 6.32 shows differences in the transmitted gain values in dB for the complete set of transmitter receiver combinations. We observe significant variation in transmitted gain due to the inclusion of high dielectric target medium. Changes observed in signal strength due to the presence of a scatterer signifies that this information can be used to reconstruct images of this discontinuity.

6.5.2 Analysis of Error Due to the Effect of Cable Coupling

In our previous discussion we suggested that there is a significant impact of cable coupling on the transmitted gain. We analyse differences between the coupling level of data acquired by two different sets of cables. We use shorter cables in our first study where we realised

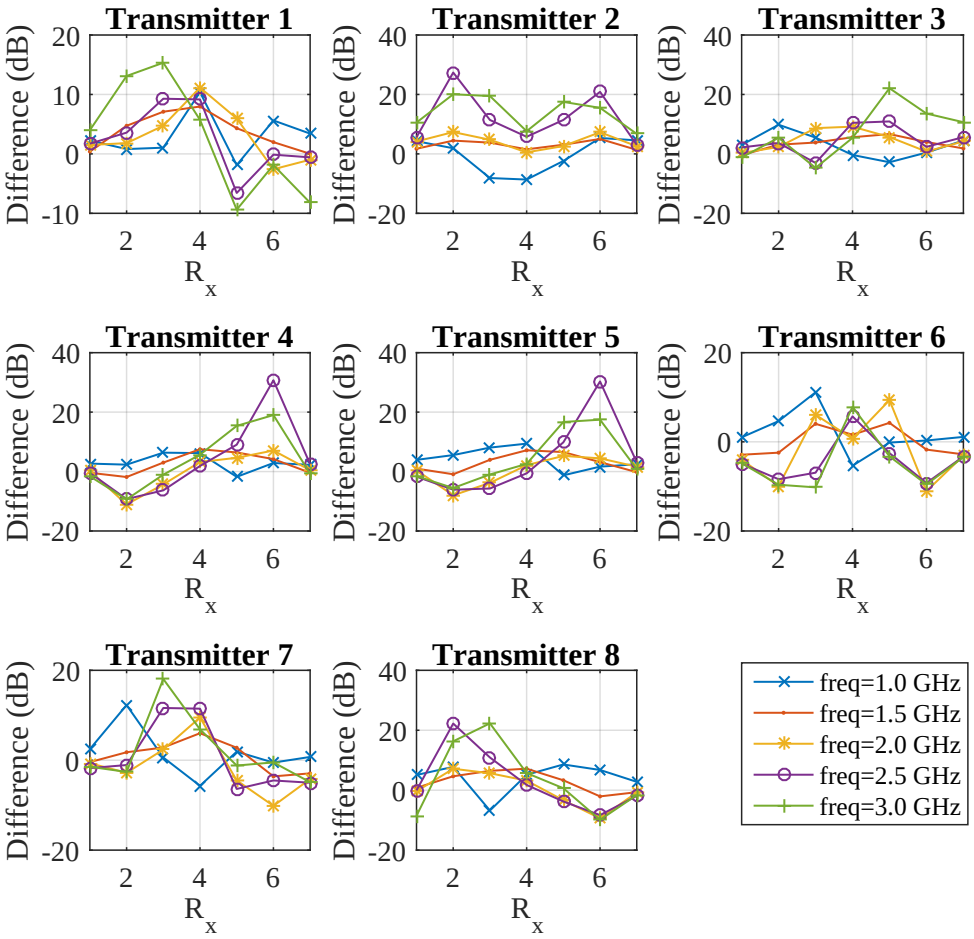

Fig. 6.32 Differences between transmitted gain (in dB) strength without and with target when eight antenna array of 130 mm diameter is immersed in 80% glycerol and a second layer of safflower oil is introduced.

that while maneuvering the antennas we encounter some scenarios where it was inevitable to have a direct overlap between the cables. To rectify direct contact between transmitter and receiver cables we introduce another longer set of cables which allows us to circumvent the challenge posed by cable overlapping.

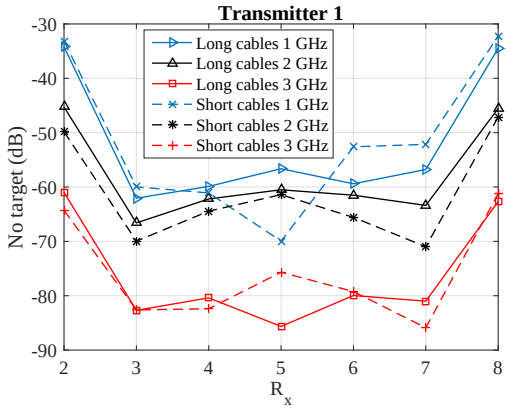

Fig. 6.33 Comparison between cables for coupling error. Longer cables which allow us to avoid the direct contact show slightly better results than shorter cables where the direct contact is inevitable for a few combinations of transmitter and receiver.

Fig. 6.33 depicts comparison between two sets of cables used in data acquisition with two layered phantom geometry where the array diameter is 150 mm and 90% corn syrup is used as immersion liquid. Transmitted gain curves for each of the frequency samples (1, 2 and 3 GHz) obtained with longer cables show better symmetry as compared with the shorter cables. Trends of the curves are very similar in both cases but particularly at 1 GHz we observe unexpected behaviour at receiver 5, 6 and 7. Referring back to Fig. 6.26 we can verify that these affected receivers suffer because of their relative positions with respect to antenna 1. Port 2 of the VNA has to be used to connect these receivers while antenna 1 is connected with port 1. In order to physically reach port 2 there is a need for stretching the cables which in turn gets in closer contact with the cable connecting antenna 1 and couples with it.

When we connect longer cables with port 2 for the same receivers, similar phenomenon as before occurs, however due to the extra bit of length of the cable we circumvent the issue by making sure there is maximum possible distance between two cables.

6.6 Reconstruction Results

Our microwave tomography algorithm is developed by our colleague, Zhenzhuang Miao at King's College London and is presented in [119, 120]. We apply our in-house microwave tomography reconstruction algorithm to various sets of data reported throughout this report to validate our system modelled in 3D CST simulations as well as experimentally. We break this analysis into two sections:

- Reconstruction of the simulation data
- Reconstruction of the experimental data

6.6.1 Reconstruction Results from 3D Simulation Data

We present reconstruction results from the 3D CST simulation data for Triton x-100, 90% corn syrup, 90% glycerol and 80% glycerol background media. We also attempt to reconstruct the data obtained from our two layer phantom study where we used second low loss immersion layer for signal transmission enhancement.

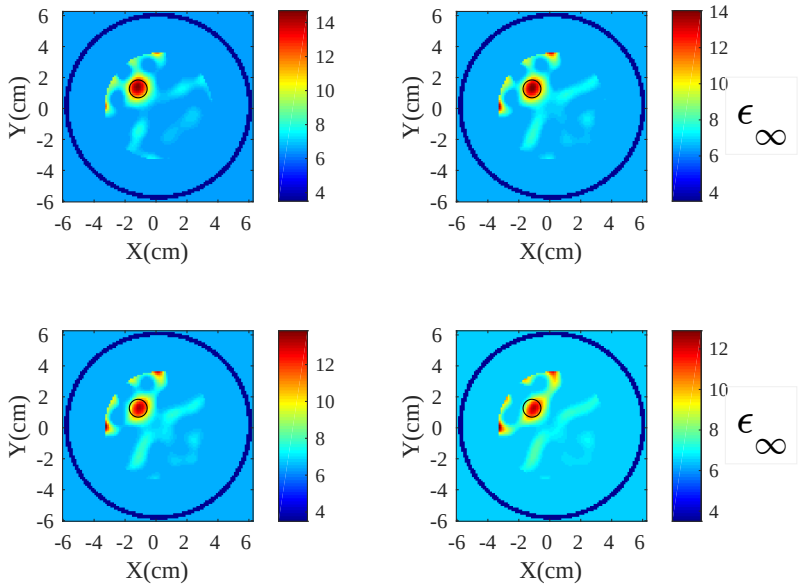

Fig. 6.34 Image reconstruction from 3D simulation data of the antenna array immersed in 90% glycerol background medium using DBIM TwIST algorithm at 1.6, 1.7, 1.8 and 1.9 GHz. Array diameter is 130 mm.

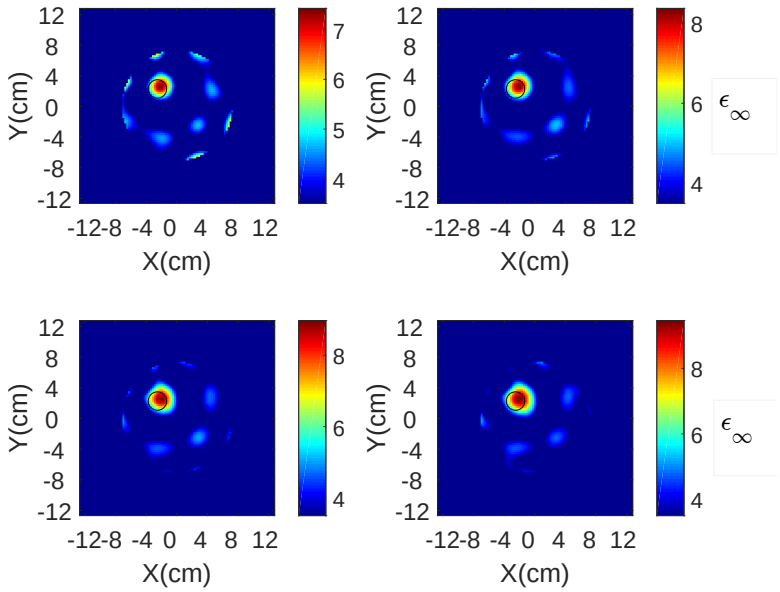

Fig. 6.35 Image reconstruction from 3D simulation data of the antenna array immersed in Triton x-100 background medium using DBIM TwIST algorithm at 1.7, 1.8, 1.9 and 2 GHz.

In Fig. 6.34 we show dielectric reconstruction of the imaging domain where we use 90% glycerol background medium and water as high dielectric scatterer. Each subplot represents reconstruction at a distinct frequency, from left to right 1.6 to 1.9 GHz at a step of 0.1 GHz.

Fig. 6.35 shows the reconstruction results when Triton x-100 is used as the background material for the system with eight antennas. Our DBIM TwIST algorithm successfully detects and localizes the target we introduced in Triton x-100 background. Moreover, the four subplots, from left to right shown in Fig. 6.35 show the reconstruction in four different frequencies i.e. 1.7, 1.8, 1.9 and 2 GHz respectively. Successful reconstruction is achieved at the operational frequency band of our antenna i.e 1.7 to 3 GHz (simulated). The images shown in Fig. 6.35 are obtained from reconstruction of infinity permittivity ε_∞ of the dielectric medium.

Fig. 6.36 depicts the reconstruction results from the case when antenna array is immersed in 90% corn syrup. The reconstruction shown in Fig. 6.36 represents ε_∞ at frequencies from 2.5 to 2.8 GHz at a step of 0.1 GHz from left to right.

Fig.6.37 represents reconstruction at 1 to 1.3 GHz when the antenna array is immersed in 80% glycerol. We observe that better reconstruction occurs at lower frequencies, the images shown in Fig.6.37 are reconstructed at 1 to 1.3 GHz from left to right. We observe that as the frequency goes higher the image quality also becomes poorer.

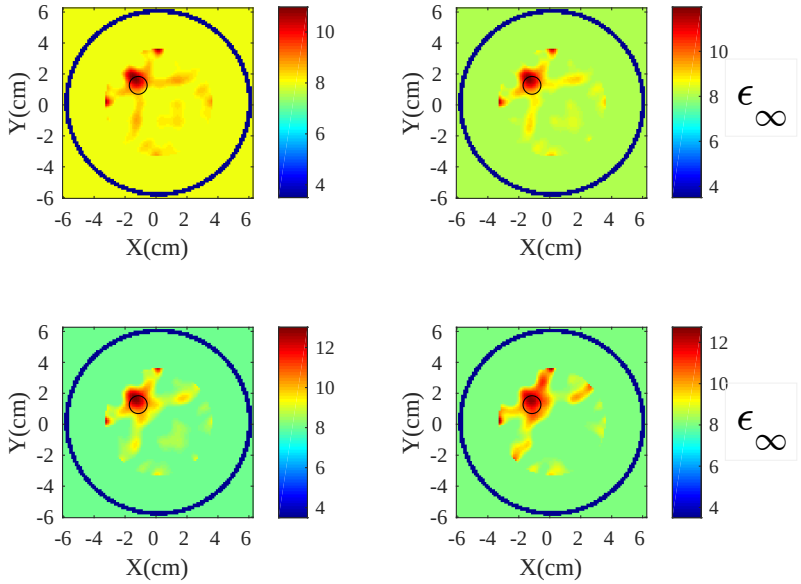

Fig. 6.36 Image reconstruction from 3D simulation data of the antenna array immersed in 90% corn syrup background medium using DBIM TwIST algorithm. Array diameter is 130 mm.

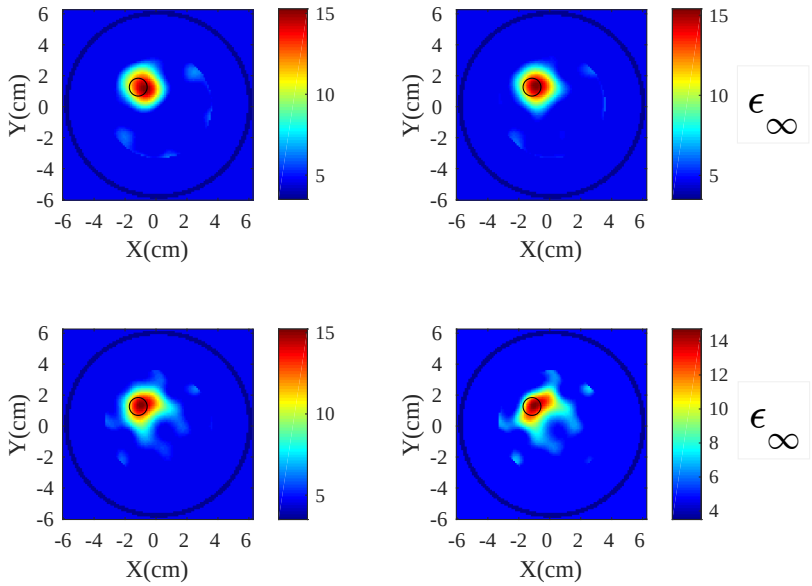

Fig. 6.37 Image reconstruction from 3D simulation data of the antenna array immersed in 80% glycerol background medium using DBIM TwIST algorithm at 1, 1.1, 1.2 and1.3 GHz.

Results of reconstruction from 3D simulations of the two layer phantom are shown in the following figures. We start with the reconstruction of two layer phantom comprised of 90% corn syrup as immersion and safflower oil as low loss medium. Image reconstruction is presented for 130 mm array diameter case with water target. Fig. 6.38 shows reconstructed images at 1.4, 1.5, 1.6 and 1.7 GHz.

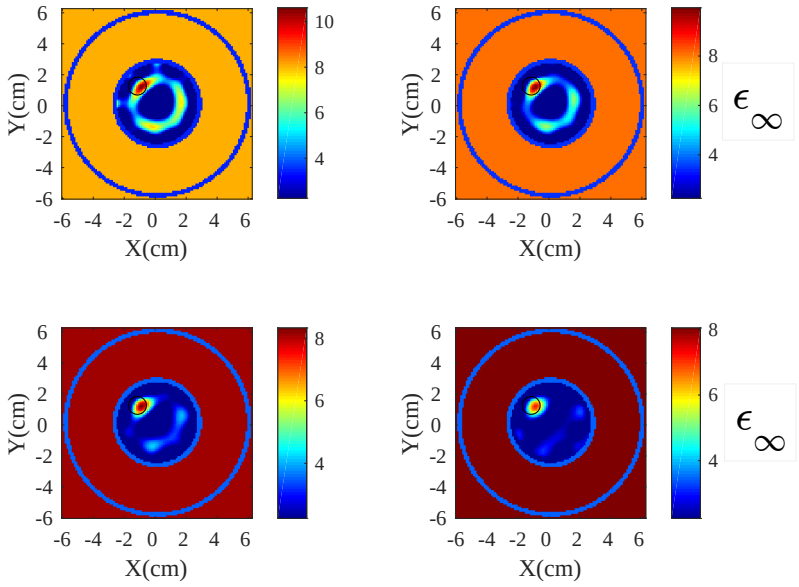

Fig. 6.38 Image reconstruction from simulation data of the antenna array immersed in 90% corn syrup two layer phantom using DBIM TwIST algorithm at 1.4, 1.5, 1.6 and 1.7 GHz. Array diameter is 130 mm.

Signal attenuation has been a constraint in acquiring experimental data when we use high loss dielectric background media, thus we introduce the second layer of low loss medium inside the domain as described before. Finally we present reconstruction from the simulation data of two layer phantom comprised of 80% glycerol and safflower oil. Fig. 6.39 shows the successful reconstruction of the imaging domain where we observe best images at 1.4 to 1.7 GHz.

6.6.2 Reconstruction Results from Experimental Data

We use the data acquired from our in-house prototype presented in section 6.3 of this Chapter. Fig.6.40 shows reconstruction from the data obtained from our prototype when antenna array is immersed in 90% glycerol and a water target is introduced. Signal propagation analysis of

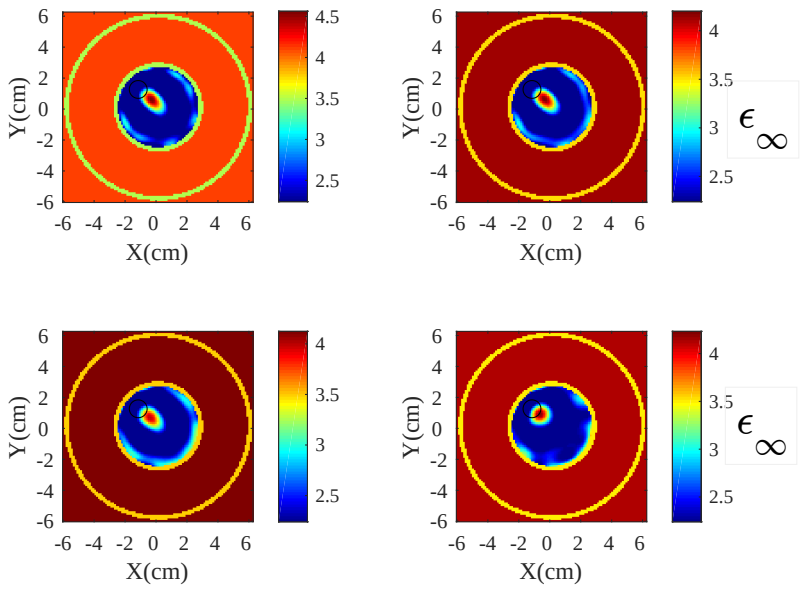

Fig. 6.39 Image reconstruction from simulation data of the antenna array immersed in 80% glycerol two layer phantom using DBIM TwIST algorithm at 1.5, 1.6, 1.7 and 1.8 GHz. Array diameter is 130 mm.

the same geometry is presented in section 6.7, here we present results of reconstruction at the same frequencies we used earlier in the reconstruction with CST simulation data. We observe that there is a complete agreement between the two results i.e. we successfully reconstruct experimental data from 1.6 GHz to 1.9 GHz.

Fig.6.41 shows reconstruction from the experimental data obtained from two layer phantom setup. Antenna array of 130 mm is immersed in 90% glycerol and target is inserted in safflower oil layer of the two layer phantom. Images presented in Fig. 6.41 are reconstructed at 1.5, 1.6, 1.7 and 1.8 GHz.

We present reconstruction results of the two layer phantom medium for 90% corn syrup and safflower oil when the antenna array diameter is 130 mm. Fig. shows reconstruction result of this scenario from 2 to 2.3 GHz. Similar study in the CST 3D simulations yielded the very similar results as depicted in Fig.6.41 albeit a little more clearer than the experimental results.

80% glycerol is the most lossy liquid as compared to all the other media we have studied, therefore in order to capture useful information from the imaging domain comprised of 80% glycerol as background medium we had to not only reduce diameter of the array but also

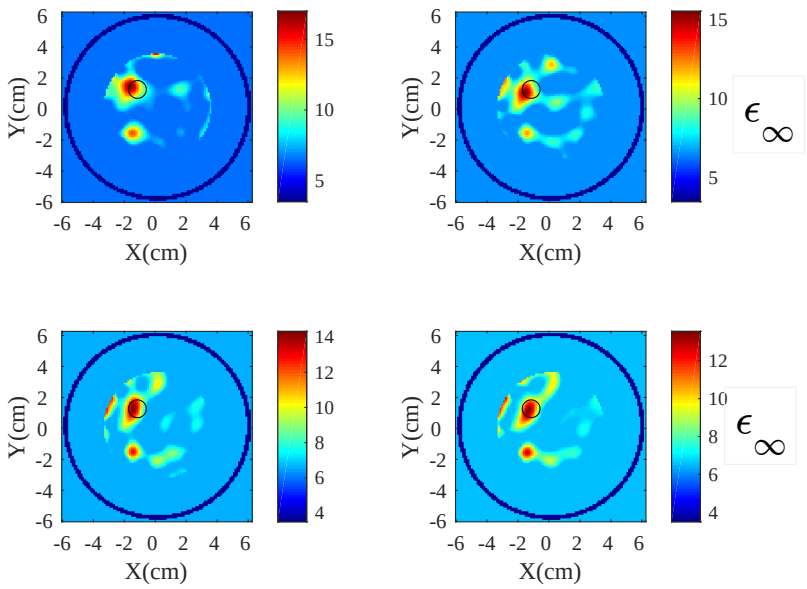

Fig. 6.40 Image reconstruction from experimental data of the antenna array immersed in 90% glycerol background medium using DBIM TwIST algorithm at 1.6, 1.7, 1.8 and 1.9 GHz. Array diameter is 130 mm.

introduce a low loss medium layer. Resulting image reconstruction with single frequency reconstruction method is shown in Fig.6.42

6.7 Frequency Selection for Reconstruction

In the preceding section we have presented some reconstruction results at few frequencies, for example with 90% corn syrup immersion medium in our two layer phantom setup we show reconstruction results at 1.5, 1.6, 1.7 and 1.8 GHz as shown in Fig. 6.41. Signal differences in dB for the same setup (with target minus without target) are shown in Fig. 6.28. Differences plots reveal that there is significant variation in the dB levels of transmitted gain when a high dielectric target is introduced. However, we do not achieve good reconstruction results at all frequencies.

Our colleague, Zhenzhuang Miao, from algorithm development for microwave tomography proposes a frequency selection method that works on the principle of correlation between the frequency samples of the differences in dB values data. We will apply his concept on our measured data to understand how reconstruction results are affected by frequency correlation. As before, we subtract 'with target' data from 'without target' case to find

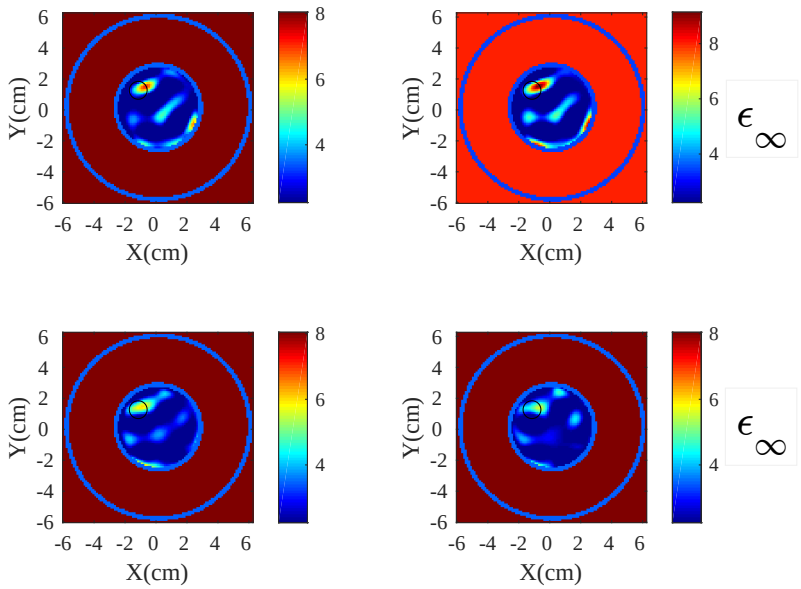

Fig. 6.41 Image reconstruction from experimental data of the antenna array immersed in 90% corn syrup two layer phantom using DBIM TwIST algorithm t 2, 2.1, 2.2 and 2.3 GHz. Array diameter is 130 mm.

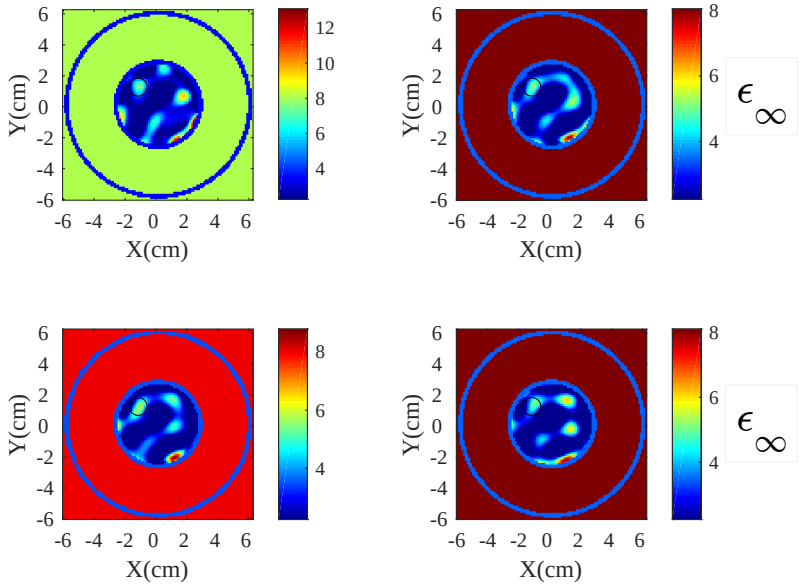

Fig. 6.42 Image reconstruction from experimental data of the antenna array immersed in 80% glycerol two layer phantom using DBIM TwIST algorithm. Array diameter is 130 mm.

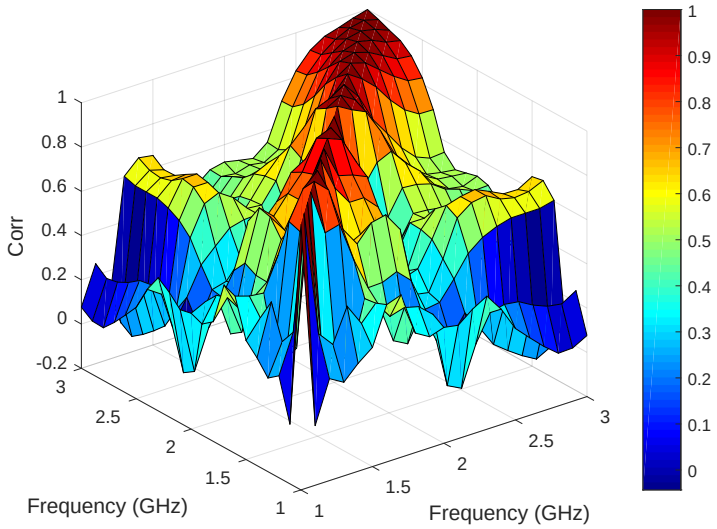

Fig. 6.43 3D Correlation map between the frequency samples of differences in dB data when with target data is subtracted from no target case for 90% corn syrup two layer phantom setup. Array diameter is 130 mm.

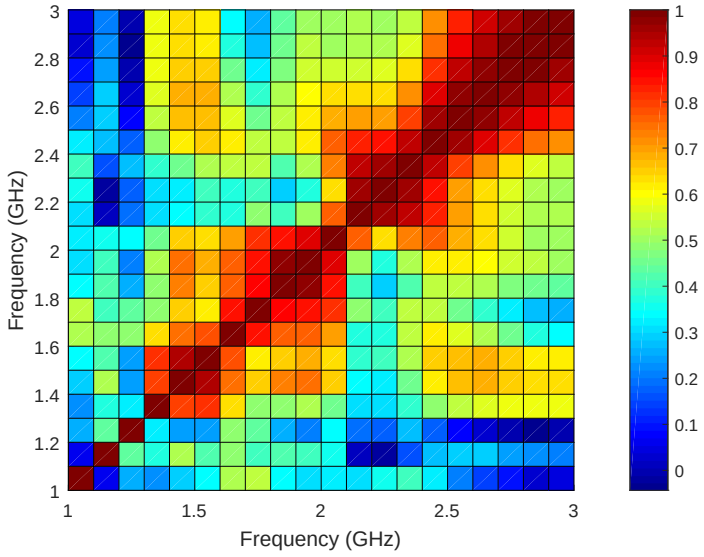

Fig. 6.44 2D Correlation map between the frequency samples of differences in dB data when with target data is subtracted from no target case for 90% corn syrup two layer phantom setup. Array diameter is 130 mm.

this difference in dB. Figures 6.43 and 6.44 show correlation maps between the frequency samples of aforementioned 'difference' data. Strong correlation is observed between higher frequency samples whereas at lower frequencies we do not observe good correlation between frequencies. We suggest that when there is strong correlation between the frequency samples those frequencies are more likely to yield good reconstruction results. We plot differences

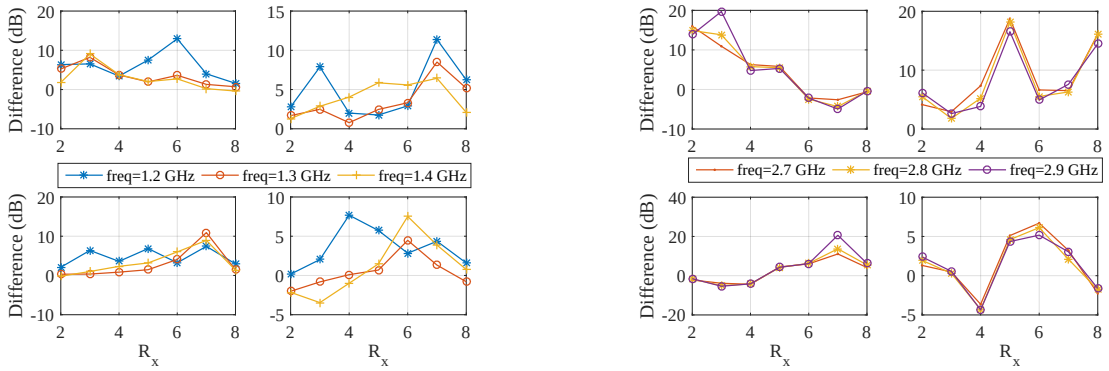

(a) (b)

Fig. 6.45 Differences between the signal levels in dBs for 130 mm eight antenna array immersed in 90% corn syrup of two layer phantom setup with second layer of safflower oil (a) frequency samples with low correlation (b) frequency samples with high correlation.

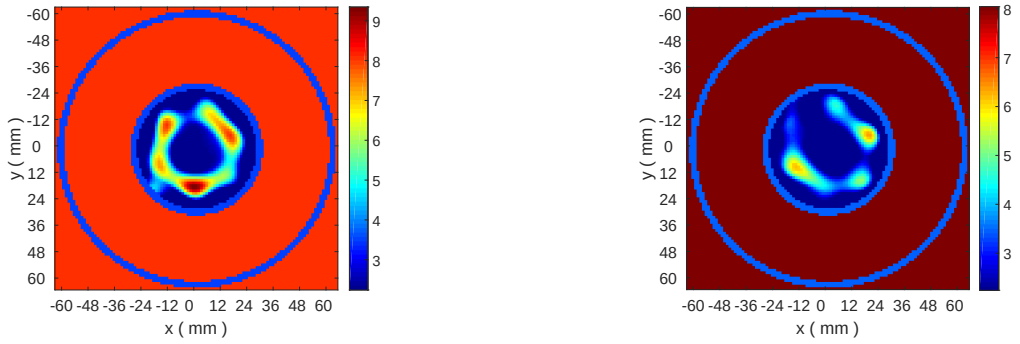

(a) (b)

Fig. 6.46 Results of reconstruction when frequencies are not correlated for 130 mm array immersed in two layer phantom setup of 90% corn syrup and safflower oil, at (a) 1.3 GHz (b) 1.4 GHz

data for the frequencies where low and high level of correlation is observed as shown in Fig. 6.44. We select 1.2, 1.3 and 1.4 GHz frequency samples to represent low correlation data and 2.7, 2.8 and 2.9 GHz for highly correlated frequency samples. We plot differences

data for four transmitters (1 to 4) at the aforementioned frequency samples. Fig. 6.45 (a) depicts differences plots for the frequency samples showing low correlation while Fig. 6.45 (b) shows the difference data of highly correlated frequencies. It is quite clear from Fig. 6.45 (a) and (b) that differences plots for low correlation case have inconsistent trends of the curves whereas for 2.7, 2.8 and 2.9 GHz the trends of differences plots is very similar.

Fig. 6.46 shows the reconstructed images at low frequencies where we observe low correlation between frequency samples. Fig. 6.47 shows reconstruction of images from highly correlated frequency samples. We observe that the dielectric profile of interior of the imaging domain has not been reconstructed successfully at low 1.3 and 1.4 GHz, artefacts have been observed in both cases. For 2.8 and 2.9 GHz, where high correlation without artefacts has been observed successful reconstruction of the target has been achieved. The target has successfully been reconstructed and localized.

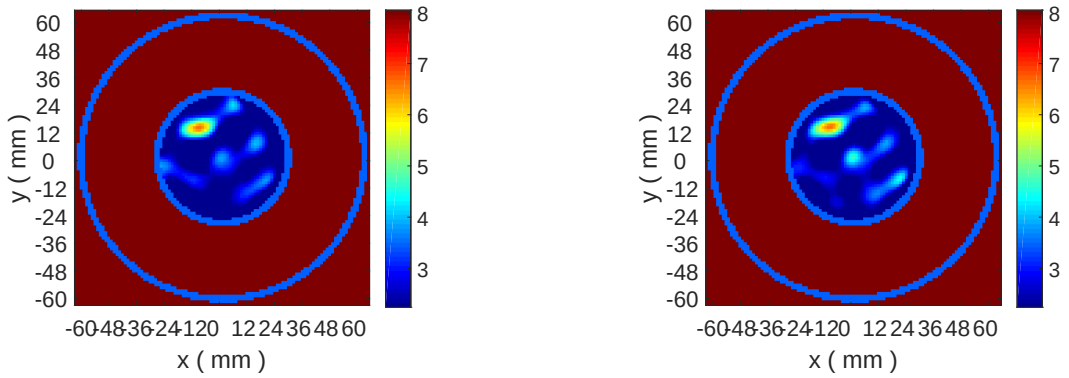

Fig. 6.47 Results of reconstruction when frequencies are highly correlated for 130 mm array immersed in two layer phantom setup of 90% corn syrup and safflower oil, at (a) 2.8 GHz (b) 2.9 GHz.

If we refer back to our correlation maps of Fig. 6.44 we realise that correlation coefficient for the two specific frequency samples shown in Fig. 6.46 i.e 1.3 and 1.4 GHz is below 30% for 1.3 GHz and below 60% at 1.4 GHz. The correlation coefficient, however, for the frequency samples shown in Fig. 6.47 i.e 2.8 and 2.9 GHz, is in the range of 90% and therefore we have better reconstruction results at these frequencies. Thus, we conclude that if the frequency show high correlation then we can obtain high quality images.

6.8 Conclusion

We have studied two types of data acquisition systems. We presented results from our rotating chamber bi-static mechanical system. We used 80% glycerol and Triton x-100 as immersion media in the first set of experiments. Dynamic range of the VNA did not allow us to pursue working with 80% glycerol due to signals below noise floor at 1.3 GHz and above. We collected data with Triton x-100 as background and considered various scenarios for introducing target in the imaging domain. We used different materials and locations for target. We also introduced fibroglandular mimic in the imaging domain and studied performance of the system by introducing target inside and outside of fibroglandular. Results obtained from the experiments with rotary mechanism suffer from significant errors, we identify physical positioning of the chamber and antennas as a significant source of error, thus we design our new system with a special focus on mitigating these errors in our design consideration. We implemented robust mechanism for positioning and adjusting antenna array, target and imaging chamber accurately and precisely in our system.

We analysed signal propagation through our proposed hardware prototype for data acquisition. We demonstrated the impact of different media and target on signal propagation using experimental data. We continued our study to propose the solution to get around the problem of weaker signals which are difficult to detect using our hardware by introducing a low loss material layer into our system. We also study the impact of scattering for large (150 mm) and small (130 mm) array diameters. We performed physical experiments to acquire experimental data and then performed analysis on the acquired data. Finally we validated our system by applying the inverse imaging algorithm to our acquired data both experimentally and numerically. We proposed a frequency selection method to select suitable frequency samples for better reconstruction by using the correlation between different frequency samples of the ‘difference’ data obtained from subtracting with target case from the homogeneous background case.

Chapter 7

Conclusion and Future Work

7.1 Conclusion

The work presented in this thesis is a first step towards building a microwave tomography system at King's College London. The goal was to address the key challenges being faced in microwave tomography such as penetration depth and image resolution. We successfully designed and implemented a very simple hardware prototype for microwave tomography that can be used for medical imaging.

We have presented various antenna designs for tomography application. Our objective was to design a compact and robust antenna suitable for microwave tomography frequency range. We optimized dual band patch antenna in low loss immersion medium. We studied balanced antipodal Vivaldi antenna BAVA for microwave tomography application. Initially our goal was to optimize the antennas in free space for our ergonomic microwave tomography system design in sight. We optimized dimension parameters of Vivaldi antenna to achieve low frequency operation, 1-3 GHz. Subsequently, we introduced a matching circuit to optimize our Vivaldi antenna for low frequency operation, as our first effort resulted in large physical structure of the antenna. Vivaldi antenna with passive matching lumped elements was found to be inefficient and despite exhbiting low frequency matching at 1 GHz, no substantial radiation was achieved at low frequency range, prompting to spurious modes the these frequencies. Subsequently, we progressed towards designing an antenna that can operate in front of a coupling medium to address the challenge of antenna matching with biological tissues (skin in most medical imaging applications). We optimized V slot triangular patch antenna for this purpose. We also realized the design of our optimized V slot antenna, good agreement between simulation and experimental results was achieved. We also proposed a compact version of V slot antenna. V slot antenna showed good response at 1 and 3

GHz when operating in front of a suitable dielectric medium, such as 90% glycerol, for matching, however we continued our efforts to design a wideband antenna as opposed to multiband resonant antennas. Moreover, the size and weight of V slot antenna also did not completely comply with our vision of the tomography system. We also deigned a very simple and compact circular patch antenna resonant at 2.5 GHz in front of 90% glycerol. We studied monopole antennas in detail as they are being used by some prominent groups actively engaged in microwave tomography research. There are pros and cons attributed to the use of monopole antennas in microwave tomography systems, particularly with the length of these wire antennas that can pose the challenge of surface waves excitation. We propose our compact patch printed monopole antenna that operates in wideband between 1-3 GHz frequency range when immersed in suitable lossy immersion media, such as 80% , 90% glycerol solutions or 90% corn syrup. Our printed monopole antenna is also capable of operating in low loss medium such as Triton x-100 from 1.7 GHz and above. We realized our compact printed monopole and performed a detailed study using this antenna to finalise our microwave tomography prototype.

We studied performance of our antennas arranged in a form of an array. We started our study of arrays comprised of four antenna elements operating in front of dielectric filled tank. We studied the performance of arrays with and without high scattering target object in the said configuration, both numerically and experimentally. We modelled our simple four antenna array tomography system operating in front of a cuboid filled with different matching media in commercially available 3D electromagnetic CST Microwave Studio to carry out our simulation study. We prepared the phantoms (matching media) and measured them with probe kit using Agilent PNA series VNA and imported the data into CST microwave studio to model or phantoms numerically to incorporate them in our simulation model for best possible realistic modelling of the system under study. We performed the experimental study of our four element antenna arrays in front of dielectric media filled acrylic tank using multiport VNAs from Rohde and Schwarz and Agilent. Our simulation results in the above mentioned geometry did not yield good contrast and our experimental study posed many different challenges. Experimental and simulation results in the above mentioned configuration were not in agreement. Simulation results showed a difference of less than 2 dB with the inclusion of strong scatterer such as PEC. Thus we conclude that in order to obtain better quality data we must immerse the antenna array in a suitable immersion liquid.

We performed our analysis of immersed antenna arrays. We optimized the dimensions of imaging domain with monopole antenna array immersed in 80% glycerol. We studied signal propagation inside the imaging domain in various scenarios to understand the causes and

effects of degrading factors on signal propagation. We performed our simulation studies using CST microwave studio. We optimized the geometry of our imaging chamber for monopole antenna using CST simulations. We also studied the impact of introducing microwave absorber and metallic sheet to mitigate the degrading phenomena such as surface wave propagation, multipath signals and external interference. The system was thus optimized for the imaging chamber dimensions. We applied the optimized system model to evaluate our compact printed monopole antenna performance in immersed configuration.

Selection of a suitable coupling medium is very critical in designing a microwave tomography system. Coupling medium plays a vital role in optimizing the performance of system as well as on the overall cost of it. There is a trade off between signal attenuation and suppression of deteriorating factors which affect data integrity such as surface waves, multipath signals and interference etc. High loss coupling media attenuate the transmitted gain so much so that they might not be detected with non custom built transceiver systems with relatively low dynamic range as indicated in our studies with 80% glycerol as background media where the signal levels drop to -180 dB from our simulation studies. The use of low loss matching media leads to significant cross coupling between the array elements, surface waves excitation etc and consequently the received data is not a true representation of the imaging domain as it is plagued by unwanted signals as indicated in our study of low loss media as background. Moreover, matching media impact performance of the antenna significantly as we observed in our study of different matching media as background using our compact patch antenna. We have also presented impact of different scatterers on signal propagation to study the effect of contrast ratio on scattering.

Our first set of experimental data in the immersed configuration of antenna array was obtained by utilizing a rotary mechanism for data acquisition. We presented the results obtained using this setup in bi-static configuration and rotation of imaging chamber in this thesis. We concluded from our first set of experiments in immersed configuration that there is a need of more robust system which allows us to position the antennas, target and imaging chamber in more robust and precise fashion. Moreover, from our first set of immersed configuration experiments we concluded that 80% glycerol as a coupling medium using a network analyser does not provide useful data beyond 1.3 GHz as the signal level drops below the noise floor of the VNA. We collected our data from the rotary data acquisition system using Triton x-100 as immersion medium, however we found out that the data suffered from errors and lacked symmetry due to inaccuracies in data acquisition process.

Based upon the information we collected from our prior sets of physical experiments i.e. non immersed and immersed arrays using rotation of chamber, we concluded several

key points to improve data acquisition process and building a robust system for further experiments. We designed and realized a very simple and low cost microwave tomography system making use of the information learnt in this study. We presented complete design of our microwave tomography prototype in this thesis. We also presented the experimental data obtained using our hardware prototype in multistatic and bi-static antenna array configurations. High signal attenuation using lossy immersion media such as 80% glycerol proved to be the bottle neck in data acquisition (due to high attenuation of the signals), therefore, we proposed a two layer phantom to circumvent the issue of high attenuation and at the same time being able to exploit advantages of a high loss dielectric medium, such as suppression of degrading factors. We conducted several experiments and simulations using multilayer phantom configuration and observed that this new configuration enhances transmitted gain significantly. The increased signal transmission was observed both in our experimental as well as in simulation studies.

We applied our in-house DBIM based inversion algorithm on the simulation and experimental data. We presented the reconstruction maps of dielectric profile of the imaging domain after applying our in-house imaging algorithm on our acquired data set. We obtained good images for a variety of our experiments conducted using single layer as well as two layer phantoms. We also acquired good reconstruction results from our 3D simulation data. We observed that the reconstruction algorithm at some frequencies yielded better results than the others, based upon that information we also proposed a frequency selection method that works on the principal of correlation between different frequency datasets. The key conclusions of this study are given below:

- Several antennas have been optimized/designed in this study and it has been concluded that the printed monopole antenna due to its compact size, wideband performance (1-3 GHz) and robustness is a good candidate for the proposed system

- Non immersed and immersed antenna arrays have been studied numerically and experimentally, it has been demonstrated that immersed configuration of the antenna arrays helps mitigate the signal degrading factors such as coupling, multipath signals and surface waves propagation

- Matching media to be used in the imaging chamber have been studied extensively to understand the impact of background material dielectric properties (permittivity and conductivity) on energy coupling into the imaging domain and the reduction of unwanted propagation phenomena, 90% glycerol has been chosen as a coupling medium

for the proposed imaging system because of the trade-off between the reduction of signal degrading factors and realizable forward transmission levels

- Double layer phantom setup has been proposed to enhance the signal transmission by immersing antenna array in the high loss medium and adding inclusion (target) inside the low loss medium. Both experimental and numerical studies have revealed high signal transmission levels
- To minimize the experimental errors, a mechanically simple, robust and precise system has been proposed to cater for precise positioning of the antenna array elements and the target that allows us to take both bi-static as well as multi-static measurements
- 2D DBIM- TwIST algorithm [119, 120] has been applied to the numerical and experimental data to validate the system performance, good reconstruction results have been acquired for both studies

7.2 Future Work

We have faced various challenges in the design and implementation of our microwave tomography hardware system, some of them we have addressed in this thesis and the others we present as future work.

In our multi-static configuration we observe significant contribution of errors from cross coupling between the cables particularly at lower frequencies. Robust mechanism for cabling and potentially replacement cables with better isolation can rectify the coupling issue.

We have used a two port network analyser to collect our experimental data. In the future a multi-port transceiver system or a switch matrix can be used for data acquisition which in turn will prove to mitigate the errors induced due to erroneous positioning of antennas while manually moving them to capture different views of the imaging domain.

Receiver sensitivity has found to be a constraint while using high loss coupling media. A transceiver system with higher dynamic range can mitigate the detection challenge of attenuated signal levels below typical VNA range of -90 dB noise floor.

More realistic phantoms with skin layer can be incorporated in the experiments to gain closer dataset to the requirement of real system. Fibroglandular content can be added to the phantom and experiments can be repeated for lower contrast scenarios. Also, contrast agents can be introduced in the study of low contrast scenarios, such as phantoms with fibroglandualr content, to gain and understanding of the impact of contrast agents on overall system sensitivity.

We can also make modifications in the dimensions of our imaging system. Larger chamber provides the flexibility of manoeuvring the antenna array position with respect to borders of the tank such as side walls, tank floor and surface of immersion interface with surroundings, which can be critical for suppressing undesired signal propagation.

In order to apply our 3D algorithms for image reconstruction the hardware design will have to be modified. Multiple rings of antenna arrays will be introduced to collect data at different heights. In order to implement the multi-ring topology we will have to extend the cylindrical chamber in vertical axis. Multiple ring topology will also give rise to more complex cabling issue as there will be an increased number of cables, which in turn will pose coupling issues. The system will have to be engineered to minimize the coupling effects. Semi rigid cables can be used to maintain the orientation of the cables such that the coupling effects are minimum and measurements are repeatable.

References

[1] S. Michaelson and J. C. Lin, *Biological Effects and Health Implications of Radio-Frequency Radiation*. New York: Plenum, 1987.

[2] J. Thuery, *Microwaves—Industrial, Scientific and Medical Applications*. Norwood, MA: Artech House, 1992.

[3] C. Polk and E. Postow, *Handbook of Biological Effects of Electromagnetic Fields*. Boca Raton, FL: CRC Press, 1996.

[4] J. W. Strohbehn and E. B. Douple, "Hyperthermia and cancer therapy: A review of biomedical engineering contributions and challenges," *IEEE Trans. Biomed. Eng.*, vol. BME-31, no. 12, pp. 779–787, Dec 1984.

[5] K. L. Carr, "Microwave radiometry: its importance to the detection of cancer," *IEEE Trans. Microw Theory Tech.*, vol. 37, no. 12, pp. 1862–1869, Dec 1989.

[6] M. Mallory, E. Gogineni, G. C. Jones, L. Greer, and C. B. Simone, "Therapeutic hyperthermia: The old, the new, and the upcoming," *Critical Reviews in Oncology/Hematology*, vol. 97, pp. 56 – 64, 2016.

[7] A. Rosen, M. A. Stuchly, and A. V. Vorst, "Applications of rf/microwaves in medicine," *IEEE Trans. Microw. Theory Tech.*, vol. 50, no. 3, pp. 963–974, Mar 2002.

[8] W.H.O. (2017) Cancer statistics. [Online]. Available: http://www.who.int/mediacentre/factsheets/fs297/en/

[9] J. L. Schepps and K. R. Foster, "The UHF and microwave dielectric properties of normal and tumor tissues: Variation in dielectric properties with tissue water content," *Phys. Med. Biol.*, vol. 25, no. 6, pp. 1149–1159, Nov 1980.

[10] D. Kissinger and J. C. Chiao, "Medical applications of radio-frequency and microwaves-sensing, monitoring, and diagnostics [from the guest editors' desk]," *IEEE Microwave Magazine*, vol. 16, no. 4, pp. 34–38, May 2015.

[11] L. E. Larsen and J. H. Jacobi, "Medical applications of microwave imaging," DTIC Document, Tech. Rep., 1985.

[12] L. E. Larsen and J. Jacobi, "Microwave interrogation of dielectric targets. Part i: by scattering parameters," *Med. Phys.*, vol. 5, no. 6, pp. 500–508, 1978.

[13] J. H. Jacobi and L. E. Larsen, "Microwave interrogation of dielectric targets. Part II: by microwave time delay spectroscopy," *Med. Phys.*, vol. 5, no. 6, pp. 509–513, 1978.

[14] L. Sha, E. R. Ward, and B. Stroy, "A review of dielectric properties of normal and malignant breast tissue," in *Proceedings IEEE SoutheastCon 2002 (Cat. No.02CH37283)*, 2002, pp. 457–462.

[15] R. Pethig, "Dielectric properties of biological materials: Biophysical and medical applications," *IEEE Trans. Electr. Insul.*, vol. EI-19, no. 5, pp. 453–474, Oct 1984.

[16] M. Lazebnik, M. Okoniewski, J. H. Booske, and S. C. Hagness, "Highly accurate debye models for normal and malignant breast tissue dielectric properties at microwave frequencies," *IEEE Microw. Wireless Comp. Lett.*, vol. 17, no. 12, pp. 822–824, Dec 2007.

[17] K. R. Foster and H. P. Schwan, "Dielectric properties of tissues and biological materials: a critical review." *CRC Crit. Rev. Biomed. Eng.*, vol. vol. 17, no. no. 1, pp. pp. 25–104, 1988.

[18] C. Gabriel, S. Gabriel, and E. Corthout, "The dielectric properties of biological tissues: I. literature survey," *Phys. Med. Biol*, vol. vol. 41, no. no. 11, p. 2231, 1996.

[19] S. Gabriel, R. W. Lau, and C. Gabriel, "The dielectric properties of biological tissues: Iii. parametric models for the dielectric spectrum of tissues," *Phys. Med. Biol.*, vol. vol. 41, no. no. 11, p. 2271, 1996.

[20] S. S. Chaudhary, R. K. Mishra, A. Swarup, and J. M. Thomas, "Dielectric properties of normal & malignant human breast tissues at radiowave & microwave frequencies." *Indian J. Biochem. & Biophys.*, vol. 21, no. 1, p. 76, 1984.

[21] A. J. Surowiec, S. S. Stuchly, J. R. Barr, and A. Swarup, "Dielectric properties of breast carcinoma and the surrounding tissues," *IEEE Trans. Biomed. Eng.*, vol. 35, no. 4, pp. 257–263, 1988.

[22] A. M. Campbell and D. V. Land, "Dielectric properties of female human breast tissue measured in vitro at 3.2 ghz," *Phys. Med.Biol.*, vol. 37, no. 1, p. 193, 1992.

[23] W. T. Joines, Y. Zhang, C. Li, and R. L. Jirtle, "The measured electrical properties of normal and malignant human tissues from 50 to 900 mhz," *Med. Phys.*, vol. 21, no. 4, pp. 547–550, 1994.

[24] M. Lazebnik, L. McCartney, D. Popovic, C. B. Watkins, M. J. Lindstrom, J. Harter, S. Sewall, A. Magliocco, J. H. Booske, M. Okoniewski *et al.*, "A large-scale study of the ultrawideband microwave dielectric properties of normal breast tissue obtained from reduction surgeries," *Phys. Med. Biol.*, vol. 52, no. 10, p. 2637, 2007.

[25] M. Lazebnik, D. Popovic, L. McCartney, C. B. Watkins, M. J. Lindstrom, J. Harter, S. Sewall, T. Ogilvie, A. Magliocco, T. M. Breslin *et al.*, "A large-scale study of the ultrawideband microwave dielectric properties of normal, benign and malignant breast tissues obtained from cancer surgeries," *Phys. Med. Biol.*, vol. 52, no. 20, p. 6093, 2007.

[26] A. Mashal, J. H. Booske, and S. C. Hagness, "Toward contrast-enhanced microwave-induced thermoacoustic imaging of breast cancer: An experimental study of the effects of microbubbles on simple thermoacoustic targets," *Phy. Med. Biol.*, vol. 54, no. 3, p. 641, 2009.

[27] A. Mashal, B. Sitharaman, X. Li, P. K. Avti, A. V. Sahakian, J. H. Booske, and S. C. Hagness, "Toward carbon-nanotube-based theranostic agents for microwave detection and treatment of breast cancer: enhanced dielectric and heating response of tissue-mimicking materials," *IEEE Trans. Biomed. Eng.*, vol. 57, no. 8, pp. 1831–1834, 2010.

[28] G. Bellizzi, O. M. Bucci, and I. Catapano, "Microwave cancer imaging exploiting magnetic nanoparticles as contrast agent," *IEEE Trans. Biomed. Eng.*, vol. 58, no. 9, pp. 2528–2536, 2011.

[29] C. Pichot, L. Jofre, G. Peronnet, and J.-C. Bolomey, "Active microwave imaging of inhomogeneous bodies," *IEEE Trans. Antennas and Propag.*, vol. 33, no. 4, pp. 416–425, 1985.

[30] J. D. Shea, P. Kosmas, S. C. Hagness, and B. D. Van Veen, "Three-dimensional microwave imaging of realistic numerical breast phantoms via a multiple-frequency inverse scattering technique," *Medical Physics*, vol. 37, no. 8, pp. 4210 – 4226, 8 2010.

[31] Z. Miao and P. Kosmas, "Microwave breast imaging based on an optimized two-step iterative shrinkage/thresholding method," in *9th European Conf. on Antennas and Propag. (EuCAP)*, 2015.

[32] D. Li, P. M. Meaney, S. A. Pendergrass, M. W. Fanning, and K. D. Paulsen, "Parallel-detection microwave spectroscopy system for breast imaging," *Rev. Sci. Instrum.*, vol. 75, no. 7, pp. 2305–2313, Jul 2004.

[33] E. C. Fear, X. Li, S. C. Hagness, and M. A. Stuchly, "Confocal microwave imaging for breast cancer detection: localization of tumors in three dimensions," *IEEE Trans. Biomed. Eng.*, vol. 49, no. 8, pp. 812–822, Aug 2002.

[34] X. Yun, E. C. Fear, and R. H. Johnston, "Compact antenna for radar-based breast cancer detection," *IEEE Trans. Antennas Propag.*, vol. 53, no. 8, pp. 2374–2380, Aug 2005.

[35] H. Kanj and M. Popovic, "Microwave-range broadband "dark eyes" antenna: detailed analysis and design," *IEEE Antennas Wireless Propagat. Lett.*, vol. 4, pp. 262–265, 2005.

[36] H. Kanj and M. Popovic', "A novel ultra-compact broadband antenna for microwave breast tumor detection," *Progress In Electromagnetics Research*, vol. 86, pp. 169–198, 2008.

[37] X. Li, S. C. Hagness, M. K. Choi, and D. W. van der Weide, "Numerical and experimental investigation of an ultrawideband ridged pyramidal horn antenna with curved launching plane for pulse radiation," *IEEE Antennas Wireless Propagat. Lett.*, vol. 2, no. 1, pp. 259–262, 2003.

[38] R. K. Amineh, M. Ravan, A. Trehan, and N. K. Nikolova, "Near-field microwave imaging based on aperture raster scanning with tem horn antennas," *IEEE Trans. Antennas Propagat.*, vol. 59, no. 3, pp. 928–940, March 2011.

[39] J. Bourqui, M. Okoniewski, and E. C. Fear, "Balanced antipodal vivaldi antenna with dielectric director for near-field microwave imaging," *IEEE Trans. Antennas Propag.*, vol. 58, no. 7, pp. 2318–2326, 2010.

[40] D. Gibbins, M. Klemm, I. J. Craddock, J. A. Leendertz, A. Preece, and R. Benjamin, "A comparison of a wide-slot and a stacked patch antenna for the purpose of breast cancer detection," *IEEE Trans. Antennas Propag.*, vol. 58, no. 3, pp. 665–674, 2010.

[41] M. Klemm, I. J. Craddock, J. A. Leendertz, A. Preece, and R. Benjamin, "Radar-based breast cancer detection using a hemispherical antenna array 2014;experimental results," *IEEE Trans. Antennas Propagat.*, vol. 57, no. 6, pp. 1692–1704, June 2009.

[42] R. Nilavalan, I. J. Craddock, A. Preece, J. A. Leendertz, and R. Benjamin, "Wideband microstrip patch antenna design for breast cancer tumour detection," *IET Microwaves, Antennas Propagat.*, vol. 1, no. 2, pp. 277–281, April 2007.

[43] A. M. Abbosh, H. K. Kan, and M. E. Bialkowski, "Compact ultra-wideband planar tapered slot antenna for use in a microwave imaging system," *Microw. Opt. Technol. Lett.*, vol. 48, no. 11, pp. 2212–2216, 2006.

[44] E. Porter, A. Santorelli, M. Coates, and M. Popović, "An experimental system for time-domain microwave breast imaging," in *Proc. 5th European Conf. Antennas and Propagation (EUCAP)*, April 2011, pp. 2906–2910.

[45] M. Jalilvand, X. Li, J. Kowalewski, and T. Zwick, "Broadband miniaturised bow-tie antenna for 3d microwave tomography," *Electronics Lett.*, vol. 50, no. 4, pp. 244–246, February 2014.

[46] J. Zhang, E. C. Fear, and R. H. Johnston, "Cross-vivaldi antenna for breast tumor detection," *Microwave and Optical Technology Letters*, vol. 51, no. 2, pp. 275–280, 2009. [Online]. Available: http://dx.doi.org/10.1002/mop.24037

[47] M. A. Al-Joumayly, S. M. Aguilar, N. Behdad, and S. C. Hagness, "Dual-band miniaturized patch antennas for microwave breast imaging," *IEEE Antennas Wireless Propag. Lett.*, vol. 9, pp. 268–271, 2010.

[48] M. Ostadrahimi, P. Mojabi, S. Noghanian, L. Shafai, S. Pistorius, and J. LoVetri, "A novel microwave tomography system based on the scattering probe technique," *IEEE Transactions on Instrumentation and Measurement*, vol. 61, no. 2, pp. 379–390, Feb 2012.

[49] P. M. Meaney, M. W. Fanning, D. Li, S. P. Poplack, and K. D. Paulsen, "A clinical prototype for active microwave imaging of the breast," *IEEE Trans. on Microw. Theory and Tech.*, vol. 48, no. 11, pp. 1841–1853, 2000.

[50] C. Gilmore, P. Mojabi, A. Zakaria, M. Ostadrahimi, C. Kaye, S. Noghanian, L. Shafai, S. Pistorius, and J. LoVetri, "A wideband microwave tomography system with a novel frequency selection procedure," *IEEE Trans. Biomed. Eng.*, vol. 57, no. 4, pp. 894–904, April 2010.

[51] S. Y. Semenov, R. H. Svenson, A. E. Boulyshev, A. E. Souvorov, V. Y. Borisov, Y. Sizov, A. N. Starostin, K. R. Dezern, G. P. Tatsis, and V. Y. Baranov, "Microwave tomography: two-dimensional system for biological imaging," *IEEE Trans. Biomed. Eng.*, vol. 43, no. 9, pp. 869–877, 1996.

[52] M. R. Casu, M. Vacca, J. A. Tobon, A. Pulimeno, I. Sarwar, R. Solimene, and F. Vipiana, "A cots-based microwave imaging system for breast-cancer detection," *IEEE Trans. Biomed. Circuits Syst.*, vol. 11, no. 4, pp. 804–814, Aug 2017.

[53] D. A. Woten and M. El-Shenawee, "Broadband dual linear polarized antenna for statistical detection of breast cancer," *IEEE Trans. Antennas and Propag.*, vol. 56, no. 11, pp. 3576–3580, 2008.

[54] S. Y. Semenov, R. H. Svenson, A. E. Bulyshev, A. E. Souvorov, A. G. Nazarov, Y. E. Sizov, V. G. Posukh, A. Pavlovsky, P. N. Repin, A. N. Starostin, B. A. Voinov, M. Taran, G. P. Tatsis, and V. Y. Baranov, "Three-dimensional microwave tomography: initial experimental imaging of animals," *IEEE Transac. Biomed. Eng.*, vol. 49, no. 1, pp. 55–63, Jan 2002.

[55] G. Bindu, A. Lonappan, V. Thomas, K. Aanandan, and K. T. Mathew, "Dielectric studies of corn syrup for applications in microwave breast imaging," *Progress in Electromagnetics Research, PIER.*, vol. 59, pp. 175–186, 2016.

[56] C. Gilmore, A. Zakaria, J. LoVetri, and S. Pistorius, "A study of matching fluid loss in a biomedical microwave tomography system," *Med. Phys.*, vol. 40, no. 2, pp. 023 101–n/a, 2013, 023101. [Online]. Available: http://dx.doi.org/10.1118/1.4788640

[57] H.-S. Lui and A. Fhager, "On the matching medium for microwave-based medical diagnosis," *Biomed. Phys. & Eng. Express*, 2017. [Online]. Available: http://iopscience.iop.org/10.1088/2057-1976/aa8a89

[58] R. Scapaticci, L. D. Donato, I. Catapano, and L. Crocco, "A feasibility study on microwave imaging for brain stroke monitoring," *Progress In Electromagnetics Research B.*, vol. 40, pp. 305–324, 2012.

[59] I. Catapano, L. D. Donato, L. Crocco, O. M. Bucci, A. F. Morabito, T. Isernia, and R. Massa, "On quantitative microwave tomography of female breast," *Progress In Electromagnetics Research.*, vol. 97, pp. 75–93, 2009.

[60] W. C. Chew, *Waves and fields in inhomogeneous media*. IEEE press New York, 1995, vol. 522.

[61] P. M. Meaney, M. W. Fanning, T. Zhou, A. Golnabi, S. D. Geimer, and K. D. Paulsen, "Clinical microwave breast imaging—2d results and the evolution to 3d," in *International Conference on Electromagnetics in Advanced Applications, 2009. ICEAA'09.*, 2009, pp. 881–884.

[62] T. M. Grzegorczyk, P. M. Meaney, P. A. Kaufman, K. D. Paulsen *et al.*, "Fast 3-d tomographic microwave imaging for breast cancer detection," *IEEE Trans. Med. Imag.*, vol. 31, no. 8, pp. 1584–1592, 2012.

[63] A. E. Souvorov, A. E. Bulyshev, S. Y. Semenov, R. H. Svenson, and G. P. Tatsis, "Two-dimensional computer analysis of a microwave flat antenna array for breast cancer tomography," *IEEE Trans. Microw. Theory Tech.*, vol. 48, no. 8, pp. 1413–1415, 2000.

[64] A. E. Bulyshev, S. Y. Semenov, A. E. Souvorov, R. H. Svenson, A. G. Nazarov, Y. E. Sizov, and G. P. Tatsis, "Computational modeling of three-dimensional microwave tomography of breast cancer," *IEEE Trans. Biomed. Eng.*, vol. 48, no. 9, pp. 1053–1056, 2001.

[65] L. Sha, L. W. Nolte, Z. Q. Zhang, and Q. H. Liu, "Performance analysis for bayesian microwave imaging in decision aided breast tumor diagnosis," in *Proc. IEEE Intl. Symp. on Biomedical Imaging, 2002.*, 2002, pp. 1039–1042.

[66] P. M. Meaney, S. A. Pendergrass, M. W. Fanning, and K. D. Paulsen, "Importance of using a reduced contrast coupling medium in 2d microwave breast imaging," *J. Electromagn. Waves and Applicat.*, vol. 17, no. 2, pp. 333–355, 2003.

[67] G. N. Bindu, S. J. Abraham, A. Lonappan, V. Thomas, C. K. Aanandan, and K. T. Mathew, "Active microwave imaging for breast cancer detection," *Progress In Electromagn. Research*, vol. 58, pp. 149–169, 2006.

[68] M. Xu, A. Sabouni, P. Thulasiraman, S. Noghanian, and S. Pistorius, "Image reconstruction using microwave tomography for breast cancer detection on distributed memory machine," in *ICPP International Conf. on Parallel Processing, 2007.*, 2007, pp. 36–36.

[69] N. Irishina, O. Dorn, and M. Moscoso, "A level set evolution strategy in microwave imaging for early breast cancer detection," *Computers & Mathematics with Applications*, vol. 56, no. 3, pp. 607–618, 2008.

[70] M. Guardiola, S. Capdevila, S. Blanch, J. Romeu, and L. Jofre, "UWB high-contrast robust tomographic imaging for medical applications," in *Electromagnetics in Advanced Applications, 2009. ICEAA'09.*, 2009, pp. 560–563.

[71] J. D. Shea, P. Kosmas, S. C. Hagness, and B. D. Van Veen, "Three-dimensional microwave imaging of realistic numerical breast phantoms via a multiple-frequency inverse scattering technique," *Med. phys.*, vol. 37, no. 8, pp. 4210–4226, 2010.

[72] A. Diaz-Bolado, P. A. Barriere, and J. J. Laurin, "On the effect of breast compression and measurement setup configuration in microwave tomography for breast cancer detection," in *IEEE Intl. Symp. on Antennas and Propag. (APSURSI), 2011*, 2011, pp. 714–717.

[73] A. Diaz-Bolado, T. Henriksson, P. A. Barriere, H. Memarzadeh-Tehran, N. Joachimowicz, C. Conessa, A. Joisel, B. Duchêne, and J. C. Laurin, J. J.and Bolomey, "Towards a planar microwave tomography system for early stage breast cancer detection," in *General Assembly and Scientific Symp., 2011 XXXth URSI*, 2011, pp. 1–4.

[74] X. Zeng, A. Fhager, and M. Persson, "Effects of noise on tomographic breast imaging," in *General Assembly and Scientific Symp., 2011 XXXth URSI*, 2011, pp. 1–4.

[75] M. Xu, P. Thulasiraman, and S. Noghanian, "Microwave tomography for breast cancer detection on cell broadband engine processors," *J. Parallel and Distributed Computing*, vol. 72, no. 9, pp. 1106–1116, 2012.

[76] M. Haynes, J. Stang, and M. Moghaddam, "Microwave breast imaging system prototype with integrated numerical characterization," *J. Biomed. Imaging*, vol. 2012, p. 2, 2012.

[77] N. A. Simonov, S. Jeon, S. Son, J. Lee, and H. Kim, "3d microwave breast imaging based on multistatic radar concept system," in *3rd International Asia-Pacific Conference on Synthetic Aperture Radar (APSAR), 2011*, 2011, pp. 1–4.

[78] K. Kwon, Y. Lim, C. Kim, N. Kim, C. Park, K. Yoo, S. Son, and S. Jeon, "Microwave tomography analysis system for breast tumor detection," *Journal. Med. Sys.*, vol. 36, no. 3, pp. 1757–1767, 2012.

[79] A. Diaz-Bolado, P. A. Barriere, and J. J. Laurin, "Study of microwave tomography measurement setup configurations for breast cancer detection based on breast compression," *Intl. J. Antennas Propag.*, vol. 2013, 2013.

[80] N. R. Epstein, P. M. Meaney, and K. D. Paulsen, "3d parallel-detection microwave tomography for clinical breast imaging," *Rev. Sci. Instrum.*, vol. 85, no. 12, p. 124704, 2014.

[81] S. C. Hagness, A. Taflove, and J. E. Bridges, "Two-dimensional FDTD analysis of a pulsed microwave confocal system for breast cancer detection: Fixed-focus and antenna-array sensors," *IEEE Trans. Biomed. Eng.*, vol. 45, no. 12, pp. 1470–1479, 1998.

[82] M. Klemm, I. J. Craddock, J. A. Leendertz, A. Preece, and R. Benjamin, "Improved delay-and-sum beamforming algorithm for breast cancer detection," *Intl. J. Antennas and Propag.*, vol. 2008, 2008.

[83] E. J. Bond, X. Li, S. C. Hagness, and B. D. V. Veen, "Microwave imaging via space-time beamforming for early detection of breast cancer," *IEEE Trans. Antennas Propag.*, vol. 51, no. 8, pp. 1690–1705, Aug 2003.

[84] J. M. Sill and E. C. Fear, "Tissue sensing adaptive radar for breast cancer detection - experimental investigation of simple tumor models," *IEEE Trans. Microw. Theory Tech.*, vol. 53, no. 11, pp. 3312–3319, Nov 2005.

[85] P. Kosmas and C. M. Rappaport, "A matched-filter fdtd-based time reversal approach for microwave breast cancer detection," *IEEE Trans. Antennas and Propag.*, vol. 54, no. 4, pp. 1257–1264, 2006.

[86] T. Henriksson, M. Klemm, D. Gibbins, J. Leendertz, T. Horseman, A. W. Preece, R. Benjamin, and I. J. Craddock, "Clinical trials of a multistatic uwb radar for breast imaging," in *Loughbrough Antennas and Propagation Conf. (LAPC), 2011 Loughborough*. IEEE, 2011, pp. 1–4.

[87] J. Bourqui, J. Garrett, and E. Fear, "Measurement and analysis of microwave frequency signals transmitted through the breast," *Int. J. Biomed. Imaging*, vol. 2012, p. 1, 2012.

[88] R. A. Kruger, K. D. Miller, H. E. Reynolds, W. L. Kiser Jr, D. R. Reinecke, and G. A. Kruger, "Breast cancer in vivo: Contrast enhancement with thermoacoustic ct at 434 mhzâ€"feasibility study 1," *J. Radiol.*, vol. 216, no. 1, pp. 279–283, 2000.

[89] L. Nie, D. Xing, Q. Zhou, D. Yang, and H. Guo, "Microwave-induced thermoacoustic scanning ct for high-contrast and noninvasive breast cancer imaging," *Med. Phys.*, vol. 35, no. 9, pp. 4026–4032, 2008.

[90] M. Pramanik, G. Ku, C. Li, and L. V. Wang, "Design and evaluation of a novel breast cancer detection system combining both thermoacoustic (ta) and photoacoustic (pa) tomography," *Med. Phys.*, vol. 35, no. 6, pp. 2218–2223, 2008.

[91] Q. H. Liu, Z. Q. Zhang, T. Wang, J. A. Bryan, G. A. Ybarra, L. W. Nolte, and W. T. Joines, "Active microwave imaging. i. 2-d forward and inverse scattering methods," *IEEE Trans. Microw. Theory and Tech.*, vol. 50, no. 1, pp. 123–133, 2002.

[92] S. Y. Semenov, R. H. Svenson, A. E. Bulyshev, A. E. Souvorov, A. G. Nazarov, Y. E. Sizov, A. V. Pavlovsky, V. Y. Borisov, B. A. Voinov, G. I. Simonova *et al.*, "Three-dimensional microwave tomography: Experimental prototype of the system and vector born reconstruction method," *IEEE Tran. Biomed. Eng.*, vol. 46, no. 8, pp. 937–946, 1999.

[93] B. J. Mohammed, A. M. Abbosh, S. Mustafa, and D. Ireland, "Microwave system for head imaging," *IEEE Trans. Instrument. Meas.*, vol. 63, no. 1, pp. 117–123, Jan 2014.

[94] G. Ruvio, A. Cuccaro, R. Solimene, A. Brancaccio, B. Basile, and M. J. Ammann, "Microwave bone imaging: a preliminary scanning system for proof-of-concept," *Healthcare Tech. Lett.*, vol. 63, no. 1, pp. 117–123, May 2016.

[95] T. Henriksson, N. Joachimowicz, C. Conessa, and J. C. Bolomey, "Quantitative microwave imaging for breast cancer detection using a planar 2.45 ghz system," *IEEE Trans. Instrum. Meas.*, vol. 59, no. 10, pp. 2691–2699, Oct 2010.

[96] V. Zhurbenko, T. Rubaek, V. Krozer, and P. Meincke, "Design and realisation of a microwave three-dimensional imaging system with application to breast-cancer detection," *IET Microw. Antennas Propag.*, vol. 4, no. 12, pp. 2200–2211, December 2010.

[97] S. Caorsi, G. L. Gragnani, and M. Pastorino, "A multiview microwave imaging system for two-dimensional penetrable objects," *IEEE Trans. Microw. Theory Tech.*, vol. 39, no. 5, pp. 845–851, May 1991.

[98] M. Klemm, I. Craddock, J. Leendertz, A. Preece, and R. Benjamin, "Experimental and clinical results of breast cancer detection using uwb microwave radar," in *IEEE Antennas Propag. Int. Symp. AP-S 2008*, July 2008, pp. 1–4.

[99] E. C. Fear, S. C. Hagness, P. M. Meaney, M. Okoniewski, and M. A. Stuchly, "Enhancing breast tumor detection with near-field imaging," *IEEE Microw. Mag.*, vol. 3, no. 1, pp. 48–56, Mar 2002.

[100] I. Ünal, B. Türetken, K. Sürmeli, and C. Canbay, "An experimental microwave imaging system for breast tumor detection on layered phantom model," in *XXXth URSI General Assembly and Scientific Symp. 2011*, Aug 2011, pp. 1–4.

[101] E. Porter, H. Bahrami, A. Santorelli, B. Gosselin, L. A. Rusch, and M. Popović, "A wearable microwave antenna array for time-domain breast tumor screening," *IEEE Trans. Med. Imag.*, vol. 35, no. 6, pp. 1501–1509, June 2016.

[102] A. T. Mobashsher and A. M. Abbosh, "Developments of tomography and radar-based head imaging systems," in *Int. Symp. Antennas Propag. (ISAP) 2015*, Nov 2015, pp. 1–3.

[103] N. Joachimowicz, B. Duchêne, C. Conessa, and O. Meyer, "Reference phantoms for microwave imaging," in *11th European Conf. Antennas Propagat. (EUCAP), 2017*, March 2017, pp. 2719–2722.

[104] E. Porter, J. Fakhoury, R. Oprisor, M. Coates, and M. Popović, "Improved tissue phantoms for experimental validation of microwave breast cancer detection," in *Proc.4th European Conf. Antennas Propagat.*, April 2010, pp. 1–5.

[105] E. Porter, A. Santorelli, A. Bourdon, D. Coulibaly, M. Coates, and M. Popović, "Time-domain microwave breast cancer detection: Experiments with comprehensive glandular phantoms," in *Asia-Pacific Microwave Conf. 2011*, Dec 2011, pp. 203–206.

[106] Q. Fang, P. M. Meaney, and K. D. Paulsen, "Singular value analysis of the jacobian matrix in microwave image reconstruction," *IEEE Trans. Antennas Propag.*, vol. 54, no. 8, pp. 2371–2380, 2006.

[107] P. M. Meaney, F. Shubitidze, M. W. Fanning, M. Kmiec, N. R. Epstein, and K. D. Paulsen, "Surface wave multipath signals in near-field microwave imaging," *Int. J. Biomed. Imaging*, vol. 2012, p. 8, 2012.

[108] I. Craddock, "Wideband antennas for biomedical imaging," *Ultra Wideband Antennas and Propag. for Communications, Radar and Imaging*, p. 437, 2006.

[109] J. C. Maxwell, *A treatise on electricity and magnetism*. Clarendon press, 1881, vol. 1.

[110] G. Kumar and K. Ray, *Broadband Microstrip Antennas*, ser. Artech House antennas and propagation library. Artech House, 2003. [Online]. Available: https://books.google.co.uk/books?id=wfl84429CsEC

[111] S. Maci, G. B. Gentili, P. Piazzesi, and C. Salvador, "Dual-band slot-loaded patch antenna," *IEE Proc. - Microw. Antennas and Propag.*, vol. 142, no. 3, pp. 225–232, Jun 1995.

[112] S. Ahsan, B. Yeboah-Akowuah, P. Kosmas, H. C. Garcia, G. Palikaras, and E. Kallos, "Balanced antipodal vivaldi antenna for microwave tomography," in *4th International Conf. on Wireless Mobile Communication and Healthcare (Mobihealth)*. IEEE, 2014, pp. 316–319.

[113] S. Ahsan, P. Kosmas, I. Sotiriou, G. Palikaras, and E. Kallos, "Balanced antipodal vivaldi antenna array for microwave tomography," in *IEEE Conf. on Antenna Measurements & Applications (CAMA)*. IEEE, 2014, pp. 1–3.

[114] H. Dobšícek Trefná, J. Vrba, and M. Persson, "Evaluation of a patch antenna applicator for time reversal hyperthemia," *Intl. J. Hyperthermia*, vol. 26, no. 2, pp. 185–197, 2010.

[115] S. Ahsan, Z. Guo, I. Gouzouasis, E. Kallos, and P. Kosmas, *Development of a slotted triangular patch antenna for microwave tomography*. Institute of Electrical and Electronics Engineers Inc., 5 2016.

[116] B. Yeboah-Akowuah, "Novel antenna designs for body-centric applications," Ph.D. dissertation, King's College London, 2017.

[117] M. Ostadrahimi, P. Mojabi, C. Gilmore, A. Zakaria, S. Noghanian, S. Pistorius, and J. LoVetri, "Analysis of incident field modeling and incident/scattered field calibration techniques in microwave tomography," *IEEE Antennas Wireless Propagat. Lett.*, vol. 10, pp. 900–903, 2011.

[118] G. Ruvio, R. Solimene, A. D'Alterio, M. J. Ammann, and R. Pierri, "Rf breast cancer detection employing a noncharacterized vivaldi antenna and a music-inspired algorithm," *Int. J. RF and Microw. Computer-Aided Eng.*, vol. 23, no. 5, pp. 598–609, 2013. [Online]. Available: http://dx.doi.org/10.1002/mmce.20694

[119] Z. Miao and P. Kosmas, "Multiple-frequency dbim-twist algorithm for microwave breast imaging," *IEEE Transac. Antennas Propagat.*, vol. 65, no. 5, pp. 2507–2516, May 2017.

[120] Z. Miao, "Implementation and optimisation of microwave medical imaging based on the multiple-frequency dbim-twist algorithm," Ph.D. dissertation, King's College London, 2017.

[121] Z. Miao, S. Ahsan, P. Kosmas, J. A. T. Vasquez, F. Vipiana, M. R. Casu, and M. Vacca, "Application of the dbim-twist algorithm to experimental microwave imaging data," in *2017 11th European Conf. on Antennas and Propag. (EUCAP)*, March 2017, pp. 1611–1614.

Acronyms

3D Three Dimensional. 46

BAVA Balanced Antipodal Vivaldi Antenna. 24

BPH Benign Prostatic Hypertrophy. 1

CST Computer Simulation Technology. 25, 38, 46

EM Electromagnetic. 46

GPR Ground Penetrating Radar. 2

MNM Multiport Network Model. 20

MRI Magnetic Resonance Imaging. 3

MT Microwave Tomography. 3

MWS Microwave Studio. 25

PEC Perfect Electric Conductor. 48

RCS Radar Cross Section. 2

UWB Ultra WideBand. 7

VNA Vector Network Analyzer. 53

VSWR Voltage Standing Wave Ratio. 41

WHO World Health Organization. 2

Appendix A

Computer Simulation Technology (CST®) Software

CST microwave studio is an ACIS modelling kernel based GUI software package for electromagnetic analysis and design in the high frequency range. It applies a fully automatic meshing to the model before starting a simulation engine. The software contains different simulation techniques depending on the specific application. Time domain, frequency domain, integral equation, multilayer, asymptotic and eigenmode solvers are the examples of application specific techniques offered in the CST software package.

Each of these methods supports meshing types best suited for its simulation technique. To enhance the accuracy of a conventional hexahedral mesh advanced techniques such as Perfect Boundary Approximation (PBA) ® and Thin sheet Technique (TST)® can be be combined with the hexahedral mesh. The package also offers frequency domain and eigenmode solvers that support linear and curved tetrahedral meshing.

Time domain solvers are based on Finite Integration Technique (FIT) offer the largest simulation flexibility. Entire broadband behaviour of the simulation device can be obtained in one run using time domain solver. However, time domain solvers are less efficient for structures that are electrically much smaller than the shortest wavelength of interest. Use of frequency domain solver is advantageous in such cases. Frequency domain solver is also a preferred method of choice when use of unstructured tetrahedral mesh is advantageous to resolve very small geometric details.

FIT was first presented in 1977 by Prof. Thomas Weiland (TU Darmstadt). FIT is used in CST® Microwave Studio is a numerical simulation method for approximation-free solutions of Maxwell's equations in their integral form for complex geometries. The resulting matrix equations of the discretized fields can be used for efficient numerical simulations. In

addition, the basic algebraic properties of this discrete electromagnetic field theory allow to analytically and algebraically prove conservation properties with respect to energy and charge of the discrete formulation and gives an explanation of the stability properties of numerical formulations in the time domain.

FIT is a two step discretization process. The first step involves confinement of an open boundary electromagnetic field problem to a simply connected bounded space, region of interest. The second step involves decomposition of the computational domain into a locally finite number of simple cells such as tetrahedral or hexahedral cells, under the premise that all cells have to fit exactly to each other. The intersection of two different cells is either empty or it must be a two-dimensional polygon, a one-dimensional edge shared by both cells or a point. This decomposition yields the finite simplicial cells serves as computational grid. The FIT procedure is shown in Fig. A.1. The spatial discretisation of Maxwell's equations is performed where degrees of freedom are introduced as integral value.

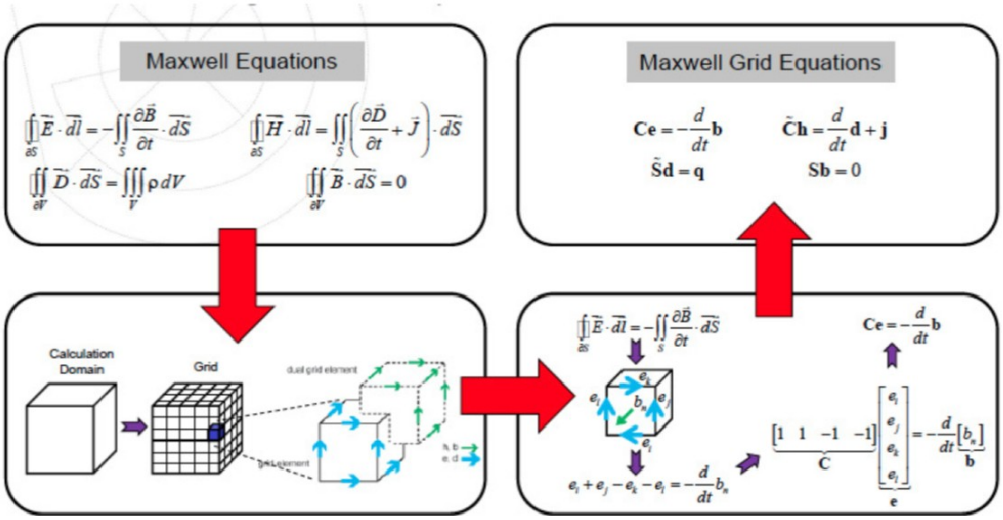

Fig. A.1 CST® MWS procedure for simulations.

The closed integral on the left side of the equation representing Faraday's law can be rewritten as the sum of four grid voltages e. The time derivative of the magnetic fluxes defined on the enclosed primary cell facets represents the right -hand side of Faraday's law equation shown in Fig. A.1. Repeating the procedure for all cell facets in the calculation domain yields the discretized matrix formulation. Where matrix C is the topological representation as the discrete equivalent of the analytical curl operator. The same scheme can also be applied to

Ampere's Law on the dual grid which involves the definition of a corresponding curl operator $\tilde{C}$ shown in top right of Fig. A.1.

In defining the necessary voltages and fluxes, their integral values have to be approximated over the edges and cell areas respectively. Therefore,the resulting coefficients depend on the average material parameters as well as the spatial resolution of the grid shown Fig. A.2.

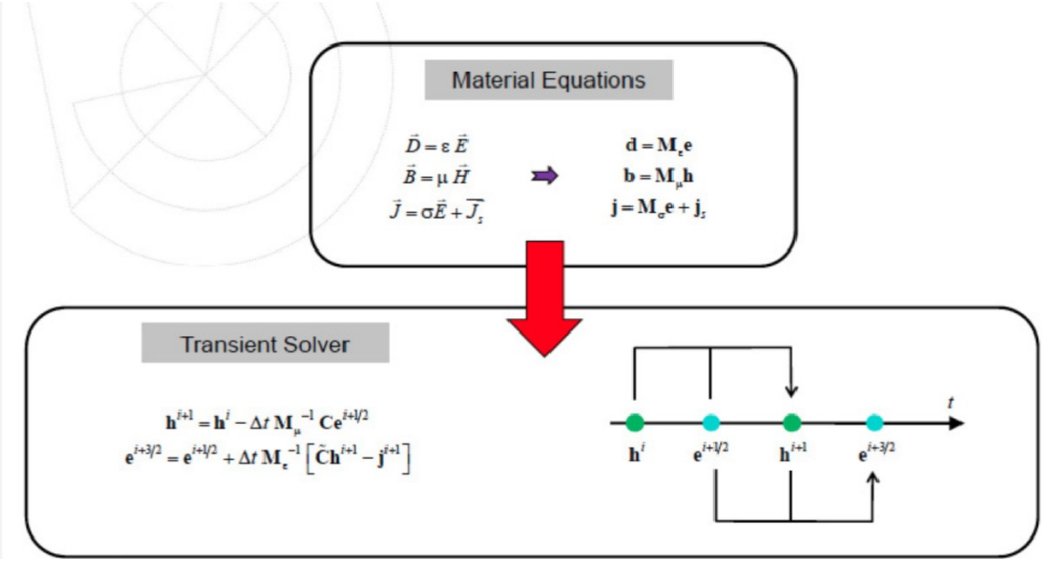

Fig. A.2 Equations for material characterization in CST® MWS.

The calculation variables are given by electric voltages and magnetic fluxes. Both of these unknowns are located alternatively in time, as in wellknown leapfrog shown in Fig. A.2. The stability limit for the time step Δt is given by Courant-Friedrich-Levy (CFL) criterion which must be fulfilled by every mesh cell.

$$\Delta t \leq \frac{\sqrt{\varepsilon \mu}}{\sqrt{(\frac{1}{\Delta x})^2 + (\frac{1}{\Delta y})^2 + (\frac{1}{\Delta z})^2}} \tag{A.1}$$